UNIVERSITY OF OKLAHOMA

GRADUATE COLLEGE

A LAGRANGIAN PERSPECTIVE OF MESOCYCLONES AND DOWNDRAFTS IN OBSERVED AND NUMERICALLY SIMULATED SUPERCELLS

A DISSERTATION

SUBMITTED TO THE GRADUATE FACULTY

in partial fulfillment of the requirements for the

Degree of

DOCTOR OF PHILOSPHY

By

DANIEL PRICE BETTEN
Norman, Oklahoma
2018

A LAGRANGIAN PERSPECTIVE OF MESOCYCLONES AND DOWNDRAFTS IN OBSERVED AND NUMERICALLY SIMULATED SUPERCELLS

A DISSERTATION APPROVED FOR THE
SCHOOL OF METEOROLOGY

BY

_____
Dr. Michael I. Biggerstaff, Chair

_____
Dr. Conrad L. Ziegler

_____
Dr. Louis J. Wicker

_____
Dr. Xuguang Wang

_____
Dr. Cameron R. Homeyer

_____
Dr. Boris N. Apanasov

Acknowledgements

Ever since I can remember, I was fascinated by the weather. When I was young, I would stand next to the window to watch lightning or stay up late to see if the rain/sleet would change over to snow. After watching my first documentary on PBS with research scientists chasing tornadoes, I knew I wanted to study severe storms. Few people are so privileged to know what they want to do at an early age, work hard, and eventually make that dream a reality. Every step of the way, I have been incredibly blessed with the support of family, friends, teachers, professors, and colleagues, without which my doctoral journey would not be remotely possible.

First and foremost, I want to thank my principal advisor and committee chair Professor Michael Biggerstaff. I first met him on a morning in June 2004, just days after he collected the dataset upon which much of this dissertation is based on. He not only convinced me to go to OU but he gave me the tools for a research project that solidified my desire to pursue my doctorate. Over the ten plus years working with him, he has been an unbelievable mentor, teacher, and friend. He empowered me with a rare freedom to pursue many of my outside-the-box ideas and research tangents. It is impossible to express my full gratitude for the opportunities and responsibilities he gave me, instilling a confidence in my abilities both as a scientist and eventual leader within our research group.

I thank Dr. Conrad Ziegler, who shared numerous insights over the years that helped me to refine my dual-Doppler and trajectory methodologies and conceptual models. I wish to thank Dr. Lou Wicker for always providing me with a modeler's perspective and teaching me the skills required to conduct my numerical modeling experiments. I want to thank the rest of my committee: Professors Boris Apanasov, Xuguang Wang, and Cameron Homeyer, for their insightful feedback, guidance and patience as I was trying to finish while working a full time

job. I additionally want to thank Drs. Luther White, Jerry Straka, and Lance Leslie who committed time as part of my original committee and unfortunately retired before I finished.

I wish to thank all of my professors in the School of Meteorology for your enthusiasm and skill in teaching incredibly complex subjects: Drs. Howie Bluestein, Alan Shapiro, Evgeni Fedorovich, Kelvin Droegemeier, Xuguang Wang, Charles Doswell, and Ken Crawford, just to name a few. Additional thanks to the SoM staff: Celia Jones, Marcia Pallutto, Christie Upchurch, Nancy Campbell, Becky Steely, and Debbie Barnhill, who were always incredibly supportive, helpful, and patient with me when I would wait to the last minute in submitting paperwork or I was dealing with bureaucratic headaches.

Spending weeks, if not months, together on field projects has built special bonds with my officemates who made the office a fun, quirky, and amazing place to work. I want to especially thank Gordon Carrie for his constant help in all things computer-related and his friendship over the many years that we have worked together in the office and out on field projects. He saved me months of time setting up software, providing invaluable computing insights, and helping me to debug code. Also, my early officemate, Dr. Ryan May, who took the time to teach me many aspects of the Python programming language, which proved instrumental in building the computational tools necessary to explore my outside-the-box ideas. Furthermore, many other colleagues contributed to my research through numerous discussions over the years: Dr. Corey Potvin, Dr. Brett Roberts, Addison Alford, Chris Schwarz, Michael Bowlan, Dr. Pat Skinner, Dr. Alex Schenkman, and Dr. David Bodine.

Finally, I want to thank my family for their never-ending love, support, and encouragement to pursue my passions throughout my entire academic journey. From a young age, my grandfather, an electrical engineer, instilled in me an intense scientific curiosity and taught me my first lessons in math, science, and computers. Much of my schooling until high school was at home, where my parents made sure I was academically challenged and prepared for a rigorous field of study. Every step along the way, they exuded a confidence in me that

allowed me to push through when I was not sure whether all the work was worthwhile. I also want to thank my brother, who provided valuable constructive feedback on my writing style on multiple occasions.

Funding for my doctoral research was provided by the National Science Foundation research grant AGS-1063537.

Table of Contents

List of Figures

Abstract

On 29 May 2004, a high-precipitation supercell thunderstorm developed in western Oklahoma and produced tornadoes during almost every distinct mesocyclone cycle over a six-hour period. The storm was exceptional in its size, lightning activity, and the duration of the parent mesocyclone lifecycles. Fortunately, the TELEX field project was in position to collect one of the best storm-scale radar datasets for a tornadic supercell with respect to the length of record, temporal resolution, and spatial coverage. The primary goal of this study was to explore the storm-scale structure of the mesocyclones, downdrafts, and low-level boundaries as the storm passed near the city of Geary, OK.

Due to a lack of available tools, the secondary goal of this study was to develop methods for elucidating Lagrangian flow behavior and highlighting the most influential flow characteristics. A trajectory mapping framework was explored and developed whereby three-dimensional trajectory behavior is mapped out in two-dimensional space, representing either a horizontal or vertical plane of reference. The framework proved adept at highlighting past or future behavior, such as prior horizontal location that reveals regions with common source regions or future attributes air parcels that eventually flow into the mesocyclone. An idealized numerical simulation was used to explore the methodology and to show the lack of sensitivity in the patterns to spatial and temporal data limitations associated with radar-based wind analyses.

After applying the trajectory mapping framework to the radar analyses, it was found that the exceptionally large and deep mesocyclone was responsible for organizing the storm-scale downdrafts throughout its lifecycle. As the midlevel circulation grew

stronger, easterly cyclonic flow opposed the environmental westerly momentum and setup a deep convergence zone associated with the rear-flank downdraft on the north side of the circulation. Near the surface, the outflow from the RFD surges was consistently demarked by secondary rear-flank gust fronts on the western and southern sides of the circulation.

Throughout the lifecycle of the mesocyclone, there was a strong correlation between the vertical structure of the mesocyclone and the location of the occlusion downdraft. When the circulation strength decreased with height, air parcels descended near the axis of rotation. However, when the gradient was negligible or increasing with height, air parcels descended on the outside of the circulation and reinforced outflow from the RFD, eventually helping initiate the occlusion process.

Finally, mesocyclone source regions were mapped out in time and space and suggested that air parcels over a shallow layer from the southern forward flank and inflow regions were reaching the mesocyclone during the mature stage of the circulation. Trajectory-based estimates of mesocyclone inflow depth and volume both increased with time as the circulation strengthened but then abruptly decreased as the inflow was cutoff by an eastward shift in the RFD. An idealized simulation was used to explore the robustness of the mesocyclone source regions and generally found similar behavior, supporting the radar-based analysis. Furthermore, it was found that the simulated mesocyclones first drew in air from the baroclinic zone in the forward flank region but eventually expanded into the inflow region as the circulations gained strength.

Chapter 1: Introduction

According to radar-based mesocyclone climatology, almost 60% of low-level mesocyclones don't produce tornadoes (Trapp et al. 2005). Moreover, observations suggest there may only be subtle storm-scale kinematic differences between tornadic and non-tornadic low-level mesocyclones (Trapp 1999; Wakimoto and Cai 2000). This ambiguity is borne out in consistently high false alarm rates (FAR) for tornado warnings across the near-storm environment spectrum (Anderson-Fey et al. 2016). Even in environments that one would expect to favor long-lived supercells, i.e. ones with high convective available potential energy (CAPE, Moncrieff and Miller 1976) and large deep-layer shear, the FAR was still above 50%. The lack of skill must therefore be due to the systematic absence of recognizable, storm-scale differences in radar presentation between tornadic and non-tornadic mesocyclones, despite a plethora of studies focused on supercell dynamics and tornadogenesis.

It is likely that the thermodynamic characteristics of the storm, unseen by radar and thus the forecasters, are more discriminating than the visible kinematic structure. Using idealized, numerical simulations, tornadogenesis has been shown to be sensitive to the strength of the cold pool (Markowski et al. 2008), the ability of the updraft to lift near-ground air via the dynamic enhancement of the updraft (Markowski and Richardson 2014), and the position of the updraft relative to the cold pool (Markowski and Richardson 2017). In many of these simulations, the buoyancy fields rapidly evolve, suggesting an element of randomness in the tornadogenesis process. Therefore, in many false alarm cases, the thermodynamic structure may have precluded

tornadogenesis even as the visible kinematic structure and near-storm environment appeared to be favorable.

Nevertheless, the occurrence of individual storms that cyclically produce tornadoes and prolific tornado outbreaks (Darkow and Roos 1970; Fujita 1973; Agee et al. 1976; Jenson et al. 1983; Johnson et al. 1987; Dowell and Bluestein 2002a; Knupp et al. 2014), suggests that a portion of the supercell spectrum, less than 20% (Burgess et al. 1982), appears to be less sensitive to their internal thermodynamic structure. The unique behavior of these storms therefore must be tied to unique, but so far unidentified, storm-scale kinematic structures or evolution. The identification of these unique structures would make it easier to connect environmental ingredients to the occurrence of prolific tornadic storms. Additionally, their presence, or lack there of, in numerical simulations can be used to validate the robustness of numerical models and whether the upper bound of the supercell spectrum is being correctly simulated.

Unfortunately, storm-scale observations with volumetric updates faster than five minutes are rare, especially when taking into consideration suboptimal radar baselines, fast storm motions, and storms with rapid mesocyclone cycling periods. There are only a handful of radar-based studies that examine more than 30 minutes of a supercell's life cycle. Many of the early studies relied on fixed-point radars located in central Oklahoma (Brandes 1977; Ray et al. 1980; Ray et al. 1981; Klemp et al. 1981; Johnson et al. 1987), which had decent baselines and collected data throughout the storm's lifecycle but had coarse temporal resolution. During the Verification of the Origins of Tornadoes Experiment (VORTEX, Rasmussen et al. 1994) project, multiple storms were observed by airborne radars (Wakimoto and Lui 1998; Wakimoto et al. 2000;

Ziegler et al. 2001; Dowell and Bluestein 2002a,b, hereafter DB02a,b), providing pseudo dual-Doppler analyses which were subject to temporal errors due to the data not being collected simultaneously and volumetric updates of five minutes, with degraded data near the ground. These analyses provided many useful insights into the structure of supercells but were not robust enough for accurate trajectory calculations.

Finally, the most recent, long duration case was observed during the second Verification of the Origins of Tornadoes Experiment (VORTEX2, Wurman et al. 2012) project in Goshen Co, Wyoming on 5 June 2009 by the Doppler on Wheels (DOWs, Wurman et al. 1997) which observed the storm from the organizing stage through the occlusion stage of the tornadic mesocyclone cycle (Markowski et al. 2012a,b; Richardson et al. 2012; Kosiba et al. 2013; Marquis et al. 2016). The resulting analyses had sufficient spatial and temporal resolution to generate robust trajectory analyses within the circulation and downdrafts. This storm is probably the most comprehensively observed storm to date, with multiple mobile radars present, environmental soundings, and surface observations from StickNets (Weiss and Schroeder 2008) and mobile mesonets vehicles. While this storm has greatly furthered our understanding of classic supercell structure, it does not represent the upper bound of the supercell spectrum as it was tornadic for a single cycle and dissipated within an hour of the tornado as it moved out of the high instability region and into a capped environment (Richardson et al. 2012; Supinie et al. 2016;). Fortunately, a previous field project was able to capture a storm within the upper bounds of supercell tornadic behavior.

In the summers of 2003 and 2004, the Thunderstorm Electrification and Lightning Experiment (TELEX, MacGorman et al. 2008) set out to observe the

electrical structure in thunderstorms on the High Plains. The available instrumentation included the Oklahoma lightning mapping array (OK-LMA), two environmental sounding units, balloon-borne electric field meters (EFM), and the recently upgraded KOUN Weather Surveillance Radar (WSR-88d) prototype. During the second summer, the project added two, C-band Shared Mobile Atmospheric Research and Teaching radars (SMART-Rs, Biggerstaff et al. 2005) to gather synchronized, volumetric data that could be synthesized into a three-dimensional wind field. The SMART-R program was initially a collaboration between the University of Oklahoma, the University of Texas A&M, the University of Texas Tech, and the National Severe Storms Laboratory (NSSL) that provided mobile radar platforms to study mesoscale meteorology.

While the goals of TELEX did not specifically target the observation of supercell thunderstorms, the field project gathered data on three different supercell storms in 2004. The storm-scale focus of the project and the objective of retrieving three-dimensional wind structure correlating with the EFM observations resulted in long observational periods for the two mobile radars, often resulting in synchronized, volumetric scans for over an hour (MacGorman et al. 2008). The storm-scale observations from TELEX have generated numerous studies on the electrification characteristics and electrical structure of supercell thunderstorms and a general sense of the corresponding storm's dynamics (Payne et al. 2010; Weiss et al. 2012; Brunning and MacGorman 2013; Calhoun et al. 2013).

On 29-30 May 2004, the TELEX field project collected one of the best storm-scale datasets ever collected on a tornadic supercell. Environmental soundings were taken along the storm's track, first near the storm's initiation along the dryline in

western Oklahoma, all the way out to central Oklahoma, detailing the heterogeneity in the environment. Multiple EFM balloons were launched, detailing the electric field structure. And most importantly, the two mobile radars collected synchronized, three-minute volumes from 2246 UTC to 0212 UTC.

This dissertation explores the storm-scale structure and dynamics during tornadic mesocyclone cycles in the Geary, OK supercell. A generalized background on supercell dynamics, with a special focus on downdraft characteristics and mesocyclone development and behavior is presented in Chapter 2. Chapter 3 details the temporal evolution and three-dimensional structure of the storm, beginning at the organizing stage and ending with the redevelopment of the mesocyclone during the next cycle. In Chapter 4, a trajectory mapping methodology is explored using a numerical model, with a particular emphasis on proxy variables that can be estimated from the radar-derived wind analysis and the sensitivity of the trajectory maps to decreased temporal and spatial resolution. The storm-scale structure and evolution of the rear-flank downdraft (RFD) is explored in Chapter 5, using bulk and individual trajectory behavior. Source regions for downdraft air are visualized and the primary downdraft flow regimes are identified, leading to speculation on potential downdraft forcing mechanisms. In Chapter 6, the structure and evolution of the mesocyclone is explored and put into context relative to the downdraft evolution. Axisymmetric structure is compared with low-level trajectory behavior and source regions and tilting regions are identified. Finally, in chapter 7, the source regions from Chapter 6 are compared with those from a numerical simulation, which demonstrates some similarities to those in Chapter 6.

Chapter 2: Background

2.1 Supercell Thunderstorm Conceptual Models

Long-lived thunderstorms with persistent updrafts were first called "supercells" by Browning (1962). Most of the early conceptual models of supercells utilized visual reports and crude radar displays from the 1950s to the mid 1970s (Browning 1963; Browning 1964; Newton 1963; Marowitz 1972). The observational limitations resulted in conceptual models primarily focusing on the precipitation structure and the location of the primary updraft (Browning and Ludlam 1962; Browning and Donaldson 1963; Ludlam 1963). They attributed the sustained organization of the storm to environmental vertical wind shear causing differential advection of the precipitation away from the updraft. Browning (1964, Figure 2.1) summarized these studies in a three-dimensional conceptual model that illustrated the unique characteristics of the persistent updraft/downdraft pair suggested in previous analyses. In their conceptual model, the primary updraft turns cyclonically as it ascends until reaching the anvil, reflecting the cyclonically curved flow in the environment. The primary downdraft originates at midlevels and rotates around the updraft before descending in the rear flank of the storm due to negative buoyancy, reinforcing the main gust front. The conceptual model also highlighted the position of the tornado as being found on the interface between the inflow and outflow.

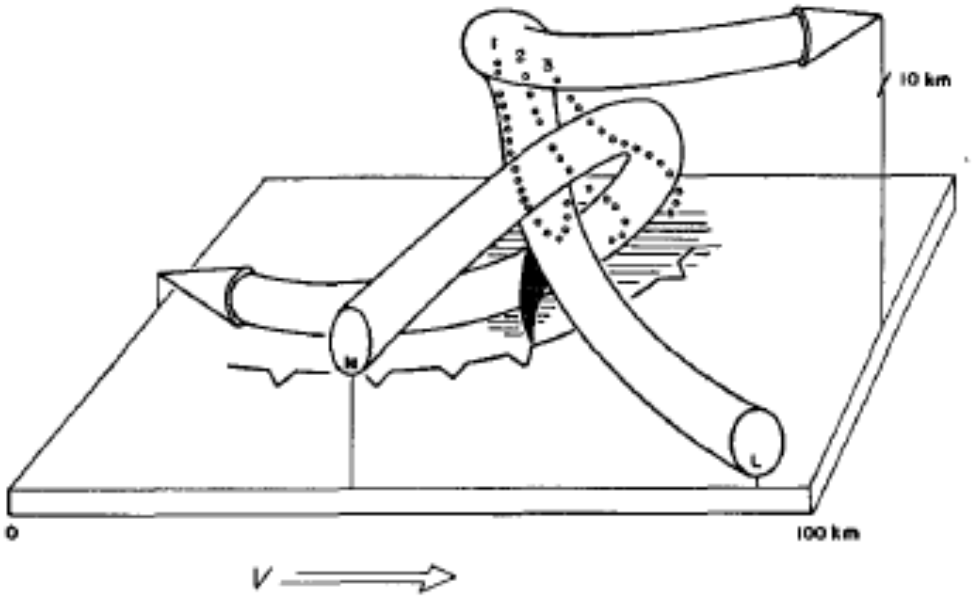

Fig. 2.1 Three-dimensional conceptual model of storm-relative airflow in the primary updraft (L) and downdraft (M) in a supercell thunderstorm. The hatched area indicates precipitation at the surface and the primary gust front is drawn as a cold front (Browning 1964).

After another decade of radar observations (Burgess et al. 1977; Barnes 1978a; Brandes 1978; Brown et al. 1978; Lemon et al. 1978) and the first three-dimensional numerical simulations (Schlesinger 1978; Klemp and Wilhelmson 1978), Lemon and Doswell (1979) formulated a substantially more detailed conceptual model of the airflow in supercell thunderstorms (Figure 2.2). The updated conceptual model three-dimensionally illustrated the areal extent and temporal evolution of the previously identified primary updraft and rear-flank downdraft (RFD) while adding a new, organized downdraft downwind of the updraft in the forward flank of the storm. The new mesocyclone conceptual model divided the evolution into three stages, an organizing stage during which the mesocyclone developed in primary updraft, a mature stage whereby the mesocyclone was found to straddle the vertical velocity gradient

between the updraft and rear-flank downdraft, and the occlusion stage where the mesocyclone is overtaken by the rear-flank downdraft outflow and dissipates.

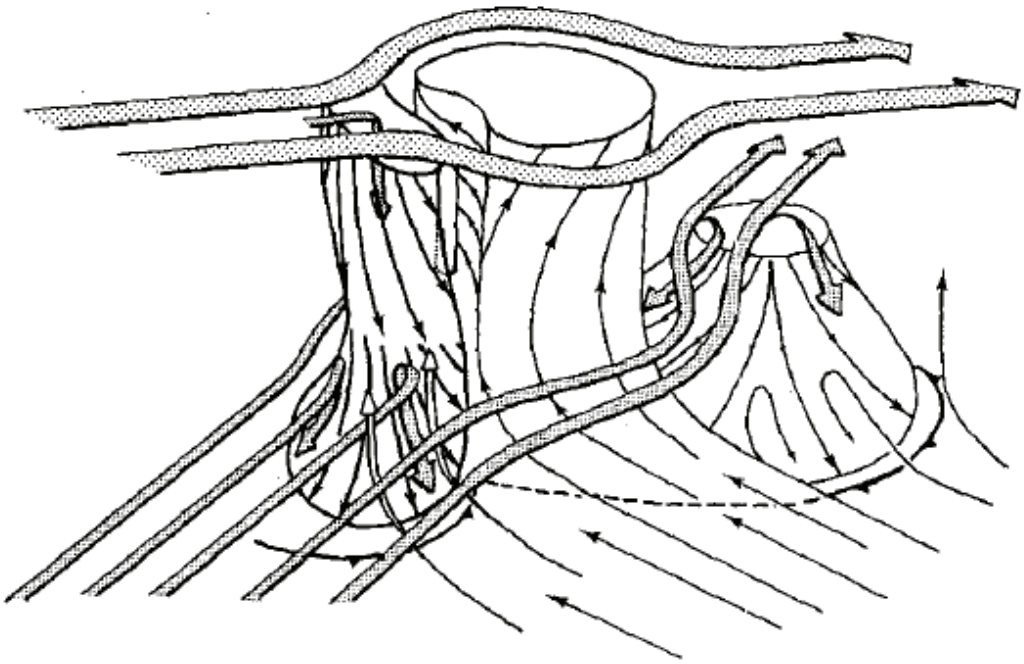

Fig. 2.2 Three-dimensional schematic of storm-relative ambient airflow (wide streamlines) and drafts in a supercell thunderstorm. Cold outflow boundaries are depicted as cold fronts and weak outflow boundaries as dashed lines (Lemon and Doswell 1979).

Although previous conceptual models portrayed the tornado as straddling the low-level buoyancy gradient, the Lemon and Doswell conceptual model was the first to illustrate the transition of the mesocyclone from being updraft dominant to downdraft dominant over its lifecycle. Impressively, the mesocyclone portion of their conceptual model has undergone little modification since it was conceived almost 40 years ago. The downdraft intersecting with the mesocyclone was later clarified as the occlusion downdraft by Klemp and Rotunno (1983) and was shown to differ in origin and forcing from the larger scale rear-flank downdraft. Observational studies confirmed the ubiquity of the occlusion downdraft in mature supercell storms, which can be as narrow as a few

kilometers (Brandes 1978; Dowell and Bluestein 1997; Wakimoto and Lui 1998; Wakimoto and Cai 2000; Ziegler et al. 2001; DB02a; Markowski et al. 2012a; Marquis et al. 2012; Kosiba et al. 2013).

At the surface, the conceptual model illustrates the dominance of the downdrafts in the rear and forward flanks of the storm. Gust fronts are depicted at the leading edge of the downdraft outflows with the rear-flank gust front (RFGF) swinging out beneath the mesocyclone as the RFD expands and the forward-flank gust front (FFGF) extending along the forward flank reflectivity core. Subsequent observations taken by mobile mesonets vehicles (Shabbott and Markowski 2006) within the forward flank regions of a dozen supercell storms revealed that tornadic supercells were often associated with weak or non-existent FFGFs, suggesting that organized forward-flank downdrafts are potentially detrimental to the development of tornadoes. This is an unsurprising finding as cold air descending downwind of the mesocyclone likely undercuts the mesocyclone, shortening its lifecycle. Recent numerical simulations by Beck and Weiss (2013) demonstrate that the more defining boundary is located between the rear and forward flanks in what they call the "left-flank convergent boundary" (LFCB), separating the cold RFD outflow from the modified storm-inflow found in the forward flank. Surface observations in multiple tornadic supercells by Weiss et al. (2015) appear to corroborate portions of their LFCB conceptual model but rapidly evolving thermodynamic characteristics within the storm make it difficult to fully investigate the temporal evolution of the thermodynamic structure near the surface.

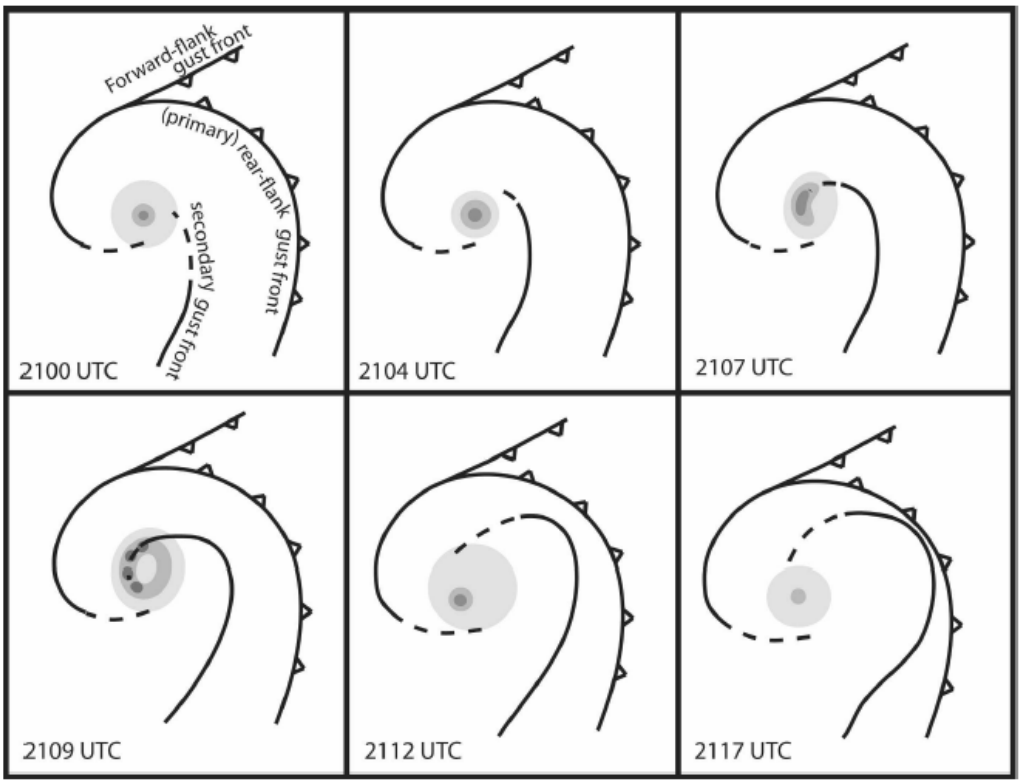

Fig. 2.3 Schematic of temporally evolving boundaries surrounding a tornadic mesocyclone. Primary gust fronts are indicated as cold fronts, secondary boundaries are drawn as solid lines, and dashed lines are used to indicate the boundaries with high uncertainty (Marquis et al. 2008).

The use of multiple mobile mesonet vehicles, essentially weather stations mounted on vehicles (Straka et al. 1996), to collect finer-scale surface observations in the hook echo region suggest that tornadic supercells tend to have weaker cold pools in the rear and forward flanks of the storm, regardless of whether they had strong or non-existent forward-flank kinematic boundaries (Markowski 2002; Markowski et al. 2002; Lee et al. 2004; Finley et al. 2004; Shabbott and Markowski 2006; Finley et al. 2008; Hirth et al. 2008; Lee et al. 2011; Skinner et al. 2011; Markowski et al. 2012a; Weiss et al. 2015). Especially around tornadoes, the thermodynamic structure was highly variable, mostly likely caused by the rapid evolution of internal downdrafts moving through the rear-flank of the storm. These internal downdrafts have also been observed

in radar-based analyses being manifested as secondary, rear-flank gust fronts (SRFGF) (illustrated in Figure 2.3 from Marquis et al. 2008; Wurman et al. 2007; Wurman et al. 2010; Kosiba et al. 2013; Skinner et al. 2014; Riganti and Houston 2017). Trajectory analyses by Skinner et al. (2015) based on assimilated radar data suggest that the internal surges are more likely associated with modulations in the dynamically driven portion of the RFD rather than the buoyancy driven primary RFD, similar but separate from the occlusion downdraft. It is unclear whether SRFGFs are driven by a portion of the occlusion downdraft or if the associated downdraft should be considered a distinct downdraft region neither associated with the primary RFD nor the occlusion downdraft (Kosiba et al. 2013, Fig. 2.4).

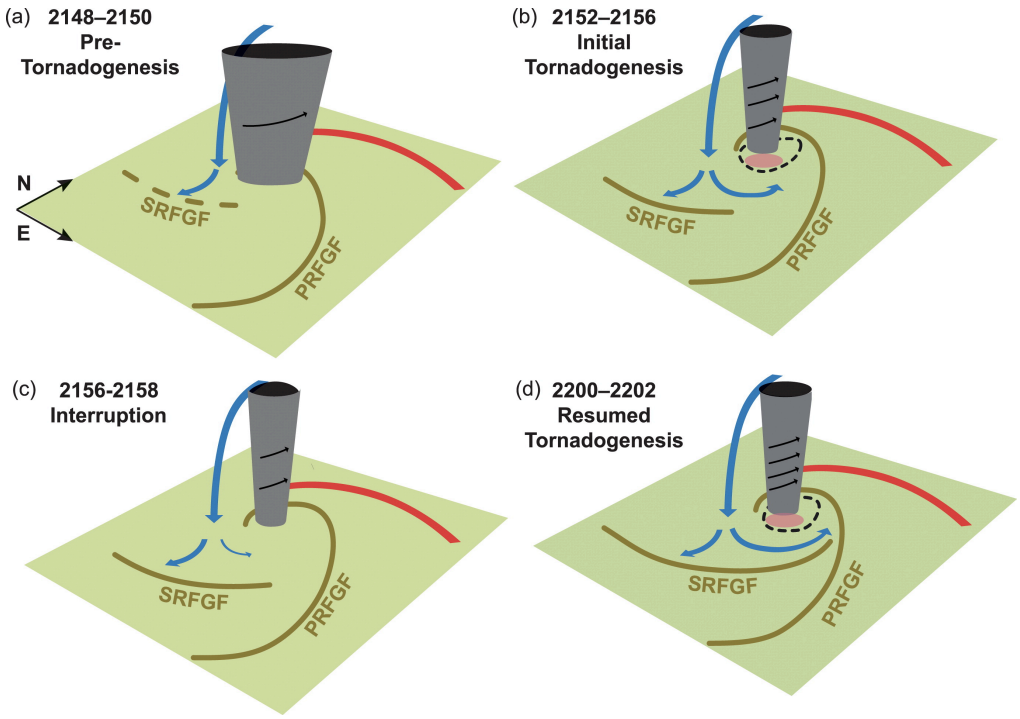

Fig. 2.4 Schematic illustrating the evolution of downdrafts and boundaries during tornadogenesis in the 5 June 2009 Goshen County storm. Blue lines indicate the position and outflow of the portion of the RFD that is supporting convergence along the secondary rear-flank gust front. Olive lines indicate the primary rear-flank gust front (PRFGF) and secondary rear-flank gust front (SRFGF). A red line depicts the position of the forward-flank gust front and they grey cylinder indicates the size and position of the tornado cyclone (Kosiba et al. 2013).

A few studies have been able to focus on supercells where the mesocyclone cyclically redevelops for hours (Burgess et al. 1982) and avoids being undercut by either of the storm-scale downdrafts. Observational studies by Dowell and Bluestein (2002a,b), and Beck et al. (2006, hereafter B06) suggested modifications to the near-ground boundaries. Instead of a persistent, forward-flank gust front (FFGF), Dowell and Bluestein (2002a) and B06 only noted weak kinematic boundaries extending north from the circulation (DB02a) or only present above the surface (B06). It seems plausible that the forward flank region of cyclic, tornadic supercells is characterized by less organized forward flank downdrafts and minimal evaporative cooling, relative to non-cycling supercells, as a strong and/or cold forward flank downdraft would be prone to undercutting the mesocyclone, cutting the mesocyclone's lifecycle short. This would explain how the occluding mesocyclones survive well into the occlusion stage, when the flux of inflow air into the occluded updraft is cutoff and the updraft draws air almost exclusively from the forward flank region (Dowell and Bluestein 2002a,b).

Following the occlusion stage, the Lemon and Doswell conceptual model described the primary updraft as having to redevelop if the supercell is going to produce another mesocyclone. The redevelopment process was further detailed by a high-resolution, idealized numerical simulation by Adlerman et al. (1999) who found that as the mesocyclone occluded and retreated rearward into the precipitation core, the primary updraft at midlevels followed suit, causing the surface gust front to become temporarily displaced from the primary updraft. However, airborne radar observations of four sequential tornadic mesocyclones by Dowell and Bluestein (2002a,b) revealed

that the primary updraft remained above the main RFGF and only a small portion of the updraft retreated rearward with the occluding mesocyclones. It should be noted that the idealized simulation was based on a sounding with a negative, storm-relative u-component of the wind between 2 and 4 km while the observed storm had a slightly positive u-component at midlevels. The differences in midlevel flow potentially explain the differing updraft behavior during redevelopment, suggesting that the two storms represent a spectrum of behavior within the subset of cyclic supercells.

2.2 Supercell Downdraft Formation

Vertical motion in thunderstorms is governed by the vertical momentum tendency equation (2.1), presented here in its compressible, nonhydrostatic form. In (2.1), w is the vertical velocity, t is time, θ_ρ is density potential temperature, π' is the perturbation Exner function, C_p is the heat capacity of air at constant pressure, and B is buoyancy due to thermal gradients and precipitation loading. Therefore, the primary downdraft forcing mechanisms are the vertical perturbation pressure gradient and buoyancy.

$$\frac{dw}{dt} = -\theta_\rho C_p \frac{\partial \pi'}{\partial z} + B \quad (2.1)$$

Ordinary thunderstorms develop downdrafts as the buoyancy of air parcels in the updraft is reduced by the entrainment of drier midlevel air, evaporative cooling, and drag due to precipitation-loading (Byers and Braham 1949). The same forcing mechanisms are present in downdrafts in supercell thunderstorms except that the environmental wind shear and the resulting storm-scale circulation produce consistent, organized updraft and downdraft zones. Although the downdrafts may be consistent, the

forcing mechanisms may vary substantially in space and time as evidenced by surface observations of buoyancy fields in the rear flank (Markowski et al. 2002; Lee et al. 2004; Finley et al. 2004; Grzych et al. 2007; Finley et al. 2008; Hirth et al. 2008; Lee et al. 2011; Skinner et al. 2011; Lee et al. 2012; Weiss et al. 2015).

Initial surface observations of wet-bulb potential temperature in the rear flank of supercells (Charba and Sasaki 1971; Lemon 1976; Barnes 1978a) suggested that environmental midlevel air was entraining into the storm and descending to the surface. Early investigations by Browning (1964) hypothesized that the storm-scale RFD was made of midlevel air wrapping cyclonically around the circulation before descending to the surface after gaining negative buoyancy due to evaporation, melting, and precipitation loading. Conversely, Lemon and Doswell (1979) attributed the RFD to descending environmental midlevel air on the rear-flank as suggested by low reflectivity at midlevels directly above low-level divergence in previous radar analyses (Nelson (1977); Barnes (1978); Ramond (1978); Klemp and Wilhelmson 1978). They hypothesized that midlevel air initially descends due to a stagnation high arising from the impingement of the mid to upper-level updraft by storm-relative westerly environmental momentum, analogous to an obstacle flow, before evaporational cooling and precipitation loading cause the air to descend further (Fig. 2.2). However, the role of the midlevel stagnation zone was clarified by subsequent numerical modeling studies by Rotunno (1981) and Rotunno and Klemp (1982), who demonstrated that the high pressure observed on the upshear side of supercell updrafts is due to the interaction of the midlevel environmental shear and the updraft, rather than a true obstacle flow. Despite the presence of an upper-level downdraft underneath the stagnation zone in a

simulation by Klemp et al. (1981), trajectories passing through the downdraft did not end up in the low-level RFD. Rather, the simulation suggested that precipitation loading and evaporational cooling were responsible for the low-level downdraft.

Alternatively, a more recent high-resolution simulation by Schenkman et al. (2016, hereafter SC16) examined multiple RFD surges, both anomalously cold and warm. In the warm RFD surges, the downdrafts were being forced by a midlevel stagnation high pressure region associated with converging flow between the midlevel mesocyclone and environmental flow (Figure 2.5). The resulting trajectory pattern revealed that air from the west at midlevels converged with trajectories from the east before descending, with the eastern trajectories having experienced more negative buoyancy forcing than those from the west. Subsequent cold RFD surges consisting primarily of western trajectories that were forced down by negative buoyancy forcing through evaporational cooling and precipitation loading. The cold RFD surge in the simulation was thus more similar to the Browning (1964) conceptual model and conclusions drawn from thermodynamic retrievals based on radar analyses (Brandes 1984; Hane and Ray 1985), that also implied the primary culprits were evaporational cooling, melting, and precipitation loading. Conversely, the warm RFD resembles that observed in tower measurements presented by Johnson et al. (1987), where downdraft zones were marked by dry, warm air being forced to descend on the west side of the mesocyclone. The forced ascent is marked by an increase in potential temperature, relative to the surrounding air, and negative pressure perturbations rather than positive perturbations found underneath cold downdrafts.

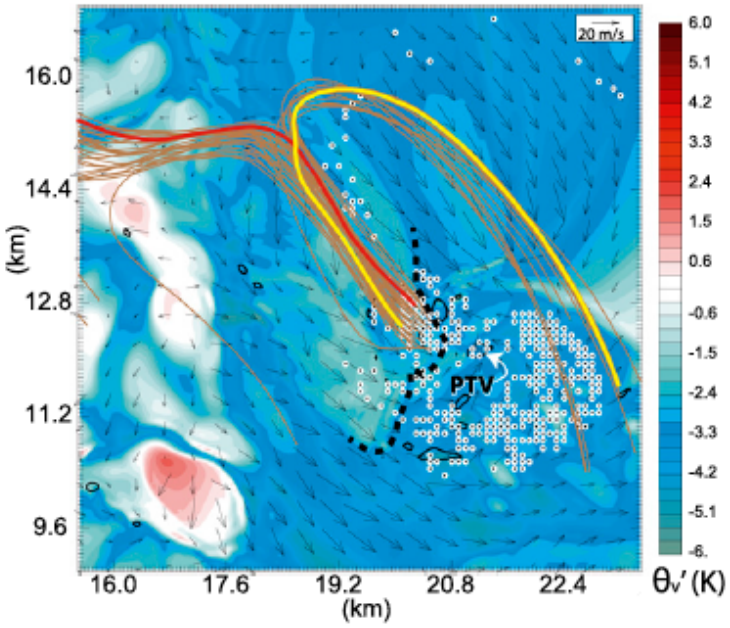

Fig. 2.5 Virtual potential temperature deficits color-shaded with a set of backward trajectories illustrating the source regions for air behind an internal RFD surge. Note the area of convergence at (x = 18.5, y = 15) between trajectories from the east and west (Schenkman et al. 2016).

Additionally, the environmental thermodynamic and wind profiles can be expected to modify the forcing mechanism and the updraft-relative position of the RFD. Simulations by Van den Heever and Cotton (2005) and Mashiko et al. (2009) suggest that precipitation loading can become more significant and even dominant when the median hail size is increased or the environment is anomalously moist, both acting to limit evaporation and melting. Meanwhile, the updraft-relative position of the RFD has been shown to be very sensitive to the storm-relative midlevel flow in simulations (Brooks et al. 1994) and anvil-level flow in observations (Rasmussen and Straka 1998). As the mid to upper level storm-relative flow is increased, precipitation is advected further downstream of the updraft and thus the forcing mechanisms associated with the precipitation are also shifted downstream, relative to the updraft. An observational climatology (Rasmussen and Straka 1998) suggested that supercells transition towards

high-precipitation structure with time, implying a shift in the location and downdraft forcing mechanism with time.

Around the low-level mesocyclone, a separate downdraft from the RFD, the occlusion downdraft (Klemp and Rotunno 1983), is forced by vertical pressure gradients associated with the tilt and strength of the mesocyclone with height. Successive numerical modeling (Wicker and Wilhelmson 1995; Adlerman et al. 1999,) and observational (Brandes 1984; Hane and Ray 1985; Wakimoto and Lui 1998; Wakimoto and Cai 2000; Skinner et al. 2014) studies confirmed the dynamic origins of the occlusion downdraft. This downdraft region can appear as a discrete downdraft from the primary RFD or as a local enhancement of the larger-scale RFD (Markowski et al. 2002). In their investigations into the forcing mechanism behind the SRFGF, Skinner et al. (2015) suggested that internal RFD surges were associated with a dynamically-induced downdraft, similar to but distinct from the traditional occlusion downdraft. Conversely, numerical simulations have found the internal surges to be the result of downdrafts driven by precipitation-loading (Mashiko et al. 2009) or midlevel flow stagnation (Schenkman et al. 2016).

While individual flow regimes can be expected to exist within the broader rear-flank downdraft, it should not be surprising that a large spectrum of rear-flank and occlusion downdraft structures have been observed and numerically simulated. Assuming the occlusion downdraft is closely connected to the vertical structure and strength of the mesocyclone, then the location of the primary RFD can be expected to dictate whether two distinct downdrafts are manifested or the occlusion downdraft is simply a local enhancement within the broader RFD. Furthermore, given the varied

forcing mechanisms associated with each downdraft, their positions relative to each other can be expected to vary across the mesocyclone lifecycle, much less across the supercell precipitation classification spectrum (i.e low-precipitation to high-precipitation).

Finally, descending motion in the forward flank region is more analogous to downdrafts in ordinary convection, whereby subsaturated environmental air flowing into the precipitation core acquires negative buoyancy through evaporative cooling, melting, and precipitation loading. While the conceptual model of Lemon and Doswell depicts the downdraft as being well-organized, surface observations in a dozen supercells suggests that air at the surface originated between 1 and 2 km, with the tornadic supercells having an average source altitude of 1.2 km (Shabbot and Markowski 2006). They also found a strong correlation between the negative buoyancy at the surface and the local relative humidity profile, demonstrating that the outflow and associated gust front in the forward flank region will vary greatly according to the local thermodynamic profile. Moderate density potential temperature deficits (~5.5 K) were found in environments with large dewpoint depressions at the surface (~ 6 K). Therefore, in environments with small dewpoint depressions, little if any low-level divergence can be expected at low-levels in the forward flank region, resulting in weak or non-existent FFGFs.

2.3 The Origins of Rotation in Supercell Thunderstorms

2.3.1 Origins of Midlevel Rotation

As early as Fawbush and Miller (1954), the presence of wind speeds increasing with height has been used as an important forecasting ingredient when making

predictions regarding the ability of storms to gain rotation about a vertical axis. Indeed, individual case studies (Browning and Ludlam 1962; Ludlam 1963; Browning and Donaldson 1963) and proximity soundings near tornadoes and composite maps of the synoptic conditions confirmed the strong association between vertical wind over the lowest 500mb of the atmosphere and the ability of storms to rotate (Fawbush and Miller 1954; Beebe 1956; Maddox 1976; Darkow and McCann 1977). Initial hypothesizes focused on the ability of the supercell updraft to advect low-level momentum up to midlevels, generating a horizontal momentum gradient between the lower momentum in the updraft and the high midlevel momentum present in the environment (Newton and Newton 1959; Newton and Frankhauser 1964). Using a simplified version of the vertical vorticity tendency equation, Barnes (1968, 1970) examined the sources of vertical vorticity generation, the tilting of horizontal vorticity by the updraft, and horizontal convergence acting on existing vertical vorticity, in radar analyses of fourteen storms. It was found that the tilting term should be on the same order of magnitude as the stretching term, and thus, in the absence of ambient vertical vorticity, they concluded that the tilting of horizontal vorticity at low-levels by the updraft must be the general source of rotation in supercells, which is illustrated in Figure 2.6.

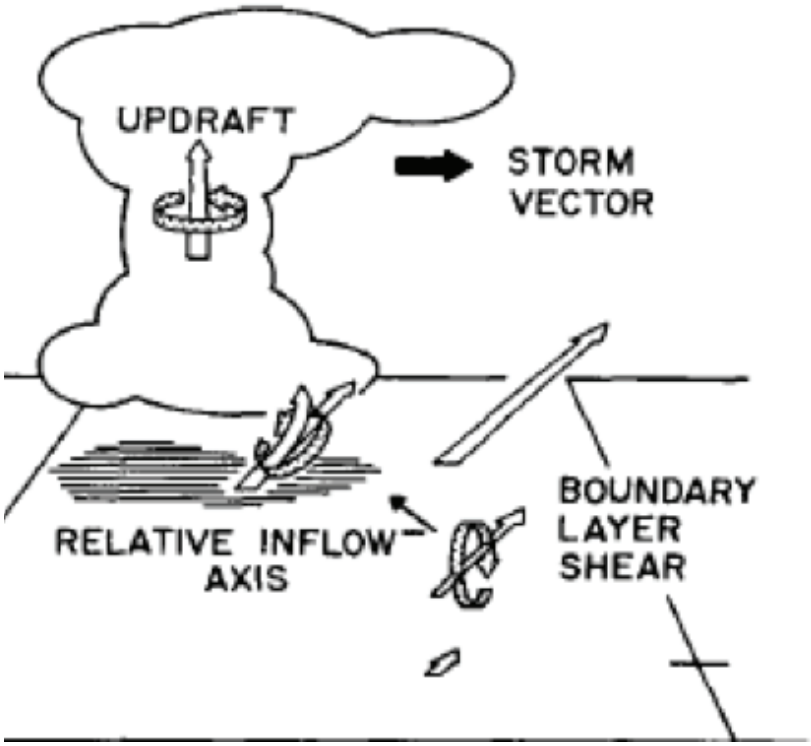

Fig. 2.6 Schematic illustrating how environmental, horizontal vorticity is tilted into the vertical axis by the updraft (Barnes 1968).

By the 1970s, it became feasible to run numerical simulations on computers, encouraging the development of complex, three-dimensional numerical models that were capable of simulating moist convection (Schlesingler 1975) and precipitation (Schlesingler 1978; Klemp and Wilhelmson 1978a). These numerical models were immediately used to investigate the sensitivity of storms to the ambient wind shear (Schlesingler 1978; Klemp and Wilhelmson 1978b) and to test the observationally driven hypothesizes. Using a non-precipitating version of his three-dimensional model, Schlesinger (1975) demonstrated that low-level, horizontal vortex tubes, associated with ambient vertical wind shear, were tilted by the updraft into two, counter-rotating, vertically oriented vortices, supporting the conceptual model drawn by Barnes (1968). Once precipitation was introduced, both numerical models were used to simulate

thunderstorms with unidirectional and veering wind profiles. In the unidirectional shear case, simulations produced a storm that eventually split into a pair of storms, one rotating cyclonically and moving anomalously to the right, and the other rotating anticyclonically and moving anomalously to the left. Conversely, when low-level, cyclonic curvature was introduced into the wind profile, the cyclonic member was favored. These results were consistent with previous observations of storm behavior in sheared environments, giving credence to the use of numerical models in studying supercell storms.

The dependence of storm splitting behavior on the curvature of the wind profile, or lack thereof, can be explained through a simple examination of the mechanisms by which storm-scale rotation is acquired. The vertical vorticity equation in height coordinates with the Boussinseq approximation is given in (2.2), where ζ is relative vertical vorticity, t is time, f is the Coriolis parameter, (u, v, w) are the zonal (u), meridional (v), and vertical (w) components of velocity, respectively, and F_U and F_V are the diffusive tendencies in u and v.

$$\frac{d\zeta}{dt} = \underbrace{(f + \zeta)\left(\frac{\partial \mathrm{u}}{\partial \mathrm{x}} + \frac{\partial \mathrm{v}}{\partial \mathrm{y}}\right)}_{\text{Stretching}} + \underbrace{\left(\frac{\partial \mathrm{u}}{\partial \mathrm{z}}\frac{\partial \mathrm{w}}{\partial \mathrm{y}} - \frac{\partial \mathrm{v}}{\partial \mathrm{z}}\frac{\partial \mathrm{w}}{\partial \mathrm{x}}\right)}_{\text{Tilting}} + \underbrace{\left(\frac{\partial F_V}{\partial \mathrm{x}} - \frac{\partial \mathrm{F}_U}{\partial \mathrm{y}}\right)}_{\text{Diffusion}} \quad (2.2)$$

This equation reveals three primary terms that contribute to changes in vertical vorticity: the stretching of vertical vorticity already present including that due to earth's rotation, the tilting of horizontal vorticity into the vertical by vertical motion, the turbulent mixing of vertical vorticity, and that generated through buoyancy gradients. If one assumes that no ambient vertical vorticity is present in the mesoscale environment and the magnitude of the Coriolis term is too small to be stretched, then vertical

vorticity must initially be generated through the tilting of horizontal vorticity. According to the horizontal vorticity tendency equation (2.3), where $v_H$is the horizontal wind, horizontal vorticity, ω_H, can be generated three different ways. Either through the tilting of vertical vorticity into the horizontal, baroclinically through horizontal buoyancy gradients, or through turbulent mixing where F_W is the diffusive tendency in w. Therefore, as Barnes (1968) hypothesized, vertical vorticity must arise in thunderstorms from the tilting of horizontal vorticity, either already present in the ambient wind profile or generated baroclinically by buoyancy gradients associated with the storm. Recent studies by Schenkman et al. (2012, 2014) and Roberts et al. (2016) have shown that frictional generation of horizontal vorticity, included in the diffusive term, can favorably contribute as well.

$$\frac{d\omega_H}{dt} = \underbrace{\omega \cdot \nabla v_H}_{\text{(Stretching + Tilting)}} + \underbrace{\nabla \text{x} (\text{B}\,\widehat{k})}_{\text{Baroclinic}} + \underbrace{\left(\frac{\partial \text{F}_W}{\partial \text{y}} - \frac{\partial \text{F}_V}{\partial \text{z}}, \frac{\partial F_U}{\partial \text{z}} - \frac{\partial \text{F}_W}{\partial \text{y}}\right)}_{\text{Diffusion}} \quad (2.3)$$

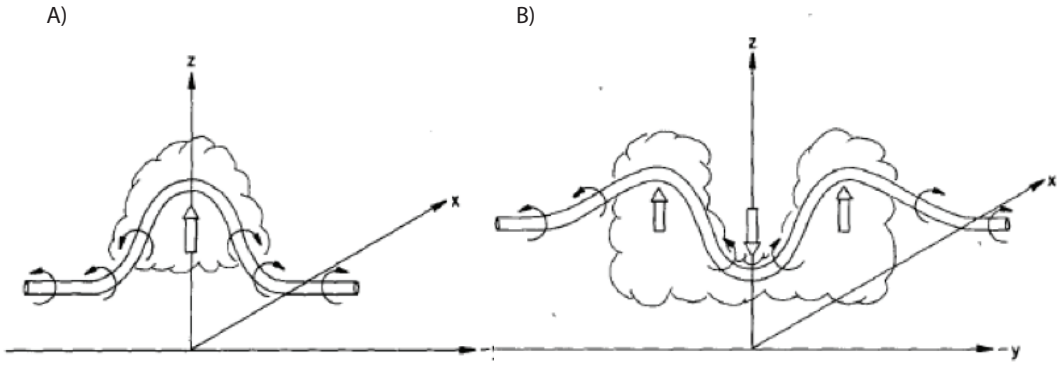

Fig. 2.7 Schematic illustrating how a horizontal vortex tub interacts with a single updraft (a) and after the storm cell splits (b) (Rotunno 1981).

An analytic model was used by Rotunno (1981) to demonstrate that when an axisymmetric updraft is imposed on a unidirectional shear wind profile, counter-rotating vortices develop in the absence of any thermodynamic effects (Fig. 2.7). While simple,

this model, consistent with the non-precipitating experiments of Schlesinger (1975), demonstrating that midlevel rotation can be acquired purely by the tilting of vertical wind shear by the updraft. In order to isolate the influence of the ambient wind shear on the updraft, Rotunno and Klemp (1982) linearized the anelastic form of the shallow, inviscid equations of motion with respect to the environmental wind profile. Then, they solved for the non-hydrostatic pressure perturbation response to the environmental wind shear interacting with the updraft (2.4) by taking the three-dimensional gradient of both sides of the equation and neglecting buoyancy. The resulting equation states that the pressure perturbation, π_L, is proportional to the dot product of the environmental

$$\nabla^2 {\pi_L}' \sim \frac{\partial \overline{\boldsymbol{V}}}{\partial \mathrm{z}} \cdot \nabla w' \qquad (2.4)$$

vertical wind shear vector, $\overline{\boldsymbol{V}}$, with the horizontal gradient of vertical motion. In this idealized scenario, high pressure will be generated on upshear side of the updraft and low pressure on the downshear side (Fig. 2.8a). The primary implication is that even if the shear vector is strong but constant with height, then the strong pressure perturbations will be induced but the vertical pressure gradient on the upshear and downshear sides of the updraft will be negligible. However, when the shear vector is turning with height, the location of the responding pressure perturbations, relative to the updraft center, are changing with height and thus generating vertical pressure gradients on the sides of the updraft. In the case of a veering shear vector, the vertical pressure gradient force will be directed upward on the right flank and downward on the left flank and therefore favoring updraft growth on the right flank of the storm (Fig. 2.8b).

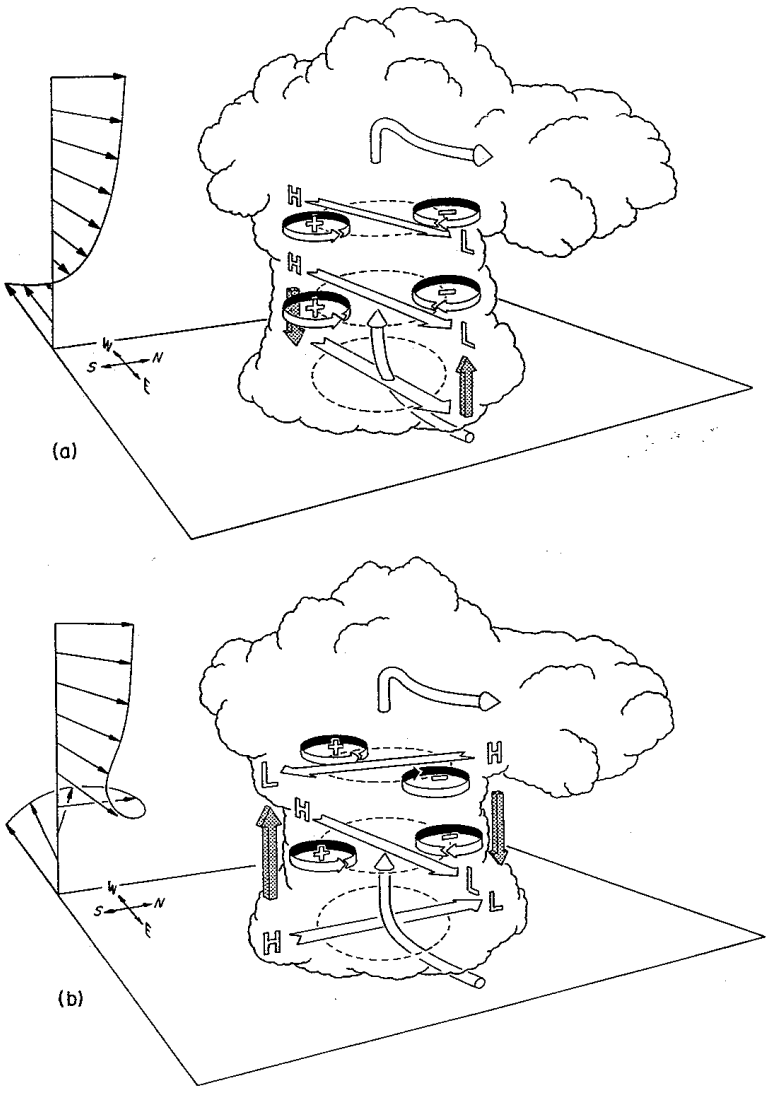

Fig. 2.8 Schematic illustrating the pressure field response (H/L) to wind profiles with (a) unidirectional shear and (b) clockwise turning of the shear vector with height. The resulting vorticity field at different levels is depicted as + (cyclonic)/ - (anticyclonic) (Klemp et al. 1987).

The influence of the environmental shear profile was put into context with respect to the other contributions to the perturbation pressure field by dividing the Laplacian of perturbation pressure into three terms, the linear π_L (2.4, environmental shear), non-linear π_{NL} (2.5, internal storm wind gradients, dominated by vertical vorticity), and buoyant π_B (2.6) contributions. Using a three-dimensional model, the

$$\nabla^2 \pi_{NL}{}' = -\left(\frac{\partial \mathrm{u}'}{\partial \mathrm{x}}\right)^2 - \left(\frac{\partial \mathrm{v}'}{\partial \mathrm{y}}\right)^2 - \left(\frac{\partial \mathrm{w}}{\partial \mathrm{z}}\right)^2 - 2\left(\frac{\partial \mathrm{u}'}{\partial \mathrm{z}}\frac{\partial \mathrm{w}}{\partial \mathrm{x}} - \frac{\partial \mathrm{v}'}{\partial \mathrm{z}}\frac{\partial \mathrm{w}}{\partial \mathrm{y}}\right) - 2\,\frac{\partial \mathrm{v}'}{\partial \mathrm{y}}\frac{\partial \mathrm{u}'}{\partial \mathrm{x}} \qquad (2.5)$$

$$\nabla^2 \pi_B{}' = \frac{\partial \mathrm{B}}{\partial \mathrm{z}} \qquad (2.6)$$

terms were compared for a unidirectional shear profile and a veering shear vector profile. In both cases, the non-linear term contributes more than the linear term and is maximized on the right and left flanks, correlating to the counter-rotating vortices arising from the tilting of horizontal vorticity. For a unidirectional shear profile, the linear and non-linear contributions are perfectly offset in space from each other, whereas in the veering shear profile experiment, the linear term contribution overlaps with the non-linear contribution, enhancing the right flank portion of the updraft and mitigating the left flank side of the updraft. This spatially biased dynamic pressure response causes the cyclonically circulation to experience vortex stretching and the anticyclonic circulation to be compressed, generating a nonlinear pressure response and thus exacerbating the favoritism of the cyclonic side of the updraft. While not overly complex, this relationship has a profound implication: it is the turning of the shear vector with height that promotes the dominance of the cyclonic member and not the turning of the wind with height, as the shear vector must be changing direction to promote vertical pressure gradients that enhance the updraft on the right side of the midlevel shear vector.

Whereas Rotunno and Klemp (1982) focused on the relationship between the updraft and the sheared environment, Davies-Jones (1984) sought to understand the relationship between the updraft and the tilting of low-level vertical vorticity. To this end, Davies-Jones (1984) developed an analytical model that would reveal the

conditions that would maximize the correlation between vertical velocity and vertical vorticity and thus maximizing the vertical stretching of vertical vorticity. The analytical model was derived in an updraft following reference frame because, as noted by Lilly (1982), the correlation of vertical vorticity and vertical velocity is sensitive to the speed and direction of the updraft. Furthermore, Davies-Jones separated the horizontal vorticity vector into two parts, the streamwise component, pointing in the direction parallel to the updraft-relative wind vector, and the crosswise component, pointing in the direction perpendicular to the updraft-relative wind vector.

The analytical solutions revealed that future vertical vorticity is maximized when the ambient shear is purely streamwise and minimized in the case of crosswise vorticity. To see why this occurs, it is helpful to evaluate horizontal vorticity along air parcels that will flow into the updraft core and thus have the greatest potential for vortex stretching. When crosswise vorticity is present, the horizontal vortex tubes associated with the future updraft parcels are advected upwards as the tilting occurs on the sides of the updraft inflow (Fig. 2.9a), resulting in counter-rotating vortices of equal strength that are uncorrelated with the peak updraft. Alternatively, when streamwise vorticity is present, the horizontal vortex tubes tilt upwards as the air parcels rise into the updraft, resulting in an increasing correlation between positive vertical vorticity and vertical velocity as the air parcel gains altitude (Fig. 2.9b). On the downwind side of the updraft, anticylconic vorticity is generated through tilting but since air parcels are experiencing decreasing vertical motion with time, stretching of the vortex is minimized. While analytical in nature, the model suggests that in environments with large, streamwise vorticity at low-levels, midlevel rotation will derive an increasing

fraction of its rotation from the tilting of low-level, streamwise vorticity rather than midlevel shear. On the other hand, if the low-level shear is primarily crosswise, then vertical vorticity generated at low-levels is less likely to advect upwards in the updraft, as it will be uncorrelated with the peak updraft. This perhaps explains how tornadic supercells often thrive in environments where the shear vector does not substantially curve with height above 3 km (Maddox 1976), as it is deriving most of its cyclonic rotation throughout its depth from the tilting and subsequent stretching of low-level streamwise vorticity.

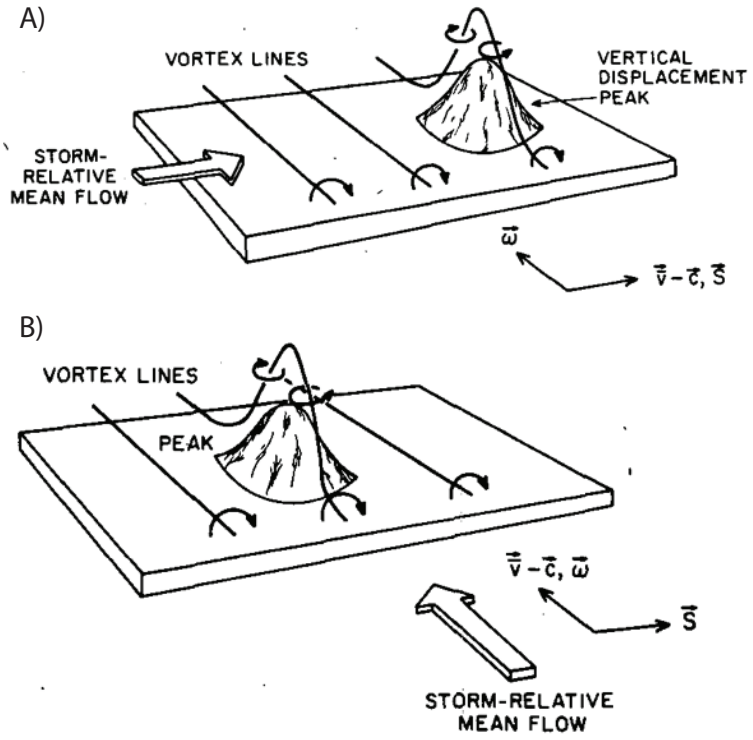

Fig. 2.9 Schematic depicting vortexlines being tilted by a symmetric updraft. The upper panel indicates storm-relative flow perpendicular to the vortexlines (crosswise), while the lower panel indicates storm-relative flow parallel to the vortexlines (streamwise) (Davies-Jones 1984).

2.3.2 Origins of Low-Level Rotation

When the incipient thunderstorm updraft forms, the vertical motion is being driven by buoyancy induced vertical accelerations, resulting in an updraft that is maximized at mid to upper levels where the potential instability is maximized (Moncrieff and Miller 1976). Furthermore, prior to the enhancement of the updraft by dynamically induced pressure perturbations, buoyant accelerations are limited to altitudes above the level of free convection (LFC). Therefore, in the case of purely streamwise horizontal vorticity being tilted by a buoyancy driven updraft, vertical vorticity will initially be generated just above the LFC and increase with altitude as it is stretched by buoyant accelerations. The positive correlation between vertical vorticity and vertical velocity dictates that as the vertical stretching of the vortex increases, vertical advection of vertical vorticity must also increase, preventing low-level vertical vorticity, here defined as 1 km above the ground, from becoming significant near the LFC, much less below it (Davies-Jones 1982). Although increasing the acceleration of the low-level updraft through dynamically induced pressure perturbations will enhance the stretching of low-level vertical vorticity, it is compensated for by increased vertical advection of said vorticity.

One early proposed mechanism by which vertical vorticity could descend towards the ground is known as the "dynamic-pipe effect" (Smith and Leslie 1979). Here, they considered a vortex in cyclostrophic balance and thus resistant to air flowing horizontally into the circulation. If the circulation strength increases with height, then the central pressure will also reduce with height, since the central pressure in a balanced vortex will be proportional to the circulation. In this scenario, air must be drawn in from

the bottom because it cannot be drawn in laterally. This in turn generates compensating subsidence on the outside of the vortex to conserve mass. The subsidence transports high angular momentum towards the ground and enhances the low-level convergence, causing the base of the vortex to descend. While this mechanism may play a role in tornadogenesis, the absence of a vortex at midlevels in cyclostrophic balance, preceding the development of the low-level mesocyclone, precludes this mechanism from being applicable to the initial development of low-level rotation (Davies-Jones and Brooks 1993).

Rotunno and Klemp (1985) presented another perspective on the conversion of horizontal vorticity into vertical vorticity through Ertel's theorem on the conservation of equivalent potential vorticity. The theorem (2.7) states that since buoyancy and equivalent potential temperature (θ_e) are highly correlated, in the absence of diabatic heating or cooling, changes in the θ_e field will directly correspond to changes in the three-dimensional vorticity field, ω, scaled by the base-state density, $\bar{\rho}$. Thus, when the θ_e isosurface slopes upward, initially horizontal vortex lines will also slope

$$\frac{d}{dt}\left(\frac{\omega \cdot \nabla\theta_e}{\bar{\rho}}\right) = 0 \quad (2.7)$$

upward (Fig. 2.10). The degree of tilting is then directly proportional to the vertical slope of the θ_e field and is thus maximized at midlevels. This theorem predicts that prior to the formation of a downdraft, regardless of whether the vorticity is streamwise or crosswise, vertical vorticity will be maximized at midlevels because that is where the θ_e slope is maximized. Moreover, it also predicts that in the absence of a downdraft, the slope will be minimal near the initial horizontal plane. In the case of an updraft in a strongly sheared environment, the precipitation and downdraft will initially be

significantly displaced from the updraft, thus causing vertical vorticity to be minimized at low-levels and maximized at midlevels. Therefore, the development of significant low-level rotation requires either the lowering of the initial tilting altitude to the ground, descending motion upstream of the updraft to increase the slope of the θ_e surface at low-levels, or horizontal vorticity must be generated baroclinically in order to pull the vortex lines off the θ_e surface.

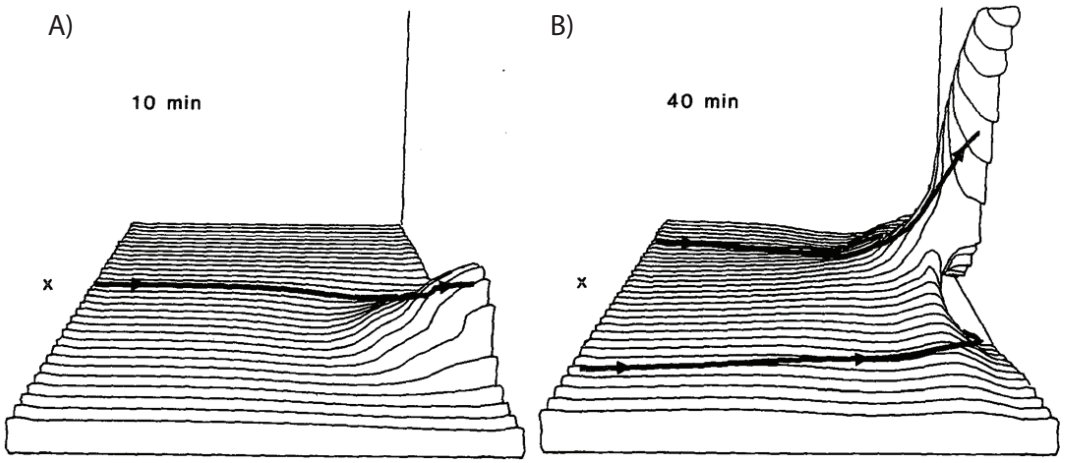

Fig. 2.10 Three-dimensional depiction of isosurfaces of θ_e as they slope upwards (downwards) in the updraft (downdraft) after 10 (a) and 40 (b) minutes of model integration time. Thick black lines indicate example vortex lines with the arrows indicating their direction (Rotunno and Klemp 1985).

1) Tilting along gust fronts

The easiest mechanism by which to lower the initial tilting altitude of air parcels entering the updraft is to force ascent by a gust front near the ground. Before finalizing his conceptual model on the development of waterspouts, Simpson (1982) proposed that thunderstorm gust fronts caused near-surface vortex tubes to tilt abruptly at the leading edge of the gust front, before entering the convective updraft (Fig. 2.11). However, analytic and numerical simulations by Davies-Jones and Markowski (2013) showed that in the absence of outside influences, the density current induces high-pressure on its

leading edge, forcing air upwards but also slowing it down in the process, compressing the gustfront-relative streamwise vorticity and vertically advecting the crosswise vorticity. The numerical simulation revealed that vertical vorticity wasn't generated near the ground even when extreme values of horizontal vorticity were present and the cold pool was substantially colder (-12 K) than most observations of tornadic supercells (Markowski et al. 2002). In idealized, three-dimensional models of supercells, vertical vorticity associated with vortex sheets along the forward-flank and rear-flank gust fronts has been shown to have baroclinic origins and were not the result of ambient low-level shear being tilted along the gust front (Gaudet and Cotton; Markowski et al. 2014). Thus, strong convergence along gust fronts alone does not appear to be an effective way at generating substantial low-level vertical vorticity.

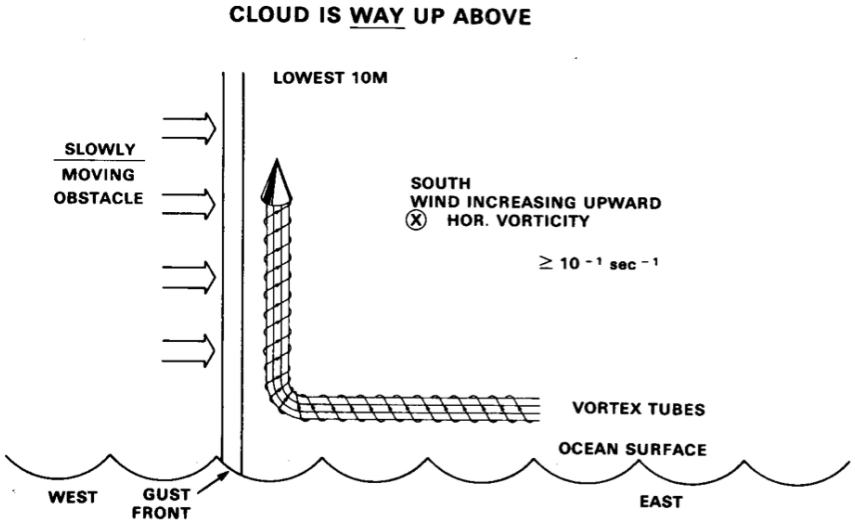

Fig. 2.11 Conceptual model illustrates how a vortex tub is abruptly tilted upwards by a thunderstorm outflow. The illustration is meant to support a conceptual model of the development of waterspouts (Simpson 1982).

Nonetheless, once dynamic pressure gradients are generated near the ground, low-level tilting is possible. In idealized experiments of non-supercell tornadoes by Lee and Wilhelmson (1997), weak mesocyclones developed along a shearing-instability,

mimicking pre-existing vertical vorticity along a stalled surface boundary. While low-level horizontal vorticity did not contribute to the formation of the initial vortices, frictionally generated, near-ground crosswise vorticity did aid in the maintenance and intensification of the vortices after they matured. When friction was turned off, low-level vorticity was dominated by the baroclinic generation of anti-streamwise vorticity along the gust front, which resulted in the generation of vertical vorticity of the opposite sign as that of the misocyclone. In this case, vertical vorticity is produced at low-levels because the crosswise component is being tilted, and thus the parcels are not required to gain altitude in the tilting process. However, the dominant tilting of crosswise vorticity required a mature misocyclone to stretch the vorticity and the vortex did not appreciably increase in strength with height. While this tilting mechanism can explain tornadoes associated with ordinary thunderstorms and small, transient vortices along the rear-flank gust front, it is doubtful that this mechanism meaningfully contributes to the development of the low-level mesocyclone in supercells. Moreover, the absence of friction and vortex sheets in low-level mesocyclone producing simulations indicates that while the tilting of near-ground crosswise vorticity may contribute in some circumstances, it is not a consistent contributor to the development of low-level rotation in supercells.

There are observational examples of substantial vertical vorticity existing at approximately 1 km altitude along the RFGF, upstream of the developing low-level mesocyclone, in cyclic tornadic supercells (Brandes 1981; Johnson et al. 1987; Dowell and Bluestein 2002a,b). These observations, along with those later presented in this paper, imply that under the right circumstances, ambient near-ground streamwise

vorticity can be tilted at sufficiently low-levels so as to produce substantial vertical vorticity (~0.01 s^{-1}) at or below 1 km. In both cases, subsidence was found ahead of the primary updraft, causing air parcels to descend prior to reaching the convergence associated with the gust front and thus allowing the θ_e surfaces to slope substantially more than would otherwise be possible.

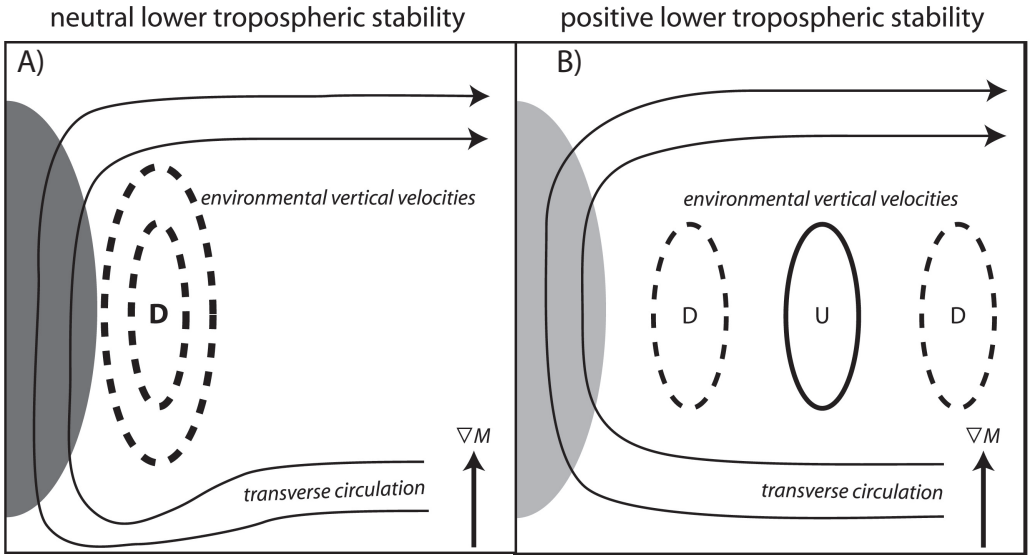

Fig. 2.12 Schematic describing the response of the vertical motion field to the release of latent heating under different stability scenarios. When the lower troposphere is neutral (a), a single, persistent region of subsidence develops because the ambient stability prevents the development of gravity waves. Alternatively, when the lower troposphere is stable, gravity waves are produced to compensate for the latent heat release. The subsidence in the neutral case advects higher momentum towards the ground, lowering the midlevel circulation (Parker 2012).

In an idealized numerical simulation, Parker (2012) found that when lower tropospheric lapse rates were neutral, the latent heat release of the updraft generated compensating subsidence on the updraft edge, causing ambient angular momentum to descend upstream of the updraft, lowering the circulation base (Fig. 2.12b). Conversely, when the lapse rates were statically stable, the latent heat release triggered gravity waves that propagated the compensating motion away from the main updraft, resulting

in negligible vertical motion (Fig. 2.12a). Thus it appears physically possible that compensating downdrafts in strongly sheared environments can amplify the tilting of streamwise vorticity in the low-level updraft and substantially lower the initial tilting altitude. Additionally, if the enhanced low-level tilting occurs at sufficiently low-levels and upstream from the low-level circulation, then near-ground trajectories tilting ambient streamwise vorticity could contribute to the rotation of the low-level mesocyclone and not simply amplify the midlevel mesocyclone.

2) Tilting of baroclinically generated horizontal vorticity

Observations of supercell thunderstorms noted a difference early on between the initial development of the midlevel mesocyclone and the low-level mesocyclone. Several observational studies have noted a dramatic shift in the vertical profile of maximum vorticity as the low-level mesocyclone develops (Brandes 1978; Klemp et al. 1981; Johnson et al. 1987). Initially, vertical vorticity is maximized aloft in the midlevel mesocyclone as previously discussed, however, as conditions become favorable for the low-level development of rotation, the low-level rotation quickly becomes stronger than the midlevel rotation. This is important because if the same mechanism that generates vertical vorticity for the midlevel mesocyclone was responsible for the low-level mesocyclone, then one would not see a reversal in the vertical profile of maximum vorticity. It was this aggregate of observations that lead Klemp and Rotunno (1983) to focus on the evolving source region of air in the developing low-level circulation. They found that the intensification of the low-level circulation coincided with the increasing ingestion of forward flank air where the ambient, low-level streamwise vorticity was augmented by the vorticity generated through horizontal buoyancy gradients. They

hypothesized that since the stretching term exponentially amplifies the initial vertical vorticity produced by the tilting term, that any increase in horizontal vorticity along a trajectory's path would result in enhanced stretching later on.

In a follow up study, Rotunno and Klemp (1985) followed material circuits originating around the low-level mesocyclone and traced them back into the environment. Bjerknes theorem (Eliassen and Kleinschmidt 1957) states that changes in circulation along the material circuit's path are only due to horizontal buoyancy gradients and friction. In their simulation of a storm in a unidirectional wind shear profile, the circulation of the material circuit around the developing low-level mesocyclone increased dramatically as it moved through the forward-flank of the storm, prior to the period of tilting in the updraft. Since the increase in circulation cannot be due to the stretching of horizontal vorticity originating in the environment, the increase in circulation had to be associated with the buoyancy gradients in the forward flank of the storm. The contribution to circulation around the material circuit due to buoyancy gradients was estimated and matched well with the temporal evolution of circulation. Their material circuit had an initial circulation that was negative, implying that the circulation associated with the low-level mesocyclone was entirely due to the baroclinic generation of circulation, rather than simply augmenting the ambient horizontal vorticity. It should be noted that the simulation used by Klemp and Rotunno (1983) contained substantially more low-level, streamwise vorticity than the unidirectional wind profile used in their 1985 simulation, potentially limiting the contribution of ambient vorticity in their circulation analysis.

Successive circulation analyses revealed similar behavior using observations (Dowell and Bluestein 1997; Markowski et al. 2012b) and high-resolution numerical simulations with more realistic microphysics schemes (Davies-Jones and Brookes 1993; Markowski al. 2014). The pervasiveness of baroclinic origins of vorticity is further supported by the near ubiquity of counter rotating vortices straddling the RFD cold pool in observed supercells (Straka et al. 2007). These vortex arches were hypothesized to arise as the primary updraft tilted baroclinically generated vortex rings emanating out of the RFD. Using several of these cases, Markowski et al. (2008) demonstrated that in fact vortex lines did connect most of the counter rotating vortices. Furthermore, they postulated that given their orientation, it was impossible for these vortex lines to have originated within the environment and must have been generated by the RFD cold pool, as environmental vortex lines would have formed a U shape in the downdraft. Based on the observed vortex arches, Markowski et al. (2008) conceptualized the formation of the low-level mesocyclone apart from the midlevel mesocyclone (Fig. 2.13), one completely baroclinically generated and associated with vortex arches and the other associated with environmental vortex lines bending upwards into the midlevel mesocyclone. Vortex arches were subsequently observed in tornadic supercells by Markowski et al. (2011; 2012a) and data assimilation experiments in Marquis et al. (2012). An idealized toy model by Markowski et al. (2014) suggested that under optimal conditions, the vortex arches are tilted into the updraft and merge with those from the environment, resulting in vertically oriented vortex lines during the mature stage of the mesocyclone. Thus, the baroclinic generation of horizontal vorticity in the forward and rear flanks of supercell storms appears to be vital and nearly ubiquitous in

supercell thunderstorms and has been accepted as the definitive reason why the low-level mesocyclone differs in behavior and appearance from that at mid levels.

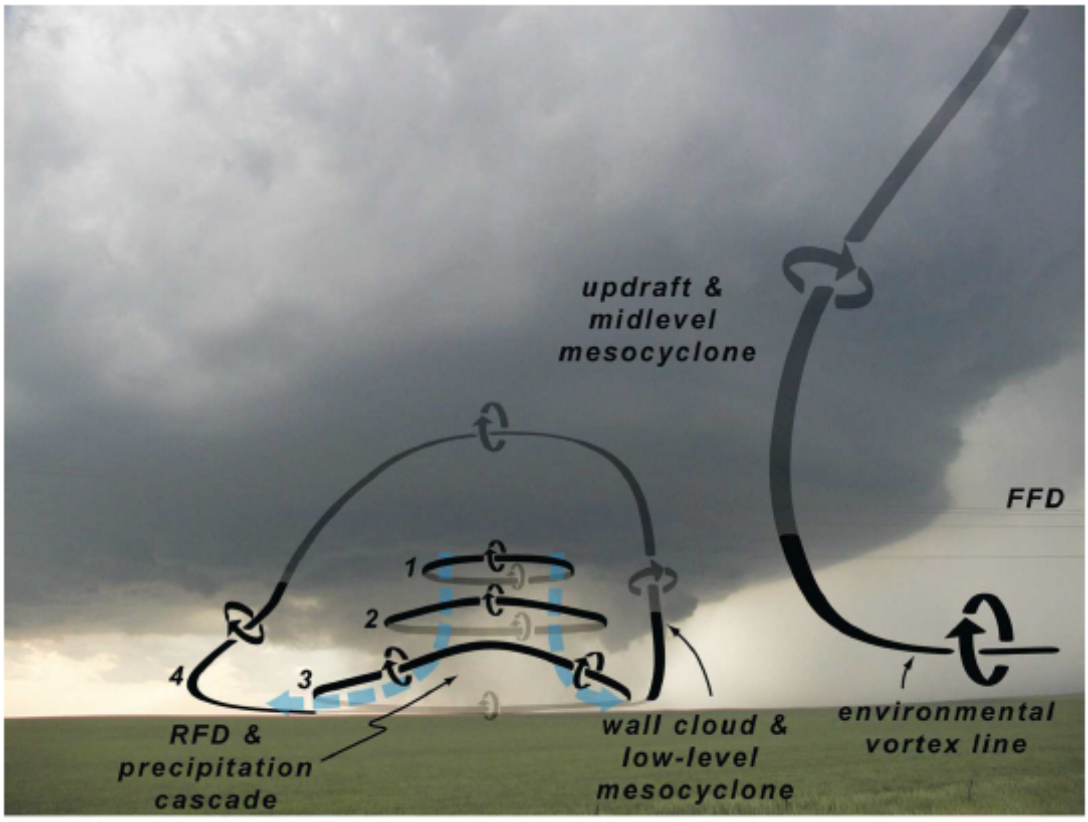

Fig. 2.13 Schematic illustrating initial vortex rings emanating out of the RFD and being tilted into arches by the main updraft. The environmental vortex line associated with the midlevel mesocyclone is also drawn to illustrate the initial separation between the low level mesocyclone and the midlevel mesocyclone (Markowski et al. 2008).

However, the addition of baroclinic generation of horizontal vorticity into the conceptual model does not provide an explanation for what makes the baroclinic generation of horizontal vorticity uniquely favorable, and potentially necessary, for the intensification of rotation at low-levels. Although it was already shown analytically that rotation near the ground required a downdraft (Davies-Jones 1982), a conceptual model using a three-dimensional supercell simulation wasn't presented until Davies-Jones and Brooks (1993). In their so-called "feet-first" explanation, Davies-Jones and

Brooks (1993) demonstrated that future low-level mesocyclone trajectories acquired positive vertical vorticity prior to the trajectory reaching it's nadir and thus allowing vertical vorticity to grow before rising significantly above the ground.

The acquisition of baroclinically generated horizontal vorticity in the forward flank was important as Davies-Jones and Brooks found that the key was the collocation of streamwise baroclinic generation of vorticity and a downdraft. The collocation allows streamwise horizontal vorticity to be generated as the parcel descends, but since the vorticity is generated horizontally while the streamline is pointed downwards, the vorticity vector slips off the streamline. Subsequently, positive upward tilting begins as the air parcel's decent slows down, allowing positive vertical vorticity to be present before the trajectory begins its ascent (Fig. 2.14). Similar behavior was seen in subsequent high-resolution simulations (Wicker and Wilhelmson (1995); Adlerman et al. (1999); Dahl et al. 2014; Markowski et al. (2014); Dahl 2015; Parker and Dahl 2015). Furthermore, many observationally based studies (Johnson et al. 1987; Dowell and Bluestein 1997; Wakimoto et al. 1998; Ziegler et al. 2001; Dowell and Bluestein 2002b; Markowski et al. 2012) have demonstrated that mesocyclogenesis is distinguished by the transition of future mesocyclone trajectories originating in the inflow from the east, to arriving from the north out of the forward flank region. This repeatedly observed transition strongly suggests that a similar mechanism occurs in observed storms as those simulated by numerical models.

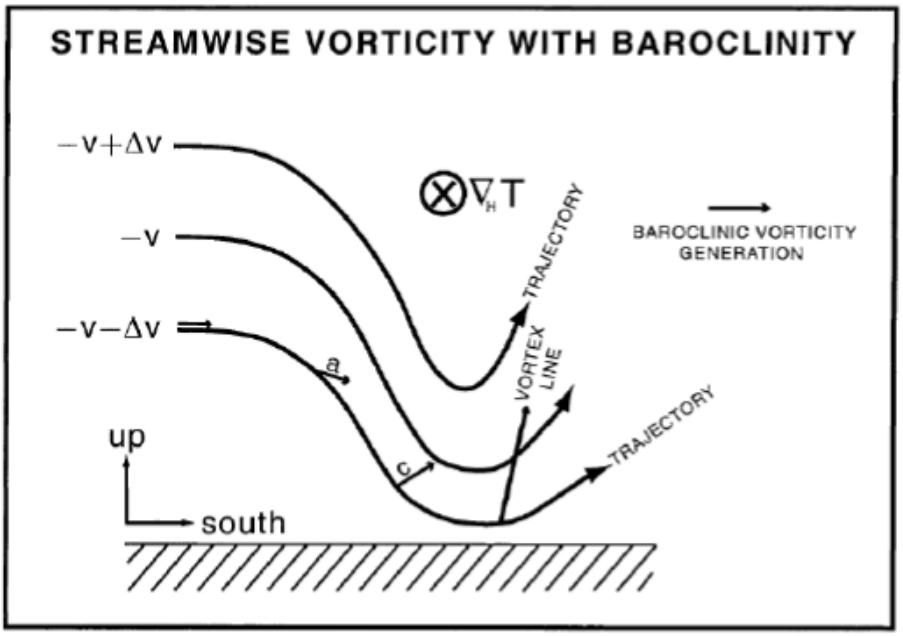

Fig. 2.14 Schematic describing the "feet-first" method by which a trajectory acquires horizontal vorticity in a downdraft, allowing the vorticity vector to slip off the streamline. The slippage of the vorticity vector then allows vertical vorticity to begin stretching prior to rising in the updraft, potentially generating large vertical vorticity values near the ground (Davies-Jones and Brooks 1993).

It should be pointed out that buoyancy gradients oriented along curved flow and positioned north of the low-level updraft require broad, cyclonic flow to already be present. Many of the aforementioned studies exhibited a rapid transition from a weak vorticity region fed by inflow air to a strongly curved flow filled with air parcels originating from the forward flank. The swiftness of the transition points to a critical point where the low pressure associated with the environmentally generated circulation drops sufficiently to cause a response in the wind field that curves the flow and orients the buoyancy gradients along the streamlines. Additionally, a recent study by Houston (2016) demonstrated that future ascent of cold pool air requires strong midlevel rotation that is optimally located above the rear-flank gust front. This point was also made through idealized toy simulations by Markowski et al. (2014) who explained the rapid

transition as the point at which the dynamically driven vertical pressure gradients become strong enough to ingest and tilt baroclinically enhanced forward flank air.

Alternatively, surface observations collected within the forward flank (Shabbott and Markowski 2006) and rear-flank (Markowski et al. 2002; Markowski 2002; Lee 2004; Finley and Lee 2004; Grzych et al. 2007; Finley and Lee 2008; Hirth et al. 2008; Lee et al. 2011) have been remarkably consistent in their conclusions that tornadic supercells are more likely to have buoyant air in the downdraft regions than in nontornadic supercells. Therefore, while the baroclinic generation of horizontal vorticity is important, it cannot come at the cost of a strong cold pool. Moreover, the lack of cold downdrafts near tornadoes indicates the ability of a weak cold pool to produce sufficient buoyancy gradients for low-level rotation to develop. This is because vertical vorticity grows exponentially in a zone of favorable stretching (Rotunno and Klemp 1985) and thus the ability of air parcels to flow into a region of favorable stretching is more important than the initial magnitude of horizontal vorticity.

2.3.3 Axisymmetric Vortex Models

Through laboratory (Ward 1972; Rotunno 1977) and numerical simulations (Rotunno 1979; Howells 1988), vortices have been shown to evolve between a one-celled vortex structure with an axial updraft, and a two-celled vortex structure with an axial downdraft. The two distinct vortex structures were theoretically connected to the ratio of the maximum tangential winds relative to the vertical velocity at the center of the vortex, deemed the swirl ratio, by Davies-Jones (1973). It was shown that as the swirl ratio increases, the vortex transitions towards a two-celled structure.

Both types of vortex behavior have been documented in observed tornadoes

(Pauley and Snow 1988; Lugt 1989), however, it is more ambiguous as to how applicable the conceptual model is to mesocyclones. In radar based dual-Doppler analyses by Brandes (1978; 1981) and Wakimoto and Lui (1998) tornadoes appeared to form during a period in which a broad mesocyclone contained descending motion near its axis of rotation. The authors theorized that as the downdraft intensified, vortex instabilities in the mesocyclone flow formed and grew to tornado strength, even as the larger mesocyclone weakened. The authors likened this vortex behavior to the vortex breakdown process observed in tornadoes, as the vortex transitions from a one-celled structure to a two-celled structure.

One major problem in such classifications of the mesocyclone is the lack of resolution in the observational datasets. In the radar data, a one-celled mesocyclone is easily classified as a vortex collocated with the updraft at low levels. However, when the mesocyclone is situated on the vertical velocity gradient, i.e. divided structure, it is difficult to classify the vortex. Brandes (1978) inferred the transition of the mesocyclone through temporal trends in vortex radius and tangential velocity. Alternatively, Wakimoto and Lui (1998) inferred vortex breakdown due to an abrupt weakening of the mesocyclone and the appearance of new vorticity maxima near the original vortex. Although both examples are consistent with a vortex breakdown process, Trapp (2000) questioned the plausibility that a boundary layer jet can form beneath the mesocyclone. Rather, their study proposed that mesocyclones could develop two-celled structure in the absence of a vortex breakdown event.

The mesocyclone structure also has important implications for how the vortex interacts with the RFD. Studies relying on theoretical (Burgers 1948; Rott 1958),

laboratory (Ward 1972), and numerical simulation (Rotunno 1984) experiments have shown that general vortex stability is sensitive to the vertical velocity tendency of the vortex along its axis. One-celled vortices were more stable and resistant to deformation by outside instabilities, such as a downdraft, compared with two-celled vortices. Mesocyclones in two storms studies by Brandes (1978) appeared to be impervious to downdrafts until they took on a two-celled structure. Unfortunately, this application of the relationship has not been studied in the context of larger-scale conceptual models of supercell evolution, like that of Lemon and Doswell (1979).

Chapter 3: Three-dimensional storm structure and low-level kinematic boundaries at different stages of mesocyclone evolution in a high-precipitation tornadic supercell

Material in this chapter is adapted from Betten et al. (2018)

3.1 Introduction

To document the evolution of the storm-scale flow structure and near-surface boundaries, it is necessary to observe the storm for more than a single mesocyclone cycle which often requires long duration radar-analyses that can be difficult to obtain due to a combination of small baselines, fast storm motions, or small storms. There are only a few radar-based wind retrievals that examine more than 30 minutes of a supercell's life cycle (Wakimoto and Lui 1998; Ziegler et al. 2001; Dowell and Bluestein 2002a, hereafter DB02a, b; Markowski et al. 2012a; DiGangi et al. 2016). All but the last two are based on airborne analyses with relatively long periods between volumetric samples and a high minimum altitude (500 m).

This chapter will present radar analyses over a 90-minute period, covering parts of three mesocyclone cycles of the 29 May 2004 Geary, OK supercell. The Geary supercell was a prolific producer of tornadic circulations. Here, we focus on documenting the internal storm structure and low-level kinematic boundaries at different stages of mesocyclone evolution to aid in developing contrasts between observed cyclic tornadic supercells and non-tornadic supercells. Additionally, for the first time, the relationship between the SRFGF, RFD, and occlusion downdraft is examined for three sequential mesocyclones.

3.2 Data Collection and Methodology

On the afternoon of 29 May 2004, during the TELEX field experiment (MacGorman et al. 2008), two Shared Mobile Atmospheric Research and Teaching (SMART, Biggerstaff et al. 2005) radars observed a tornadic, high precipitation supercell near Geary, OK for about three hours. Many aspects of the deployment were optimal for retrieving and examining the storm-scale kinematic structure, including a slow storm motion (12 m s^{-1}), a large storm (60 km long), a long mesocyclone cycle frequency (90 minutes), and a large baseline (40 km) that allowed the storm to stay within the region in which dual-Doppler wind retrievals (Brandes 1977; Ray et al. 1980; Biggerstaff and Houze 1993) could be constructed for a long period of time. The radars operated in sector-scan mode, collecting 120° azimuthal swaths of data from 0.5 to 59° in elevation over a ~2.5 minute period with a repeat cycle of three minutes. Nine of these volume scans, ranging in time from 2320 to 0052 UTC, were analyzed in the cloud electrification study by Calhoun et al. (2013). Here, 23 volume scans from 2358 to 0120 UTC have been analyzed. Their temporal coverage is illustrated in Figure (3.1). Additionally, an environmental sounding unit stayed ahead of the storm and launched soundings in the near-storm environment at 2230 and 2330 UTC on 29 May, and at 0030 and 0130 UTC on 30 May 2004.

The radar data were interpolated onto a Cartesian grid using a hybrid Cressman (Cressman 1963) and natural neighbor (Sibson 1981) weighting scheme that maximizes the local resolvable scale of the observations. The wind synthesis was performed using the National Center for Atmospheric Research (NCAR) software package Custom Editing and Display of Reduced Information in Cartesian Space (CEDRIC; Mohr et al.

1986) following a procedure similar to Palucki et al. (2011). A two-step Leise filter (Leise 1982) was used to dampen horizontal wavelengths less than 4.5 km and eliminate horizontal wavelengths less than 3.0 km. The filter was applied to minimize the introduction of artifacts in the temporal evolution, arising from changes in the effective resolution due to changing beam-crossing angles and range from the radar.

Cohen and Schultz (2005) demonstrated that baroclinic zones should be manifested where weak buoyancy gradients are magnified along persistent confluent zones. The instantaneous asymptotic contraction rate, a solely kinematic quantity, was shown to reveal where baroclinic zones developed as deformation and rotation were allowed to act on a weak baroclinic boundary.

To find boundaries in the Geary, OK supercell, the contraction rate was calculated at altitudes of 250 m and 1000 m. The contraction rate is only a valid indicator of baroclinic zones if the enhanced regions are persistent long enough for the air parcels to converge and tighten the buoyancy gradient. The applicability of the instantaneous asymptotic contraction rate was tested through a comparison with a thermodynamic retrieval (not shown) using a diabatic Lagrangian analysis (DLA, Ziegler 2013a) for the 9 June 2009 case from Ziegler (2013b). Following the guidance of Cohen and Schultz (2005), the contraction rate compared favorably to the low-level thermodynamic boundaries revealed by the DLA. A future study will examine the thermodynamic structure of this case in more depth using a DLA. In this study, the contraction rate will be used to illuminate regions where thermodynamic boundaries may exist or develop in the future.

3.3 Storm Overview

3.3.1 Storm environment

On 29 May 2004, storms initiated along a dryline in far western Oklahoma before moving across the state, at approximately 2130 UTC. Prior to obtaining low-level rotation, storm motion was towards the northeast. As the southern most cell gained low-level rotation (~2245 UTC), the mean storm motion gradually shifted towards the east-southeast. This storm, hereafter referred to as the Geary storm, evolved into a high precipitation supercell (Moller et al. 1994) and began cyclically producing tornadoes at 2333 UTC and continued to produce tornadoes until 0651 UTC. The storm produced a total of 18 tornadoes and numerous large hail reports, with several reports over 4 inches in diameter (*Storm Data, NOAA, 2004*). Additionally, according to observations by a mobile Doppler on Wheels (DOW; Wurman et al. 1997; Wurman, personal communication), a total of eight tornadoes (or tornado-like subvortices), including one that lasted 24 minutes and two anti-cyclonic tornadoes, were observed during the 90-minute period of interest in this study (Fig. 3.1). Herein the stages of mesocyclone evolution follows Burgess et al. (1982), with the distinction that we refer to the period when the outflow from the RFD begins to push the primary RFGF away from the circulation as the "occlusion stage" rather than the dissipating stage. A more in depth discussion of the mesoscale environment and evolution on 29 May 2004 can be found in Calhoun et al. (2013).

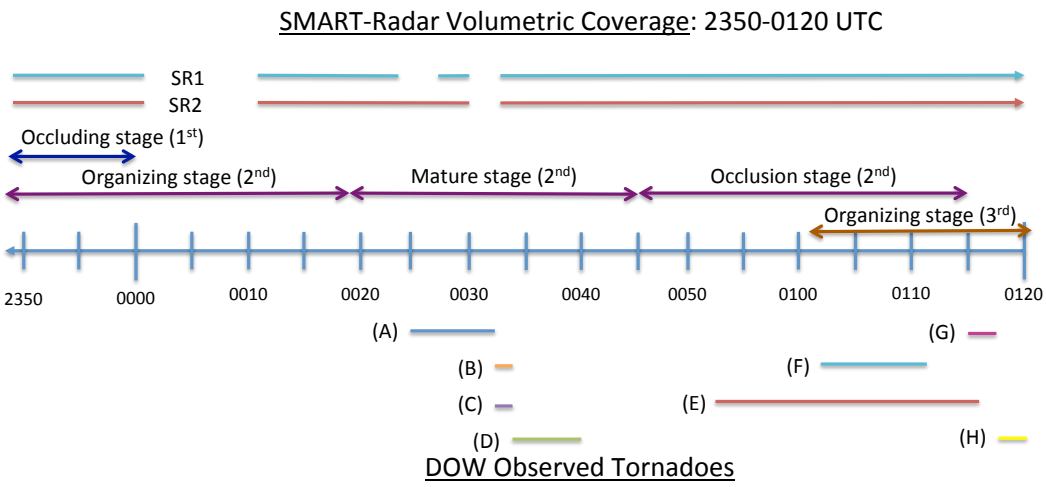

Fig. 3.1 Timeline for SMART-radar observations, mesocyclone lifecycles, and tornado lifecycles (marked from (A) to (H) as indicated by a DOW radar that was close to the hook echo).

The storm-scale environment during the observational period is represented by a Mobile GPS Advanced Upper-air Sounding (MGAUS) system sounding launched 75 km southeast of the storm near Minco, OK at approximately 0008 UTC (Fig. 3.2). The sounding contained large amounts of instability, with a mixed-layer CAPE of ~3300 J kg^{-1}, while a substantial low-level stable layer remained between 850 mb and 700 mb with a mixed-layer convective inhibition of 67 J kg^{-1}. It is possible that the strength of the stable layer, in addition to the strong low-level storm-relative winds, aided the longevity of the storm by preventing the outflow from surging ahead of the main updraft (Ziegler et al. 2010). The storm-relative helicity (SRH) was also extremely high at 461 m^2 s^{-2}, well above the threshold seen in strongly tornadic supercell environments (Thompson et al. 2003). Interestingly, there was a significant weakness in the wind profile between 2 and 5 km where the zonal component was nearly constant and the meridional component weakened 6 m s^{-1}.

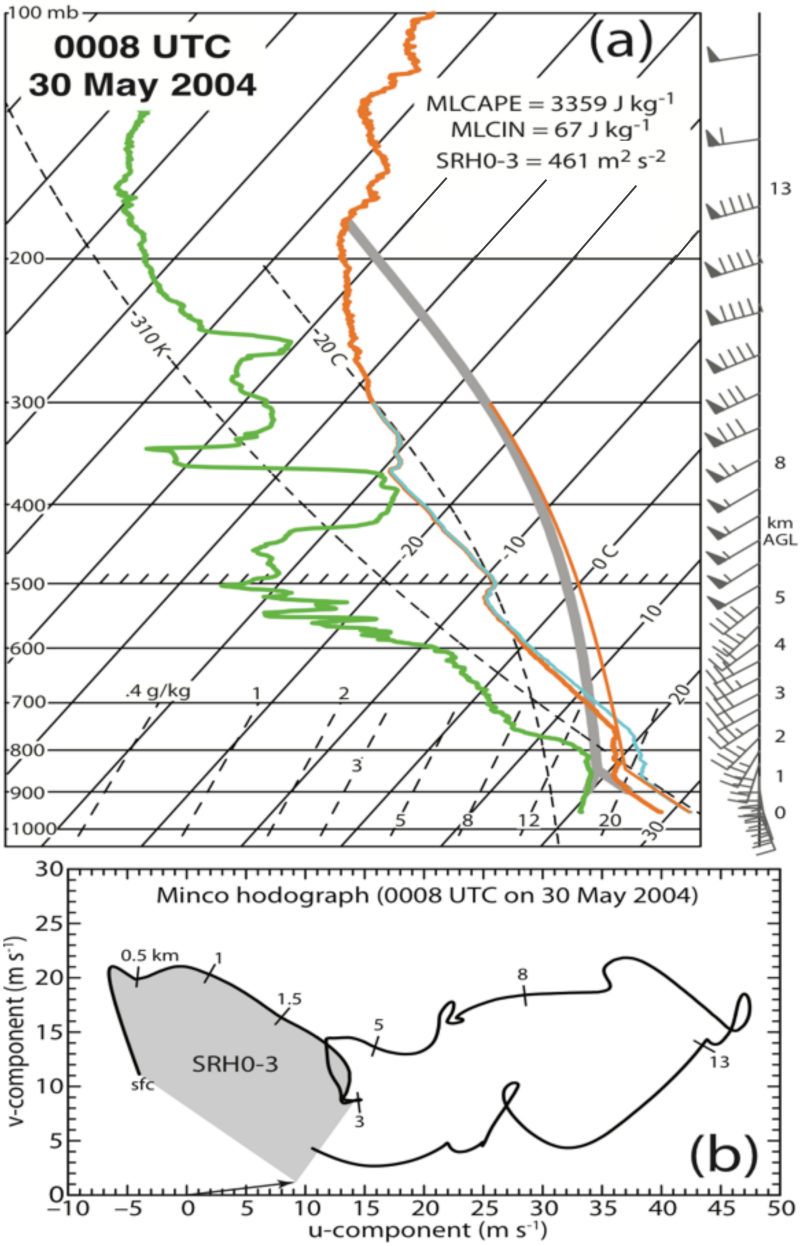

Fig. 3.2 MGAUS sounding in Minco, OK at 0008 UTC on 30 May 2004. In (a) is the thermodynamic sounding with parameters in the upper left-hand corner. In (b) is the hodograph with the 0-3 km SRH shaded in grey and an arrow indicating the average storm-motion.

3.3.2 Storm evolution overview

Time-height plots from the dual-Doppler analysis of maximum vertical velocity, minimum vertical velocity, and maximum vertical vorticity in a 20 km x 20 km box centered on the low level mesocyclone are shown in Figure 3.3. Spurious updrafts and

downdrafts on the edge of the data domain were removed so that trends in the drafts inside the hook echo could be examined.

The pulsing nature of the updrafts and downdrafts is immediately evident. Several low-level updraft maxima propagated upward during two periods, 0019-0039 UTC and 0045-0118 UTC. Both periods were initiated when the low-level gust front surged to the southeast, temporarily enhancing the convergence along the primary RFD gust front. The downdraft minima in the box are from the primary RFD region northwest of the circulation, the rainy downdraft region north of the circulation, and the occlusion downdraft region. As indicated by downdraft magnitudes exceeding 12 m s^{-1} at 3 km altitude, periods of prolonged low-level downdrafts were observed from 0019-0039 UTC and again from 0052-0115 UTC, with the two most intense downdrafts occurring at 0022 UTC and 0052 UTC. Tropospherically deep subsidence occurred for an extended period after 0042 UTC, coincident with a tendency for the maximum updraft speed to decrease at mid and upper levels. The period between 0102-0112 UTC had weak downdrafts as the occluding tornadic mesocyclone was substantially displaced from the main gust front and the new mesocyclone had yet to intensify.

The transitions in storm character are also evident in the vertical vorticity field. Vorticity increased over a deep layer between 0015-0025 UTC, which coincided with the intensification of deep vertical drafts. Maximum vorticity then decreased

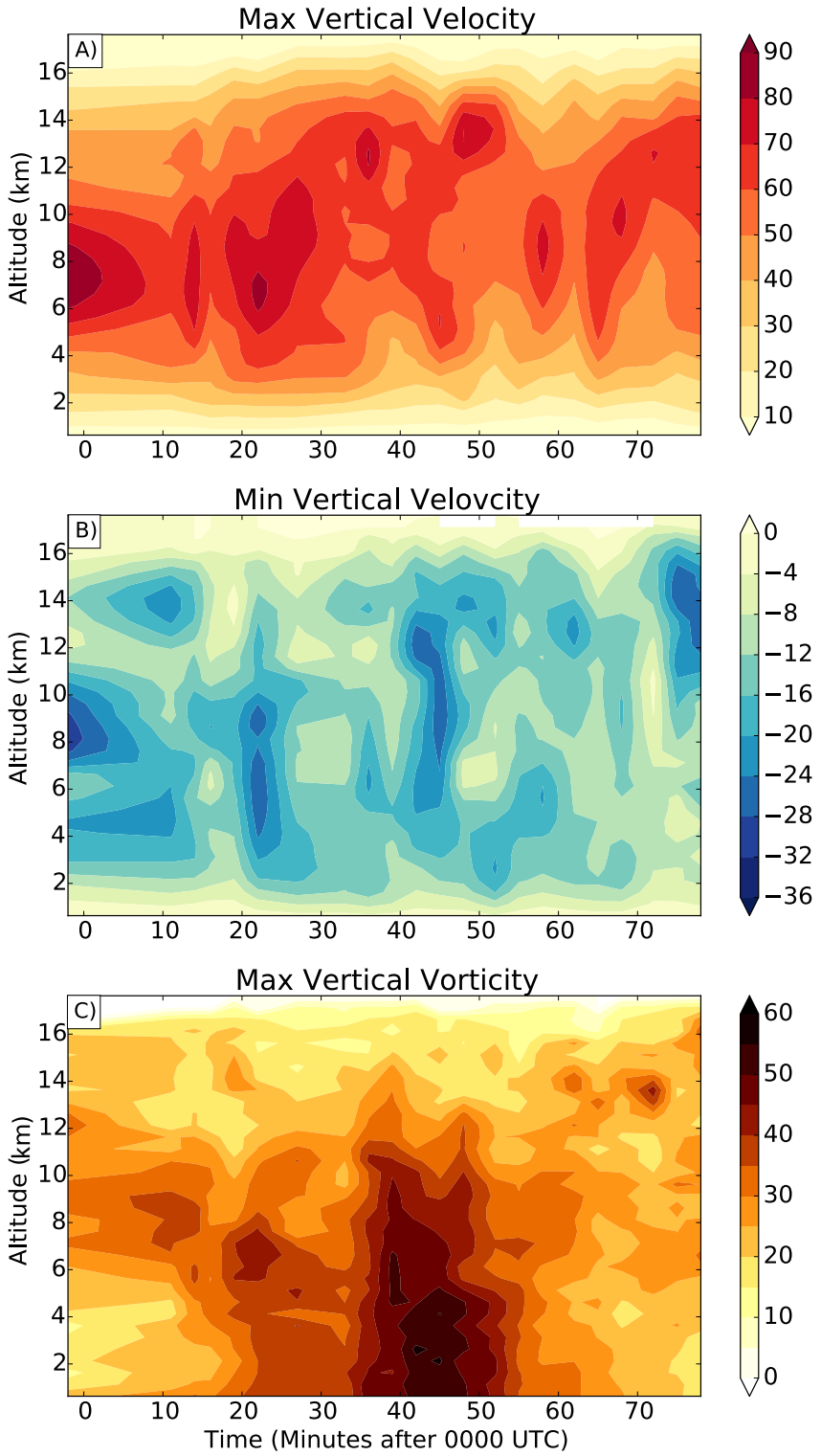

Fig. 3.3 Time-height plots of (a) maximum vertical velocity (m s^{-1}), (b) minimum vertical velocity (m s^{-1}), and (c) maximum vertical vorticity (1x10^{-3} s^{-1}) within 8 km of the low-level mesocyclone center for the downdraft and domain wide for maximum vertical velocity and vorticity.

throughout the troposphere coincident with the upward propagating updraft pulse and a weakening of the maximum downdrafts between 0030-0035 UTC. Afterward, a sharp increase in vertical vorticity occurred with additional strengthening coincident with the development of the tropospherically deep subsidence and weakening updrafts by 0045 UTC.

3.4 Kinematic structure at different stages of the mesocyclone lifecycle

3.4.1 Organizing stage: 2358-0022 UTC

1) KINEMATIC BOUNDARIES

At 2358 UTC, the Geary supercell was undergoing cyclic mesocyclogenesis (Burgess et al. 1982; DB02a, b; B06). The old occluded circulation (Fig. 3.4a, x=-63, y=28) and the associated precipitation core (Fig. 3.5a) were located northwest of the new, organizing mesocyclone (Fig. 3.4a, x =-53, y=24) consistent with a stage 3 structure in the conceptual model of B06. During the organizing stage, the primary rear-flank gust-front (RFGF, solid red line in Fig. 3.4a) was draped along the southern periphery of the storm outflow on the storm's southern flank. Meanwhile, secondary rear-flank gust fronts (SRFGFs) outlined the edge of the occlusion downdraft outflow associated with the occluding circulation (solid dark blue line) and the new rainy downdraft (dashed light blue line), which developed on the north side of the developing circulation.

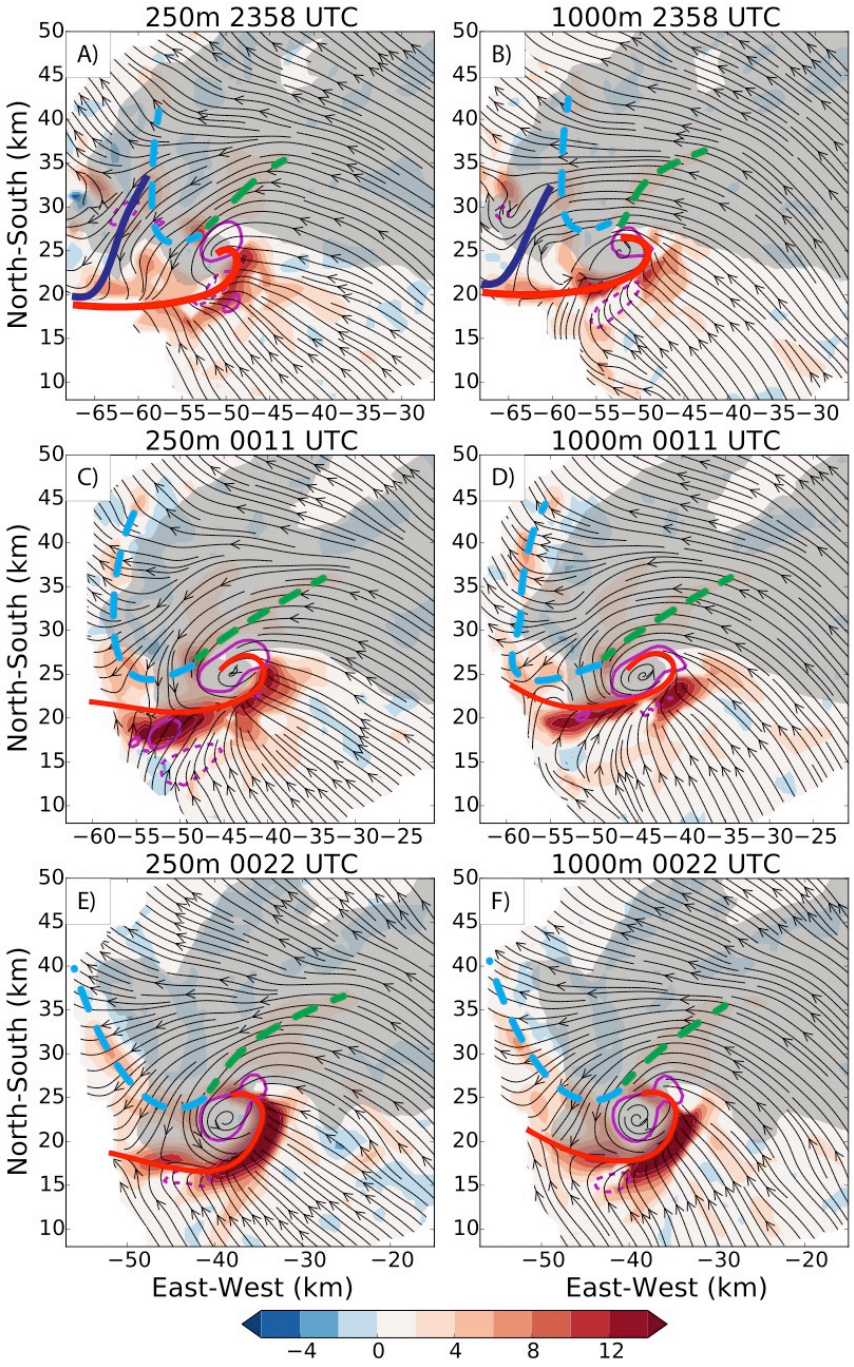

Fig. 3.4 Storm-relative streamlines at an altitude of 250 m (left column) and 1000 m (right column) at 2358 UTC (top row), 0011 UTC (middle row), and 0022 UTC (bottom row) with the asymptotic contraction rate overlaid in color in units of 10^{-3} s^{-1} according to the color scale. Near-surface boundaries are drawn with the primary rear flank gust front (RFGF) in red, the secondary rear flank gust front (SRFGF) in light blue, the previous mesocyclone cycle's secondary rear flank gust front in dark blue, and the forward flank convergence boundary (FFCB) in green. Reflectivity greater than 40 dBZ is shaded in grey. Vertical vorticity maxima are annotated with magenta contours at -5 (dashed), 10, and 30 (solid) X 10^{-3} s^{-1}.

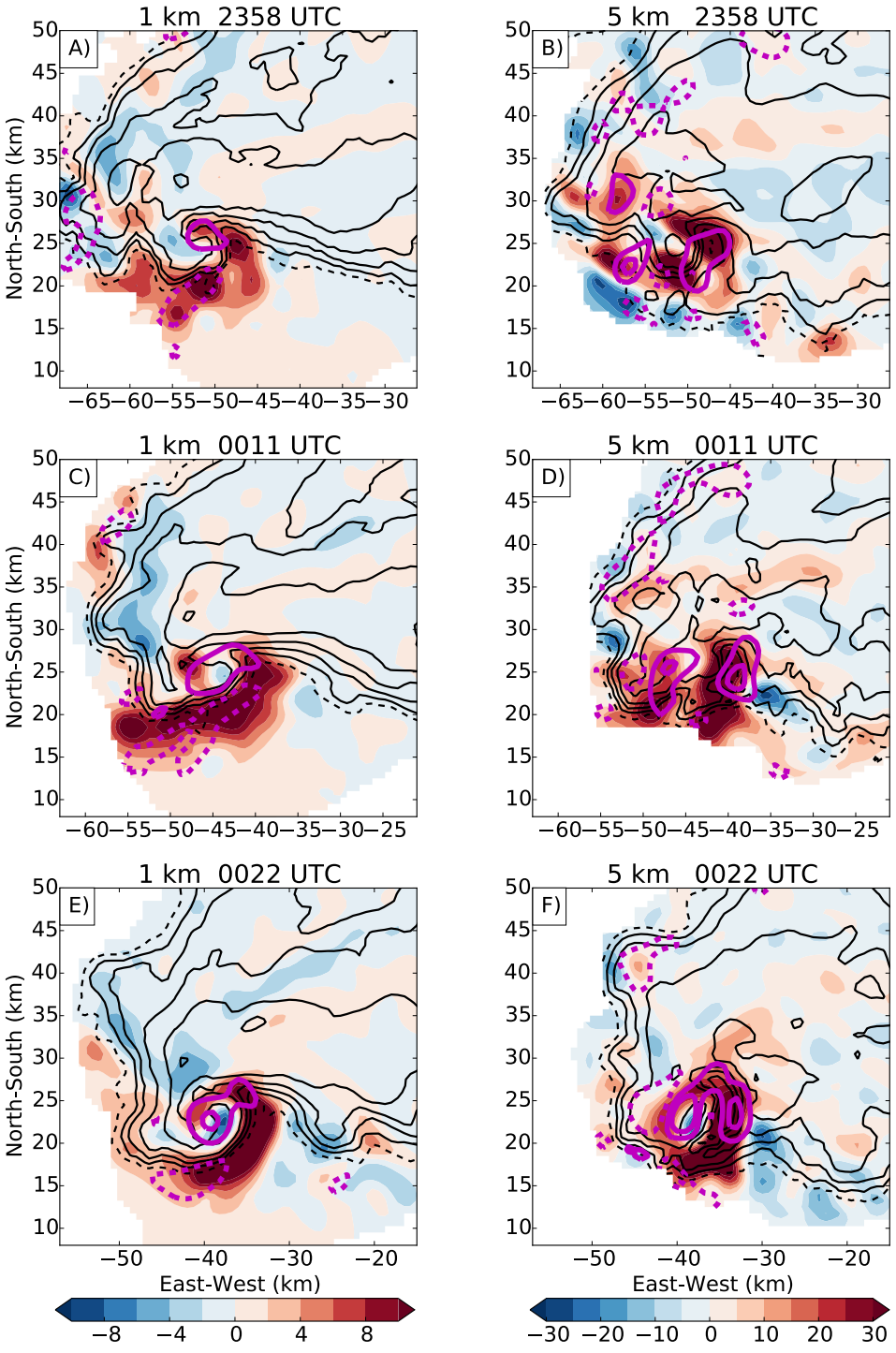

Fig. 3.5 Horizontal cross-sections at 1 km altitude (left column) and 5 km altitude (right column) for the 2358 UTC (top row), 0011 UTC (middle row), and 0022 UTC (bottom row) analysis of vertical velocity (in m s^{-1}, according to the color scale), radar reflectivity greater than 20 dBZ (contoured every 5 dB with 20 dBZ dashed and high values solid). Vertical vorticity maxima are annotated in magenta at -5 (dashed), 10, and 30 (solid) (X 10^{-3} s^{-1}).

As the occluding circulation retreated, in a storm-relative sense, to the northwest side of the storm, the associated SRFGF expanded southward, such that the southern end merged with the primary RFD (Fig. 3.4a). By 0011 UTC (Fig. 3.4c), the new SRFGF had surged westward, overtaking the old outflow region, as the RFD strengthened (Fig. 3.5c, x=-54, y= 27) and the low-level updraft zone and vertical vorticity field became better organized (Fig. 3.5a, c). Interestingly, the primary RFGF near the developing circulation did not surge southward until the end of the organizing stage (0022 UTC), waiting instead for an occlusion downdraft to develop and strengthen on the south side of the circulation (Fig. 3.5e).

On the eastern edge of the rainy downdraft, persistent positive asymptotic contraction was noted extending northeastward through the forward flank of the storm and will hereafter be referred to as the forward-flank convergent boundary (FFCB, dashed green line in Fig. 3.4). We have chosen to distinguish it from the left-flank convergent boundary found by Beck and Weiss (2012) because it was located in the forward flank and appears too weak to be the delineating boundary between modified inflow and cold RFD outflow, as was found in their study. Moreover, despite the presence of a midlevel forward flank downdraft, a distinct forward flank gust front was never present in the analysis— in agreement with previous studies (DB02; Markowski et al. 2002; B06; Skinner et al. 2014). At this time, only portions of the FFCB demonstrated enough convergence to classify it as a kinematic boundary. Eventually, this boundary was collocated with noticeable convergence during the occlusion stage. Though oriented towards the northeast, the FFCB remained on the northwest side of the

circulation as the vortex expanded to the southwest and increased in asymmetry (Fig. 3.5c).

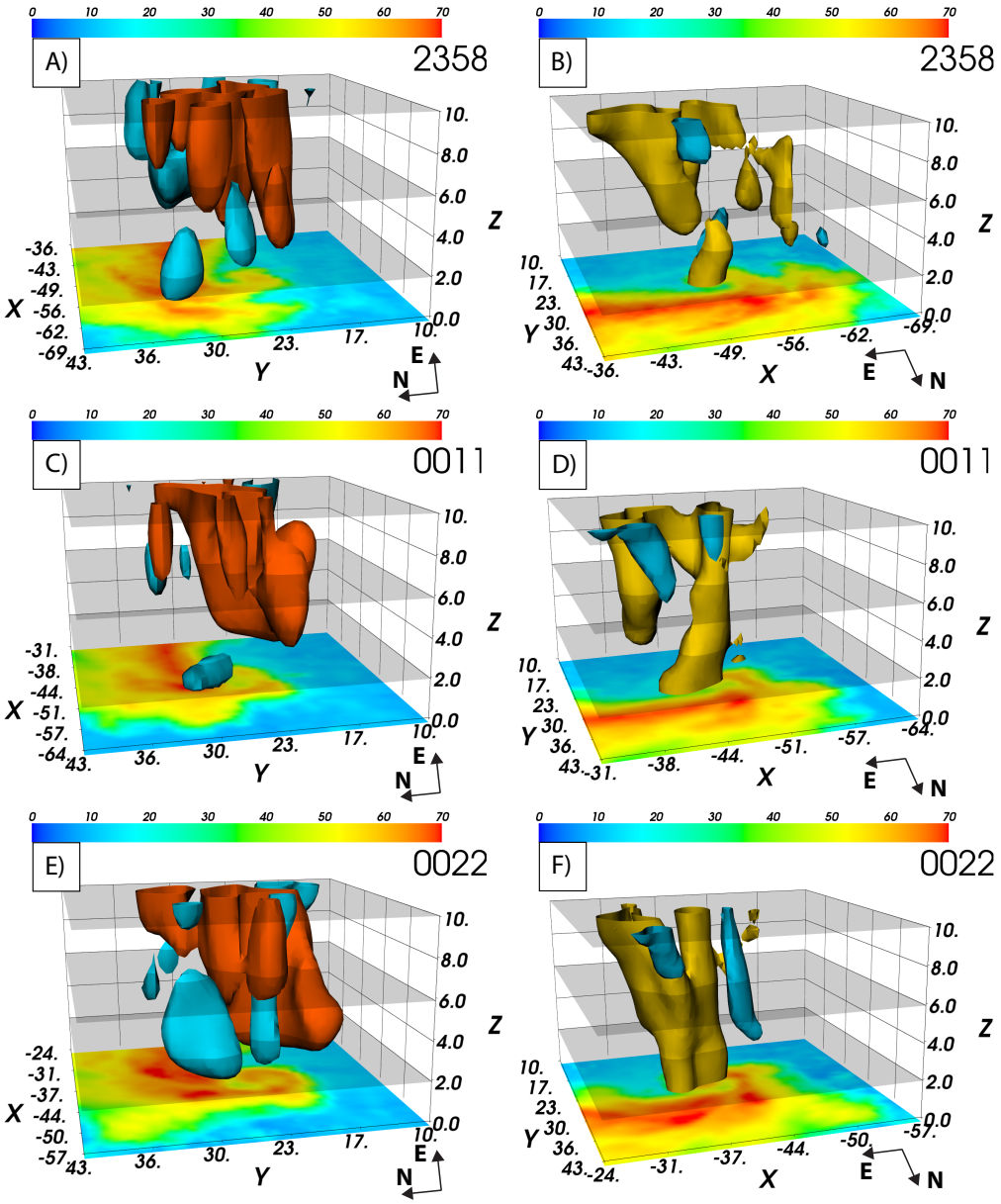

Fig. 3.6 Three-dimensional isosurfaces of vertical velocity (-5 m s^{-1} [blue] and 20 m s^{-1} [red] left column) and, vertical vorticity (-1 X 10^{-3} s^{-1} [blue] and 1 X 10^{-3} s^{-1} [gold] right column) for 2358 UTC (upper row), 0011 UTC (middle row), and 0022 UTC (bottom row) Radar reflectivity (in dBZ according to the color scale) at 1 km altitude is plotted at the bottom of each panel. Horizontal planes at 2, 6, and 10 km are shaded grey for reference. Note that panels a, c, and e are oriented with a perspective of looking at the storm from approximately the west while panels b, d, and f are oriented with a perspective of looking at the storm from approximately the north.

2) PRECIPITATION AND VERTICAL DRAFT EVOLUTION

During mesocyclogenesis, the heaviest precipitation at mid levels (Fig. 3.5b, x=-53,y=35) was associated with the occluding circulation. As the new mesocyclone became better organized and the primary updraft strengthened, the new rear-flank precipitation core intensified (Fig. 3.5d, f). At lower levels, the western portion of the new hook echo doubled in size between 2358 and 0022 UTC (Fig. 3.5a, e) as the new mesocyclone substantially strengthened (Fig. 3.5c). The low-level reflectivity storm-scale structure was then maintained throughout the mature stage of the mesocyclone (0022-0052 UTC).

As the mesocyclone transitioned from the genesis to the end of the organizing stage, the downdraft structure changed significantly. The downdrafts in the rear-flank region (Fig. 3.5a, x=-63, y=24; see also Fig. 3.6a, c) were at their weakest point during mesocyclogenesis. Indeed, rising motion on the east side of the occluded circulation divided pockets of sinking motion associated with the old circulation and the new hook echo (Fig. 3.5a, x=-55, y= 24). By 0011 UTC, a centralized low-level RFD region had developed (Fig. 3.5c, x=-53, y=27). Initially, the RFD was shallow. By 0022 UTC, however, the RFD was part of a deep region of subsidence that extended up to midlevels (Fig. 3.6e). Between 0011 and 0022 UTC, the occlusion downdraft (Fig. 3.5c, x=-45, y= 25 and Fig. 3.5e, x=-39, y=22) doubled in strength while remaining separated from the RFD by the occlusion updraft to its northwest. This separation can best be seen when the vertical motion field is viewed three-dimensionally (Fig. 3.6e). Furthermore, the SRFGF (Fig. 3.4c) was clearly positioned *between* the RFD and

occlusion downdraft regions, suggesting that the potentially colder RFD air was not advecting into the low-level circulation at this time.

During mesocyclogensis (2358 UTC), the updraft straddled the hook echo at low and midlevels (Fig. 3.5a, b), coincident with weak outflow in the new hook echo region. The western part of the updraft zone appeared to be connected to the occluding circulation, especially at 5 km (Fig. 3.5b, x=-58, y = 30). However, as the new RFD strengthened and the SRFGF surged southward (Fig. 3.5c), convergence was enhanced on the western end of the RFGF (Fig. 3.4c, x=-58 to -45, y=18), resulting in a strong, but elongated low-level updraft. By 0022 UTC, the gust front bulged out towards the southeast, shifting the strongest convergence and low-level updraft eastward, coincident with the intensification of the low-level occlusion downdraft, giving it the classic kidney-bean shape (Fig. 3.5e, x=-35, y=20). The updraft pulse generated at 0022 UTC can be seen rising upward in height in the time-height plot (Fig. 3.3a). Not surprisingly, as the low-level updrafts became better organized, the midlevel updraft took on a more classic horseshoe-shape (Fig. 3.5f).

3) EVOLUTION OF VERTICAL VORTICITY

Initially at 2358 UTC, the developing low-level mesocyclone vortex (Fig. 3.4a, x=-53, y= 25) was small, symmetric, and collocated with an updraft while also decreasing in size with height (Figs. 3.5b, 3.6b). The anti-cyclonic circulation to the south (Fig. 3.4a, x=-53, y=19) formed a pair of counter-rotating low-level vortices near the tip of the hook echo, which could be indicative of vortex arch structure and the tilting of baroclinically generated vorticity (Straka et al. 2007; Markowski et al. 2008). Vortex lines connecting the two vortices were not found, however, possibly the result of

degraded vertical resolution from the eastern radar, which was almost 60 km away from the mesocyclone at 2358 UTC.

Three-dimensional isosurfaces of vertical vorticity (Fig. 3.6b, d, f) demonstrate that the low-level mesocyclone was initially separate from the midlevel mesocyclone but appeared to deepen as it evolved from genesis to mature stage during the organizing period. At 0011 UTC, the low-level mesocyclone at 1 km (Fig. 3.5c, x=-45, y=24) was connected with the midlevel vorticity maxima (Fig. 3.5d, x=-48, y=24) west of the main updraft, resulting in the main mesocyclone vortex becoming a distinct circulation from the vorticity collocated with the primary updraft (Fig. 3.5d, x=-40, y=24). This evolution suggests that during the organizing stage, the low-level mesocyclone, rather than connecting to the traditional midlevel mesocyclone via vortex line surgery (Markowski and Richardson 2014), grew upward with time. While not evolving in a traditional manner, similar midlevel vorticity structures have been observed in previous radar-based analyses (Brandes 1978; Klemp et al. 1981; Ziegler et al. 2001; DB02a). Both regions of vorticity evolved separately in time and will be distinguished as the mesocyclone vortex, or just mesocyclone (Fig. 3.5f, x=-38, y=23), and the updraft shear region vorticity (Fig. 3.5f, x= -33, y=23). The fact that these are two distinct columns of vorticity is better elucidated in the 3-D isosurface of vertical vorticity at 0022 UTC (Fig. 3.6f).

During the middle of the organizing stage (Fig. 3.6d), the vortex was broadest at low-levels, decreased in size with height, and was tilted towards the west-southwest. However, following a RFD surge at 0019 UTC, the mesocyclone became much more consistent in size and strength with height (Fig. 3.6f) and became centered on the

vertical velocity gradient (Fig. 3.5e, x=-40, y=22) producing a divided vortex structure at 0022 UTC. This transition in mesocyclone behavior is consistent with the conceptual model described by Lemon and Doswell (1979) as the mesocyclone transitions between the organizing and mature stages.

3.4.2 Mature stage: 0027-0039 UTC

1) KINEMATIC BOUNDARIES

The kinematic boundaries from the asymptotic contraction rate analysis during the mature stage of the second mesocyclone are shown in Fig. 3.7. As the storm progressed on into the mature stage, the next RFD surge at 0027 UTC (Fig. 3.8a, x=-39, y=27) caused the SRFGF to also surge southward (Fig. 3.7a, x=-38, y= 20) along the western edge of the mesocyclone circulation. During this period, the SRFGF was well defined by the asymptotic contraction rate as the boundary lay within a region where the asymptotic contraction rate approached 10^{-2} s^{-1}. After the initial southward surge between 0022 and 0027 UTC, the SRFGF and associated zone of enhanced asymptotic contraction rate did not progress any further south over the next 12 minutes. Furthermore, there was a delay between the southward surge in the SRFGF and changes in the position of the primary RFGF. The delay implies that different downdraft flow regimes were reinforcing the primary and secondary RFGFs, potentially delaying the subsequent occlusion of the circulation. Following the RFD surge, the FFCB briefly tightened up into a noticeable kinematic boundary (Fig. 3.7c, x=-32, y=27), straddled by a moderate updraft and downdraft (Fig. 3.8c).

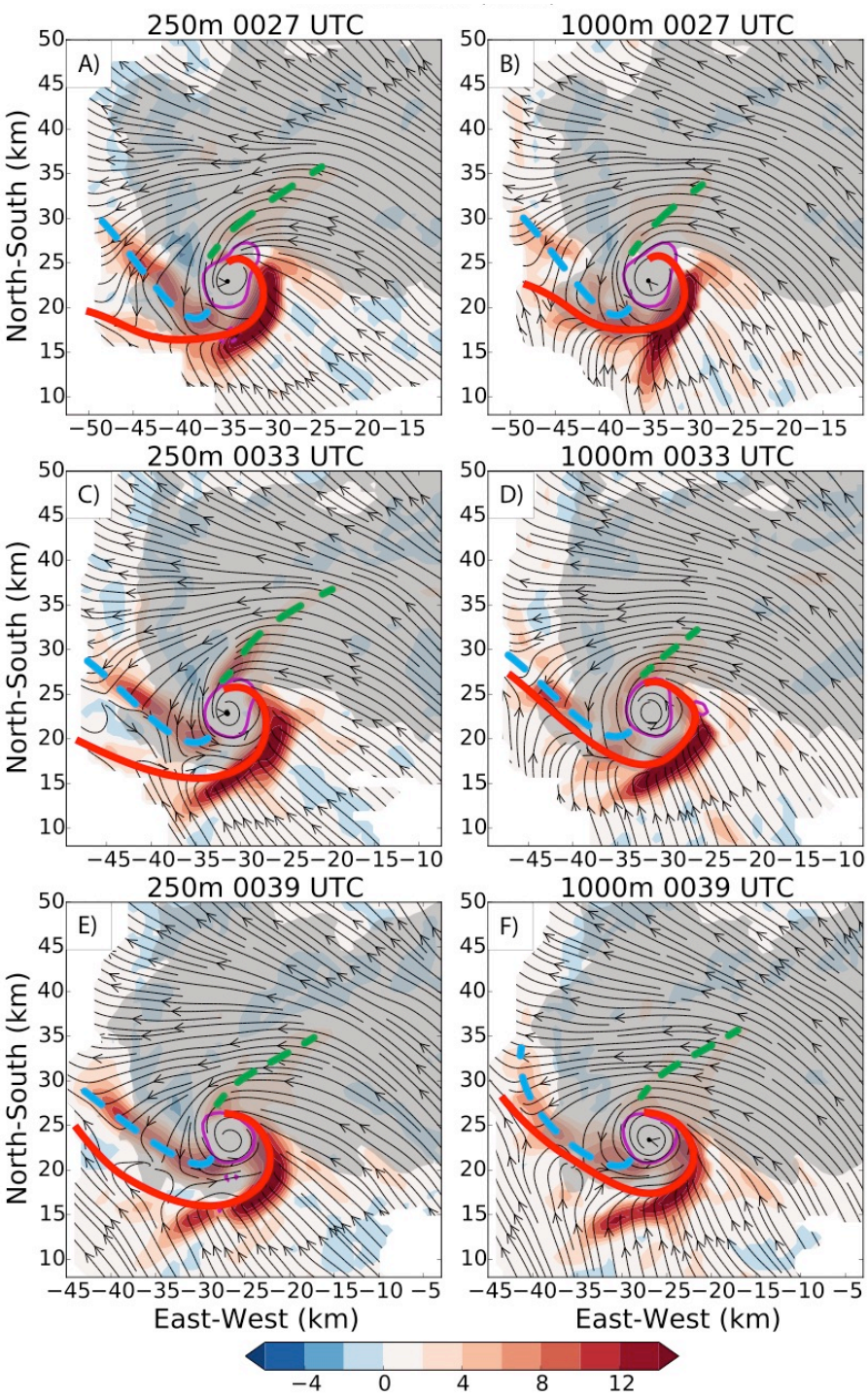

Fig. 3.7 Same as Fig. 3.4.

2) PRECIPITATION AND VERTICAL DRAFT EVOLUTION

Part of the reason the cold pool behind the SRFGF did not contribute directly to the primary RFGF cold pool during this time is that the 0027 UTC RFD surge led to the

development of a northwest-southeast-oriented band of updraft at the leading edge of the SRFGF (Fig. 3.8a, x=-44, y=25) that extended well into the mid levels of the atmosphere (Fig. 3.8b, d, f). This updraft region was consistently located behind the main gust front and leading reflectivity gradient (Figs. 3.7, 3.8). The western updraft (Fig. 3.8e, x=-35, 22) remained discrete from the primary updraft, even its trailing section, at mid (Fig. 3.8f, x=-33, y= 14) and upper levels. At low-levels, this updraft region may have limited the penetration of the RFD surge into the mesocyclone. At mid levels, the western updraft zone limited the entrainment of environmental dry air into the RFD, which would also likely have limited the strength of the surface cold pool.

The downdraft structure also changed dramatically between the organizing and mature stage of the mesocyclone. In the early organizing stage, the RFD at one km altitude was elongated and located along the back edge of the radar reflectivity gradient (Fig. 3.5b). During the mature stage, the near surface RFD became more compact and was continually collocated with the highest radar reflectivity just northwest of the mesocyclone (Fig. 3.8a, c, e). Even though the low-level downdraft intensified, or at least maintained its strength over the period, the volume somewhat decreased with time (Fig. 3.9a, c, e). The radar analyses also revealed a temporally persistent region of sinking motion on the southeast side of the main updraft that began at 0022 UTC and was present at low (Fig. 3.8a, x= -26, y=18) and midlevels (Fig. 3.8b, x=-27, y=17). This downdraft was particularly strong (< 20 m s^{-1}) at mid levels during the latter part of the mature stage (Fig. 3.8f). Since this region was near the clear air south of the reflectivity core, the downdraft was most likely dynamically driven through

compensating subsidence associated with the primary updraft, which was in part being dynamically accelerated by the embedded midlevel vorticity.

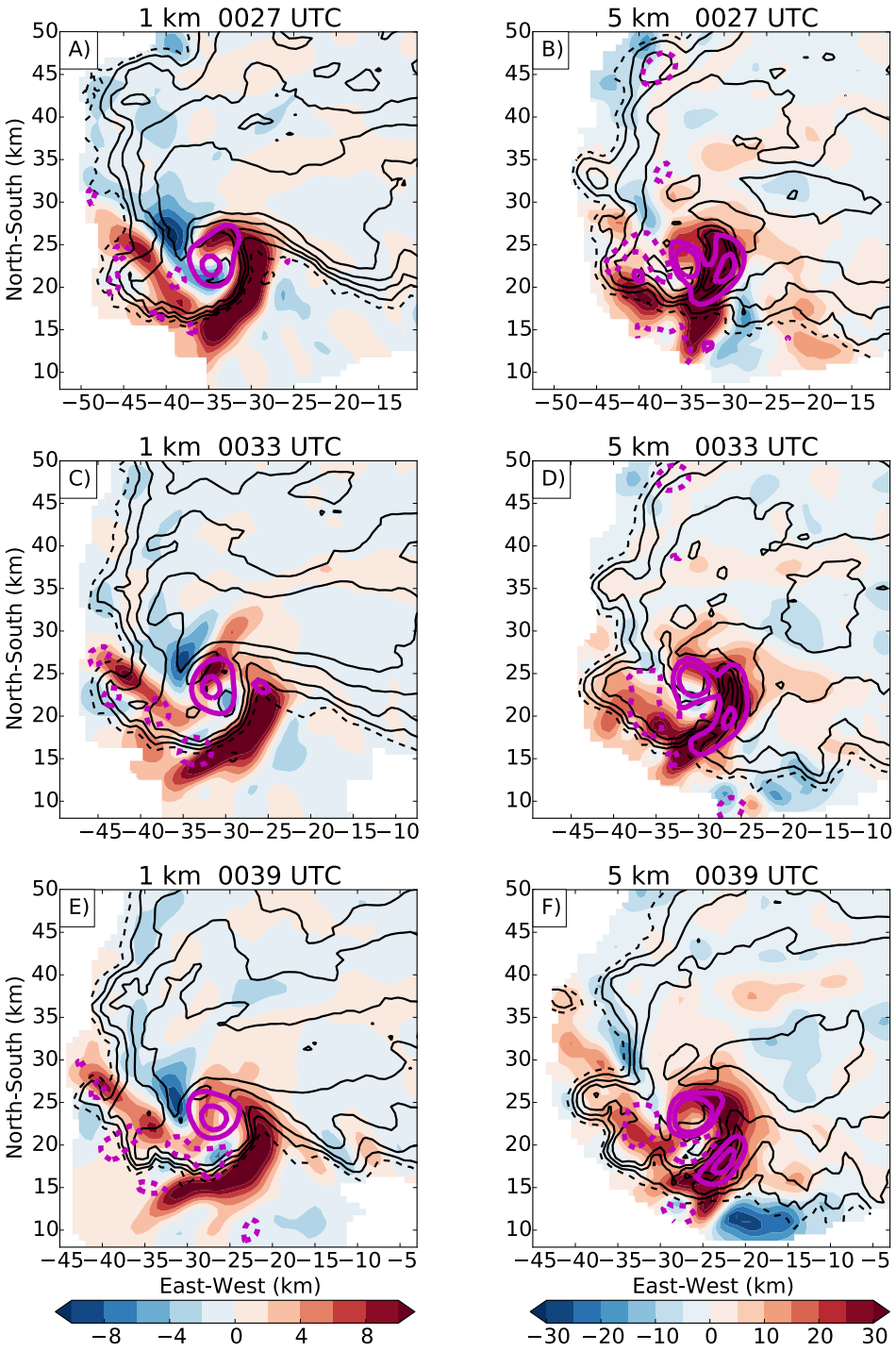

Fig. 3.8 Same as Fig. 3.5

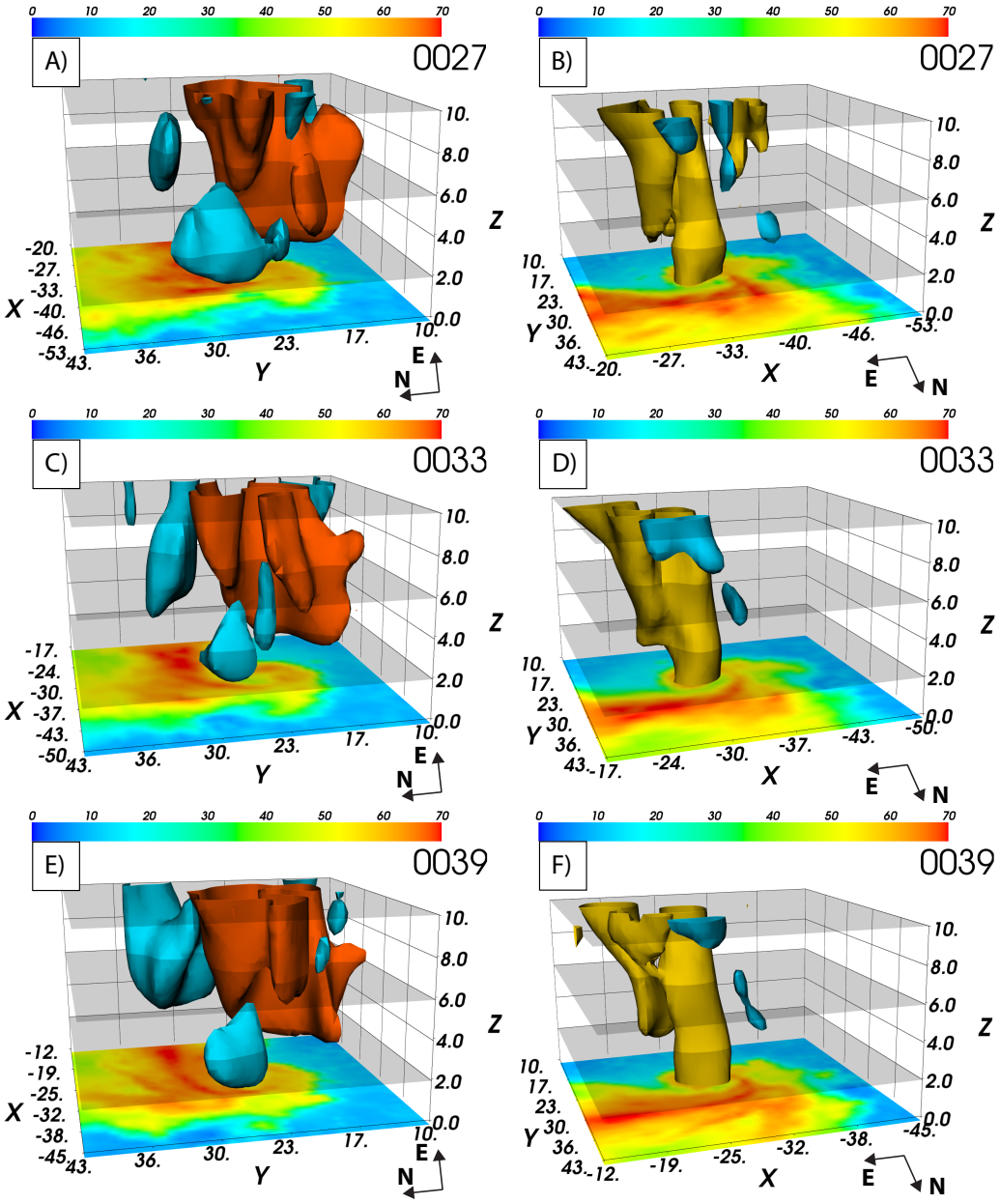

Fig. 3.9 Same as Fig. 3.6

At mid levels, the forward flank downdraft expanded with time while remaining collocated with the highest radar reflectivity in that part of the storm (Fig. 3.8b, d, f). The horizontal expansion and increase in depth with time is well illustrated by the -5 m s^{-1} isosurface of vertical motion in Figure 3.9a, c, e. While the forward flank downdraft increased in size and intensity at mid-to-upper levels, it remained weak near the surface,

consistent with the lack of a well-defined surface boundary along the forward flank of the storm.

The occlusion downdraft evolved throughout the mature stage as well. Initially, the occlusion downdraft was embedded near the center of the mesocyclone on the south-southwest side of the circulation (Fig. 3.8a, x= -35, y= 21). With time, the occlusion downdraft shifted outward and rotated cyclonically around the circulation and was located on its southern periphery by 0039 UTC (Fig. 3.8e, x= -26, y= 16). The depth of the occlusion downdraft also varied significantly with time (Fig. 3.9a, c, e).

In addition to the occlusion downdraft, there was evidence of a distinct occlusion updraft, particularly near the surface at 0033 UTC (Fig. 3.8c, x= -32, y= 25). The occlusion updraft was less obvious at the beginning of the mature stage (0027 UTC) as it appeared to be a northern appendage of the primary updraft zone. With time, however, the core of the primary updraft (denoted by its maxima) shifted *clockwise* relative to the mesocyclone, producing better separation between the primary and occlusion updrafts.

As the core of the primary updraft shifted clockwise relative to the mesocyclone, a precipitation streamer abruptly appeared (Fig. 3.8e, x=-14, y=20). This streamer signified a southward shift in the forward flank reflectivity core into the inflow region and probably increased the amount of rain-cooled air feeding into the low-level updraft. The near surface radar reflectivity in the mesocyclone region also evolved with time. At the beginning of the mature stage, the mesocyclone area precipitation distribution was shaped more like an anchor than a hook. As the mesocyclone became more symmetric and the axis of the RFD rotated from northeast-oriented (Fig. 3.8c) to

northwest-oriented (Fig. 3.8e), the low-level reflectivity evolved back into a classic "hook" shape. Otherwise, the magnitude and distribution of radar reflectivity changed little during the mature stage of the mesocyclone.

3) EVOLUTION OF VERTICAL VORTICITY

During the mature stage of its lifecycle, the vertical structure of the mesocyclone transitioned from being broader at the base relative to mid and upper levels (Fig. 3.9b), to being similar in diameter with height. This transition was likely associated with stretching of vertical vorticity by the vertical gradients in vertical motion as the mesocyclone went from a divided vertical velocity structure to being dominated by the occlusion updraft that intensified with height (Fig. 3.8). Interestingly, the deep mesocyclone continued to intensify even though it was horizontally displaced from the primary updraft. The vertical velocity gradients in the primary updraft also amplified vertical vorticity, but this updraft shear region vorticity structure was well separated from the vorticity that connected to the low-level mesocyclone (Fig. 3.8b, d, f and Fig. 3.9b, d, f). As the updraft core shifted clockwise relative to the mesocyclone vortex, the updraft shear region vorticity also shifted clockwise and became fully disconnected from the mesocyclone vortex by 0039 UTC.

Despite the initial presence of the occlusion downdraft inside the mesocyclone flow prior to mesocyclone intensification, a tornado formed approximately at 0025 UTC and lasted until 0032 UTC (Fig. 3.1, tornado A). In a PPI from SR2 at 0025 UTC (Fig. 3.10a, x=-35, y=22), a tornado vortex signature (Brown et al. 1978) can be observed at the center of the broader mesocyclone circulation. Additionally, in the description of the

damage survey in Storm Data, three sub-vortices (Fig. 3.1, labeled B, C, D) formed within the parent mesocyclone between 0030 and 0040 UTC.

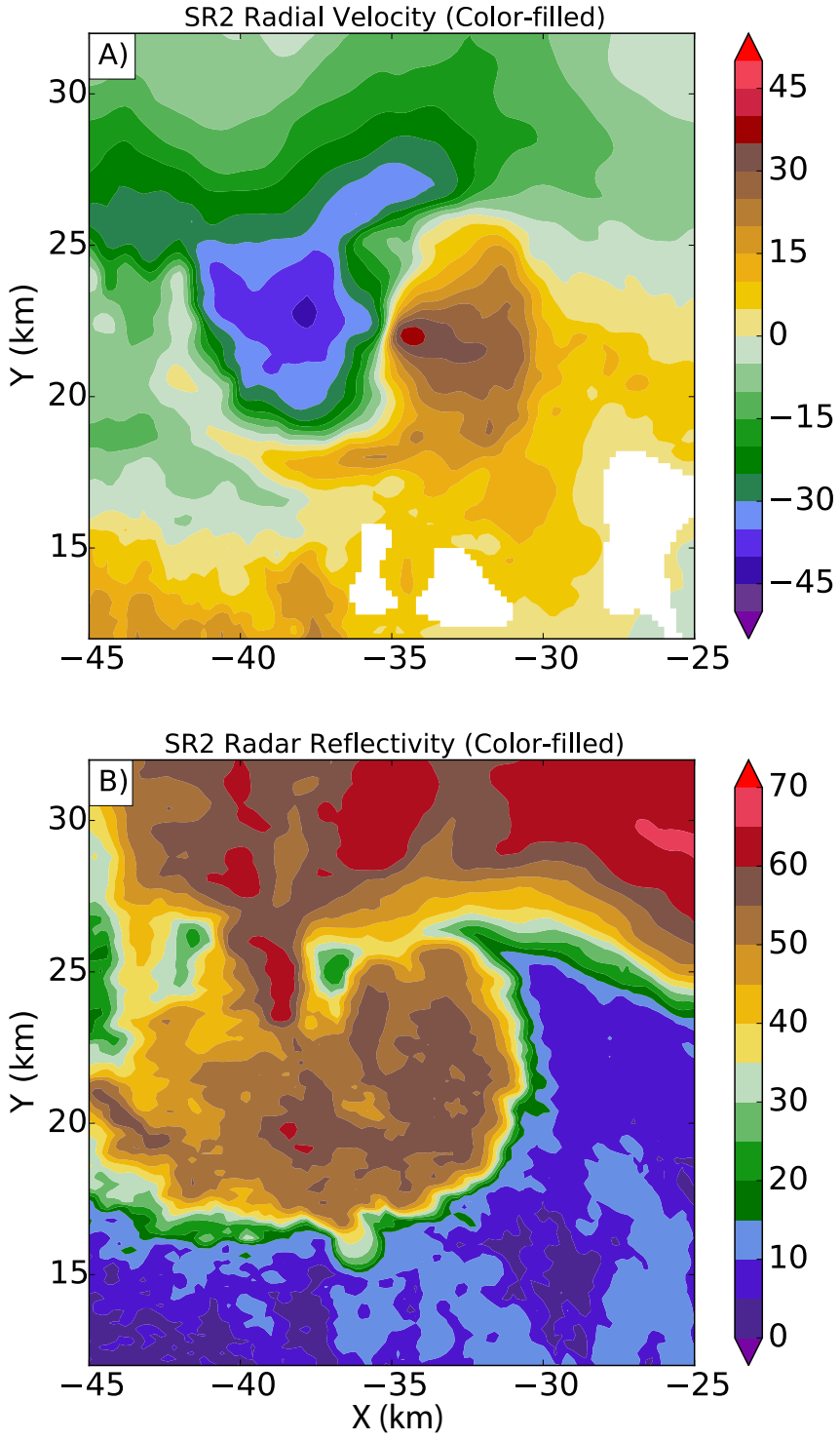

Fig. 3.10 Plan Position Indictor scans at 0.5° elevation of (a) radar reflectivity factor and (b) radial velocity from SR2 at 0028 UTC on 30 May 2004.

3.4.3 Occlusion stage: 0042-0052 UTC

1) KINEMATIC BOUNDARIES

During the occlusion stage, the diagnosed kinematic boundaries continued to be well defined by the asymptotic contraction rate (Fig. 3.11). The onset of the occlusion after 0042 UTC was marked by a southeastward surge in the RFGF (compare Figs. 3.7a, c with Fig. 3.11a, c), while the SRFGF remained attached to, but expanded eastward to encompass, the occluding circulation. In a storm-relative sense, the circulation moved west-northwestward. Similar to the end of the mature stage, the primary RFGF and SRFGFs were nearly co-located at midlevels (Fig. 3.11d, f), as the southerly environmental air flowed over the shallow western end of the primary RFGF and converged with midlevel air within the storm that was flowing southwestward around the western side of the mesocyclone.

The FFCB also remained attached to the occluding mesocyclone. But the boundary shifted eastward in association with the southeast low-level environmental inflow being cut-off from the circulation (Fig. 3.11e).

2) PRECIPITATION AND VERTICAL DRAFT EVOLUTION

Unlike the mature stage, where the RFD stayed along the northwest exterior of the mesocyclone, the primary RFD circulated around the western and southern sides of the mesocyclone during the occluding stage (Fig. 3.12a, c) and merged with a deep, strong occlusion downdraft (Fig. 3.13a, c, e) *within* the southern edge of the mesocyclone prior to 0052 UTC. The relative strengths of the RFD and occlusion downdrafts also switched between the mature and occlusion stages of the mesocyclone. During this period the occlusion downdraft (Fig. 3.12f, x=-18, y=24) was significantly

stronger than the RFD (Fig. 3.12f, x=-23, y=27). The relative strength of the occlusion downdraft and the limited southward extent of the SRFGF suggest that the occlusion downdraft played a more significant role in the occlusion of the mesocyclone compared to the RFD. Nevertheless, the cyclic rotation of the RFD air and the development of the strong occlusion downdraft were responsible for the eastern expansion of the diagnosed SRFGF and the surge in the primary RFGF, and also coincided with expansion of the high reflectivity core on the southwestern side of the hook echo. This increase in reflectivity was a dramatic change from the skinny reflectivity core on the west side of the circulation that had been present for over 30 minutes.

During the occlusion process, the vertical velocity structure within the mesocyclone transitioned from being mostly upward motion to a more divided structure. Interestingly, this divided vertical velocity structure existed into the mid levels (Fig. 3.12 b, d, f). The updraft on the northern side of the mesocyclone again appeared to be separated from the primary RFGF updraft region, which continued to shift its core clockwise relative to the mesocyclone. As the RFGF moved away from the mesocyclone, the low-level convergence weakened and the low-level updrafts diminished (Fig. 3.3a, Fig. 3.11c, Fig. 3.12e). At mid levels, the main updraft transitioned from the classic "horse-shoe" shape into a broader area of updraft with several embedded maxima (Fig. 3.12d, f).

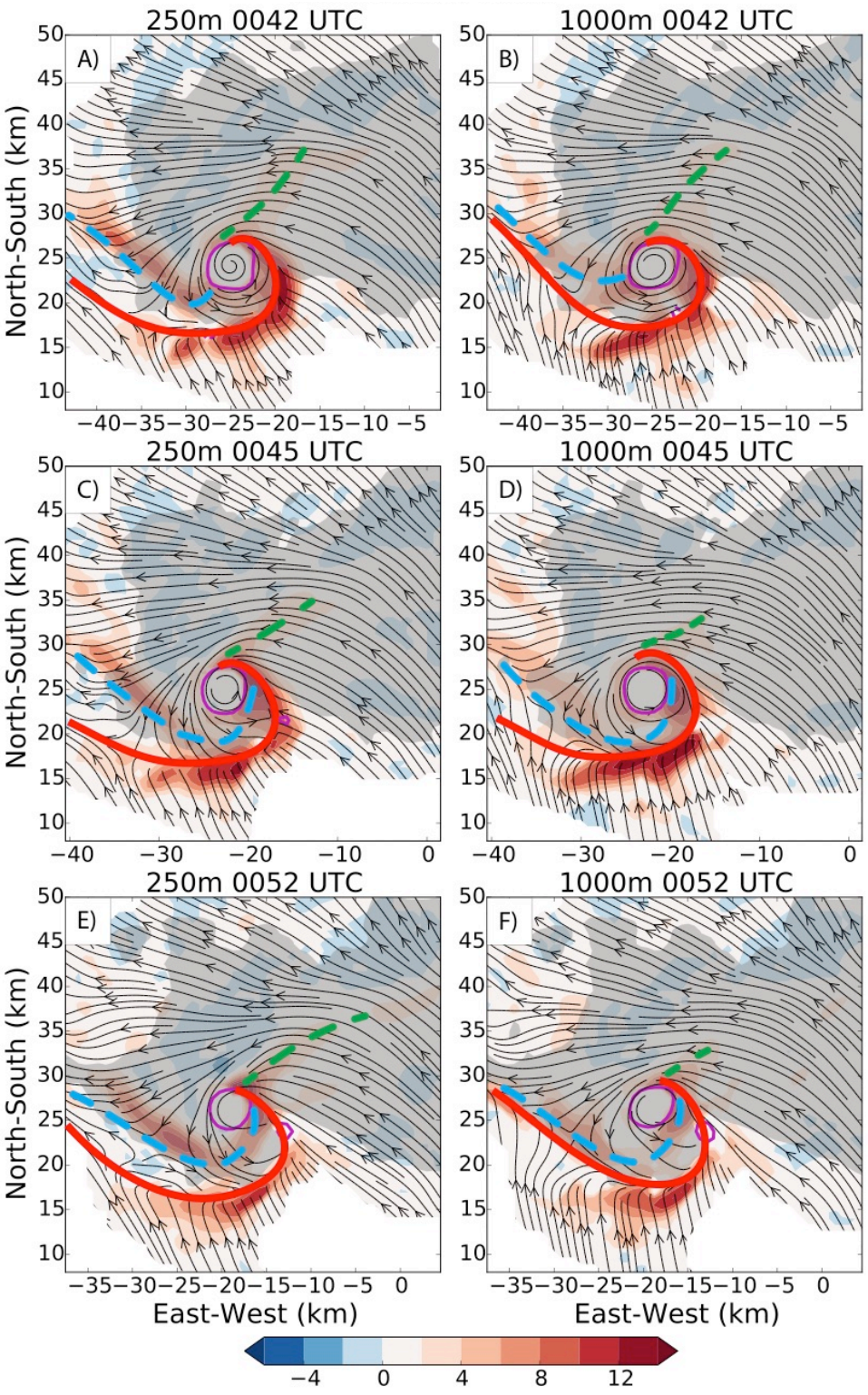

Fig. 3.11 Same as Fig. 3.4

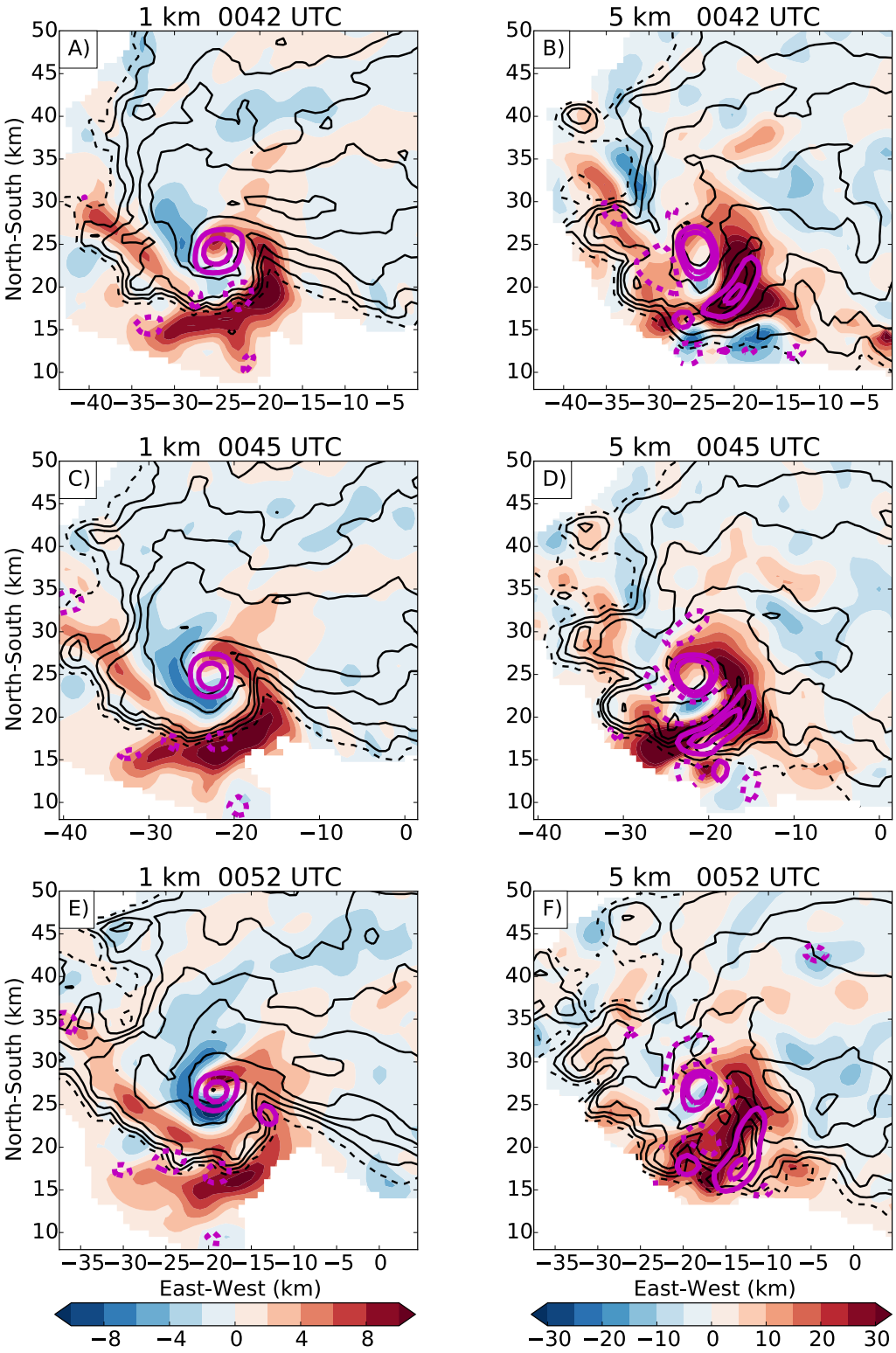

Fig. 3.12 Same as Fig. 3.5

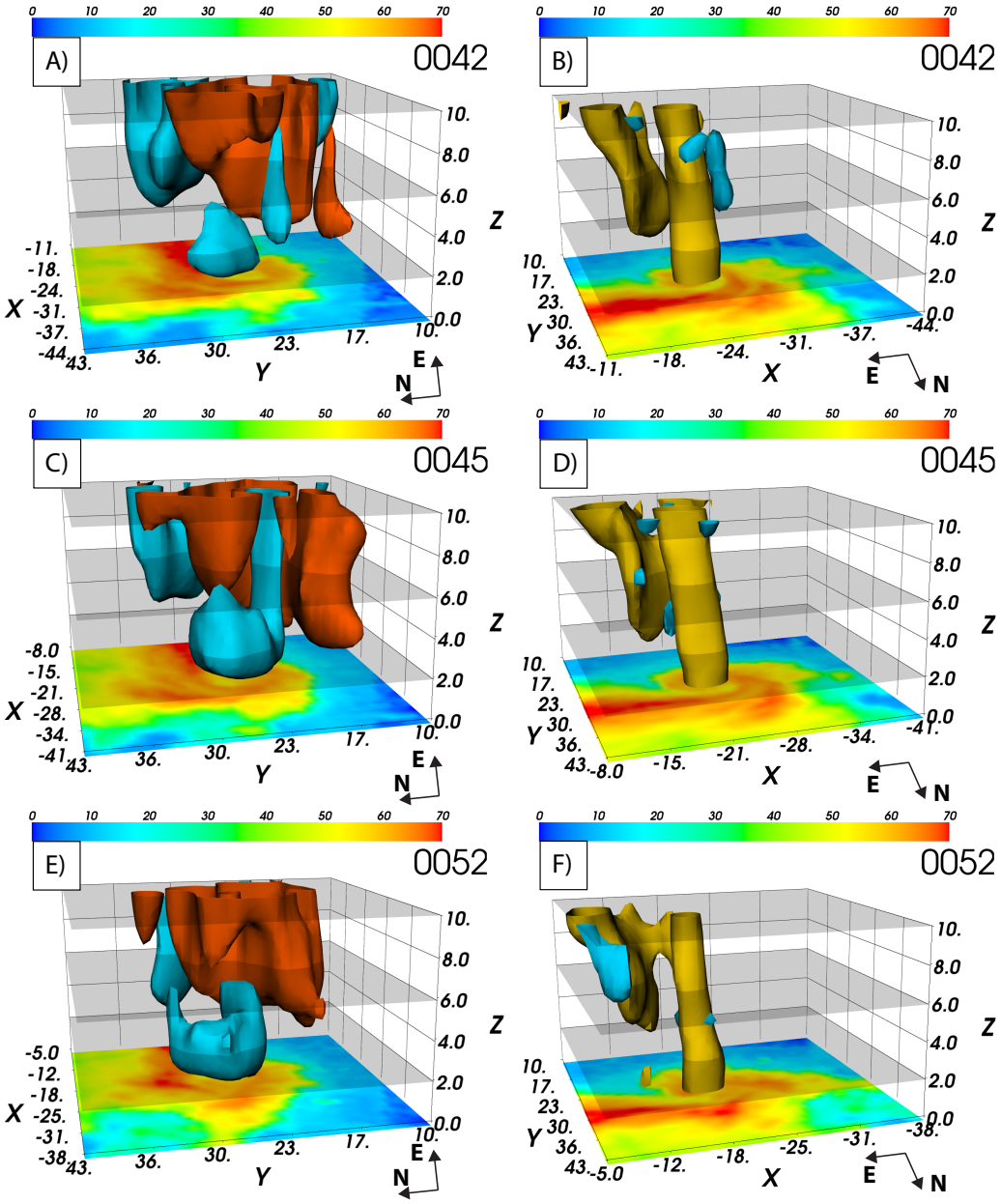

Fig. 3.13 Same as Fig. 3.6

3) EVOLUTION OF VERTICAL VORTICITY

Initially, the mesocyclone itself remained collocated with the occlusion updraft (Fig. 3.12a, x =-25, y = 24) over a deep layer and therefore continued to intensify until 0045 UTC (Fig. 3.3c). Additionally, as sinking motion wrapped around the low-level circulation, the mesocyclone became more symmetric and decreased in scale. Even

though another tornado didn't form until 0052 UTC, the peak analyzed vertical vorticity was observed at 0045 UTC (Fig. 3.3c). This is most likely due to the scale of the most intense rotation decreasing below the resolvable scale of the analysis.

Meanwhile, at midlevels, the mesocyclone vortex continued to separate from the updraft shear region vorticity (Fig. 3.12d, f; Fig. 3.13 b, d, f), with a region of anti-cyclonic vorticity developing between the two positive vorticity regions at 0045 UTC (Fig. 3.12d, x=-22, y = 20). At 0052 UTC, a small but new and distinct vorticity maximum can be seen at low-levels (Fig. 3.12e, x=-12, y=23; Fig. 3.13 f). It developed beneath the northern tip of the updraft shear region vorticity and later elongated and intensified into the next mesocyclone.

3.4.4. Redevelopment stage: 0058-0108 UTC

1) KINEMATIC BOUNDARIES

As the mesocyclone continued to occlude, the primary RFGF pushed east (Fig. 3.14a, c, e) and became detached from the circulation around 0105 UTC, or about 15 minutes after the occlusion process began (Fig. 3.14c). The FFCB also detached from the occluding mesocyclone but remained connected to the primary RFGF at the location of the developing region of cyclonic vorticity (Fig. 3.14c, e), even at mid levels (Fig. 3.14d, f). In contrast to the previous mesocyclone cycle, the FFCB was manifested as a kinematic boundary in the asymptotic contraction rate analysis. However, the asymptotic contraction rate associated with the SRFGF diminished. Near the end of the redevelopment stage, the asymptotic contraction rate on the east side of the mesocyclone marked the eastern extent of the old SRFGF and the western extent of a new SRFGF.

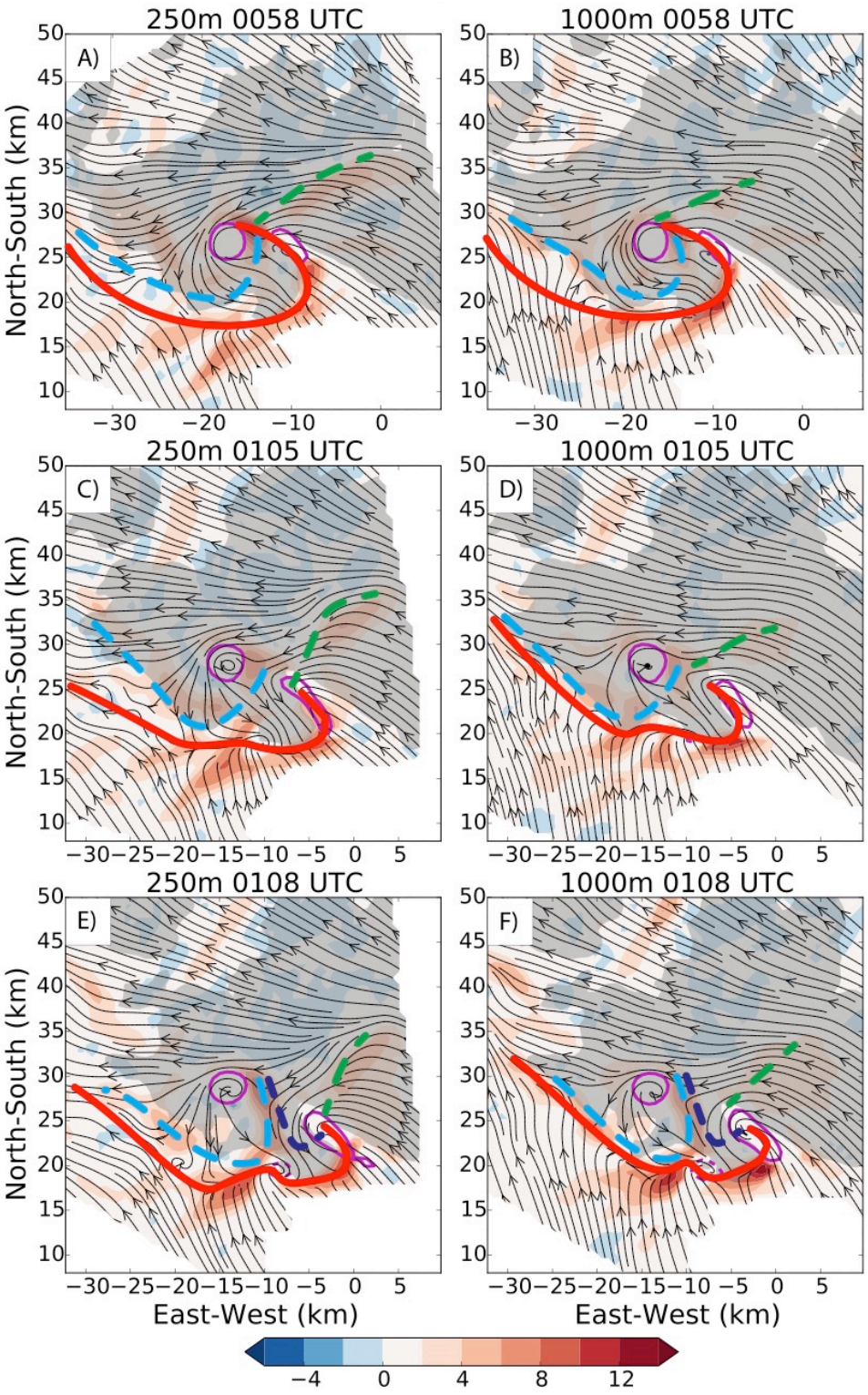

Fig. 3.14 Same as Fig. 4, except the old SRFGF is in blue and the new SRFGF is in dark blue.

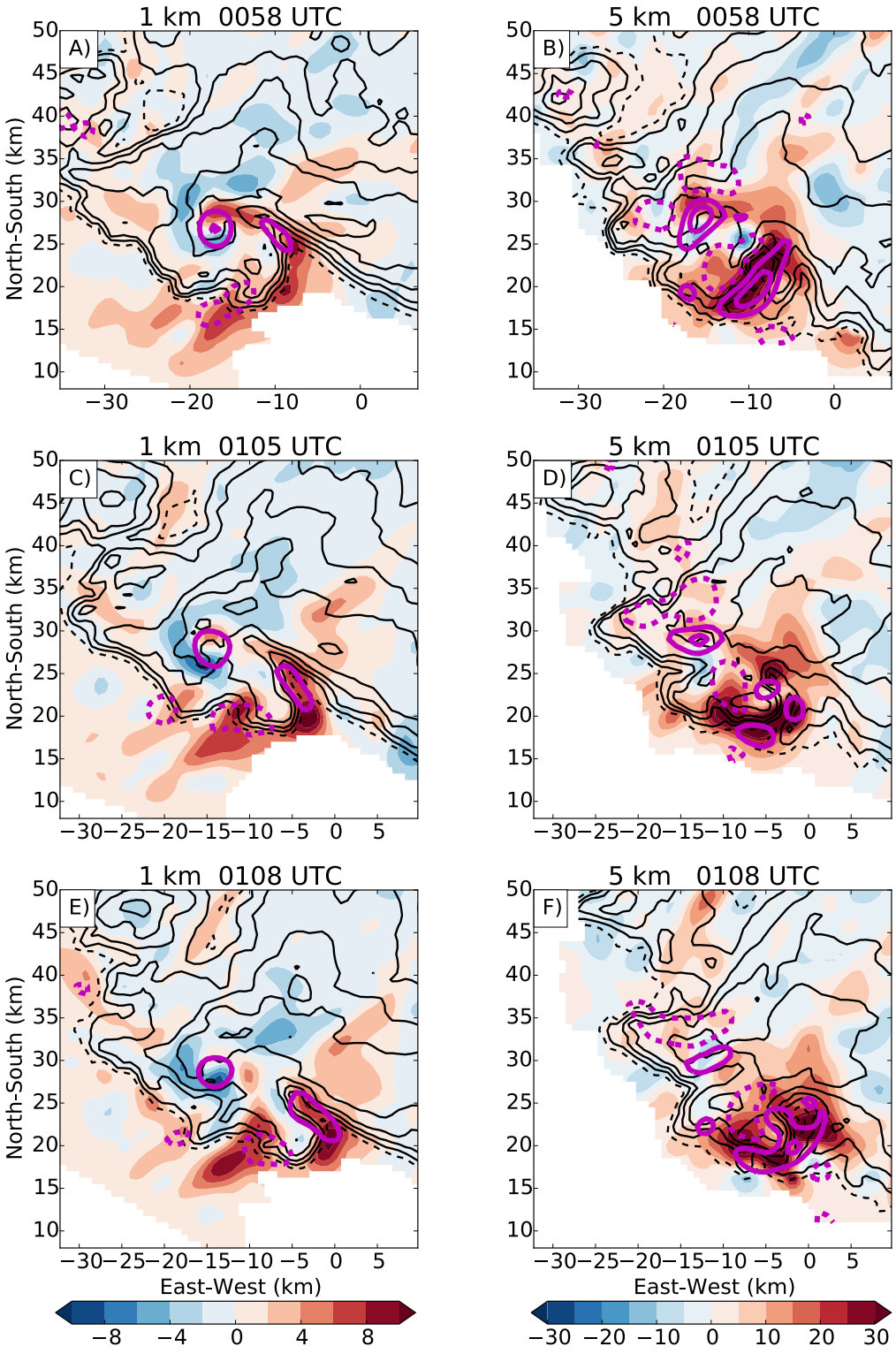

Fig. 3.15 Same as Fig. 3.5 but negative vorticity contour is -5x10^{-3} s^{-1}.

2) PRECIPITATION AND VERTICAL DRAFT EVOLUTION

An elongated reflectivity core formed between the occluding circulation and the primary updraft (Fig. 3.15c, x=-9, y=23) as the hook echo region underwent significant changes, particularly along the primary RFGF where two inflow notches were observed. The main updraft was in the southeastern inflow notch where the new mesocyclone developed (Fig. 3.15c, x= -4, y= 22) while a secondary updraft formed in the smaller inflow notch in the RFGF south of the occluding mesocyclone (Fig. 3.15e, x= -13, y= 17). Near-surface streamlines (Fig. 3.14) indicate that the southeastern inflow remained attached to the occluding circulation until about 0105 UTC when the winds switched from east-northeasterly to north-northeasterly.

At mid levels, these two updrafts formed a more contiguous region of upward motion (Fig. 3.15d, f; Fig. 3.16c, e). Similar to the organizing stage at 2358 UTC, updraft at low and middle levels straddled the elongated reflectivity core (Fig. 3.15e, f), thus maintaining a "U" shape. Despite the surging outflow relative to the occluding circulation, the RFGF remained underneath the midlevel updraft (Fig. 3.15f), similar to the 8 June 1995 Mclean, TX storm of DB02a. Perhaps the favorable balance between the relative strengths of the inflow and outflow allowed the new mesocyclone to spin up quickly.

The strongest downdraft in the rear flank region was associated with the occluding mesocyclone and stayed mainly on the western edge of the weakening circulation, though a new occlusion downdraft formed in the southern part of the occluding mesocyclone at 0108 UTC (Fig. 3.15e, x= -14, y =26). Additionally, downward motion to the northeast of the occluding mesocyclone was observed

throughout this period (c.f. Fig. 3.15e, x= -5, y=32). This northeastern RFD aided the development of the new SRFGF observed in the 0108 UTC asymptotic contraction rate analysis. The increased northerly component of flow on the eastern side of the occluding mesocyclone coincided with development of this new RFD. This may imply that the pressure gradient force associated with the occluding mesocyclone sufficiently weakened in the elongated inflow region to allow the wind to align with the pressure gradient force from the new RFD.

Interestingly, the southwestern band of updraft that had been prevalent for more than 30 minutes during the mature and occluding stage of the mesocyclone evolution had weakened considerably and no longer separated the old SRFGF from the primary RFGF.

3) EVOLUTION OF VERTICAL VORTICITY

The occluded portion of the RFGF was at the center of the so-called vorticity-rich region in the Burgess et al. (1982) conceptual model. This region developed underneath the northern tip of the updraft shear region vorticity (Fig. 3.15e) and, as the vorticity region elongated, extended upward in height (Fig. 3.14d, x= -5, y= 24) producing a deep column of vorticity (Fig. 3.16d) associated with stretching in the primary updraft after 0058 UTC (Fig. 3.15e, f). As with the organizing stage of the previous low-level mesocyclone, a cyclonic/anti-cyclonic vorticity couplet formed on the edge of the elongated hook echo with vortex arches connecting the two. Also during this period, the first of the two substantial anti-cyclonic tornadoes formed in the southern anti-cyclonic region at 0102 UTC and lasted for approximately nine minutes. A deep anti-cyclonic vorticity column associated with this tornado can be observed in

the 3-D isosurface plot at 0105 and 0108 (Fig. 3.16d, f). Meanwhile, the occluding tornadic mesocyclone continued moving rearward and noticeably shrank at low-levels while becoming more tilted towards the east-northeast in height (Fig. 3.16b, d, f) as it became dominated by subsidence (Figs. 3.15e, 3.16f).

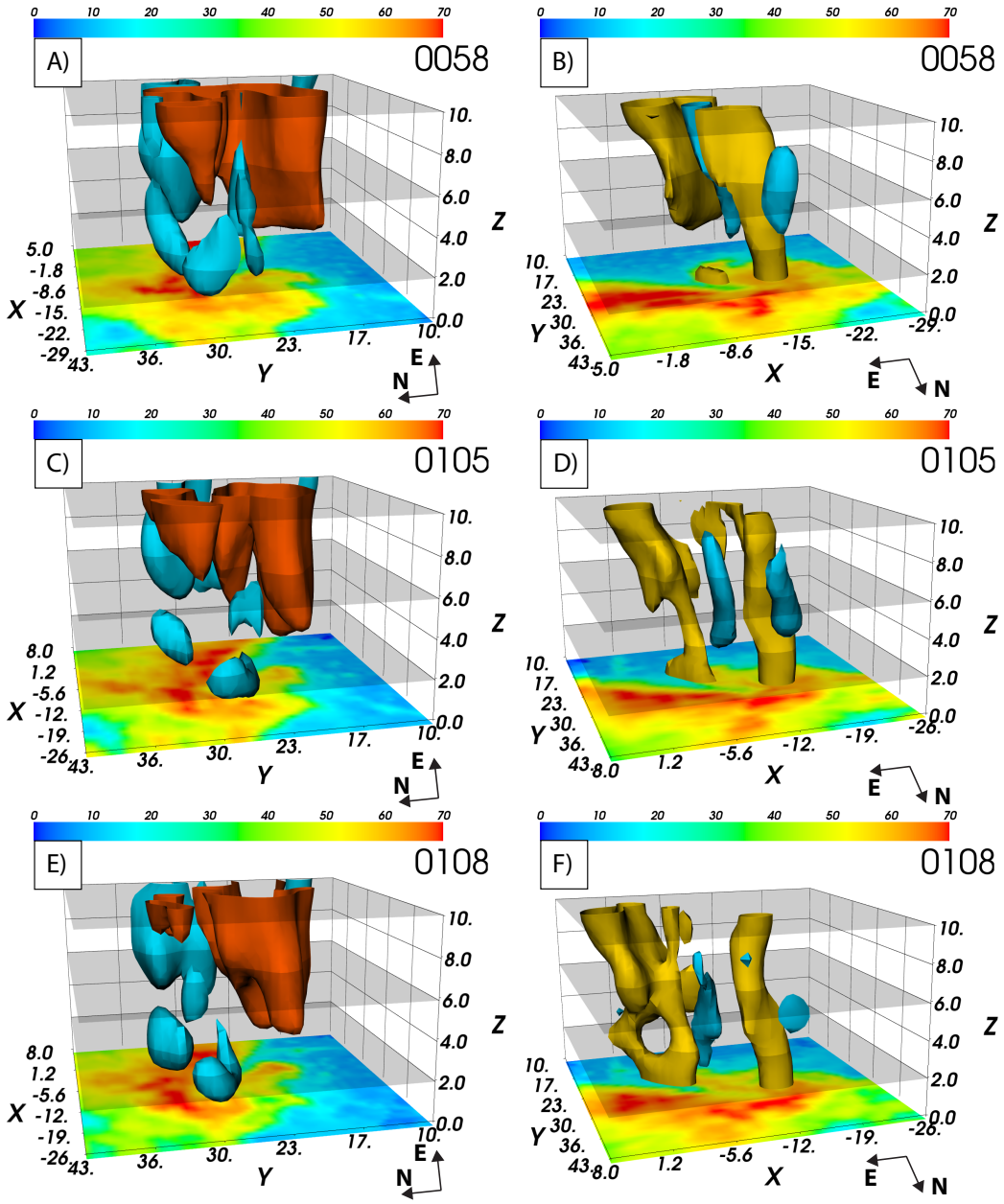

Fig. 3.16 Same as Fig. 3.6

3.4.5 New organizing stage: 0112-0118 UTC

1) KINEMATIC BOUNDARIES

The new SRFGF pushed south and eventually wrapped around the southern end of the new mesocyclone, which had developed rapidly from the elongated vorticity region (Fig. 3.17a, c, e). The SRFGF also pushed westward with time, appearing to undercut the occluding circulation and aiding in the demise of its associated tornado (Fig. 3.17b, c). By the end of the new organizing stage, the new SRFGF was nearly indistinguishable with the old SRFGF, which had merged with the primary RFGF on the western side of the domain (Fig. 3.17e).

2) PRECIPITATION AND VERTICAL DRAFT EVOLUTION

The westward SRFGF surge was coincident with strengthening of the new RFD and the expansion of the hook echo (Fig. 3.18c,e). In many ways, the old RFD and occluding mesocyclone during 0112 - 0118 UTC were similar in structure to the old RFD and occluding circulation during the previous organizing stage (2358 – 0022 UTC; compare Fig. 3.5 with Fig. 3.18). The strongest downdraft was initially with the older mesocyclone. But as that circulation dissipated, the old RFD weakened with the remaining subsidence mostly along the western edge of the hook echo. Even as the primary RFD strengthened and shifted south (Fig. 3.18a, x=-5, y = 32, Fig. 3.18e, x=-1, y = 27), the downdraft was shallow and was located below rising motion at midlevels (Fig. 3.19a, c, e), similar to the updraft structure observed in the previous cycle.

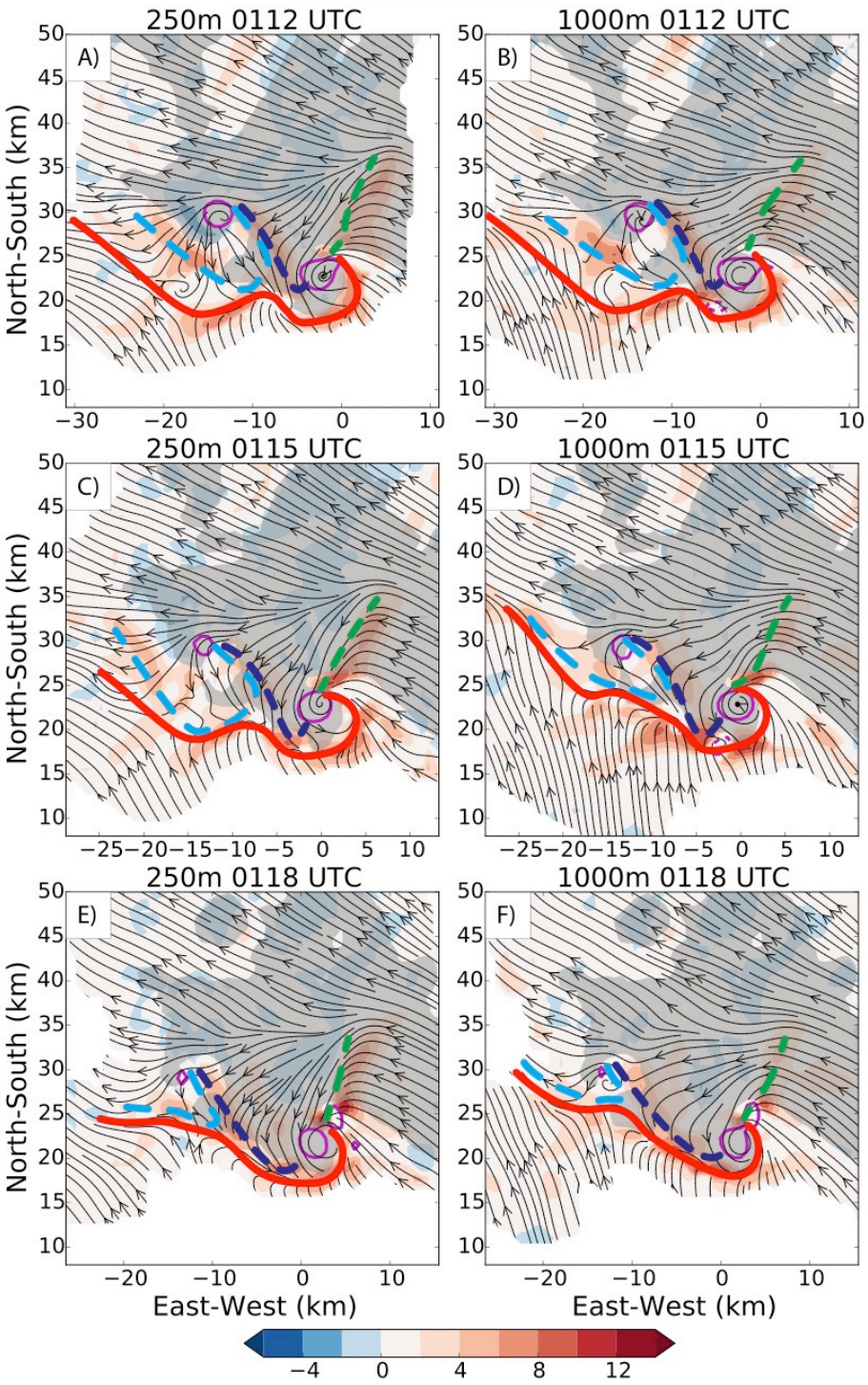

Fig. 3. 17 Same as Fig. 3.4

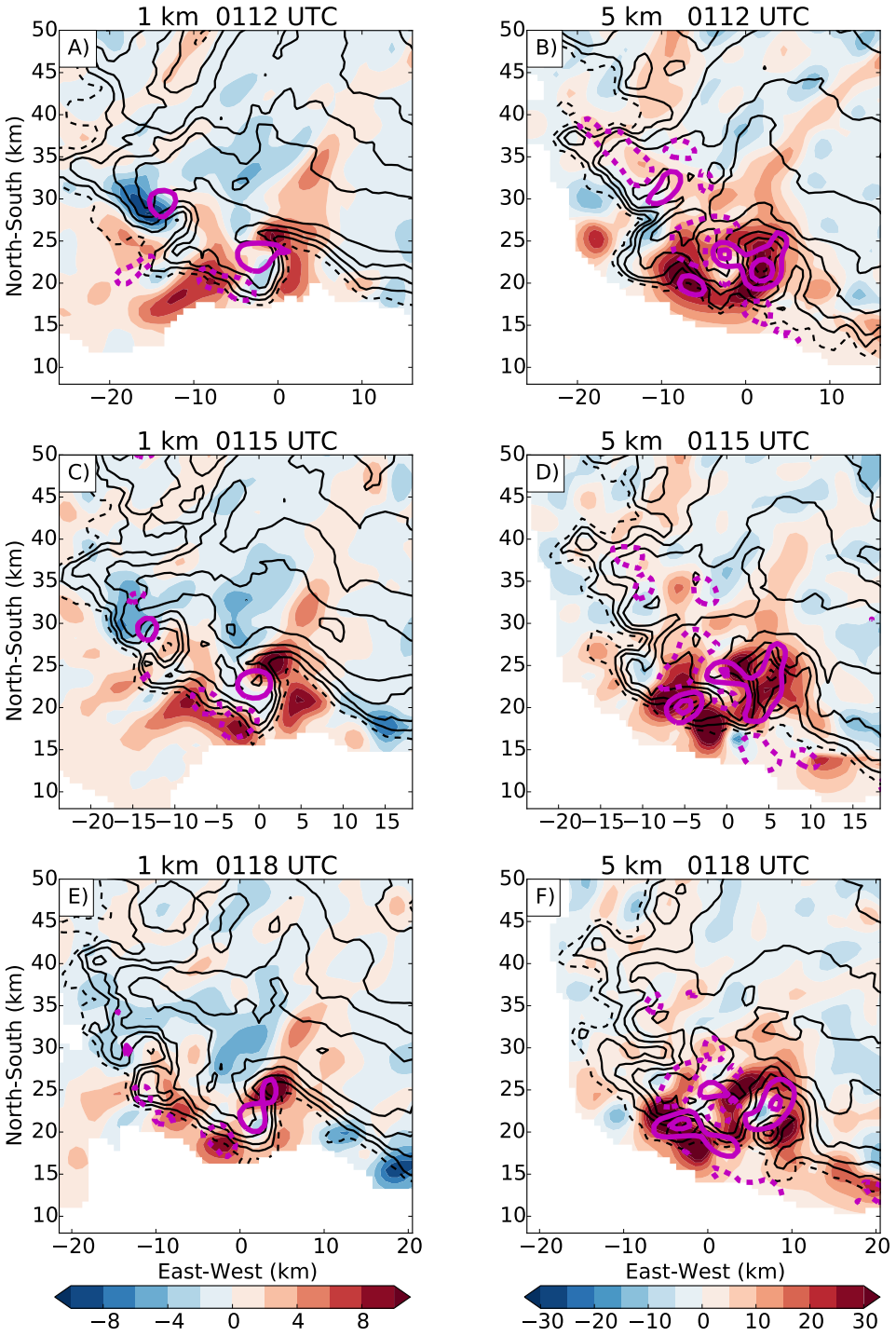

Fig. 3.18 Same as Fig. 3.5 but negative vorticity contour is -5x10^{-3} s^{-1}.

The pattern of vertical motion at mid levels during 0112 – 0118 (Fig. 3.18b, d, f) strongly resembled that between 2358 – 0011 UTC (Fig. 3.5b, d). Moreover, the

primary low-level updraft region of the new mesocyclone consisted of discrete updraft cores, which were just starting to form a more contiguous band, similar to the structure at 2358 UTC. As before, the southwestern updraft band was not present during the organizing stage of the new mesocyclone. However, the structure of the new SRFGF and associated asymptotic contraction rate analysis suggests that a new southwestern band would form during the mature stage of the new cycle, just as was observed in the prior mature stage cycle.

3) EVOLUTION OF VERTICAL VORTICITY

The occluding, tornadic mesocyclone (Fig. 3.18a, x= -14, y = 30) continued to move rearward in time and became tilted with height towards north-northeast (Fig. 3.19b). The size of the occluding circulation had decreased at all levels. By 0115, the midlevel vorticity maximum had vanished and only a small maximum near the surface remained (Fig. 3.19d). Observations suggest that the tornado dissipated at approximately 0115 UTC.

Meanwhile, the second anti-cyclonic tornado occurred between 0115 - 0118 UTC. The three-dimensional vorticity analysis reveals how the original anti-cyclonic vorticity column grew a perturbation that split into two separate anti-cyclonic circulations at 0115 UTC (Fig. 3.19b, d). The first anti-cyclonic tornado dissipated as the second tornado formed around this time. The second tornado was associated with the northwestern circulation.

The organizing new low-level mesocyclone, which had benefited from stretching in the primary updraft during its formative stage, was starting to become a distinct vorticity column as it shifted southwestward relative to the updraft shear region

vorticity between 0115 – 0118 UTC (Fig. 3.19d, f). This break between the vorticity column associated with the low-level mesocyclone and the deep vorticity column associated with the primary updraft had apparently already occurred prior to 2358 UTC in the previous mesocyclone cycle.

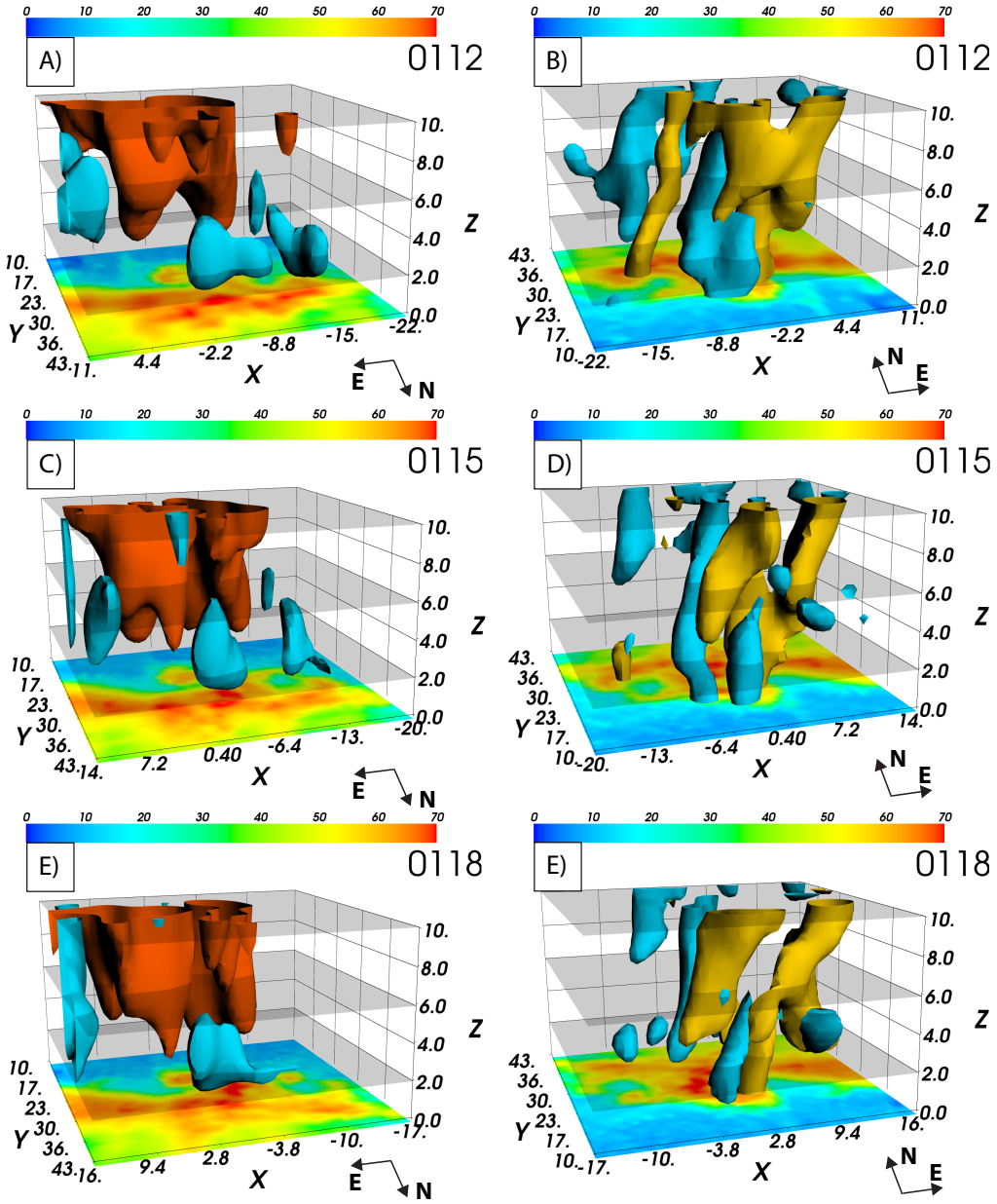

Fig. 3.19 Same as Fig. 3.6, except the orientation has changed. The vertical velocity (left column, panels a, c, and e) are from the perspective of looking at the storm from roughly the north. The vorticity (right column, panels b, d, f) are from the perspective of looking at the storm from roughly the south.

3.5. Discussion

Figure 3.20 summarizes the evolution of low-level kinematic boundaries diagnosed from the asymptotic contraction rate analysis from the end of the first mesocyclone to the organizing stages of the third mesocyclone. Identifiable boundaries were plotted relative to low-level downdrafts, reflectivity, and midlevel vorticity structures. Unlike the previous near-surface boundary illustrations, a distinction was made between kinematic (solid) and solely persistent regions of enhanced contraction rate that became kinematic boundaries in the future (dashed).

The organizing mesocyclone stage was observed for two different mesocyclone cycles: at 2358 UTC (Fig. 3.20a) and 0112 UTC (Fig. 3.20k). Multiple hook echoes were present during each cycle, one associated with the occluding circulation and the other associated with the new circulation. The SRFGFs associated with the occluding circulations both retreated to the northwest side of the storm and extended southward towards the primary gust front during both cycles.

While the occluding circulation was significantly stronger during the later cycle, the most impactful storm-scale difference at the two times was the deep, anti-cyclonic tendency on the west side of the hook echo at 0112 UTC (Fig. 3.21b, x=-8, y=24) compared to the weak cyclonic tendency observed at 2358 UTC (Fig. 3.21a, x=-58, y=23). This difference is consistent with the development of anti-cyclonic tornadoes during the second organizing stage, whereas the previous organizing stage did not produce anti-cyclonic tornadoes. The meso-anticyclone associated with the anti-cyclonic tornadoes during the second cycle caused the RFGF to bend northward and

potentially slowed the southward advances of the SRFGFs associated with the occluding and developing circulations.

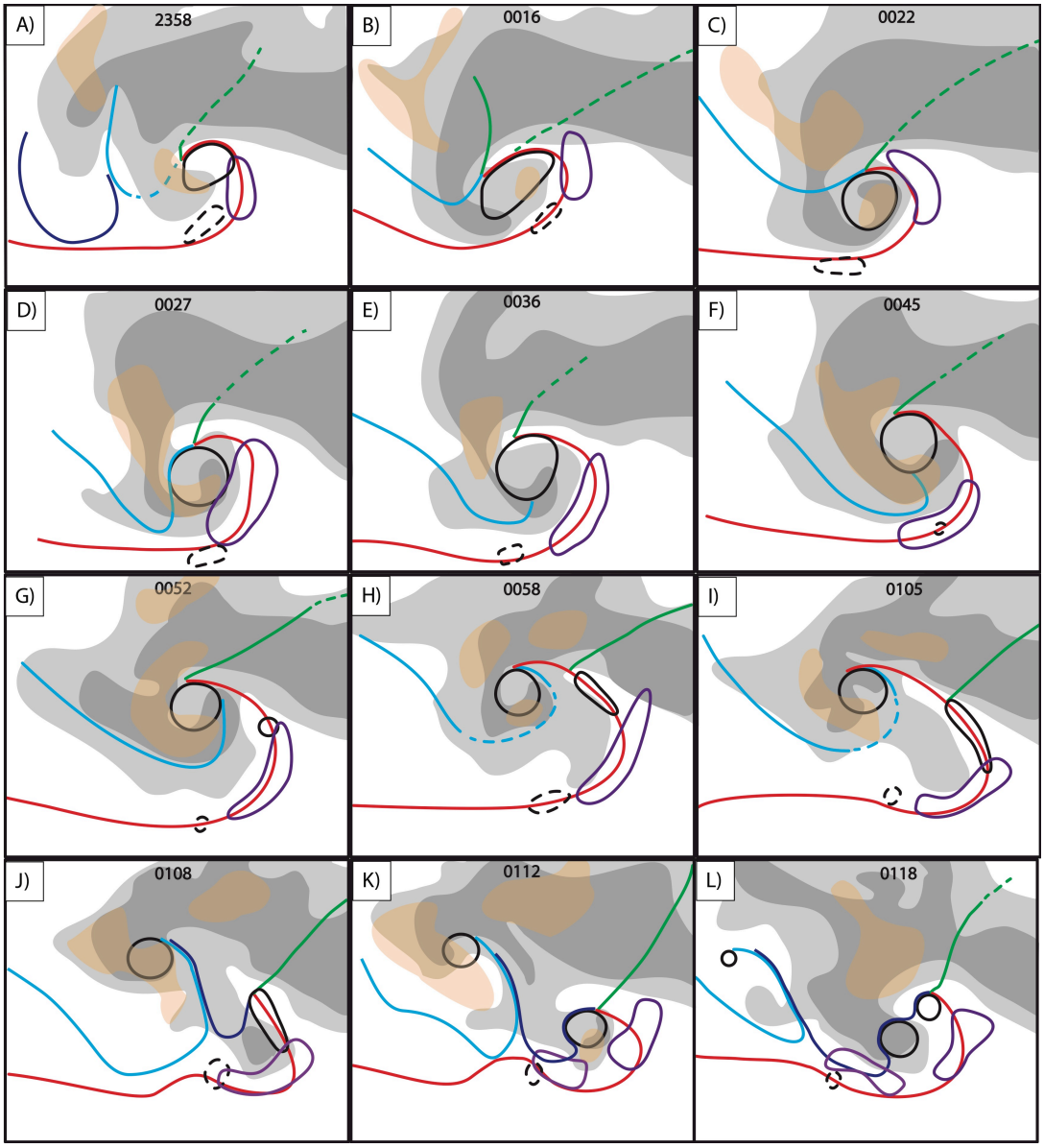

Fig. 3.20 Near-surface boundaries are outlined in solid colors: red is the primary RFGF, green is the FFCB, light blue is the SRFGF, dark blue is the new SRFGF. The near-surface mesocyclones are indicated in black ovals, the midlevel updraft shear region vorticity is indicated by purple ovals. Reflectivity was shaded grey at 40 and dark gray at 50 dBZ and downdraft stronger than –5 m s^{-1} at an altitude of 2 km is shaded in yellow.

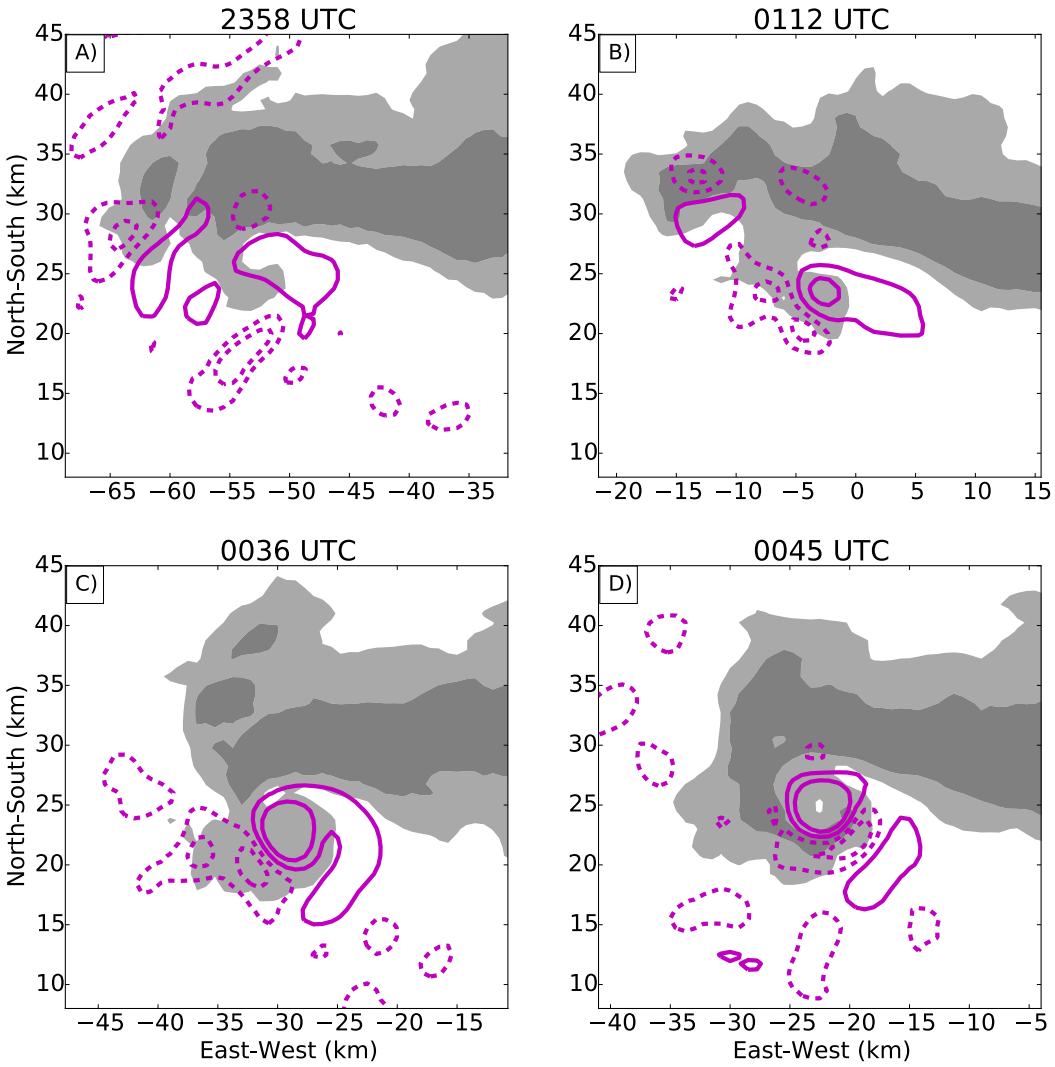

Fig. 3.21 Reflectivity at 30 and 50 dBZ has been contoured at an altitude of 250 m in grey and 0-5 km average vertical vorticity has been contoured in magenta.

By the end of the first organizing stage (0016 UTC; Fig. 3.20b), divergence from the old RFD had reinforced a kinematic boundary extending north from the circulation and the SRFGF to the west. Interestingly, the implied intersection of the three boundaries remained on the northwest side of the circulation as the vortex expanded to the southwest and increased in asymmetry. In contrast, the triple-point was on the northeast side of the circulation during the second organizing stage, between 0112 and 0118 UTC (Fig. 3.20k, l). This difference was due to the new RFD that

formed to the northeast of the developing mesocyclone during the second organizing stage. A similarly strong new RFD was lacking in the prior organizing stage.

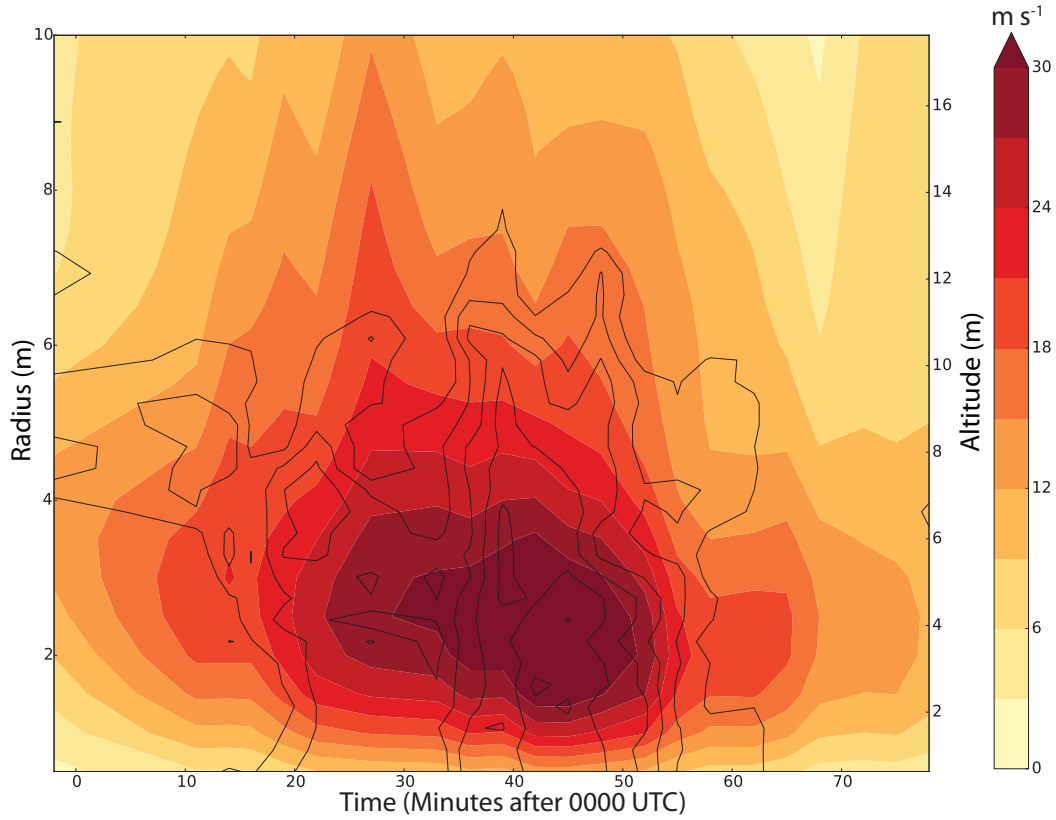

Fig. 3.22 Time-radius plot of azimuthally averaged tangential velocity for the second mesocyclone color-filled at an altitude of 1.25 km. Maximum vertical velocity in time and height from Fig. 3.2c has been overlaid in black contours every $5x10^{-3}$, starting at $30x10^{-3}$.

The low-level mesocyclone symmetry and size appeared to correlate with the location of the triple-point. As the triple-point evolved eastward, between 0027 and 0045 UTC (Fig. 3.20 d-f), the symmetry of the mesocyclone increased and its size decreased. Before 0027 UTC, azimuthally averaged tangential velocity around the low-level mesocyclone increased at all radii (Fig. 3.22). However, as the eastern portion of the SRFGF was reinforced by a strong occlusion downdraft, which allowed the SRFGF to progress around the low-level circulation, tangential velocity stagnated for radii

larger than 3.5 km. This stagnation lasted until the onset of the occlusion stage after 0045 UTC. For radii smaller than 3.5 km, the azimuthally averaged tangential velocity continued increasing as the low-level mesocyclone intensified to its maximum at 0045 UTC. Thus, the deep mesocyclone intensification period starting at 0036 UTC was preceded by a contraction of the larger-scale vortex while the inner core of the mesocyclone intensified.

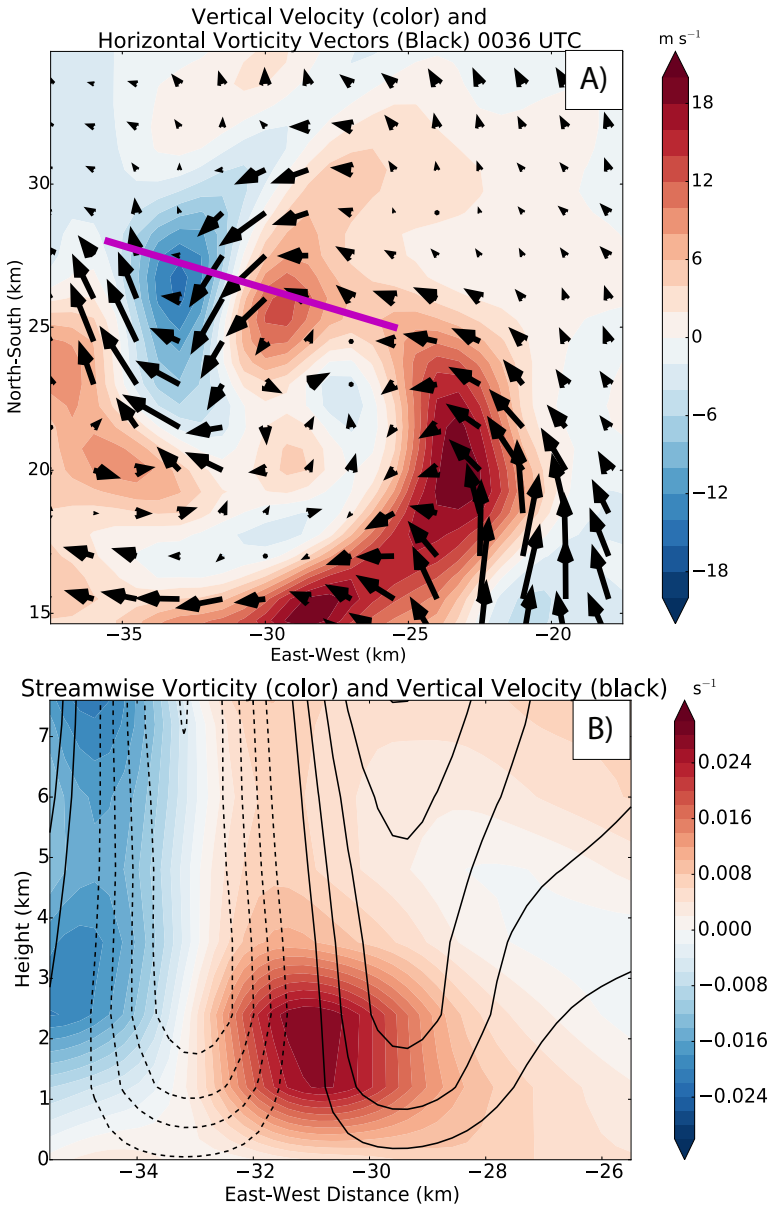

Fig. 3. 23 (a) Vertical velocity is contoured in color at an altitude of 1.25 km, black arrows are horizontal vorticity vectors at 750 m, and the magenta line represents the cross-section in (b). (b) Vertical cross-section across the horizontal rotor. Streamwise vorticity is colored and vertical velocity is contoured in black (every 3 m s^{-1}).

However, just prior (at 0033 UTC), convergence and asymptotic contraction rate were maximized along the FFCB for about six-minutes (Fig. 3.7c). This asymptotic contraction rate feature was associated with a strong horizontal vorticity rotor that formed on the edges of the RFD between up-and-downdraft couplets (Fig. 3.23). The

updraft-downdraft couplet straddling the FFCB appeared similar to that observed in multiple storms by Brandes (1978) during the transition into the tornadic stage of those storms.

The kinematic structure of the horizontal rotor observed here is also similar in appearance to the rotor in a high-resolution simulation by Schenkman et al. (2012). The updraft portion of the rotor was responsible for enhanced stretching on the north side of the low-level vortex (Fig. 3.23b) until 0039 UTC. Low-level maxima in streamwise vorticity on the north side of a low-level mesocyclone have been found to result from baroclinically-generated horizontal vorticity along the forward flank gust front (Klemp and Rotunno 1983) and from frictionally-generated horizontal vorticity in the near-ground inflow (Schenkman et al. 2012). In support of the Klemp and Rotunno mechanism, the forward flank region was mostly characterized by weak, positive contraction rate and thus existing thermal gradients in the forward flank region would aid solenoidal development. However, the rotor was somewhat transient. A more continuous feature would likely have resulted from the baroclinically-generated mechanism. Alternatively, the observed rotor here appears similar to that simulated by Schenkman et al. (2012) where horizontal vorticity was maximized above the surface. Moreover, the orientation of the rotor, southwest to northeast, is perpendicular to the near-ground inflow wind and thus parallel to the frictionally generated vorticity vector upstream from the horizontal rotor. The lack of thermodynamic observations and vertical resolution near the ground prohibit drawing more firm conclusions as to the formation mechanism of the horizontal rotor in this analysis.

The southern part of the primary RFGF did not push farther southward until the SRFGF progressed around the southern edge of the circulation (Fig. 3.20e-g). Despite the RFD intensification, convergence along the FFCB (Fig. 3.7a) did not noticeably change, suggesting that the increased outflow from the RFD was directed mainly westward towards the SRFGF. Indeed, preceding the onset of the occlusion stage, the SRFGF pushed westward (Fig. 3.20f, 0045 UTC) and a deep meso-anticyclone rotated from being on the southwest side of the cyclonic mesocyclone to being the southeast side (Fig. 3.21c, d). The resulting change in large-scale deformation was reflected in the low-level reflectivity, which rapidly expanded on the western side of the hook echo.

The near-surface boundary evolution during the occlusion stage was consistent with the conceptual models of Burgess et al. (1982), DB02a, b, and the high-resolution observations of Marquis et al. (2012). The onset of the occlusion stage after 0045 UTC was marked by a southeastward surge in the RFGF, while the SRFGF remained with the occluding circulation. The occluding tornadic mesocyclone remained connected to the occluded portion of the RFGF until northerly winds from the RFD overwhelmed the occluded RFGF. Concurrently, convergence along the FFCB extended well to the northeast and then advanced eastward along the primary RFGF, as the primary RFD finally began shifting eastward relative to the occluding low-level circulation. In contrast to the previous mesocyclone cycle, the FFCB was associated with substantial convergence throughout the redevelopment of the new mesocyclone (Fig. 3.20h-l). The enhanced axisymmetric contraction rate and northerly low-level winds (Fig. 3.13, Fig. 3.17) suggest that the cold pool underneath the RFD was potentially stronger than during the previous cycle.

The elongated vorticity region then formed into the new mesocyclone vortex as the SRFGF surged southward, much earlier than the previous cycle, and eventually wrapped around the southern end of the new vortex (Fig. 3.20l). Thus, while the cycle durations were similar, the timing of the storm-scale evolution was significantly different than the previous cycle. The differences were most likely the result of the storm-scale organizing stage structures propagating forward in time but could also be due to changes in the environment, as stability and low-level storm-relative helicity increased towards the east. Nevertheless, the new mesocyclone produced tornadoes at 0145 and 0204 UTC (*Storm Data, 2004*), with similar reflectivity evolution during the occlusion process (0145-0220 UTC).

3.6 Conclusions

On 29-30 May 2004, two C-Band, mobile Doppler SMART radars observed a tornadic supercell near Geary, OK for three hours. Deep, volumetric sector scans allowed for dual-Doppler analyses to be generated for an unprecedented ninety-minute period up to 18 km in height and over approximately 100 km by 100 km area horizontally. The Geary supercell was an exceptional storm in size and flash rates (Calhoun et al. 2013) and produced tornadoes over a seven-hour period, including all three cycles during the observed period (*Storm Data, 2004*). In this study, the dissipating (organizing) stage of the first (third) cycle was captured along with the entire lifecycle of the second cycle. The mesocyclone cycles lasted an exceptionally long seventy-minutes each, resulting in slower storm-scale evolution than most previously observed storms. Despite the cycle duration, the prolonged observational

length allowed for the comparison of two organizing stages of mesocyclone development.

In general, the primary RFD was continuously found to the north or northwest of the low-level circulation during the organizing and mature stages, and to the northeast during the occlusion stage. Thus, the rear-flank and the occlusion downdrafts were generally manifested as spatially separate downdrafts for cycles two and three, until the occlusion stage almost fifty minutes into the cycle. At mid levels, the updraft continuously surrounded the hook echo on the right and left flanks, potentially limiting evaporation due to the mixing of dry air with the environment on the western edge of the hook echo precipitation core. The updraft configuration might explain why the most persistent downdraft found in the hook echo region was the occlusion downdraft inside the mesocyclone circulation.

Secondary RFD gust fronts (SRFGFs) were found on the western side of the circulation for all three mesocyclone cycles, including most of the second cycle that was well sampled. However, the SRFGFs did not reach the primary RFD gust front (RFGF) until the occlusion stage. Instead, during the mature and occluding stages, the SRFGF convergence forced a deep updraft on the southwestern side of the hook echo region, which resulted in recycling the RFD outflow. During the dissipating (organizing) stage of the old (new) mesocyclone observed at 2358 and 0108-0118 UTC, multiple SRFGFs were inferred simultaneously. However, the SRFGFs of the second and third cycle were different in that the SRFGF surged southward into the hook echo much earlier during the third cycle than the second cycle.

In the classical mesocyclogenesis conceptual model (Lemon and Doswell 1979; Rotunno and Klemp 1985; Adlerman et al. 1999; Markowski et al. 2008; Markowski 2014), the incipient low-level mesocyclone becomes positioned underneath the primary updraft during the mature stage of its lifecycle, allowing it to deepen and intensify. However, the low-level mesocyclone evolution presented in this study is more similar to the alternative kinematic progression documented by Dowell and Bluestein (2002a). In their conceptual model, a small portion of the updraft, here described as an occlusion updraft, separated from the primary updraft during the mature stages of the mesocyclones and provided the necessary stretching for intensification and tornadogenesis. During the end of the first and all of the second cycles of this storm, however, the low-level mesocyclone was not connected to the primary updraft. Instead, the low-level mesocyclone was connected to vorticity aloft that was continuously associated with the occlusion updraft, separated in space from the primary updraft region. Stretching in the primary updraft produced a separate deep region of vorticity. But this updraft shear region vorticity generally did not extend down to the surface and it remained separate from the mesocyclone during the portions of the second cycle that were observed.

During the first organizing stage, the low-level mesocyclone vortex weakened with height and was tilted towards the northwest. But during the mature stage, the vortex was stretched by vertical gradients *in an occlusion updraft* such that maximum vorticity was nearly constant in height and the resultant erect vortex reached a maximum depth of 13 km. In contrast, the incipient and organizing stages of the third mesocyclone better followed the evolution documented in previous literature. The third

low-level mesocyclone developed in a vorticity rich region underneath the vorticity associated with the updraft shear region. This mesocyclone benefited from stretching by vertical velocity gradients in the primary updraft. Hence, during the early-to-middle part of the second organizing stage, the third mesocyclone was connected to the midlevel vorticity associated with the primary updraft. However, the final analysis at 0118 UTC suggests that the new mesocyclone was in the process of becoming disconnected from the primary updraft region vorticity. Since the incipient stage of the second mesocyclone was not well sampled, it is not clear if the previous cycle transitioned from being associated with the primary updraft to being separated. Regardless, it is clear that the second mesocyclone's intensification was due to an occlusion-type updraft and not the main updraft along the primary RFGF.

The RFGF, SRFGF, and the FFCB all converged to a triple point on the north side of the circulation for most of the life cycle of the mesocyclone. As the mesocyclone matured during the second cycle, the triple point progressed eastward, due to the eastward progression of the RFD that was enhanced by an occlusion downdraft within the mesocyclone. It is important to note that the SRFGFs observed in this storm were associated with surges within the RFD and were not associated with distinctly separate downdrafts. While a forward flank gust front was not observed, the FFCB advanced eastward during the occlusion stage to the position that the forward flank gust front has been found in other studies.

The analyses documented here will provide a framework for future studies that examine differences in storm-scale kinematic structure between tornadic and non-tornadic supercells, particularly as more long-duration supercell data sets are collected

and analyzed. Additionally, the trajectory mapping method developed by Betten et al. (2017) will be used to elucidate the source regions of air for the low-level rear-flank and occlusion downdrafts that other studies have shown to drive the primary and secondary gust fronts. Source regions for the mesocyclone vortex and the midlevel updraft shear region will also be investigated to understand the different sources of vorticity and tilting mechanisms.

Chapter 4:A Trajectory Mapping Technique For The Visualization and Analysis of Three-Dimensional Flow in Supercell Storms

The material of this chapter is adapted from Betten et al. (2017)

4.1 Introduction

One of the most commonly used methods to characterize three-dimensional motion in complex flows is to examine Lagrangian trajectories. In supercell storms, conclusions about the behavior and source of low-level vortices in numerical simulations (Rotunno and Klemp 1985, Wicker and Wilhelmson 1995, Adlerman et al. 1999, Mashiko et al. 2009, and Schenkman et al. 2014) and observational studies (Johnson et al. 1987, Wakimoto et al. 1998, Ziegler et al. 2001, Markowski et al. 2012) have been based, in large part, on the behavior of air trajectories. However, a recent study by Dahl et al. (2012) examined potential errors in individual backward trajectories that had been previously overlooked, indicating that trajectories originating at low levels east of a storm's gust front may have larger errors than other trajectories originating further aloft. Thus, conclusions based on a limited set of trajectories may be biased due to undiagnosed local variability in trajectory errors.

Trajectories have primarily been visualized by overlaying the trace of parcel positions relative to the model or analysis grid at a specific analysis time. Variables along the trajectory such as altitude, vertical vorticity, or forcing terms from the vorticity equation are viewed as a time series. While helpful in illustrating key concepts in fluid motion, the evolution of specific features, the representativeness, and the spatial scales of the trajectory behavior cannot be determined from a few trajectories. With the exception of Klemp et al. (1981) who used trajectories to visualize the source altitude of

air in a midlevel updraft, comprehensive analysis of trajectory behavior has not been thoroughly explored or visualized. For example, regions of strong deformation will lead to strong gradients in trajectory behavior that are difficult to visualize using only a few tens of trajectories. However, if thousands of trajectories are initialized on a fine, regularly spaced grid and analyzed in a Cartesian frame of reference, the resulting spatial pattern of trajectory behavior and diagnostics should lead to an improved understanding of storm kinematics and dynamics.

In this chapter, we develop such a trajectory mapping method and demonstrate its robustness and utility using high-resolution output from a numerical model. The method will be shown to provide insight into the source of air parcels at a given level, the time history of vorticity including effects of diffusion, and time-averaged forcing of vertical momentum. We also compare the trajectory behavior obtained from the simulated supercell storm to trajectories computed from a dual-Doppler radar analysis of a well-observed supercell storm.

4.2 Methodology

4.2.1 Numerical Simulation

A numerical simulation was carried out using the CM1 Cloud Model (Bryan and Fritsch 2002), version 17 with the Ziegler Volume-Density (ZVD, Mansell et al. 2010), two-moment microphysics scheme. The simulation was initialized with a single warm bubble in a homogenous environment based on a composite sounding from Topeka, KS for 8 May 2003 (Fig. 4.1). This sounding was chosen based on its proximity to multiple tornadic supercells. The sounding resulted in the simulation of a quasi-steady supercell storm defined here following Foote and Frank (1983), as a continuous zone of updraft

feeding the convective storm with new updraft pulses forming within the existing updraft zone. The weighted essentially nonoscillatory (WENO) advection scheme (Shen and Zha 2010) was applied for both kinematic and scalar quantities because it dampened errors associated with features near the smallest resolvable scale and resulted in smoother fields than the traditional 5^{th} and 6^{th} order advection schemes. The WENO method led to better agreement between integrated tendencies and the resulting field than 5^{th} or 6^{th} order advection schemes.

The horizontal grid spacing was 250 m in the middle 70 km of the domain and was stretched to 5000 m on the outer boundaries. The vertical grid spacing was stretched from 100 m at the bottom to 500 m at the top, resulting in a model domain of 175x175x16.2 km^3. The horizontal boundaries are open-radiative while the lower and upper boundaries are free-slip. Storm motion was estimated and subtracted out to keep the storm in the middle of the domain over the lifetime of the simulation.

4.2.2 Observational Case

The trajectory mapping technique was also applied to radar analyses from the Geary, Oklahoma 2004 supercell observed by two Shared Mobile Atmospheric Research and Teaching (SMART, Biggerstaff et al. 2005) radars during the TELEX (Macgorman et al. 2008) project. Wind retrievals were performed using NCAR software REORDER and CEDRIC (Miller and Fredrick 1998) from synchronized radar volumes collected every three minutes. The radars were located on a 40 km baseline and an analysis was performed on a 100 km x 90 km x 18 km grid with a horizontal resolution of 750 m and a vertical resolution of 500m. A low-pass filter was used to smooth the transition between the dual-Doppler analysis and a nearby balloon sounding.

The storm advection correction technique described in Ziegler et al. (2013), where the analysis at two times are advected to the time of the trajectory, was used to reduce errors in trajectories due to the large-scale advection of the storm.

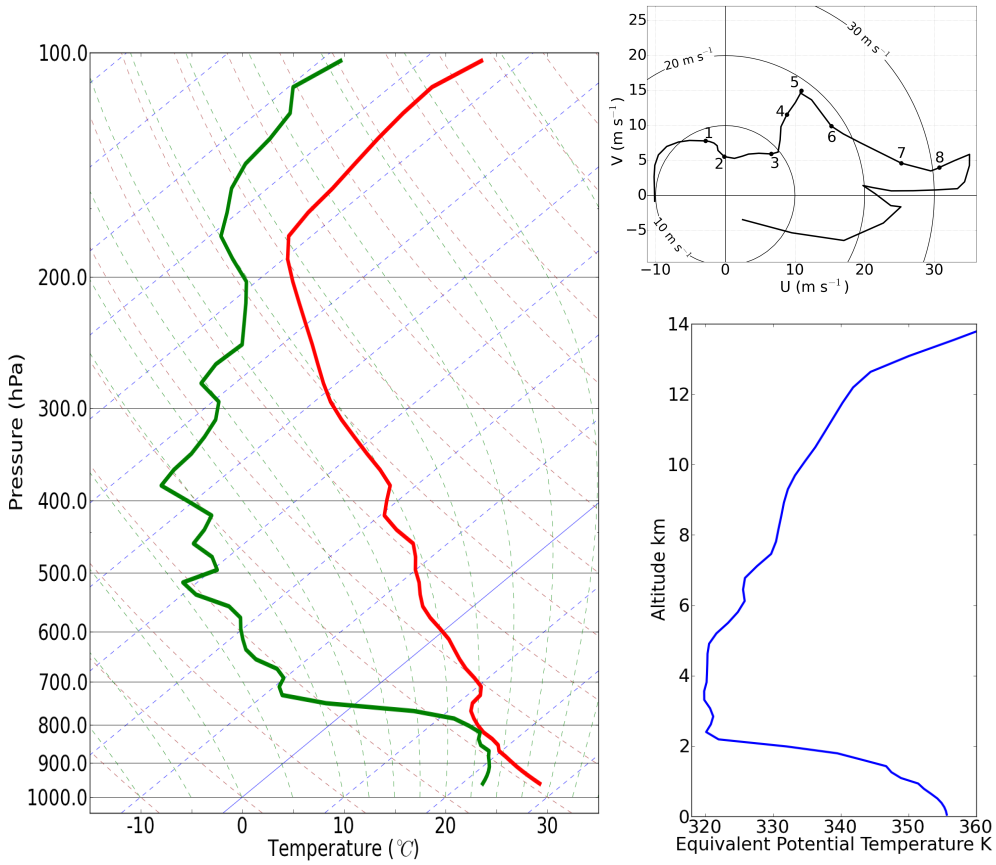

Fig. 4.1 Thermodynamic profile (left), storm-relative hodograph (upper right) with heights labeled in km, and equivalent potential temperature profile (AGL) (lower right) for the sounding used in the model. The sounding is a composite from the 1800 UTC and 0000 UTC soundings at Topeka, KS 8 May 2003.

4.2.3 Trajectory Methodology

The trajectory algorithm used in this study was written to optimize the initialization of a regularly spaced grid of trajectories with 4th order Runge-Kutta temporal integration. Trajectory time steps were based on the scale of the analysis and the resolved flow characteristics, resulting in a time step of 0.5 s for the simulated storm and five seconds for the observed storm. These time steps were found to be optimal, as

smaller time steps did not affect the final positions or integrated quantities. Model data on the Arakawa C grid was directly interpolated to the trajectories using cubic spline interpolation, while temporal evolution was linearly interpolated. The gradients were calculated locally by interpolating the variables to a cube around each trajectory and then calculating the spatial gradients valid at the center of the cube, thus ensuring that the gradients at the trajectory points are the same gradients that are felt by the trajectories.

Comparisons between forward and backward trajectories over 200 s using the algorithm developed here yielded root-mean square differences on the order of 10 m, or about five percent of the grid spacing. The resulting algorithm also compared favorably against trajectories calculated from the built-in algorithm in CM1. Given the good agreement between forward and backward trajectories the utility of the trajectory mapping framework is illustrated using mostly backward trajectories

4.3 Trajectory Map Framework

A trajectory map is defined as a two-dimensional Cartesian visualization of a specific variable at a specific time along its trajectory. The trajectory maps are derived by initiating trajectories at every grid point on the original model or analysis grid and interpolating diagnostic quantities to the trajectory location during the backward (or forward) time integration. The trajectory map is then created by displaying the previous (or future) values of a quantity at the initial grid locations of individual trajectories. Hence, these maps reveal spatial patterns of the past (or future) values in the original two-dimensional plane. This method is very similar to the "domain-filling" method employed by Fisher et al (1993) to illustrate trajectory behavior in the stratosphere.

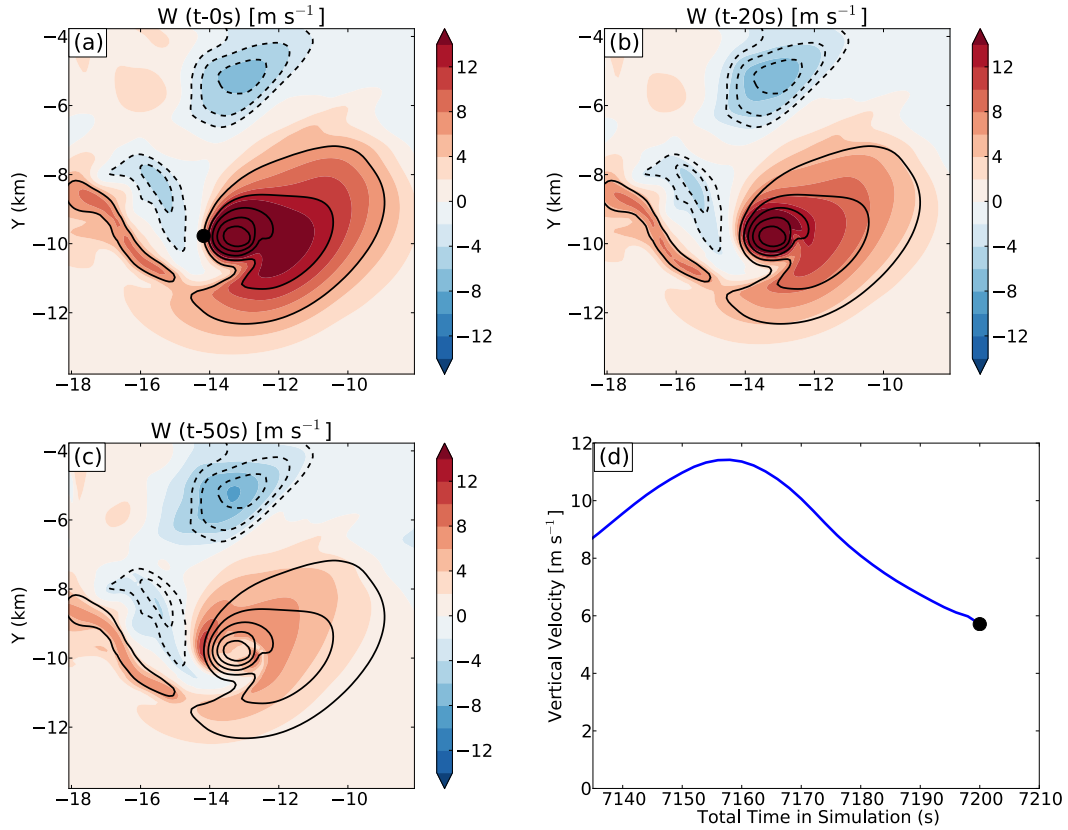

Fig. 4.2 (a) One km vertical motion at 7200 s into the simulation. (b) Horizontal map of vertical motion at 7180 s for all the backward trajectories that initiated at 1 km at 7200 s. (c) Same as (b) but integrated back to 7150 s. In (a)-(c) black contours of vertical motion every 2 m s^{-1} for negative values and 6 m s^{-1} for positive values at 1 km altitude and at 7200 s have been overlaid for reference. (d) Example of the time series of vertical motion along a single backward trajectory initiated at 7200 s at the point denoted by the black dot in (a).

To illustrate the transformation from Eulerian space to a trajectory map, the vertical velocity of trajectories at one km altitude is shown in Fig. 4.2. At the initial time (Fig. 4.2a), the trajectory map reflects the vertical velocity as indicated by the overlapping of the color-filled and black contours of vertical motion. Figures 4.2b, c illustrate the horizontal variability of the past values of vertical motion for all the air parcels that end at one km altitude at 7200 s in the simulation. Thus, the spatial scale of the updraft intensification and the relative strengthening of the downdrafts can be visualized simultaneously. In contrast, single trajectories, like those in Fig. 4.2d, do not

provide the spatial scale and structure of the air parcel evolution that is depicted in the trajectory maps.

The choice of the time, or integration period, depends on the purpose of the analysis, storm size, flow speed, and rate of evolution of the flow features of interest. For reference, the simulation produced a low-level updraft region ~ 5 km wide, while the observed supercell had an updraft region ~ 15-20 km wide. Thus, the observational case should require a significantly longer integration period than the simulated supercell for similar illustrative purposes. If the purpose is to gain a temporally comprehensive visualization of the vertical motion of air parcels, then one might plot the average vertical motion over a 50-100 s period rather than the instantaneous value at a specific time. On the other hand, if the purpose is to visualize parcel altitude origins, then one might plot the past altitude of the air that ended up at a particular altitude at a particular time in the simulation.

For example, backward trajectories showing the prior altitude of air that end at 1 km altitude at 7200 s into the simulation are show in Figure 4.3. As the trajectories are integrated backwards in time, spatial gradients appear in regions having strong deformation as differential advection alters the path of individual trajectories (Fig. 4.3). In the trajectory-mapping framework, the effects of deformation and flow evolution have been integrated together into a single, visual analysis. Instead of viewing fields such as vertical motion as a single snapshot in time on the horizontal grid, the trajectory mapping method enables the integrated time history of the flow field to be viewed concisely.

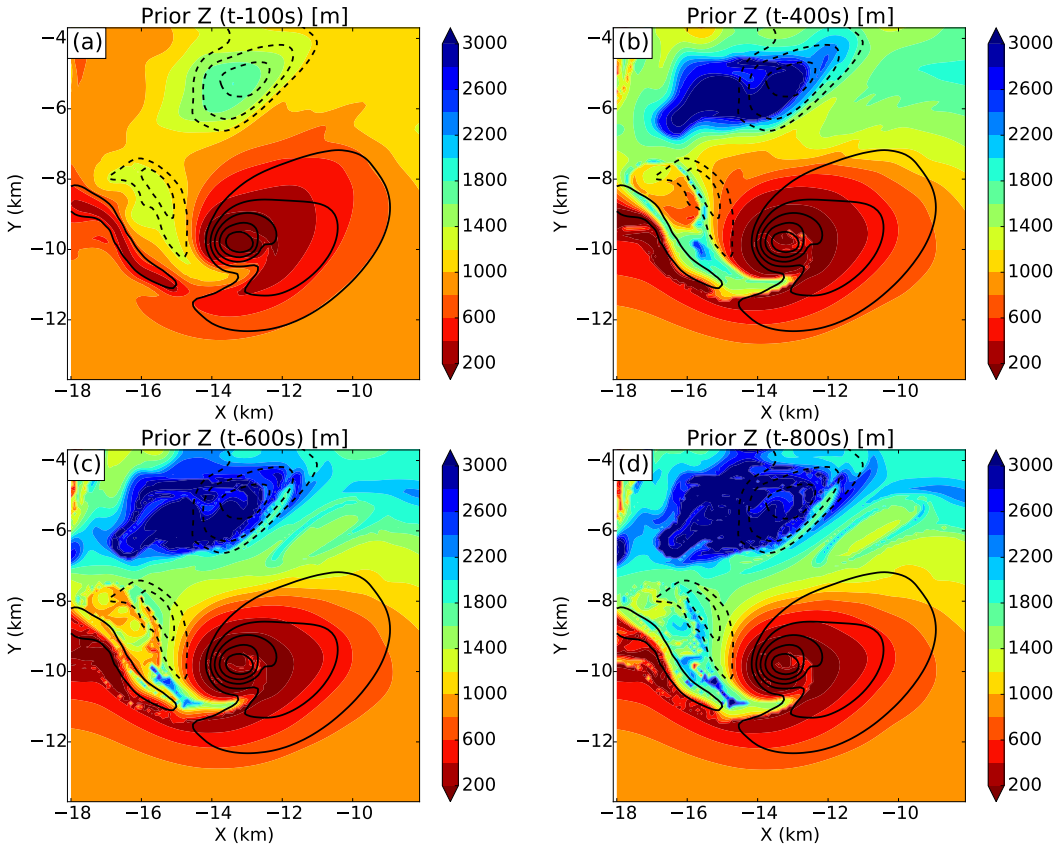

Fig. 4.3 (a) Prior altitude, 100 s in the past, initialized at 1 km altitude at 7200 s in the model simulation. (b) Same as (a) except that the backward trajectories have been integrated for 400 s, (c) 600 s, and (d) 800 s. Note that points with a height of 1000 m indicates the parcel either did not move vertically or ended at 1 km altitude again between the beginning and ending periods of the integration. In (a) - (d), black contours of vertical motion every 2 m s^{-1} for negative values and 6 m s^{-1} for positive values at 1 km altitude and at 7200 s have been overlaid for reference.

Some quantities will converge to a constant value along trajectories once they are integrated back to the environment, such as source altitude. However, since the point in time of convergence depends on the initial trajectory position and the surrounding flow, the time of convergence will vary spatially. This point is illustrated in Figure 4.3, where prior altitude has been plotted at four different times. Prior altitude converged first in regions of rising trajectories (warm colors) and took longer in regions with sinking trajectories (cold colors). Eventually, almost all of the backward

trajectories that were initialized at 7200 s and at a 1 km altitude, converged to their source altitudes in the environment as the integration period was increased to 800 s.

It is important to note that both backward and forward trajectory maps contain useful insight to parcel flow evolution. Backward trajectory maps are optimal for understanding the processes that have forced the current flow characteristics while forward trajectory maps are optimal for understanding the future behavior of the flow characteristics, and illustrating source regions for future updrafts, downdrafts, and flow features like mesocyclones.

4.4 Trajectory Map Applications

The benefit of the trajectory-mapping framework is demonstrated here through analysis of quantities typically examined in studies of supercell storms. The source of air in the low-level mesocyclone, the forcing of vertical momentum, and the developing vertical vorticity in and near the mesocyclone are presented for the simulated storm. The model output is also used to elucidate the proxies of observational applications where detailed thermodynamic data is often unavailable.

4.4.1 Low-level mesocyclone air source regions

To determine the horizontal extent of the areas that contributed to the low-level mesocyclone at a height of 1 km, a forward trajectory map was initiated at 7000 s at an altitude of 50 m. The selection of 50 m is illustrative but was guided by the mean vertical displacement within the mesocyclone found in the 200 s backward trajectory analysis (compare Figs 4a, b). In practice, many maps would be initialized at different altitudes within the height range diagnosed from the backward trajectory map. To reflect the broadest horizontal extent of air that was at 50 m altitude at 7000 s that could

have flowed through the mesocyclone by 7200 s, the maximum vertical vorticity below 1 km along the forward trajectory is plotted (Fig. 4.4d) rather than the final vorticity. As with the prior altitude maps, the future maximum vertical vorticity was generated by contouring the future values of vorticity at the original (x, y) locations where the forward trajectories were initiated. While the future values in Fig. 4.4d are significantly larger than the initial vorticity values of the trajectories (Fig.4c), this does not suggest that vorticity was increasing everywhere outside of the mesocyclone. Rather the area of high future vorticity elucidates those individual forward trajectories that later pass through the low-level mesocyclone. The surface to 1 km layer was chosen to focus on the low-level mesocyclone. Positive vertical vorticity values inside the low-level mesocyclone were significantly higher than any other region below 1 km in the simulation domain, thus any air parcel trajectory that experiences future vertical vorticity on the same order of magnitude as that found in the mesocyclone, but originating outside of the mesocyclone, can be assumed to have passed through the low-level mesocyclone at some point in the future. Examining the areas with values of vorticity greater than 0.06 s^{-1} (very light blue, white, and red colors in Fig. 4.4a, d), it is clear that air from several kilometers away in nearly all directions converged into the low-level mesocyclone between 7000 and 7200 s into the simulation. But the largest source area was from the north, in a region of general subsidence at both 7000 s (Fig. 4.4d) and 7200 s (Fig. 4.4a).

By comparing both backward and forward trajectories, it is possible to visualize the spatial distribution of the source height (for backward trajectories) and the

horizontal source extent (from forward trajectories initialized at the earlier time) of air that contributed to the low-level mesocyclone at a particular time.

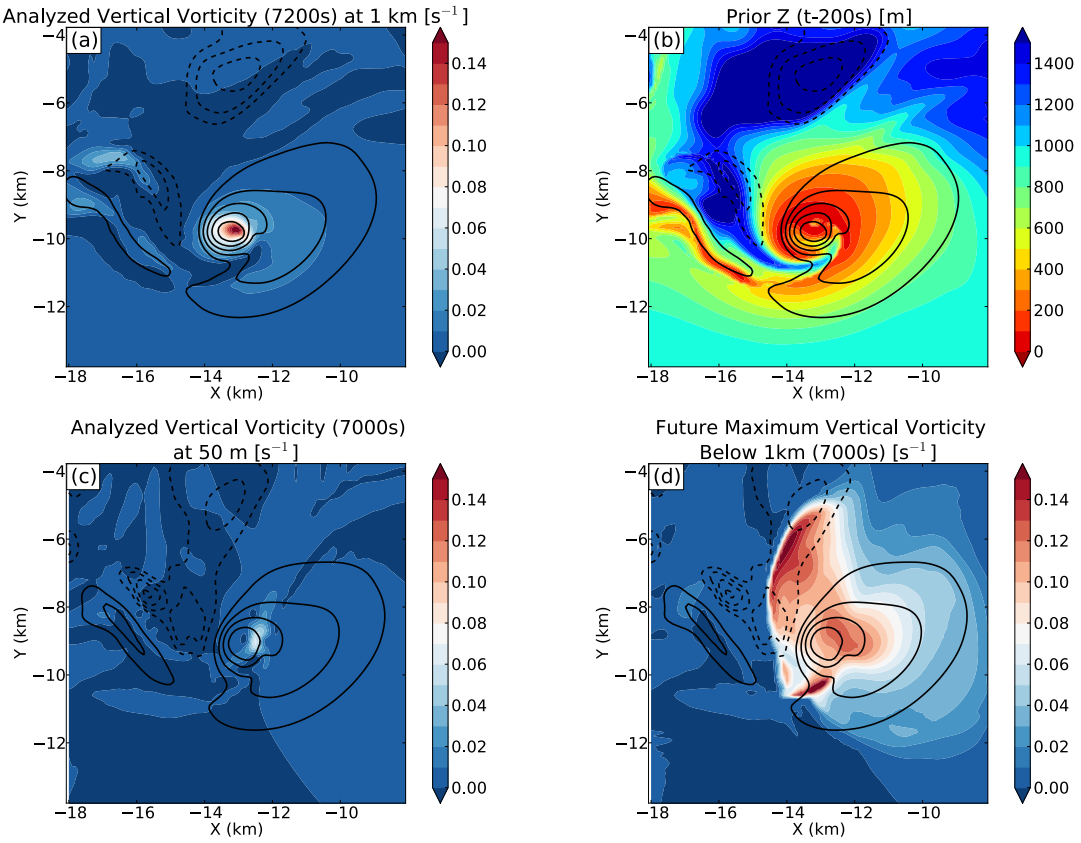

Fig. 4.4 (a) Analyzed vertical vorticity, in s^{-1} according to the color scale, at 1 km altitude and 7200 s into the model simulation. (b) Prior altitude, in m, 200 s into the past. Contours of vertical velocity, every 2 m s^{-1} for negative values and 6 m s^{-1} for positive values, for 1 km altitude at 7200 s have been overlaid in (a) and (b). (c) Analyzed vertical vorticity, in s^{-1}, at 50 m altitude and 7000 s into the simulation. (d) Maximum vertical vorticity below 1 km altitude along 200 s forward trajectories initiated at 50 m at 7000 s into the simulation. The location of the color-filled contours reflects the grid points where the forward trajectories were initiated and not the future position at which the maximum vorticity values were realized. Contours of vertical velocity, every 2 m s^{-1} for negative values and 6 m s^{-1} for positive values, for 1 km altitude at 7000 s have been overlaid in (c) and (d).

4.4.2 Application to the forcing of vertical motion

Trajectory maps have a large number of applications as any variable that is observed or numerically simulated can be interpolated to a trajectory. Tendency equations are often used to elucidate the evolution of storm characteristics such as

vorticity or vertical motion. Individual or combined terms in tendency equations can be integrated and plotted just as easily as prior variable states. Hence, trajectory mapping can be used to examine the relation between past forcing and current flow features. As noted by Gaudet and Cotton (2006), advection will displace the resulting field from the parent forcing region. In their example, the occlusion downdraft was displaced from the location of the negative vertical motion tendency, showing the inherent complexity between the resulting motion field and the processes that created the flow.

The displacement between the forcing and the resulting momentum at later times can be demonstrated by comparing the vertical motion field to the RHS of the vertical motion tendency equation (4.1) and the Lagrangian integration of the terms over an arbitrary time period (Fig. 4.5). Equation (4.1) is the compressible, nonhydrostatic form of the vertical momentum equation in the numerical model where w is the vertical velocity, t is time, π' is the perturbation Exner function, C_p is the heat capacity at constant pressure for air, g is acceleration due to gravity, z is height, θ_ρ is density potential temperature, and B is the buoyancy force defined by (4.2). The term $\theta_{\rho 0}$, in (4.2) is the environmental base state density potential temperature that varies only in height.

$$\frac{dw}{dt} = -\theta_\rho C_p \frac{\partial \pi'}{\partial z} + B \quad (4.1)$$

$$B = g \frac{\left(\theta_\rho - \theta_{\rho 0}\right)}{\theta_{\rho 0}} \quad (4.2)$$

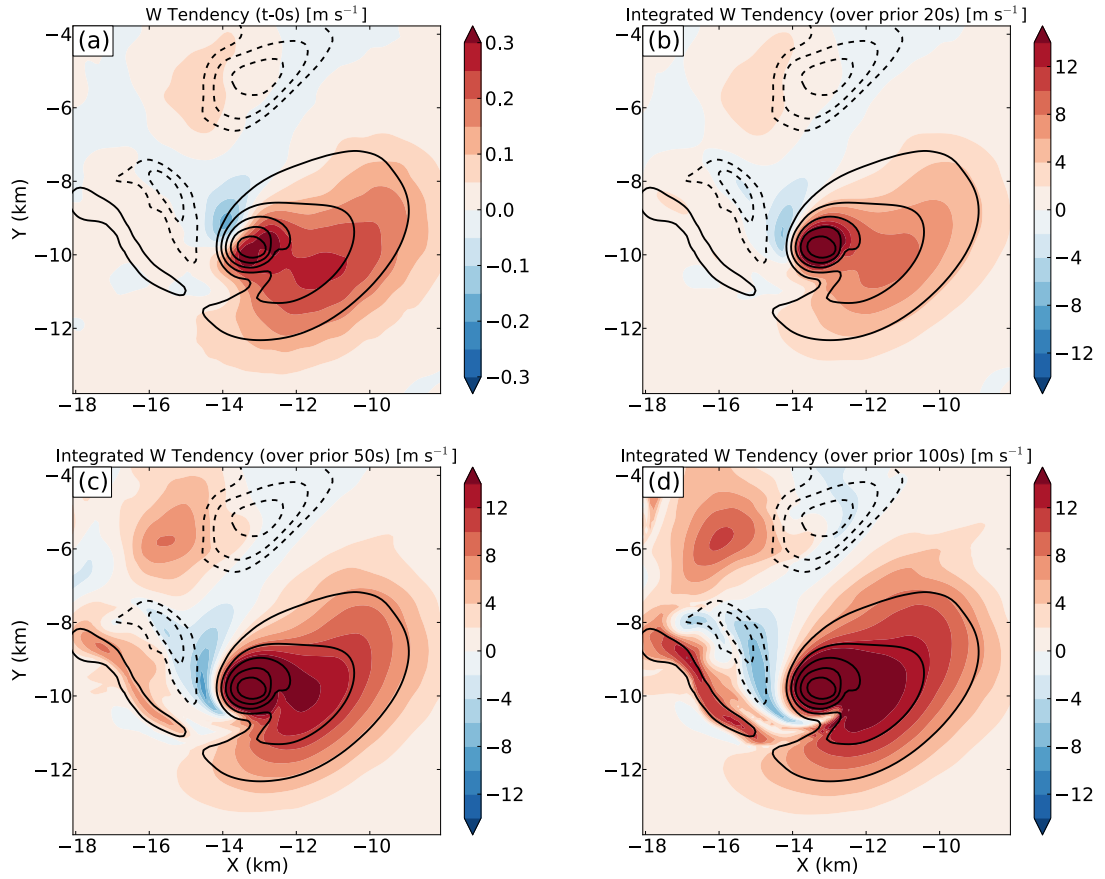

Fig. 4.5 (a) Instantaneous vertical velocity tendency in m s^{-2}, at 7200 s at 1 km in altitude in the numerical simulation. (b) Vertical motion tendency from integration of the RHS of (4.1) along 20 s backward trajectories initialized at 7200 s at 1 km in the model. (c) Same as (b) except for 50 s backward trajectories. (d) Same as (b) and (c) except for 100 s backward trajectories. Black contours in every panel are the instantaneous vertical motion every 2 m s^{-1} for negative values and 6 m s^{-1} for positive values at 7200 s at 1 km altitude in the model.

Using the Emmanuel (1994) approximation for density potential temperature (4.3), the buoyancy force can be written as (4.4), where r_h is the hydrometeor mixing ratio, θ is potential temperature and virtual potential temperature, θ_v, was decomposed into its environmental base state (θ_{v0}) and perturbation θ_v'. Note that the environmental base state virtual and density temperatures are equivalent since there are no hydrometeors in the environment.

$$\theta_\rho = \theta_v - \theta * r_h \quad (4.3)$$

$$B = g\left[\frac{\theta_v'}{\overline{\theta_{\rho 0}}} - \frac{\theta}{\overline{\theta_{\rho 0}}} r_h\right] \quad (4.4)$$

At the initial time (Fig. 4.5a), the strongest drafts, particularly the downdrafts, are notably displaced from the peak tendencies. As the backward integration period is increased from 50 to 100 s, insight into the important timing of vertical motion tendency for the different vertical drafts at time t-0 becomes apparent. The updraft maximum in Figure 4.5a is strongly forced for the entire previous 100 seconds. Additionally, the updraft band in Figure 4.5a that extends from (x=-18, y=-8) to (x=-16, y=-11) was a residual draft accelerated between 50 and 100 seconds prior to time t-0. The same is true for the downdraft immediately east of the updraft band and for all the weak vertical drafts above y > -7. Hence, the trajectory maps can help illustrate the relative age of the vertical drafts by comparing the integrated forcing at different times from the backward trajectories; thereby revealing which drafts have been recently accelerated and which ones are merely coasting.

To establish the primary forcing mechanism for the updrafts and downdrafts, specific terms in the tendency equations were integrated along the trajectories. In Fig. 4.6, the terms of the vertical motion tendency equation have been integrated over 200 s period and separated into the buoyancy (Fig. 4.6b) and vertical pressure gradient (VPG, Fig. 4.6d) contributions. The precipitation loading (Fig. 4.6c) contribution to buoyancy was also plotted. By comparing the contributors to vertical motion, regions where forces support or oppose one another can be ascertained. Note that the Exner function formulation of the tendency equation implicitly contains the pressure contribution to

buoyancy (Doswell and Markowski 2004) so that a small part of the buoyancy is contained in the vertical pressure gradient. Additionally, the VPG has not been separated into dynamic and buoyant contributions (Rotunno and Klemp 1982). Thus, while both buoyancy (Fig. 4.6b) and the VPG (Fig. 4.6d) resulted in forcing of vertical motion, they largely negated each other in some areas.

For example, consider the forcing terms for the rear-flank downdraft (Ludlam 1963, Lemon and Doswell 1979, and Klemp and Rotunno 1983) centered at (x=-13.5,y= -5.5 km) in Fig. 4.6a. It is clear that precipitation loading (Fig. 4.6c) and negative buoyancy (Fig. 4.6b) counters the mostly positive vertical pressure gradient force (Fig. 4.6d) to increase the downdraft strength from its initial value at t-200 s (Fig. 4.6e). The northwest-southeast oriented downdraft band at (x=-15 km, y= -9 km) is separated from the main downdraft region and was primarily forced by a negative VPG, similar to occlusion downdrafts simulated by Klemp and Rotunno (1983), Wicker and Wilhelmson (1995), and Adlerman et al. (1999). In contrast, the northwest-southeast oriented updraft band from (x, y) of (-18, -8 km) to (-15, -11 km) in Fig. 4.6a was forced by a combination of buoyancy (Fig. 4.6b) and VPG (Fig. 4.6d). Meanwhile, the main updraft was forced almost entirely by the VPG.

For an observationally based dataset, vertical draft forcing could be difficult to diagnose due to the lack of pressure and thermodynamic information. Nonetheless, one could estimate the hydrometeor mixing ratio from radar reflectivity and thus integrate the precipitation loading contribution over trajectories (Wakimoto et al. 1998). This technique might differentiate downdrafts in the hook echo region that are dynamically driven from those that are more buoyancy driven by precipitation loading.

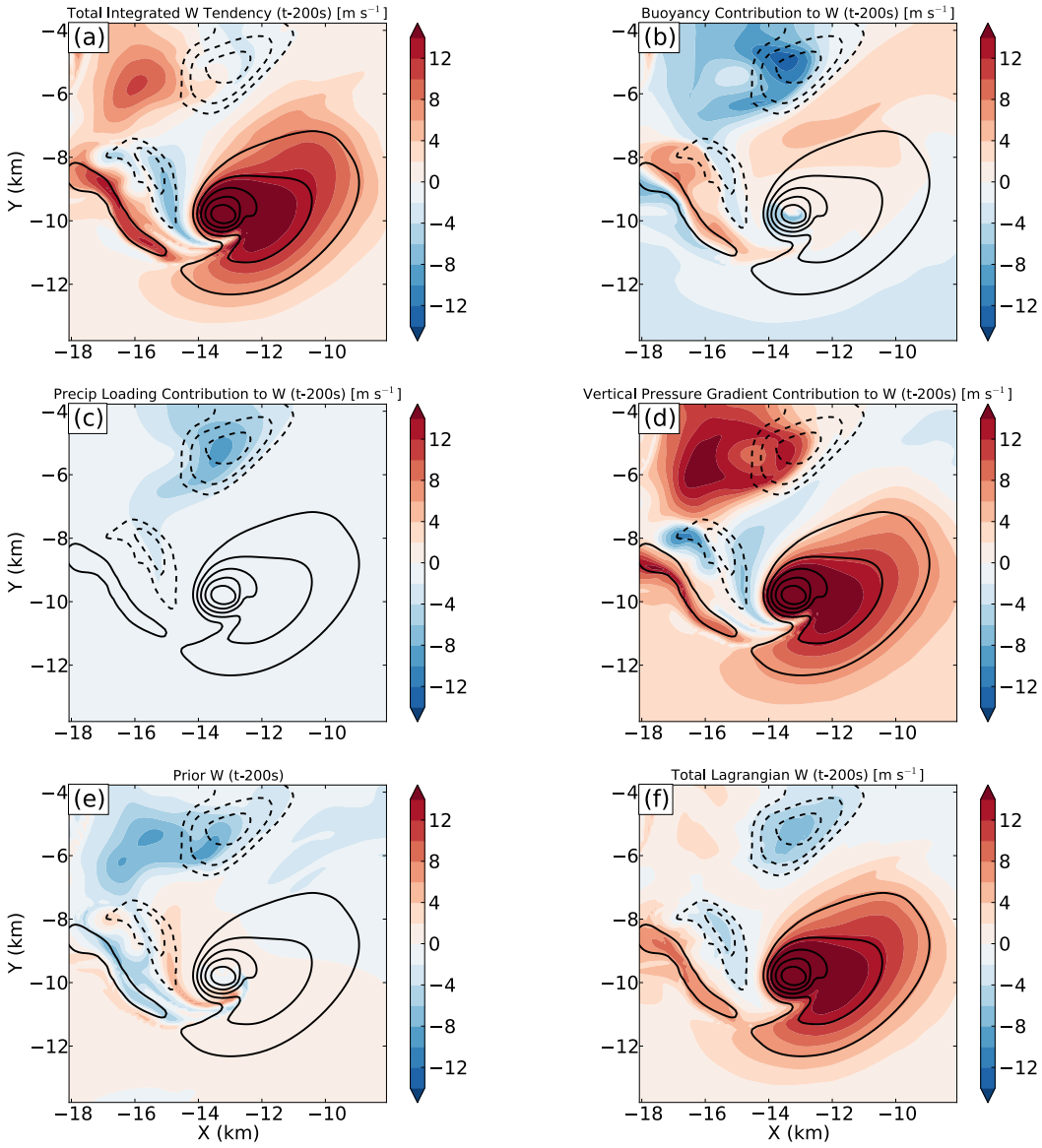

Fig. 4.6 Vertical motion tendency terms integrated backwards 200 s from an initial time of 7200 s at 1 km in the model (color-filled). Panel (a) shows the total tendency, (b) the contribution by buoyancy, (c) precipitation loading term, and (d) the amount associated with the vertical pressure gradient force. The vertical motion at 7000 s from backward trajectories initiated at 7200 s at 1 km is shown in (e). The initial condition from (e) is used in the 200 s forward integration of the tendency equation along trajectories to produce the Lagrangian vertical motion in (f), valid at 7200 s at 1 km altitude. Black contours in every panel are the instantaneous vertical motion every 2 m s^{-1} for negative values and 6 m s^{-1} for positive values at 7200 s at 1 km altitude in the model.

The robustness of the trajectories can be further tested by comparing the simulated vertical motion in the model (black contours) to the vertical motion obtained

by starting at t-200 sec and integrating the tendency terms forward. Figure 4.6e shows the past vertical motion at t-200 sec for all the trajectories that end at one km altitude at 7200 seconds into the simulation. Starting with these vertical motions and integrating the vertical motion tendencies along the trajectories produces the color filled plot of vertical motion in Figure 4.6f. Even after 200 s, there is very strong agreement between the vertical motion obtained through forward integration of the tendencies and the instantaneous vertical motion, denoted by the black contours, at t-0. Thus, the trajectory mapping analysis of vertical motion tendency is robust for this simulation over at least 200 s.

4.4.3 Application to the forcing of vertical vorticity

The vertical vorticity equation in height coordinates is given in (4.5) where, ζ is relative vertical vorticity, t is time, f is the Coriolis parameter, (u, v, w) are the zonal (u), meridional (v), and vertical (w) components of velocity, respectively, ρ is density, P is pressure, and, F_U and F_V are the diffusive tendencies in u and v. The solenoidal term in (4.5) was several orders of magnitude less than the other terms and hereafter is neglected.

$$\frac{d\zeta}{dt} = (f + \zeta)\left(\frac{\partial \mathrm{u}}{\partial \mathrm{x}} + \frac{\partial \mathrm{v}}{\partial \mathrm{y}}\right) + \left(\frac{\partial \mathrm{u}}{\partial \mathrm{z}}\frac{\partial \mathrm{w}}{\partial \mathrm{y}} - \frac{\partial \mathrm{v}}{\partial \mathrm{z}}\frac{\partial \mathrm{w}}{\partial \mathrm{x}}\right)$$

$$+ \left(\frac{\partial F_V}{\partial \mathrm{x}} - \frac{\partial F_U}{\partial \mathrm{y}}\right) + \frac{1}{\rho^2}\left(\frac{\partial \rho}{\partial \mathrm{x}}\frac{\partial \mathrm{P}}{\partial \mathrm{y}} - \frac{\partial \rho}{\partial \mathrm{y}}\frac{\partial \mathrm{P}}{\partial \mathrm{x}}\right) \quad (4.5)$$

The diffusion term in (4.5) combines the effects of sub-grid scale turbulent mixing (Smagorinsky 1963) and numerical diffusion associated with the model advection scheme. Fortunately, CM1 has the option to output the exact turbulent mixing diffusion and a simplified approximation of the numerical diffusion. The numerical

diffusion estimate is based on a single, forward, time step assuming a 5th-order advection scheme. In reality, the model goes through three small time steps over the same time period and uses a WENO advection scheme, integrating the three time steps using a 3rd order Runge-Kutta method (Shen and Zha 2010). Exact determination of numerical diffusion from the WENO scheme is beyond the scope of this study. The simplified approximation obtained from CM1 is likely an underestimate of the true amount of numerical diffusion implicit in the simulation. Total diffusion was calculated separately from the other terms on the RHS of (4.5) to isolate its effect on the change in vorticity and because diffusion estimates are not readily available in most observational studies.

Unlike the tendency equation for vertical motion, the vertical vorticity equation is not a separable differential equation. Instead, (4.5) must be integrated starting with an initial value for ζ and then using the prior value of ζ in the current estimate of the stretching term. A 4th order Runge-Kutta integration method was used in calculating (4.5) along trajectories to mitigate error during periods of exponential ζ growth. In the discussion section to follow, "integrated vertical vorticity" refers to the integration of only the tilting and stretching terms in (4.5) over an arbitrary time period. "Lagrangian vertical vorticity" refers to the "integrated vertical vorticity" plus the initial value of vertical vorticity at that point in the past.

Backward trajectory analyses over a 50-second period initiated at 7200 s and 1 km in the simulation (Fig. 4.7a) shows that the total change in vertical vorticity (the LHS of [4.5]) was mostly positive, especially in the mesocyclone. There is generally good agreement between the total change in vorticity along the backward trajectories

and the integrated vertical vorticity over the same period (Fig. 4.7b), suggesting that tilting and stretching were the dominant terms in the vorticity equation. However, near the vortex center (Fig. 4.7a, x = -13.3, y = -9.6 km), the average difference (Fig. 4.7c) approached 50 percent of the total change. Indeed, large differences, both positive and negative, were found in most regions where the vorticity gradient itself was large.

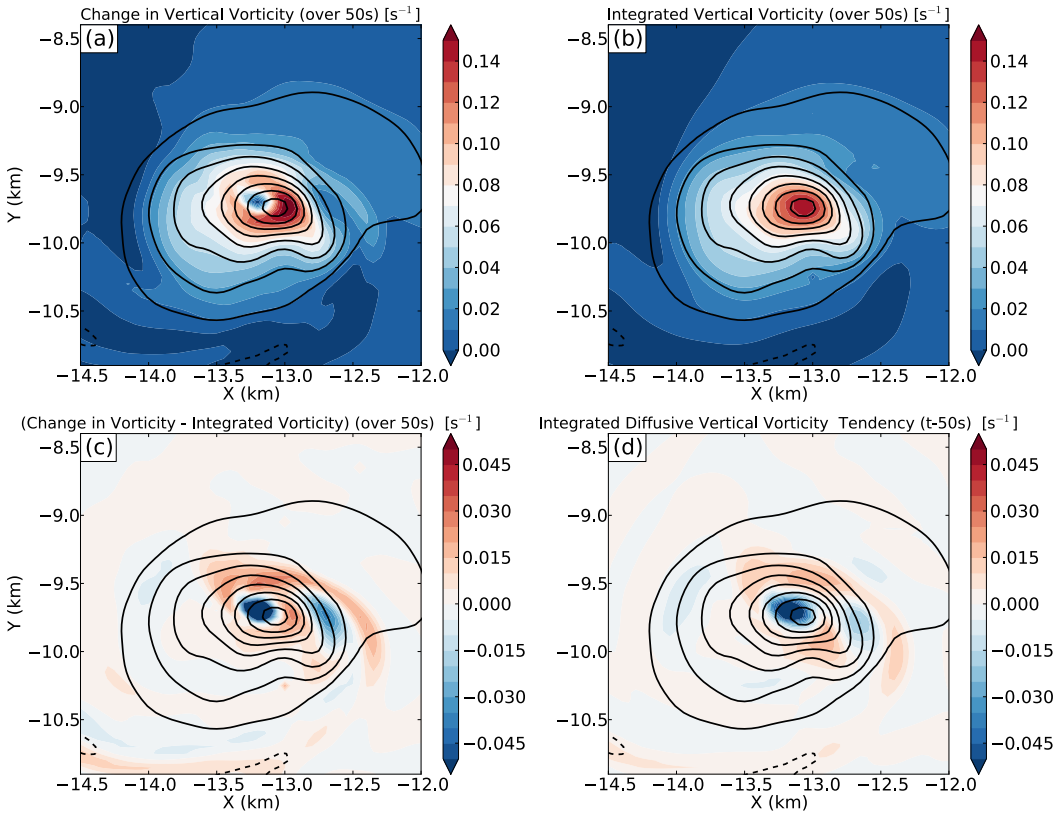

Fig. 4.7 Application of backward trajectory mapping to vertical vorticity analysis. (a) Total change in vertical vorticity (LHS of [4.5]) in s^{-1} according to the color scale, for a 50-second backward trajectory initialized at 7200 s at 1 km altitude in the simulation. (b) Integrated vertical vorticity, from tilting and stretching alone, along 50-second backward trajectories. (c) The difference found by subtracting (b) from (a). (d) Integrated change in vorticity from diffusion, including both sub grid-scale turbulent mixing and the simplified numerical diffusion estimate, along 50-second backward trajectories. For reference, in each panel, vertical vorticity at 7200 s at 1 km altitude, has been contoured in black every 0.02 s^{-1}.

To determine whether these differences were due to the total diffusion (sub-grid scale turbulent mixing plus numerical diffusion), total diffusion was calculated along

the same backward trajectories (Fig. 4.7d). A residual vorticity term R was also constructed according to (4.6). R represents the actual total diffusion in the model since the solenoidal term is small in comparison.

$$R = \frac{d\zeta}{dt} - (f + \zeta)\left(\frac{\partial \mathrm{u}}{\partial \mathrm{x}} + \frac{\partial \mathrm{v}}{\partial \mathrm{y}}\right) - \left(\frac{\partial \mathrm{u}}{\partial \mathrm{z}}\frac{\partial \mathrm{w}}{\partial \mathrm{y}} - \frac{\partial \mathrm{v}}{\partial \mathrm{z}}\frac{\partial \mathrm{w}}{\partial \mathrm{x}}\right) \quad (4.6)$$

Considering the difference between the simplified estimate of numerical diffusion and the actual numerical diffusion in the model, the agreement between the change in vorticity residual (LHS in (4.6), Fig. 4.7c) and the estimated changes associated with total diffusion (Fig. 4.7d) are remarkable. The spatial patterns of positive and negative regions are nearly collocated. The main discrepancy is that the magnitude of the estimated diffusion appears to be low. Interestingly, sensitivity tests in which the WENO advection scheme was replaced with a 5^{th} order or even a fully-explicit 6^{th} order advection scheme resulted in greater differences between the total diffusion using the simplified numerical estimate from CM1 and the residual vorticity change in Fig. 4.7c. Therefore, while the estimated total diffusion using the explicit turbulent mixing diffusion and the simplified numerical diffusion from version 17 of the CM1 model underestimates the amount of diffusion actually occurring in the model, the estimated total diffusion does explain the bulk of the discrepancy between the total change in vorticity along the backward trajectories and the integrated vertical vorticity.

The close agreement between the estimated total diffusion (Fig. 4.7d) and the residual vorticity change (Fig. 4.7c) suggests that the trajectory mapping technique itself did not introduce significant errors in the vorticity analysis. More importantly, the spatial pattern of diffusion can be elucidated by trajectory mapping. This may be the first time that the effects of diffusion on the vorticity field have been quantified within a

simulation over the entire mesocyclone. Regions where the impact of diffusion is large would correspond to regions where unguided analysis of individual trajectories could lead to misinterpretations of the model vorticity budget along the trajectory.

4.4.4 Proxies for Observational Applications

Often in observational cases, only the kinematic properties of the storm are observed. Thus, thermodynamic properties and behavior have to be inferred from the kinematics. Trajectory mapping can be a useful tool to evaluate the utility of observable quantities that may be used as proxy for basic thermodynamic structure. The quantity that will be examined here is source height, which will be shown to be a proxy for equivalent potential temperature, θ_e, as suggested by Markowski et al. (2002) because it is conserved for reversible, moist adiabatic processes.

In most observational studies, θ_e is not available within the storm system. Thus, this proxy must be evaluated in the numerical simulation. In Fig. 4.8, prior altitude at 100 s and 800 s is compared to θ_e at t-0 s and 800 s along trajectories. Over the shorter period, prior altitude is indicative of the recent vertical motion history of trajectories and suppresses the impact of past transient updrafts and downdrafts on the interpretation of the true source altitude of the trajectory. However, once the trajectories are traced back long enough, in this case 800 s, then prior altitude (Fig. 4.8c) can then be considered a good qualitative proxy for θ_e. The required trajectory integration period is dependent on the scale of motion and magnitude of the flow. In this case, it is 800 seconds. But for larger storms, the integration period could be more than 1500 seconds.

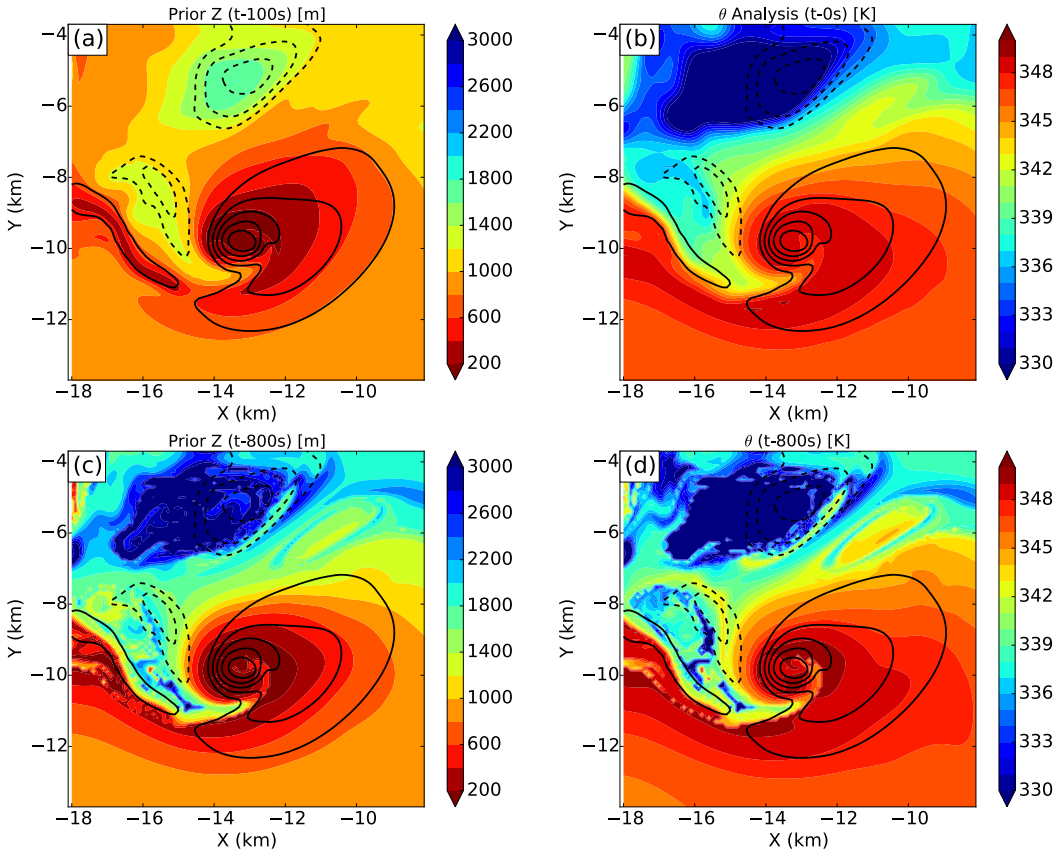

Fig. 4.8 Prior altitude after 100 s (a) and 800 s (c) and equivalent potential temperature at 0 s (b) and prior equivalent potential temperature at 800 s (d), with analyzed vertical motion (black every 2 m s^{-1} for negative values and 6 m s^{-1} for positive). The trajectories were initiated 7200 s in the model, at an altitude of 1 km.

4.5. Sensitivity to Observational Sampling

Trajectory maps have been shown to be useful in elucidating the spatial pattern of fluid behavior in a numerical model when data are available at every time step and at every grid point. Observational datasets typically have coarser temporal and spatial resolution. For instance, mechanically-scanning research radar volumetric scans of convective storms often require 2-3 minutes and have horizontal wavelength resolutions of 1-2 km (e.g. Lund et al. 2009; Bruning et al. 2010; Palucki et al. 2011). To determine the impact of sparse and infrequent data on trajectory maps, sensitivity tests were conducted using the model framework.

4.5.1 Spatial Resolution Test

The effect of spatially under sampling storm structure was examined by applying a Gaussian filter (sigma = 1.5) over horizontal planes in the numerical model output. The filter essentially removed energy at wavelengths less than four times the horizontal grid spacing, or less than 1 km for the 250 m resolution model grid. Coarse spatial resolution did not appreciably influence 800 s backward trajectories of prior altitude or prior θ_e (compare Figs. 4.9a, b with Figs. 4.8c, d). The filtered model output produced smoother trajectory maps with lower amplitude extrema. But the physical behavior of the source region for the primary vertical draft was preserved, as was the scale of the downward-moving air that intruded into the west (left) side of the mesocyclone.

To test the significance of course resolution on the trajectory map of vertical vorticity changes, the Lagrangian vertical vorticity field over 100 s backward trajectories was computed. The final Lagrangian-derived vertical vorticity map is found by integrating (4.2) without the solenoidal and diffusion terms and by adding the initial vorticity at the beginning of the trajectory. Since the result depends on the filtered initial vorticity, only the impact from the Gaussian filter on the initial high-resolution vorticity are shown in Fig. 4.9c. Note that the filtered initial condition has lower amplitude, smoother structure, and a maximum that is displaced to the west (left) of the original high-resolution vortex. The Lagrangian vertical vorticity map, computed from 7100 to 7200 s into the simulation (Fig. 4.9d) resulted in sharper gradients, high peak amplitude, and a smaller displacement of the vortex center than the filtered initial condition. Indeed, the Lagrangian vertical vorticity map is very similar to the original high-

resolution vorticity at 7200 s. The mapped Lagrangian vertical vorticity responded to the same large-scale deformation that had caused the vortex in the model to become concentrated. Thus, mapping the Lagrangian-derived vertical vorticity recovered some of the structure in the vorticity field that was removed by the filter.

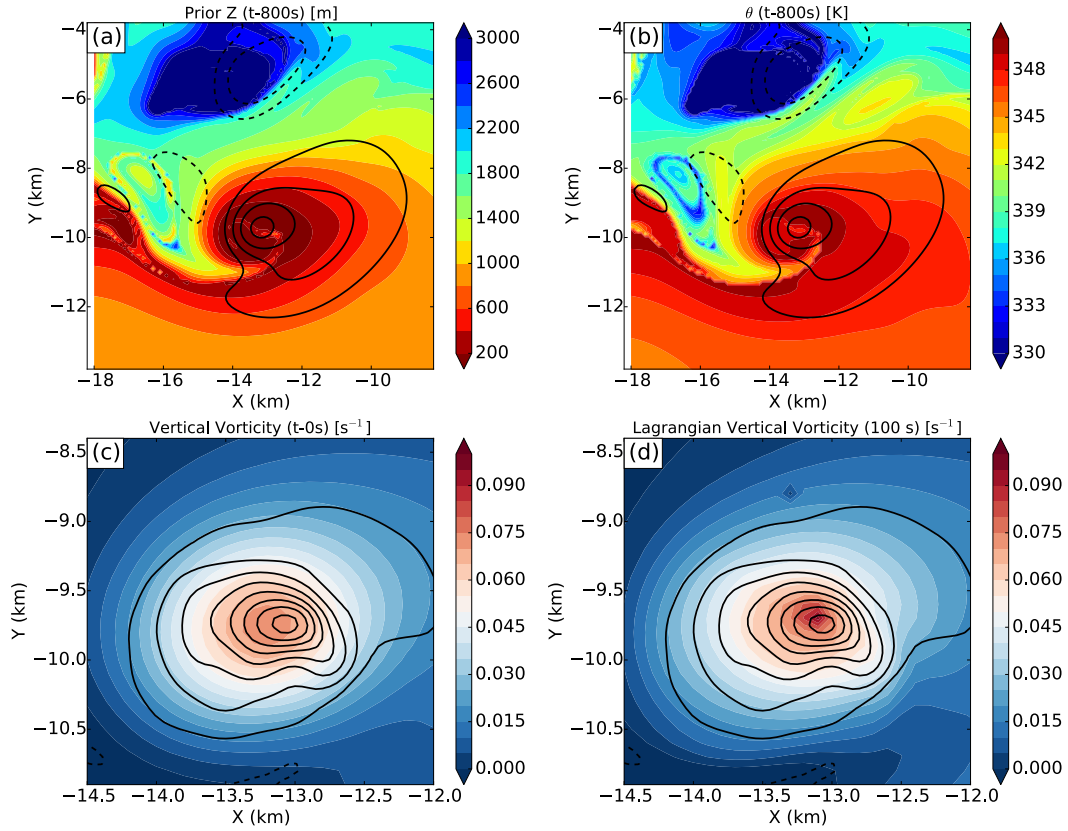

Fig. 4.9 Results after spatial filtering has been applied with a data frequency of 2 s. (a) Prior altitude and (b) equivalent potential temperature after 800 s of trajectory integration, with analyzed vertical motion (black every 2 m s^{-1} for negative values and 6 m s^{-1} for positive). (c) Analyzed vertical vorticity and (d) Lagrangian vertical vorticity after 100 s, with the original, analyzed (t-0) vertical vorticity (black contours every .02 s^{-1}) overlaid.

The impact of low spatial resolution but high temporal resolution is especially germane to observations collected by phased-array radars (Heinselman et al. 2008; Isom et al. 2013; French et al. 2014). Phased-array systems provide data every few seconds but with spatial resolution comparable to, or slightly worse than, existing mechanically-

scanning weather radars. Hence, trajectory mapping analyses help improve the intrinsic resolvable spatial scale of fluid behavior and better match the frequency obtained from phased-array radar observations.

4.5.2 Combined spatial and temporal resolution test

To evaluate the trajectory mapping technique relative to more commonly available radar datasets from mechanically-scanning radars, the filtered model output was further degraded by reducing the temporal resolution of the model output to 180 s. The trajectory location between time steps was computed using the advection correction scheme described in Ziegler et al. (2013).

Limiting the temporal resolution of the filtered model output to 180 s resulted in little additional loss of fidelity in the 800 s backward trajectory maps of prior altitude and θ_e (compare Figs. 4.10a, b with Figs. 4.9a, b). Indeed, the greatest impact on the trajectory map structure was due to coarse spatial rather than limited temporal resolution of the data used in computing the trajectories. Regardless, even for the relatively poor temporal and spatial scales associated with currently available radar observations, the trajectory maps revealed the history and thermodynamic characteristics of the vertical drafts quite well.

The Lagrangian vertical vorticity map also did not suffer much additional change in trajectory behavior from the limited temporal sampling (compare Fig. 4.10d with Fig. 4.9d). The resolved scale and spatial pattern of the trajectory map was very similar to that for just the degradation in spatial resolution. The deformation in the flow along the trajectories acted to sharpen the horizontal gradients, increase the magnitude of the extrema to better match the actual maxima, and helped force the vortex center to

be closer to the actual vortex center at 7200 s as compared to the initial condition (Fig. 4.9c and Fig. 4.10c).

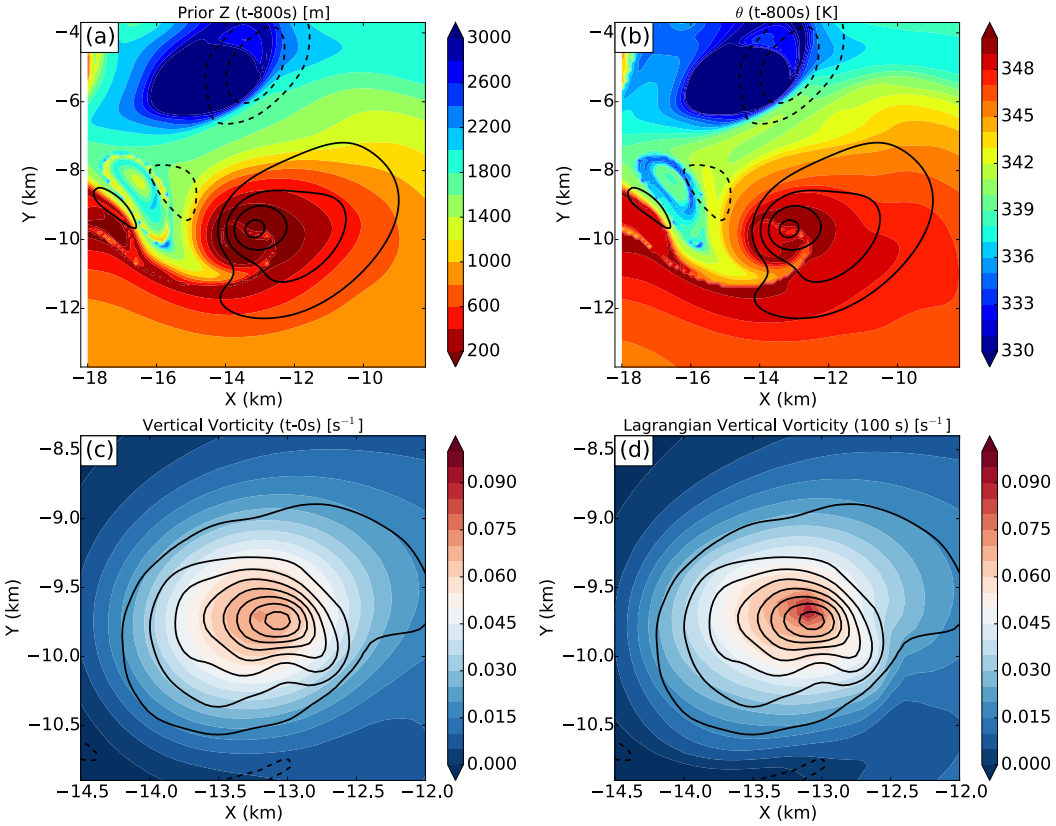

Fig. 4.10 Same as Fig. 4.9, except that in addition to the spatial scale being smoothed, the model output frequency has been reduced to 180 s.

For the storm circulation examined here, which is of a size (2-3 km in diameter) and duration (~10 minutes) that is common to observed classic supercell storms (Burgess et al. 1982), the trajectory mapping analysis of the flow behavior was not significantly impacted by limiting the data to the resolution typical of wind retrievals for research radars.

Nevertheless, there were areas that showed sensitivity to sampling resolution. The prior altitude values exhibited small-scale variability in the rear flank downdraft region to the west of the mesocyclone (c.f., near x=-16, y= -9 km in Fig. 4.8c). The variability in prior altitude was related to a small region of deformation associated with

counter-rotating vortices to the west of the mesocyclone and outside the area of precipitation at earlier times. Air that later arrived within this part of the rear-flank region was comprised of a mixture of air that passed through or between these vortices. The lower spatial and temporal resolution trajectory maps of prior altitude (Fig. 4.9a, 4.10a) did not capture the subtlety of this flow and hence did not exhibit as much variability in this region. Instead, the lower-resolution sampling resulted in an averaged structure. In that manner, the lower resolution sampling resulted in errors relative to the higher-resolution trajectory maps. But these errors do not appear to be dynamically significant to the storm's evolution.

Moreover, the trajectory mapping framework better defines the intrinsic spatial scales of the observed flows, which helps match gains in temporal resolution achieved by phased-array radars. In general, the steadiness and scale of the dominant flow characteristics relative to the resolution of the observational sampling is a fundamental factor in the success of the trajectory mapping method in diagnosing internal storm behavior. For storms in which the flow is more transient, or significantly under sampled spatially, the consistency of the deformation and thus the trajectory behavior can be expected to be more sensitive and the resulting analyses to have larger errors.

4.6. Observed Supercell Trajectory Maps

The sensitivity tests in the previous section indicate that that backward trajectory maps should reveal the spatial pattern of air behavior in storms observed at 2-3 minute intervals with spatial resolutions of 1-2 km wavelengths. A high-precipitation supercell was observed at those scales by the two SMART radars (Biggerstaff et al. 2005) during TELEX 2 (MacGorman et al. 2008) on 29 May 2004. Payne et al. (2010) and Calhoun

et al. (2013) studied the polarimetric and lightning characteristics, respectively, of the storm with regard to its kinematics diagnosed from dual-Doppler wind retrievals. The wind retrievals have been extended to cover a ~75 minute period at about 150 s intervals.

Prior altitudes over a period of 1000 s were determined using backward trajectories initiated at 1 km altitude at three different times to illustrate the spatial pattern of the airflow around the low-level mesocyclone (Fig. 4.11). The prior altitude maps appear similar to the simulation, with the biggest exception being the larger scale of the observed high-precipitation mesocyclone. One-thousand seconds before 0024 UTC on 30 May 2004 (Fig. 4.11a), the air that eventually filled the mesocyclone at 1 km altitude came primarily from lower levels. However, there were small regions within the mesocyclone that contained air from above 1 km. This air had been transported in a small downdraft near the vortex center. Later, this air flowed around the vortex, and mixed with air from altitudes closer to 1 km (Fig. 4.11b).

Outside the mesocyclone, evidence of a rainy-downdraft (Brandes 1978) prior to 0024 UTC was observed to the northwest (upper-left area in Fig. 4.11a). Air from the rainy downdraft mixed with air from a stronger rear-flank downdraft that occurred before 0036 UTC, as indicated by the larger area of higher altitude sources to the west and northwest of the vortex center at that time (Fig. 4.11b). These downdrafts did not cause the mesocyclone to occlude. However, their arrival appears coincident with the concentration and symmetrization of the mesocyclone suggesting that the downdrafts helped to organize the low-level mesocyclone (compare Fig. 4.11a with 4.11b). A much stronger downdraft occurred prior to 0048 UTC (Fig. 4.11c) in the southeastern sector

of the mesocyclone. The sharp gradient in the pattern of prior altitude helps delineate the location of the rear-flank gust front at 0048 UTC. Compared to the earlier times, the gust front had clearly surged ahead of the mesocyclone at 1 km altitude, typical of the initial shape of a meso-vortex occlusion process (Burgess et al. 1982 and Dowell and Bluestein 2002) Similarly, the analyzed vertical vorticity at 0048 UTC became amplified as the low-level mesocyclone was stretched, consistent with trajectories originating from a level below 200 m.

The method of mapping Lagrangian trajectories in a Eulerian framework to better visualize the spatial scale and airflow behavior yields valuable insight to the mesocyclone evolution that is difficult to discern from individual dual-Doppler analyses. More importantly, given that deformation within this storm was quasi-steady over the entire analysis period, the backward trajectory map clearly delineated the gradients separating different source regions of air that was observed at 1 km altitude near and within the mesocyclone. Hence, trajectory maps can be an invaluable tool that aids the understanding of observed storm evolution at a higher resolution than the individual analyses used to construct the maps. Future studies based on trajectory map analysis will focus on the role of downdrafts on the mesocyclone evolution and will extend the method to less steady, multicell convective systems.

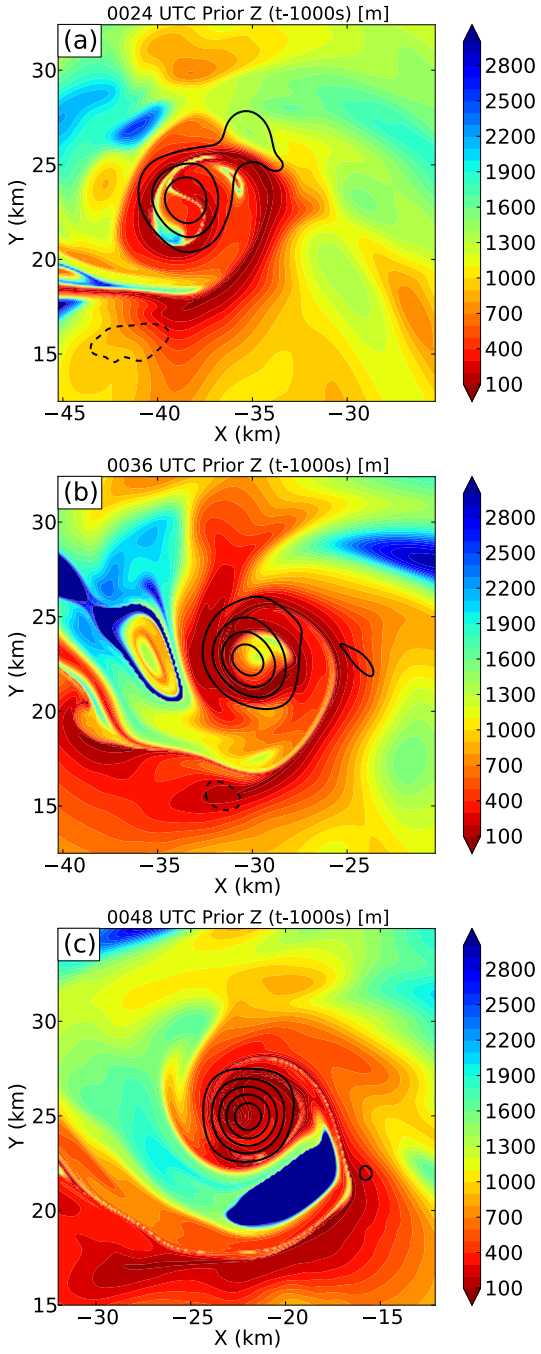

Fig. 4.11 One-thousand second backward trajectory maps initiated at 1 km altitude from the 29-30 May 2004 Geary, OK dual-Doppler wind retrievals. Prior altitude at 1000 s in the past (color-filled) is plotted for trajectories initiated at (a) 0024 UTC 30 May, (b) 0036 UTC, and (c) 0048 UTC. Analyzed positive vertical vorticity at each analysis time is contoured in black (every 0.01 s^{-1}).

4.7 Discussion and Conclusions

A trajectory mapping framework, similar to Klemp et al. (1981), has been presented and demonstrated to improve the robustness of analyzed characteristics of fluid flows and eliminate the need to generalize fluid motions through a small set of select trajectories. While the examination of individual Lagrangian trajectories has been a vital tool in understanding both observed and numerically simulated thunderstorms, they are subject to questions of representativeness and accuracy, especially those computed from observations. Backward trajectory maps have been shown to vividly illustrate the potential errors in randomly choosing a trajectory based on vertical velocity or vorticity due to deformation zones that cause gradients in trajectory behavior significantly smaller than the grid spacing. Although there is still value in examining individual trajectories, the trajectory mapping framework provides a more robust perspective and an invaluable sense of representativeness that would not be available otherwise.

One important caveat is the choice of integration periods presented in this paper. The spatial structure and scale of trajectory behavior is completely dependent on the scales of motion and deformation. An integration period of 100 seconds could be sufficient for a region of small-scale motion while a similarly structured but much larger scale of motion could require an integration period of 500 or 1000 s to illustrate comparable flow behavior. Therefore, one must explore a range of integration periods to understand the scales of motion before deciding on a representative integration period.

The trajectory mapping framework was applied to analyze the source region of air within the low-level mesocyclone, the forcing of vertical momentum, and the

development of vertical vorticity in and near the mesocyclone. Air within the low-level mesocyclone was found to have converged from a broad area surrounding the circulation, particularly from north of the circulation in a region that had been subjected to subsidence over much of the trajectory integration period. The main updraft was found to have been accelerated by the vertical pressure gradient force over the entire integration period while other vertical drafts were influenced primarily by precipitation loading and thermal buoyancy. The development of vertical vorticity in the region in and near the mesocyclone was dominated by tilting and stretching. More importantly, however, dissipation from both turbulent mixing and numerical diffusion explained much of the difference between the actual change in vertical vorticity and that computed from the tendency equation following the trajectories. We believe this to be the first study to quantify the integrated impact of numerical and turbulent diffusion on the production of vertical vorticity. The trajectory mapping analysis, therefore, illustrates regions in which calculation of vorticity budgets from individual trajectories may contain significant uncertainty.

The trajectory mapping method was also used to show that prior altitude determined from backward trajectories over a sufficiently long period was a good proxy for equivalent potential temperature. The robustness of the trajectory map was tested by degrading the spatial and temporal resolution of the model output. While individual trajectories may be susceptible to a lack of temporal and spatial resolution, the larger scale behavior of the trajectory maps did not significantly change when the data frequency and resolved spatial scale was limited to scales typical of research radar datasets. Moreover, the deformation experienced by the trajectories sharpened the

spatial scale of the analyses, which may help to match improved temporal resolution from phased-array radars. Thus, we are confident that provided a slowly evolving storm (relative to the frequency of the observations), much can be learned from radar-based trajectory maps.

To further elucidate the utility of trajectory maps for observed storms, the prior altitude from 1000 s backward trajectories integrated at three different times were used to evaluate the source regions of air in the mesocyclone of a high precipitation supercell observed during 29-30 May 2004. The trajectory maps showed the horizontal structure and evolution of descending air parcels for both the rainy downdraft and the rear-flank downdraft. These flow regimes were tracked in time as they wrapped around the mesocyclone, coincident with a period of vortex intensification. Future observational studies using the trajectory mapping framework will examine these downdrafts and their impact on the evolution of the low-level mesocyclone.

Chapter 5: Evolution of Storm-Scale Downdrafts in a High-Precipitation Tornadic Supercell Thunderstorm

5.1. Introduction

Many observational studies have shown that the strength and position of the rear-flank downdraft (RFD) can vary substantially during the mesocyclone life cycle (Barnes 1978a; Klemp et al. 1981; Dowel and Bluestein 1997; Wakimoto and Lui 1998; Wakimoto and Cai 2000; Ziegler et al. 2001; Dowell and Bluestein 2002a, b; French et al. 2008; Markowski et al. 2012a; Kosiba et al. 2013; Skinner et al. 2014). Additionally, the forcing mechanisms may vary substantially in space and time as evidenced by surface observations of buoyancy fields in the rear flank, especially around tornadoes (Markowski et al. 2002; Lee et al. 2004; Finley et al. 2004; Grzych et al. 2007; Finley et al. 2008; Hirth et al. 2008; Lee et al. 2011; Skinner et al. 2011; Lee et al. 2012; Weiss et al. 2015). The thermodynamic composition of the RFD is important to understand because it impacts the longevity of supercells (Brooks et al. 1994) and influences the tornadogenesis process (Markowski et al. 2002; Markowski et al. 2003; Markowski and Richardson 2014; Schenkman et al. 2014; Marquis et al. 2012). These studies demonstrated that warm RFDs were more favorable to tornadogenesis because negatively buoyant cold air is more difficult to lift and thus limits future stretching of vertical vorticity.

An observational climatology (Rasmussen and Straka 1998) noted that many supercells transition towards high-precipitation structure with time. As the mid- to upper level storm-relative flow is increased, precipitation is advected further downstream of the updraft and thus the forcing mechanisms associated with the

precipitation are also shifted downstream, relative to the updraft (Brooks et al. 1994; Rasmussen and Straka 1998). Therefore, it is not unreasonable to expect downdraft forcing mechanisms to be spatially displaced in high-precipitation supercells, relative to its position in classic supercells. The circulation-relative shift may result in the altered importance of downdraft forcing mechanisms, which could have profound implications for the associated thermodynamic composition of the downdraft outflow.

While many studies have demonstrated potential forcing mechanisms for downdrafts in the rear-flank region, few studies have focused on the evolution of the storm-scale RFD over a mesocyclone cycle. The dataset examined in Chapter 3 (Betten et al. 2018), is believed to have the best combination of longevity and temporal sampling by two Doppler radars in a supercell storm and thus is ideal to compare trajectory behavior over a period only matched by numerical simulations. This chapter examines the RFDs from Chapter 3 in more detail, focusing on the evolving forcing mechanisms, location, and behavior over an hour-long period.

5.2. Methodology

The dual-Doppler wind retrievals from Chapter 3 are used here to calculate three-dimensional air parcel trajectories and to perform trajectory-mapping analyses (Chapter 4, Betten et al 2017). To dampen evolution errors associated with the inherent three-minute temporal resolution in the wind retrieval database, a storm morphing methodology described by Ziegler (2013a) was employed to advect and linearly interpolate, in time steps of 30 seconds, the radar reflectivity and horizontal winds. Vertical motion was diagnosed from the interpolated horizontal flow. Advection velocity estimates were made between each analysis that maximized the correlation

between the low-level vertical vorticity of the two corresponding radar volumes at the central time. This advection correction step mitigated unphysical minima between radar volumes in the low-level vertical vorticity field. Viewing the resultant trajectory maps in a high-temporal resolution animation (not shown) confirmed that the storm-scale structure evolved smoothly in time. Analyses in the previous chapter showed that the resultant trajectory mapping analyses revealed the spatial distribution of airflow behavior and source regions for storm-scale features observed in the simulated storm.

Trajectories integrated prior to 2358 UTC, the earliest radar volume, assumed a steady storm motion and a steady kinematic structure, similar to the assumption made by Ziegler (2013a). Unfortunately, the radar was operated in RHI (Range Height Indicator) mode between 2358 and 0012 UTC, thus trajectory maps will not be shown before 0016 UTC. Additional radar volumes are also missing at 0025 and 0030 UTC, creating gaps of six minutes each.

5.3. Environment

The near-storm environment surrounding the Geary supercell was characterized by large mixed-layer convective available potential energy (MLCAPE, 3359 J kg^{-1}), strong deep layer shear (27 m s^{-1} of 0-6 km shear), and extreme low-level helicity (~ 461 m^2 s^{-2} 0-3 SRH) (Figure 3.2). Despite storm-relative anvil flow of 30-33 m s^{-1}, suggestive of classic supercell structure (Rasmussen and Straka 1998), the midlevel flow at 2-5 km layer were significantly weaker, 8-12 m s^{-1}, and suggestive of high-precipitation supercell structure (Brooks et al. 1994). Vertical profiles of virtual potential temperature (θ_v) and equivalent potential temperature (θ_e) (Figure 5.1) reveal the presence of a stable layer between 900 m and 2000 m. The profile yielded a mixed-

layer lifting condensation level (ML-LCL) of 1.1 km and a much higher level of free convection (LFC) at 2.3 km, resulting in 67 J kg-1 of convective inhibition (CIN).

The near-storm thermodynamic environment had two significant impacts on the behavior of thermodynamically driven downdrafts in the storm. The first is that environmental air below the stable layer (2000 m) should have limited evaporation potential as it flows into the storm due to high ambient relative humidity. The second is that it was more difficult for buoyancy driven downdrafts to reach the surface due to the low level stable layer. Downdraft trajectories in simulations by Naylor et al. (2012) demonstrated that as downdraft parcels pass below a stable layer, they immediately become less negatively buoyant, requiring them to be significantly colder in order to reach the surface, as compared to less stable environments.

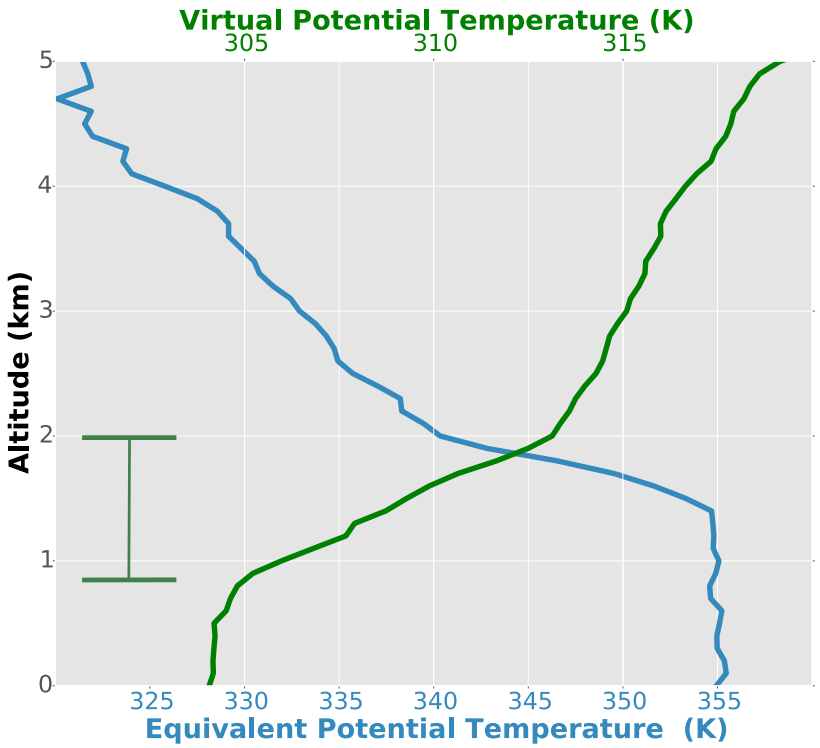

Fig. 5.1 Vertical profiles of equivalent potential temperature (blue) and virtual potential temperature (green) based on the Minco sounding over the lowest 5 km. A stable is highlighted between 900 and 2000 m, evident in the strongly sloped virtual temperature profile.

5.4. Gross Downdraft Temporal Evolution

To examine downdraft behavior over the observed period, the storm-scale downdrafts were divided into sub-regions as defined in previous studies. The classic supercell conceptual model of Lemon and Doswell (1979) divided the supercell downdrafts into two primary regions, the rear-flank downdraft (RFD) situated upstream from the primary updraft and the forward flank downdraft (FFD) situated downstream of the primary updraft. Additional studies identified the "rainy downdraft" (RRFD) (Brandes 1978) and "occlusion downdraft" (ORFD) (Klemp and Rotunno 1983) as separate features within the overall RFD area that exhibited consistent, but uniquely identifiable behavior from the primary RFD and will be hereafter be called RRFD and ORFD respectively. The downdraft regions have been identified and labeled on top of the Lemon and Doswell (1979) conceptual model which has been reoriented to match the low-level reflectivity structure of the Geary, OK supercell analyzed here (Figure 5.2). It should be noted that while the RFD region extended at times up to 30 km north of the low-level mesocyclone, the defined *northern* extent of the overall RFD region in subsequent analyses was limited to 10 km range from the mesocyclone to concentrate on the downdraft region most likely to influence the circulation. Any grid point with a vertical velocity below -2 m s^{-1} was classified as a downdraft grid point and assigned a regional classification as described above.

The total horizontal area represented by the grid points meeting the criteria above has been summarized for each downdraft region as time-height plots (Figure 5.3). Note that the contoured range is region specific. The areal extent of the RFD region appears to be periodic, with maxima at 0028 and 0052 UTC (Figure 5.3a) with the

second RFD surge being almost twice as deep as the first. The minimum in RFD areal extent (0038 UTC) corresponded to the deep intensification phase of the mesocyclone (Chapter 3). Meanwhile, the areal extent of the RRFD (Figure 5.3b) varied somewhat independently from that of the larger scale RFD (Figure 5.3a). The main expansion of the RRFD occurred after the 0045-0058 UTC RFD surge.

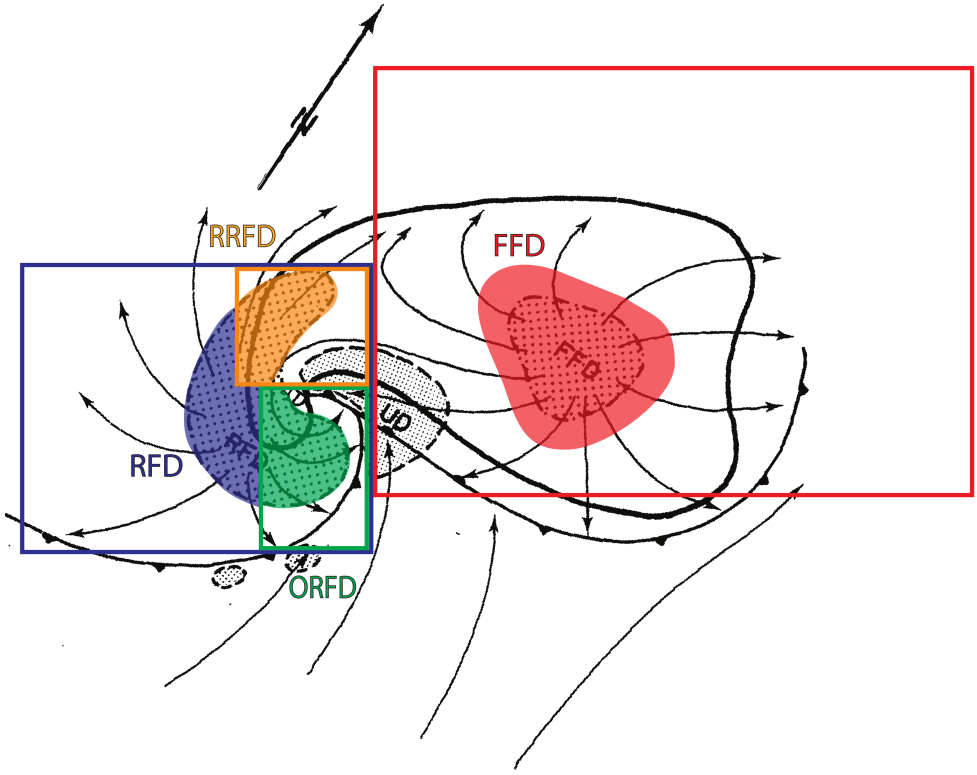

Fig. 5.2 The Lemon and Doswell (1978) conceptual model has been rotated and reproduced here, with the different downdraft regions designated. Downdrafts in the blue box were designated as rear-flank (RFD), red as forward-flank (FFD), green as the occlusion sub-region of the RFD (ORFD), and orange as the rainy sub-region of the RFD (RRFD).

For much of the lifecycle of the second mesocyclone examined in Chapter 3, the circulation was located in the vertical velocity gradient, which resulted in the near-continuous presence of a downdraft around and inside the mesocyclone. The ORFD areal extent (Figure 5.3c) was highly correlated to the primary RFD area (Figure 5.3a) but was smaller in area, especially prior to the mesocyclone intensification stage (0035-

0045 UTC). Furthermore, in contrast to the RFD and RRFD, which generally decreased in size below the stable layer near 2 km, the ORFD area was more frequently maximized below the stable layer. This would be consistent with different driving mechanisms for the ORFD, the RRFD, and the larger-scale RFD.

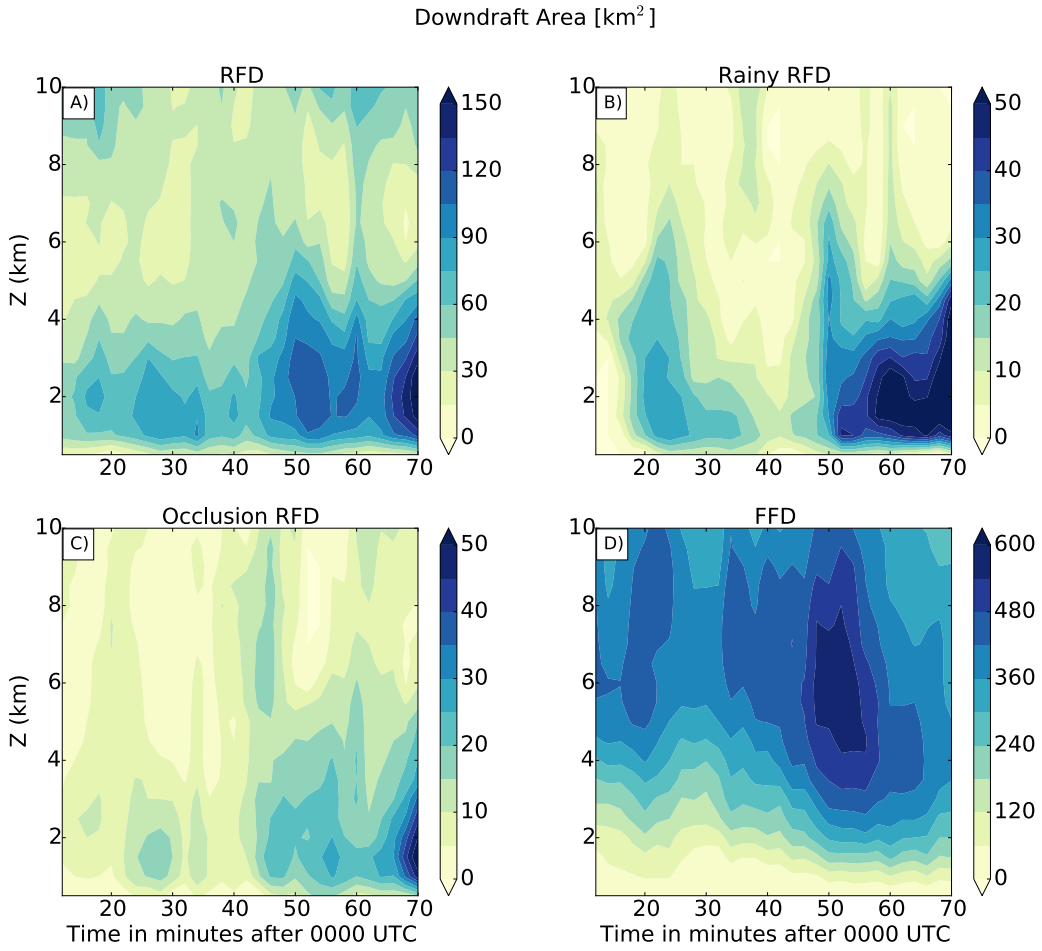

Fig. 5.3 Horizontal area (km^2) for different downdrafts regions, defined in Figure 5.2, varying in time (minutes after 0000 UTC) and altitude (km). The regions shown are (a) the RFD region, (b) the "rainy" RFD, (c) the occlusion sub-region of the RFD, and (d) the FFD region.

The FFD (Figure 5.3d) appeared to exhibit an even stronger aversion to penetrating below the stable layer near 2 km altitude than the other downdrafts, as the areal extent was maximized at substantially higher altitudes than the RFD region. This

behavior is consistent with the absence of a well-defined forward flank gust front (Chapter 3).

To examine the impact of the downdrafts on the low-level gust fronts, a ten-minute backward trajectory mapping analysis was conducted for each analysis time (Figure 5.4). The trajectories were initiated at 500 m altitude at all grid points. Those trajectories that experienced a downdraft stronger than -2 m s^{-1} within the prior ten minutes were denoted to have been associated with a downdraft. The sum of the area affected by downdraft serves as an estimate of the low-level accumulation of downdraft air parcels in the different regions of the storm.

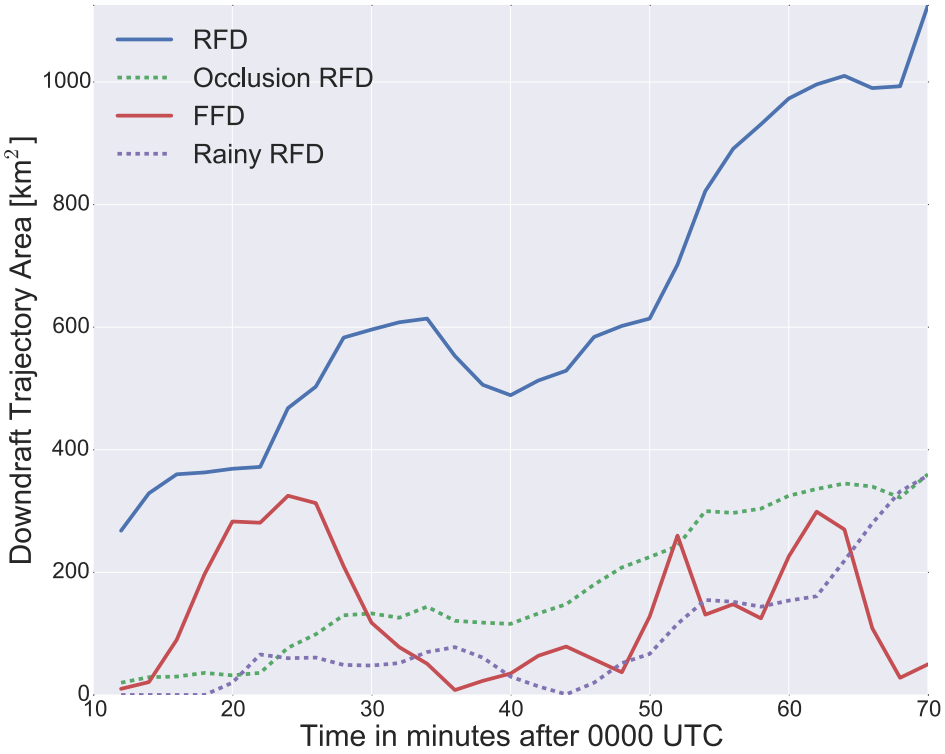

Fig. 5.4 Horizontal area (km^2) represented by backward air parcel trajectories initialized at 500 m altitude that experienced a downdraft (w < -2 m s^{-1}) over the prior 10 minutes. The primary downdraft regions outlined in Figure 5.3 are represented by solid blue (RFD) and red (FFD) lines and the sub-regions are represented as dashed green (ORFD) and purple (RRFD) lines. The RFD area includes the individual sub-regions.

The RFD and its sub-regions generally accumulated downdraft air near the ground as time progressed. Local maxima in low-level downdraft trajectory area (blue line, Figure 5.4) generally correspond to RFD intensification periods (Figure 5.3a). However, a decrease in near-ground downdraft trajectory area was observed between 0035 and 0040 UTC. The reduction of low-level downdraft air following the 0022-0032 UTC RFD surge suggests that while the RFD was strong, low-level outflow was not expanding, consistent with the weak response of the secondary RFD gust front to the first RFD surge noted in Chapter 3. During the second RFD surge, after 0040 UTC, the initial expansion of downdraft air was attributed to air parcels passing through the RRFD (purple line) and ORFD (green line). Yet, the major expansion in downdraft area extent was delayed until 0048 UTC, when outflow from the primary RFD began spreading out during the occlusion stage of the mesocyclone and the rear flank gust front surged away from the low-level circulation (Chapter 3).

Chapter 3 also noted the presence of an updraft situated on the western side of the hook echo and speculated that it potentially shielded the RFD from the entrainment of dry midlevel environmental air into the downdraft. The total vertical mass flow rate in the western updraft band was estimated for grid points with vertical velocity greater than 2 m s^{-1} that were located west of the mesocyclone and north of the primary RFD gust front (Figure 5.5). Unlike the primary updraft zone farther east, the western updraft was only significant during the mature stage of the mesocyclone cycle, growing initially at low-levels and building upwards. The intensification period between 0040-0045 UTC followed the 0022-0032 UTC RFD surge but corresponded to the minimum in low-level downdraft area, strongly suggesting that the RFD outflow may have been

recycled into the western updraft band rather than bolstering the SRFGF. The updraft began weakening after 0045 UTC as the mesocyclone occluded, disappearing almost completely by 0100 UTC.

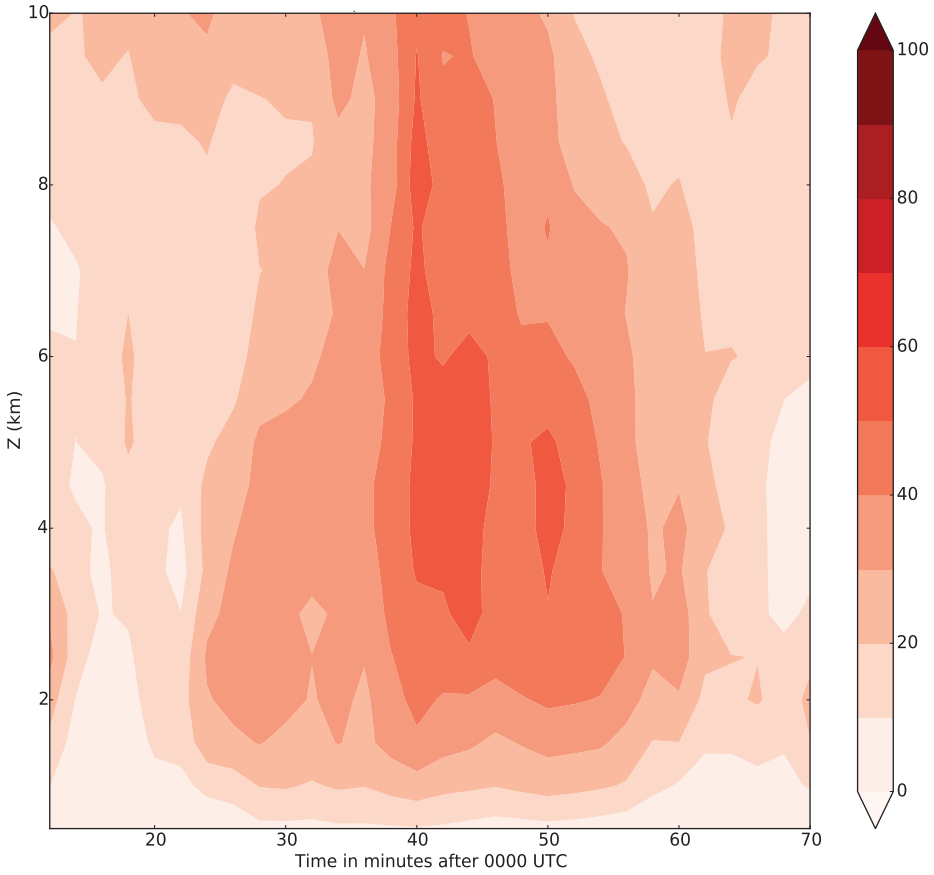

Fig. 5.5 Total vertical mass flow rate (1x 10^7 kg s^{-1}) of the western updraft region, defined as the region west of the mesocyclone and north of the primary RFD gust front, for grid points with a vertical velocity greater than 2 m s^{-1}. Density was calculated from the sounding shown in Figure 3.2.

5.5. RFD Trajectory Evolution

5.5.1 1st RFD Surge (0022-0032 UTC)

During the first RFD intensification period, the downdraft was approximately 6 km deep (Figure 5.6a) and positioned on the northwest side of the mesocyclone (Figure 5.6b). The downdraft was also continuously sheltered by the western updraft, which extended above 10 km (Figure 5.6c). Rather than being aligned with the heaviest

precipitation, the downdraft maximum was offset to the outer side of the reflectivity maxima in the hook echo (Figure 5.6b, d, f) and radar reflectivity generally decreased with height within the downdraft (Figure 5.6a, c, e), suggesting that melting and precipitation loading played a larger role at low-levels compared to mid levels. Conversely, the vertical reflectivity gradient increased with height in the occlusion downdraft (Figure 5.7a, c, e), which was consistently situated within a substantial negative vertical gradient in vertical vorticity observed near the tip of the hook echo (Figure 5.7b, d, f). The strongest vertical gradient of vorticity was found between 1 and 3 km, potentially explaining the shallow nature of the downdraft at 0028 and 0032 UTC.

Previous studies have used trajectories to examine the paths of individual air parcels in updrafts, downdrafts, and enhanced vorticity regions (Klemp et al. 1981; Brandes 1984; SC16). Alternatively, Chapter 4 demonstrated the utility of initializing trajectories on a constant plane and mapping their behavior to their initiating positions to elucidate the spatial scale and pattern of fluid flow behavior.

The advection of air that has experienced significant vertical displacement due to downdrafts can be visualized by plotting the maximum prior altitude (MPA) over the prior 600 seconds (Figure 5.8). Horizontal planes of trajectories were initialized at altitudes of 5 km (Figure 5.8a, d g), 3 km (Figure 5.8b, e, h) and 1 km (Figure 5.8c, f, i). Regions of positive correlation between negative vertical velocity and MPA (e.g., Figure 5.8e; x= -39, y=27 km) reveal vertically continuous downdrafts, whereas negative vertical velocity with negligible MPA (e.g., Figure 5.8e; x= -36, y= 21 km) implies a porous downdraft where air is flowing through horizontally rather than

vertically. This effect can be seen when comparing MPA with vertical velocity at 3 km and 5 km at all three times in Figure 5.8. The RFD only extended up to 5-6 km altitude (Figure 5.6), thus, air at 5 km was just beginning to enter into the downdraft and, consequently, had small prior vertical displacement (Figure 5.8a, x=-44, y=27 km). In contrast, at 3 km the strongest downdraft was collocated with large MPA (c.f., Figure 5.8b, x=-44, y=27 km).

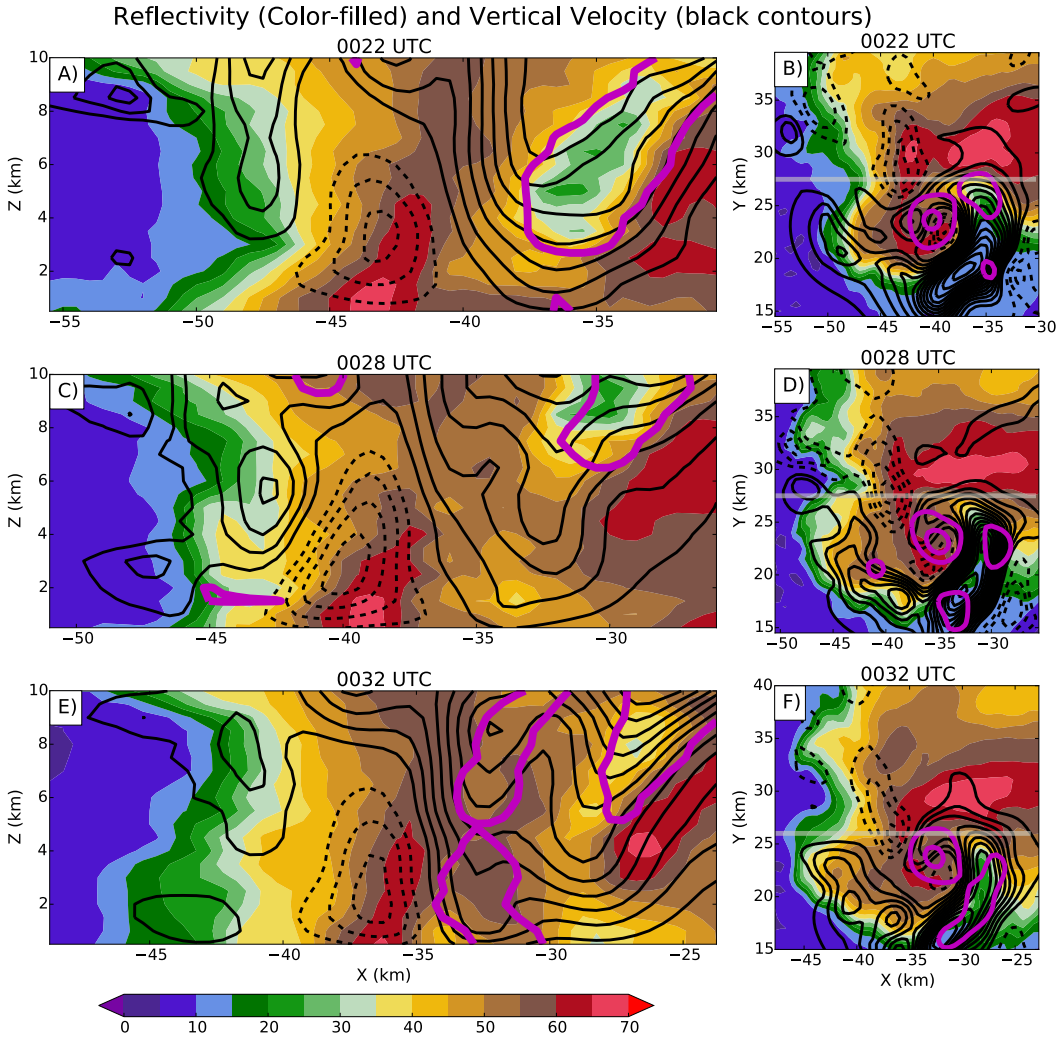

Fig. 5.6 Vertical X-Z cross-sections (a, c, e) and 3.1 km altitude horizontal cross-sections (b, d, f) of radar reflectivity (according to the color bar) and vertical velocity (contoured in black every 4 m s^{-1}, with positive [negative] values denoted by solid [dashed] lines) for three times during the first RFD surge. Vertical vorticity has been contoured in magenta for $1x10^{-2}$ and $3x10^{-2}$ s^{-1}. The grey line on the horizontal cross-sections refers to the location of the vertical cross-sections.

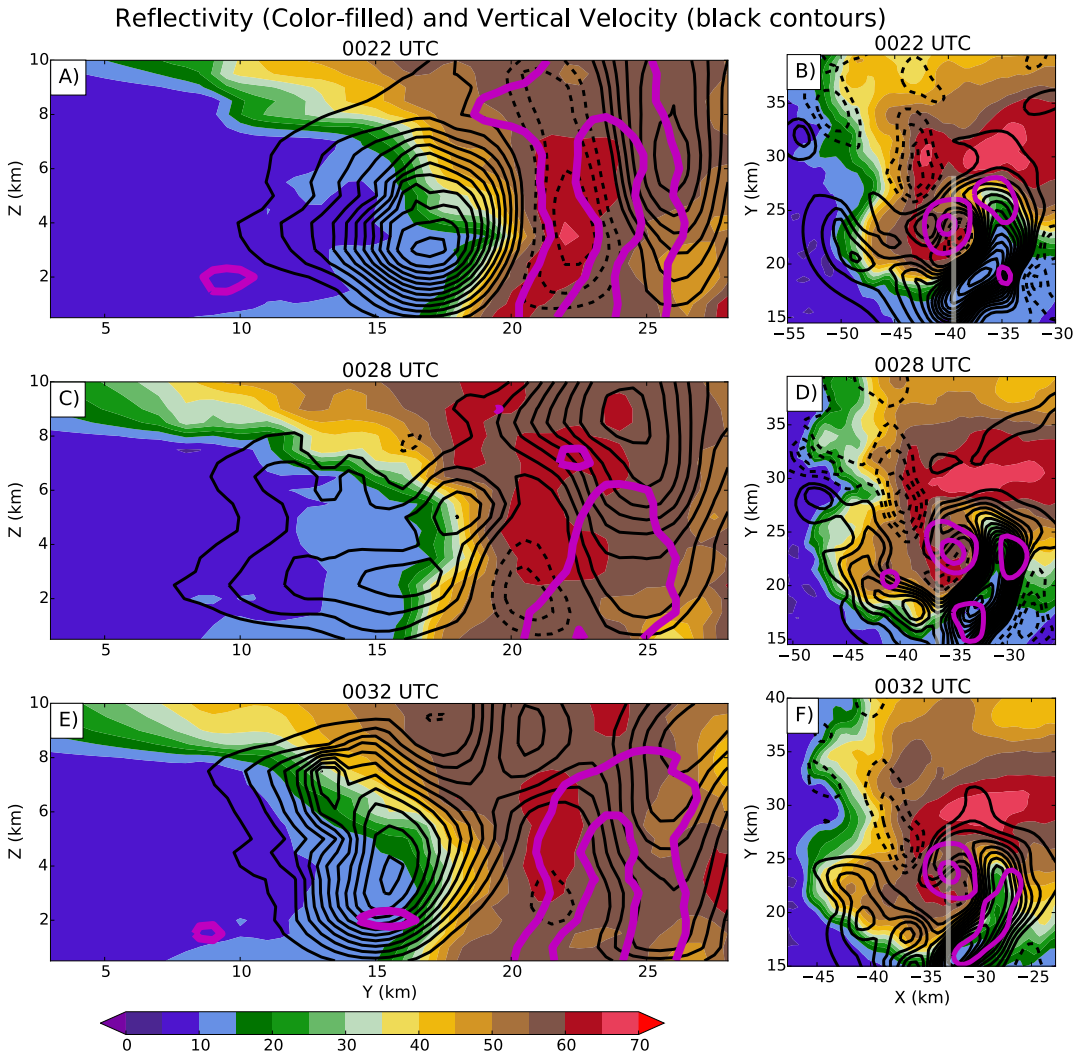

Fig. 5.7 Same as in Figure 5.6, except for a north-south cross-section through the occlusion downdraft.

At 0028 the primary midlevel RFD at 3 km altitude was comprised of only a small ribbon of descending air consistently extending north-northwestward from the mesocyclone (c. f., Figure 5.8e, x=-38 y = 25 to x=-42, y= 35 km). The downdraft was seemingly caught between cyclonically rising air from the primary updraft to the east and anti-cyclonically rising air from the western updraft. Nevertheless, at low-levels strong horizontal flow advected the descending air initially towards the southwest, significantly displacing the region with the largest vertical displacement from the center

of the downdraft (Figure 5.8f, x = -42, y = 24 km). As the downdraft intensified aloft, the low-level region containing MPA greater than 5 km expanded (Figure 5.8i) and shifted south-southwest, representing the first southward surge of the SRFGF. As the low-level outflow surged outward, it enhanced convergence underneath the western updraft, which strengthened the updraft and resulted in a significant amount of downdraft outflow entering the western region updraft. The recycling of the RFD air by the western updraft is evidenced by the majority of the western updraft at 1 km having a MPA greater than 2 km (Figure 5.8i, x = -43, y = 25 km), which contrasts the much lower MPA in the primary updraft along the leading edge of the RFGF.

Even with the merging of the vertical velocity minima associated with the RFD and occlusion downdrafts at 0028 UTC, the associated downdraft flow regimes do not appear to merge, as the regions were still separated by trajectories with negligible MPA (Figure 5.8i, x=-34, y=20 km). In general, at all three levels, the occlusion downdraft on the southern edge of the circulation was associated with much smaller MPA than the primary RFD. The trajectories associated with the occlusion downdraft were continuously advected into the center of the mesocyclone at 1 km as indicated by the 2-3 km MPA values wrapping around and reaching into the center of the circulation (c.f., Fig. 5.8f, x = -35, y = 24 km). This MPA signature bears a stronger resemblance to an axial downdraft flow structure (Davies-Jones 1986) than to a traditional divided mesocyclone structure (Lemon and Doswell 1979).

Individual trajectories were initiated (Figure 5.9) at 1 km (blue) and 3 km (green) in the vicinity of the RFD where PMA was maximized (yellow dots Figure 5.8). Initially, low-level RFD air parcels originated east of the circulation in the inflow

region, rising in the northern portion of the primary updraft before descending in the RFD (Figure 5.9a). However, the flow was more complex aloft where some trajectories rose in the primary updraft while others originated in the southern part of the western updraft.

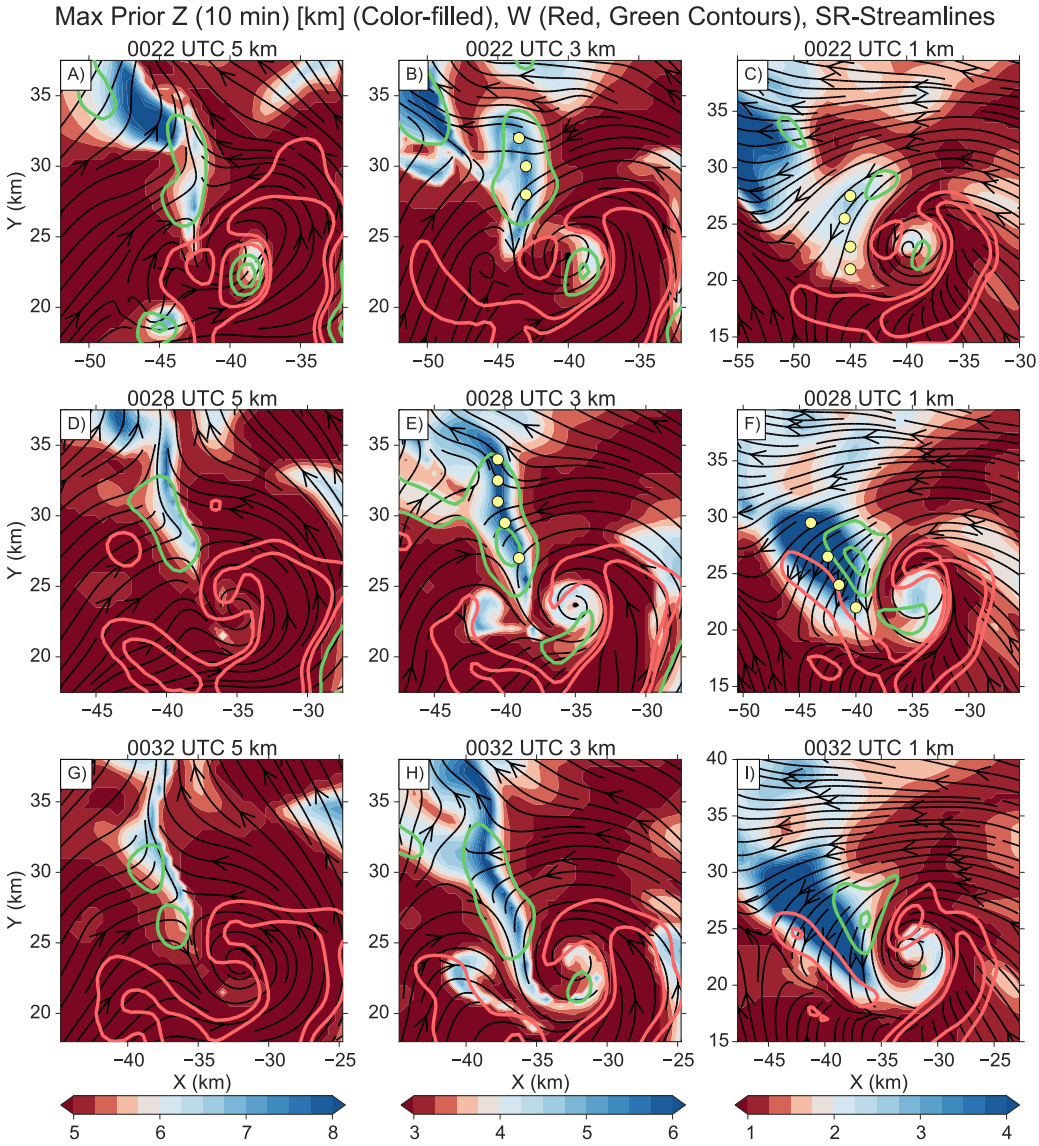

Fig. 5.8 The maximum prior altitude (in km according to the color scale) experienced by trajectories over the last 10 minutes during the period covering the first RFD surge (0020-0032 UTC). Horizontal, storm-relative streamlines are overlaid in black. Positive vertical velocity is contoured at 5, 10 (10, 20) m s^{-1} at 1 km (3 km and 5 km) in light red. Negative vertical velocity is contoured at -5, -10 (-10, -20) m s^{-1} at 1 km (3 km and 5 km) in light green. Yellow dots at 1 km and 3 km indicate the initial locations for the 3D trajectories shown Figure 5.9.

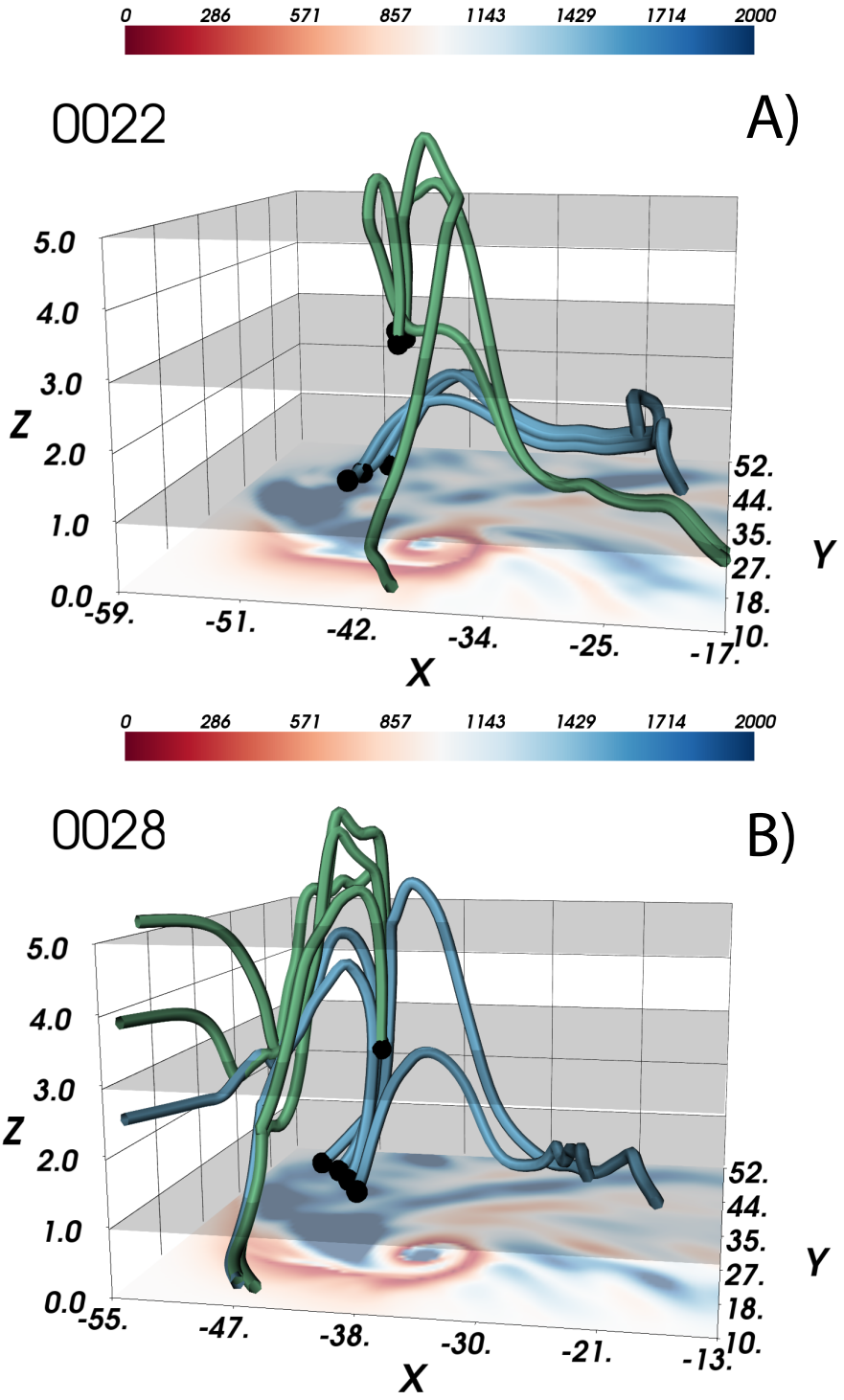

Fig. 5.9 Three-dimensional backward air parcel trajectories initialized in the RFD region at locations shown in Figure 5.8 for (a) 0022 UTC and (b) 0028 UTC. The blue (green) trajectories were initiated at one (three) km altitude. For reference, the prior altitude of 400-sec backward trajectories initialized at 1 km is displayed at the bottom of the grid. Additionally, grey horizontal planes were drawn at 1 km, 3 km, and 5 km for reference.

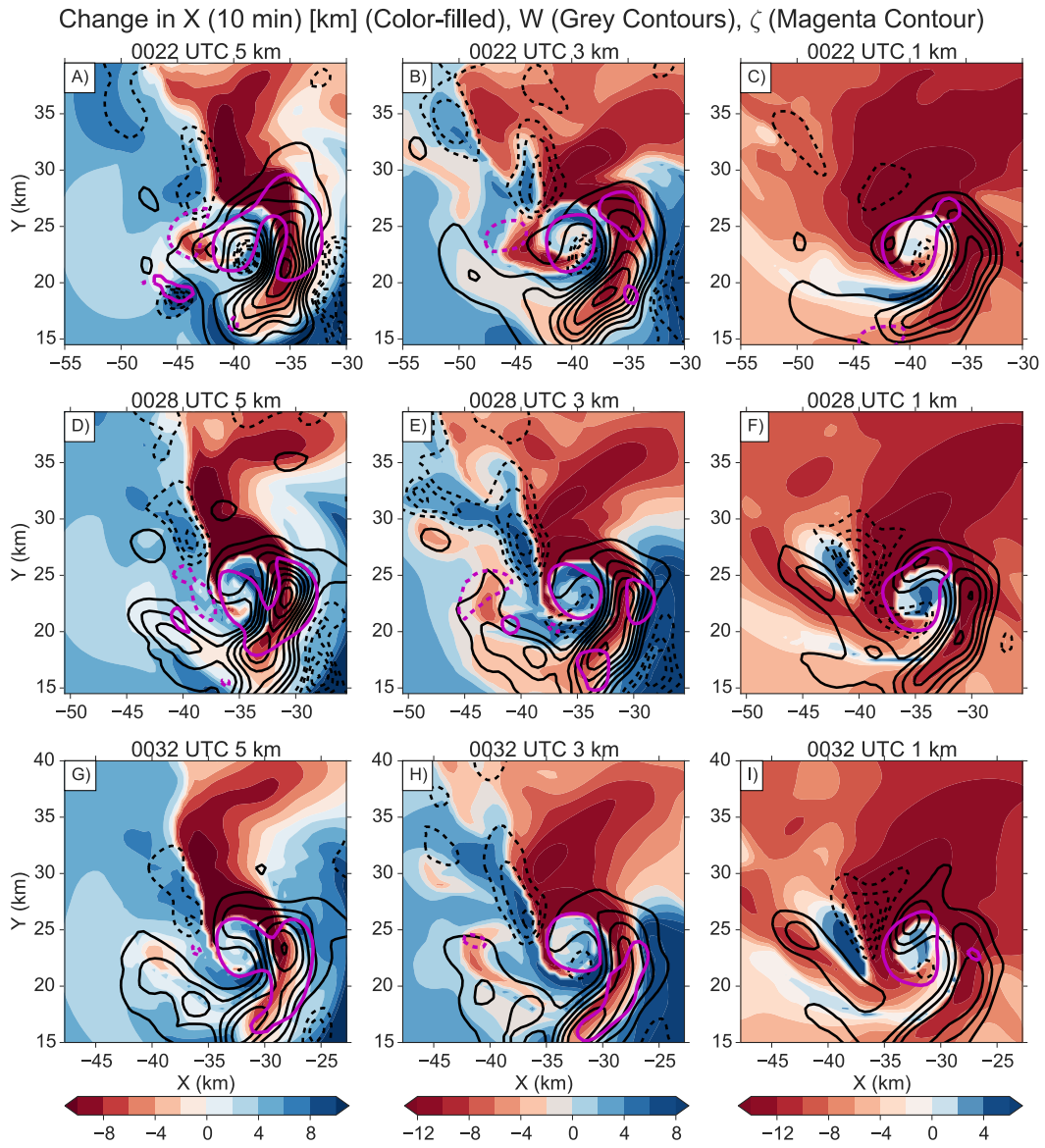

Fig. 5.10 Backward trajectory maps of the change in storm-relative east-west distance over the last 10 minutes. Horizontal trajectory maps were initialized at the altitudes indicated on the plots. The $1x10^{-2}$ s^{-1} vertical vorticity contour is overlaid is magenta and vertical velocity is contoured in black with solid (dashed) lines for positive (negative values). At 1 km (c, f, i), positive (negative) velocities are contoured every 4 (2) m s^{-1}. At 3 km and 5 km (a, b, d, e, g, h), positive (negative) velocities are contoured every 8 (4) m s^{-1}.

The downdraft flow regimes at 1 km and 3 km were clearly distinct from each at 0022 UTC. By 0028 UTC, however, the low-level flow regime better reassembled that aloft. Air parcels at the center of the low-level RFD at 1 km altitude took a nearly

identical path as those that were initiated at 3 km (Figure 5.9b). Other trajectories originated from the east but entered the downdraft above 5 km and joined with the central downdraft flow regime. The overall trajectory behavior of the downdraft flow above 5 km suggests that air from the east and west was converging aloft before descending in the downdraft.

The converging flow regimes evident both in the individual three-dimensional trajectories (Figure 5.9) and the strong midlevel gradients in MPA (Figure 5.8) can more easily be illustrated by examining storm-relative zonal displacement, change in x position, over a 10 minute period from a backward trajectory analyses (Figure 5.10). An examination of zonal displacement for trajectories initiated at 5 km (Figure 5.10a, d, g) and 3 km (Figure 5.10b, e, h) indeed reveals that in the vicinity of the midlevel downdraft (dashed contours), air parcels from the east (warm colors) and west (cool colors) were converging. Between 0022 and 0028 UTC, an enhancement of western air occurred (compare Figure 5.10b, x=-45, y=27 km; Figure 5.10e, x= -40, y=27 km), coincident with a slight westward shift in the primary RFD and the forming of a continuous convergence zone extending north-northwestward from the mesocyclone.

A vertical cross-section through the primary RFD (Figure 5.11a) further illustrates that the downdraft at this time consisted of two flow regimes with predominately western sourced air aloft and eastern sourced air at low-levels. Individual trajectories drawn on the cross-section demonstrates that even at 7 km, the western air converging into the cyclonic flow regime originated at lower levels and gained altitude through the western updraft before descending. Hence, the midlevel convergence was not comprised of true midlevel environmental air but rather consisted

of low-level air that had risen through the western updraft. The low-level source of the air feeding the RFD at middle levels likely reduced the potential for evaporational cooling in the RFD. The descending western trajectories appear at low-levels between 0022 and 0028 UTC (Figure 5.10f, x = -42, y = 25 km) demonstrating that the southward surge of the secondary RFD gust front noted in Chapter 3 was the result of vertical transport of western sourced air.

To investigate whether the primary downdraft developed underneath a high pressure stagnation zone, as was the case in SC16, the dynamic portion of the diagnostic pressure equation (5.1) from Rotunno and Klemp (1985) was calculated using the wind

$$-\nabla(c_p\bar{\rho}\bar{\theta}\pi_{d)} = \bar{\rho}\left[\left(\frac{du}{dx}\right)^2 + \left(\frac{dv}{dy}\right)^2 + \left(\frac{dw}{dz}\right)^2 - \frac{d^2 ln\bar{\rho}}{dz^2}w^2\right]$$

$$+\ 2\bar{\rho}\left[\frac{du}{dy}\frac{dv}{dx} + \frac{du}{dz}\frac{dw}{dx} + \frac{dv}{dz}\frac{dw}{dy}\right] \quad (5.1)$$

analyses and the environmental sounding (Figure 5.11c, g). In (5.1), (u, v, w) are the zonal (u), meridional (v), and vertical (w) components of velocity, respectively. c_p is the specific heat capacity at constant pressure, and the environmental sounding was used to estimate the base state potential temperature ($\bar{\theta}$) and density ($\bar{\rho}$,).

Even though the Laplacian does not directly represent the dynamic pressure field, here represented by the perturbation Exner function (π_d), maxima and minima are located in the same areas. Thus, the Laplacian field can be used to infer if the downdrafts were located within a region conducive to dynamic forcing, even though dynamic pressure and its vertical gradients cannot be calculated along trajectories.

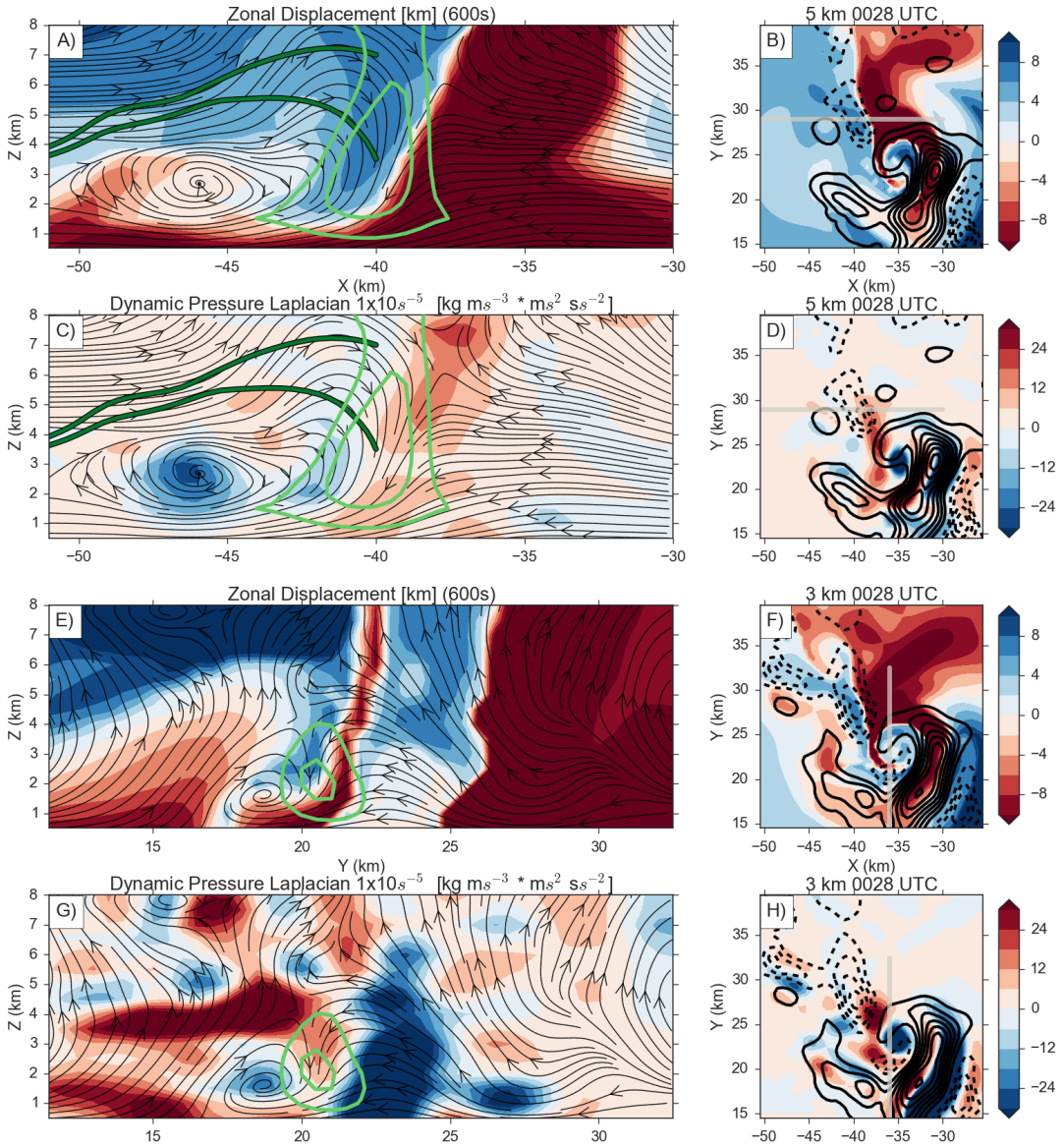

Fig. 5.11 Panels (a, b and e, f) show vertical and horizontal cross-sections of the zonal displacement from 600 s backward trajectories with storm-relative streamlines in black and downward vertical motion contoured at -2 and -4 m s^{-1} in solid green for 0028 UTC. Panels (c, d and g, h) show vertical and horizontal cross-sections of the dynamic pressure Laplacian at 0028 UTC with storm-relative streamlines in black and downward vertical motion contoured at -2 and -4 m s^{-1} in solid green.

Not surprisingly, a maximum in the dynamic pressure Laplacian was found between 5 and 8 km, upstream of the downdraft (Figure 5.11c, x=-38), supporting the idea that the primary RFD at midlevels was being forced in a similar way as the warm

RFD surge in SC16. Additionally, the occlusion downdraft (Figure 5.11e, y=21), which straddled a narrower mid-to-low level convergent zone between eastward and westward moving air, was associated with a region of dynamic pressure Laplacian that increased rapidly with height from low-to-mid levels. This structure is consistent with the previously noted strong vertical gradient in vertical vorticity and, as found in previous studies (Klemp and Rotunno 1983; Wakimoto and Lui 1998), suggest the occlusion downdraft was dynamically forced.

5.5.2 2nd RFD Surge (0045-0058 UTC)

Following the first RFD surge, the RFD shrank in peak area (Figure 5.3a), before slowly increasing in size again after 0042 UTC. Rapid expansion of the storm-scale RFD occurred after 0045 UTC and was coincident with the waning of the western updraft (Figure 5.5). The midlevel primary RFD did not significantly change between 0032 (Figure 5.6f) and 0042 UTC (Figure 5.12b), as it was still found extending toward the northwest, away from the mesocyclone, in a narrow ribbon. However, by 0048 UTC, the primary RFD appeared to separate into two distinct downdrafts (Figure 5.12d, x=-30, y = 37 and x=-26, y = 26) as the southern half of the RFD shifted southward and expanded horizontally. Similar to the first RFD surge, the portion of the downdraft close to the circulation was only 5-6 km deep (Fig. 5.12a, c, e) and straddled by updraft on both sides. Reflectivity descended from midlevels with time on the western side of the circulation (Figure 5.12a, x=-34, z=6; Figure 5.12c, x=-30, z=4; Figure 5.12e, x=-27, z=1) producing a horizontally expanding reflectivity region at low-levels between 0042-0052 UTC on the western side of the hook echo (Figure 5.12b, d, f). The western

side of the low-level downdraft also expanded with time, in association with this descending reflectivity core.

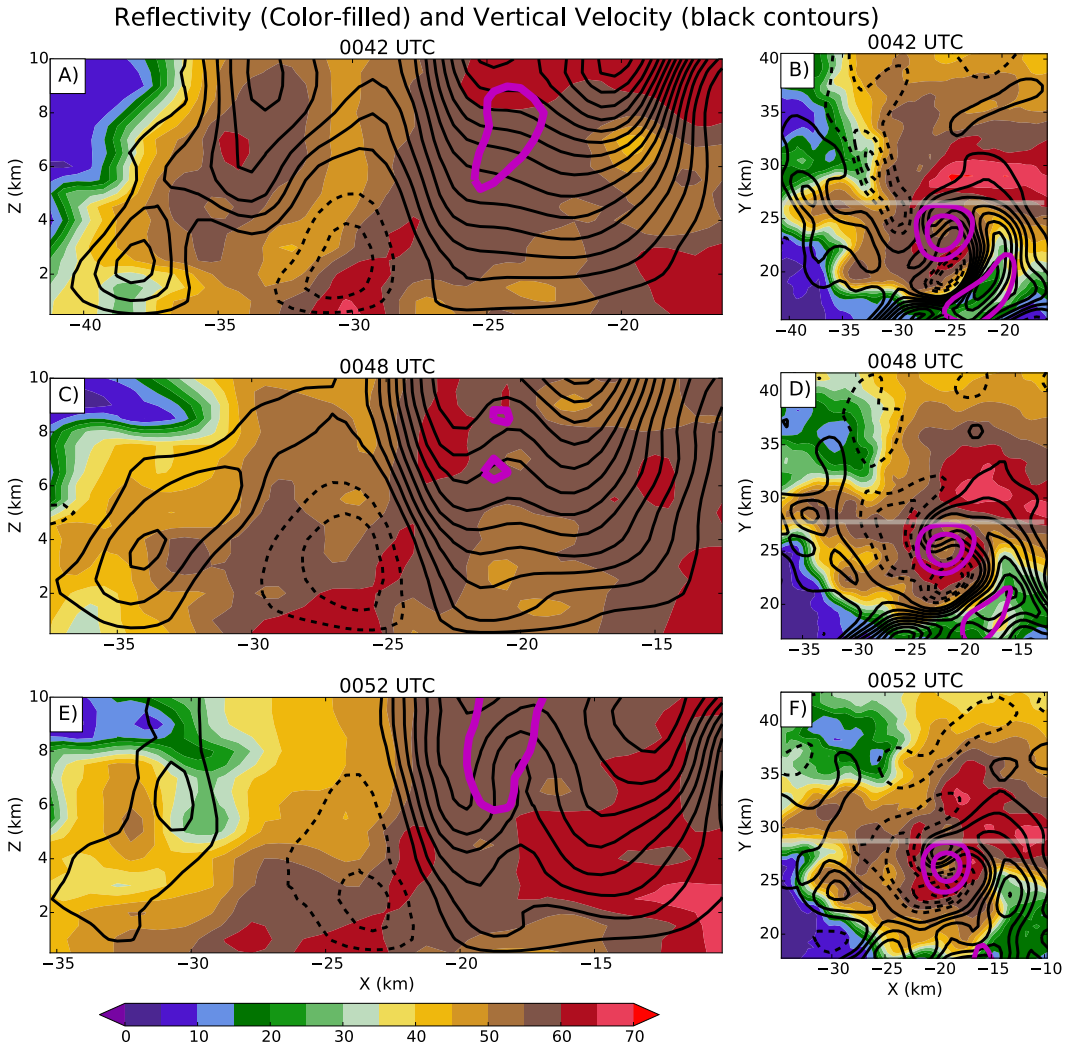

Fig. 5.12 Same as Figure 5.6 but for the second RFD surge.

Unlike the first RFD surge, the second one was characterized by an occlusion downdraft (Figure 5.13b, x=-25, y = 19) that was stronger and deeper with height than the primary RFD (compare Figure 5.13a, c, e with Figure 5.12a, c, e). Moreover, the relationship between the mesocyclone and the occlusion downdraft changed. Earlier, the mesocyclone exhibited a two-cell structure (Figure 5.7c, f, i) with air parcels consistently descending near the center of the circulation. At 0042, the mesocyclone

transitioned to a single-celled structure with rising trajectories at the center and the occlusion downdraft displaced to the south (Figure 5.13a,b). The vertical motion in the mesocyclone increased with altitude, leading to rapid intensification by stretching in what Chapter 3 referred to as an occlusion updraft. After the intensification, the mesocyclone developed a two-cell divided structure once again (Figure 5.13e).

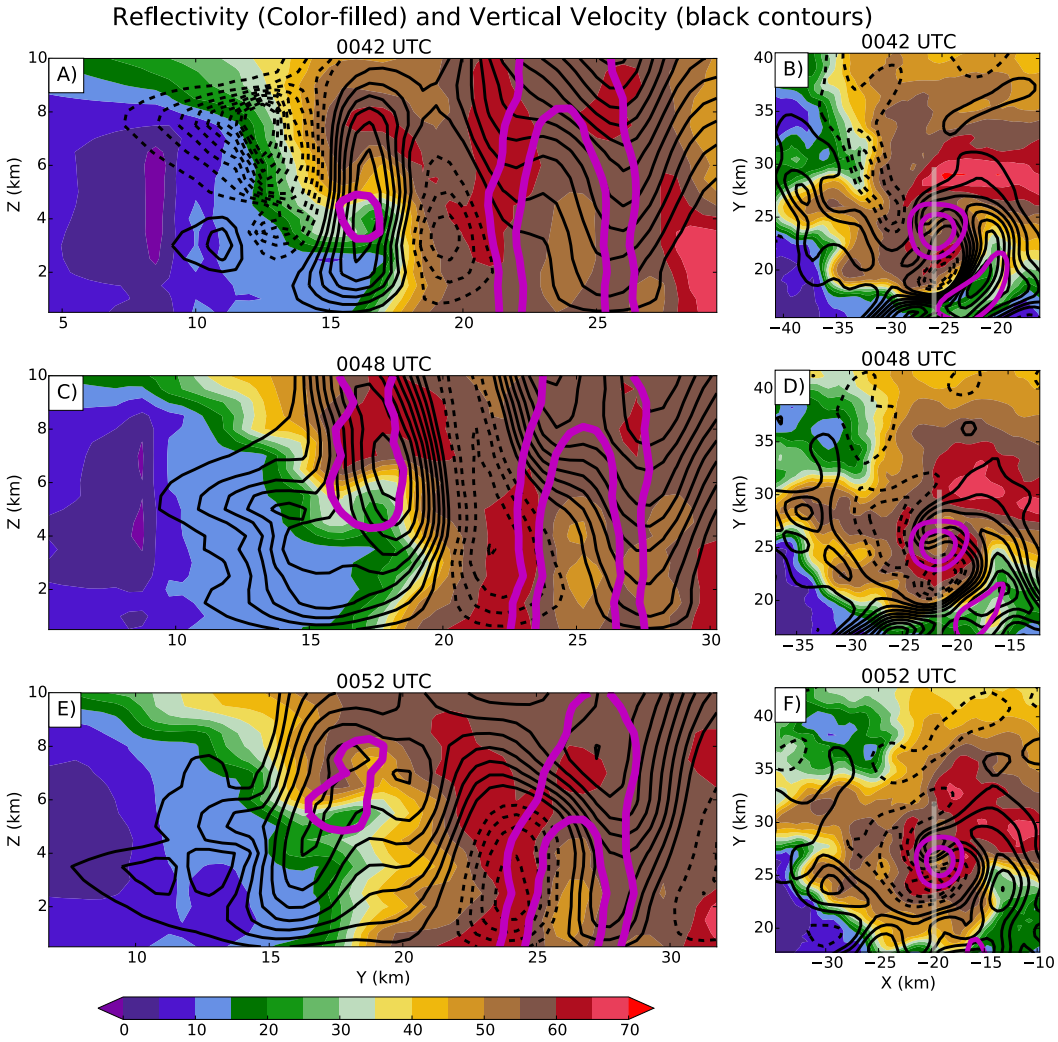

Fig. 5.13 Same as Figure 5.7 except for the second RFD surge.

At mid levels, the air within the occlusion downdraft between 0042 and 0048 UTC consisted of air that had been at significantly higher altitudes just ten minutes prior (Figure 5.14 a, b, d, e), implying a more continuous downdraft flow regime than at

earlier times. Additionally, the air within the occlusion downdraft at mid levels experienced greater eastward zonal displacement (Figure 5.15 a, b, d, e) than during the first RFD surge (Figure 5.11). In contrast, the primary RFD mainly straddled the converging eastern and western flow regimes, especially at 3 km altitude before 0052 UTC.

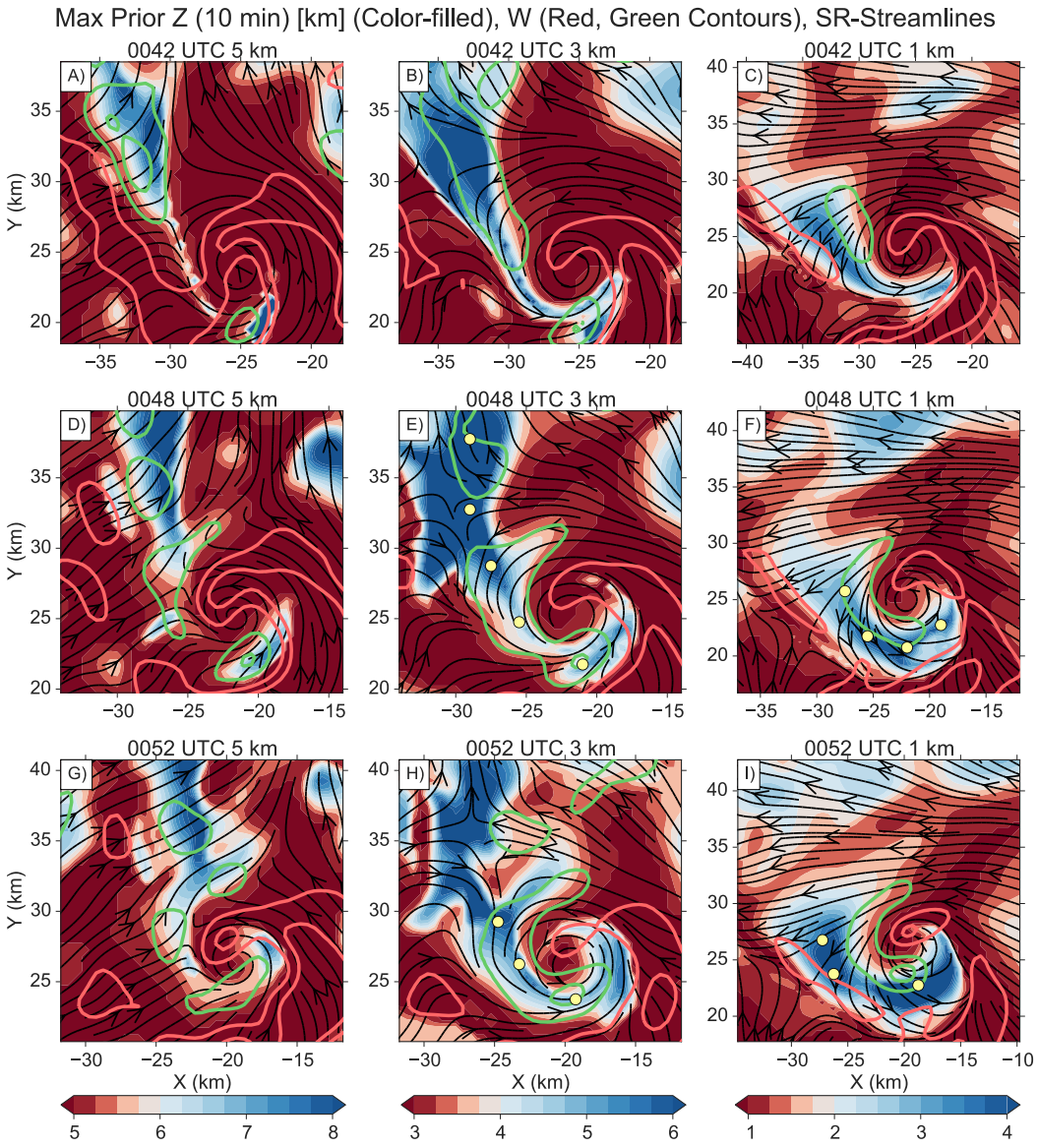

Fig. 5.14 The same as Figure 5.8 except for the period before and during the second RFD surge (0045-0058 UTC).

Between 0048 and 0052 UTC, the outflow from the primary RFD and the occlusion downdraft merged to produce a broad area of high MPA at 1 km (Figure 5.14 f, i). Unlike the previous RFD surge, the second surge was able to transport air that had previously been at midlevels downward and away from the circulation towards the south and southeast of the mesocyclone. This eastward push of combined outflow (Figure 5.15 f, i) helped to accelerate the RGFG and led to the occlusion stage of the mesocyclone reported in Chapter 3.

The northern portion of the primary RFD at midlevels (Figure 5.14a, x=-33, y= 32) weakened with time and was characterized by a horizontal expansion of the region of descending air where it had been much more narrow in previous analyses (compare with Figure 5.8g). Additionally, the confluent zone at 5 km shifted about 8 km eastward, such that it went from extending northwest from the mesocyclone to extending north of the mesocyclone (Figure 5.14a, d, g). The eastward shift was coincident with a veering of the winds in the region north of the mesocyclone at 5km (Figure 5.14a, x=-25, y= 32, d x=-22, y = 32) suggesting that the storm-scale cyclonic flow associated with the midlevel mesocyclone had weakened, disrupting the previous balance along the convergent zone and allowing the westerly momentum to progress further into the storm (Figure 5.15).

The RFD downdraft at 3 km shifted eastward with the convergent zone at 5 km, even though convergence at 3 km remained maximized further west (Figure 5.15h, x = -25, y = 30). This relationship persisted throughout the occlusion stage of the main mesocyclone as the midlevel convergence zone continued shifting east (Figure 5.16a, x = -10, y = 35; 5.16g, x = -4, y = 36) past the occluding low-level mesocyclone.

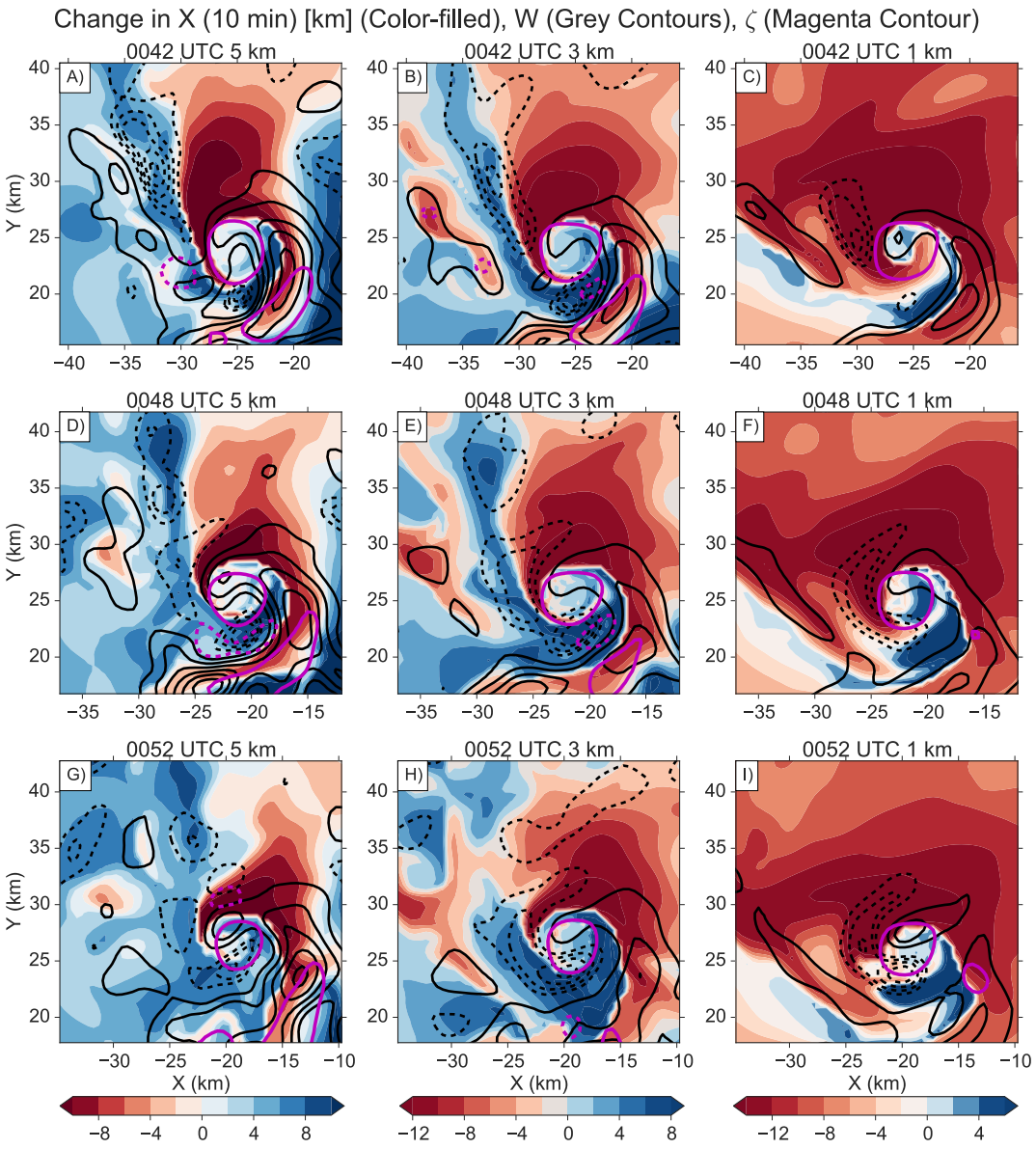

Fig. 5.15 Same as Figure 5.10, except for the period just before and during the second RFD surge.

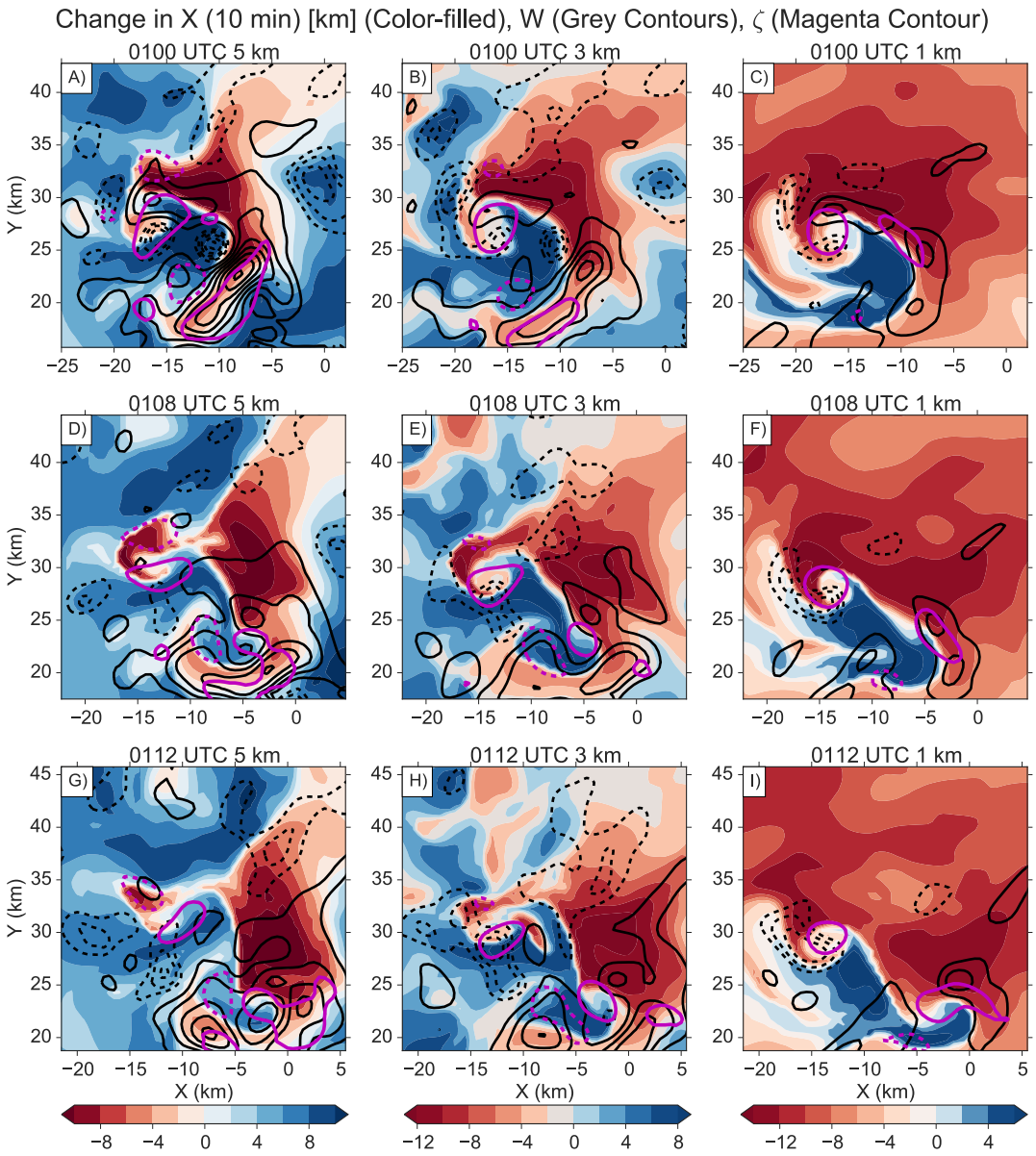

Fig. 5.16 Same as Figure 5.10, except for during the occlusion stage of the main mesocyclone.

Individual backward trajectories initiated at 1 and 3 km altitude within the high MPA regions associated with the primary and occlusion downdrafts (Figure 5.17) exposed a more complex flow during the second downdraft surge. The eastern and western flow regimes discussed earlier are still evident in the trajectories. But by 0052 (Figure 5.17b) an increasing number of trajectories passed through the storm and

entered the western updraft prior to participating in the downdrafts. Moreover, the trajectories that had descended from substantial altitudes, which had previously been directed towards the center of the vortex, were now being directed towards the outer core of the mesocyclone. This circuitous route was most notable for the occlusion downdraft. Adding additional complexity, some of the air that was drawn into the western updraft before entering the RFD at 0052 UTC had actually been affected by the previous low-level RFD surge that occurred 10-15 minutes earlier. The subsidence associated with the previous RFD surge is reflected in the downward path the trajectories took before rising into the western updraft. No doubt that the recycling of air from the downdrafts diminished the buoyancy of the western updraft. Likewise, the negative thermal buoyancy in the RFD and occlusion downdrafts was likely minimized since much of the air originated at low levels in the environment ahead of the storm.

The overturning horizontal circulation can be seen in cross-sections through the southern primary RFD at 5 km (Figure 5.18a, b), which shows that the recycling flow regime was substantially deeper than during the first surge (Figure 5.11). Additionally, western updraft air was converging with mesocyclone air above the downdraft, with an accompanying maximum in the dynamic pressure Laplacian (Figure 5.18c, x=-22, z=5). Interestingly, as denoted by the trajectories in Figure 5.18, air in the high dynamic pressure region above 5 km apparently originated in the environment around 7 km and not the western updraft, unlike the first RFD surge. The impingement of potentially dry environmental air aloft is consistent with a substantial decrease in reflectivity with time above 8 km west of the downdraft (Figure 5.12a, c, e).

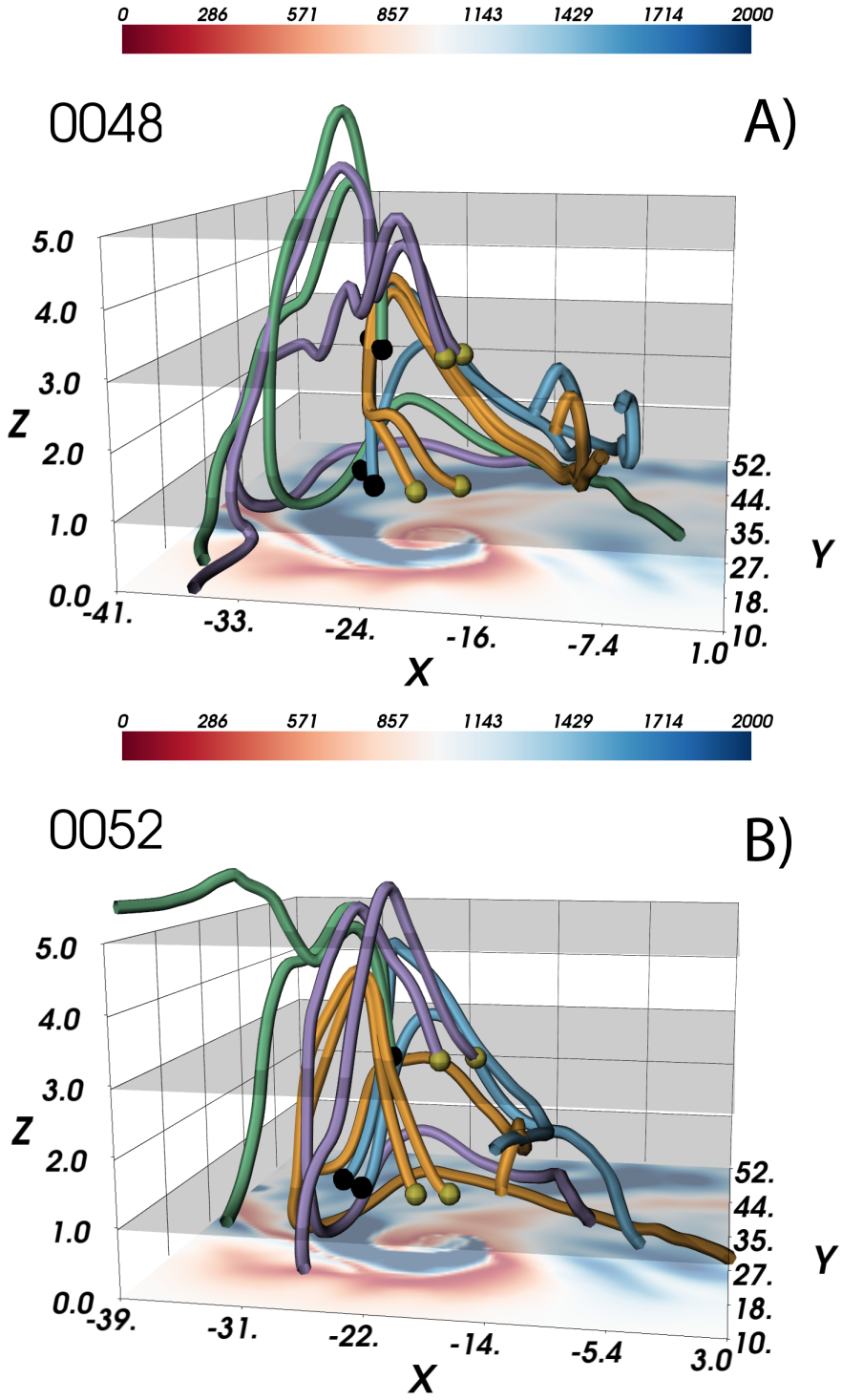

Fig. 5.17 Similar to Figure 5.9 except for the second RFD surge. Occlusion downdraft trajectories have yellow initiation points, with orange (purple) trajectories being initiated at one (three) km altitude.

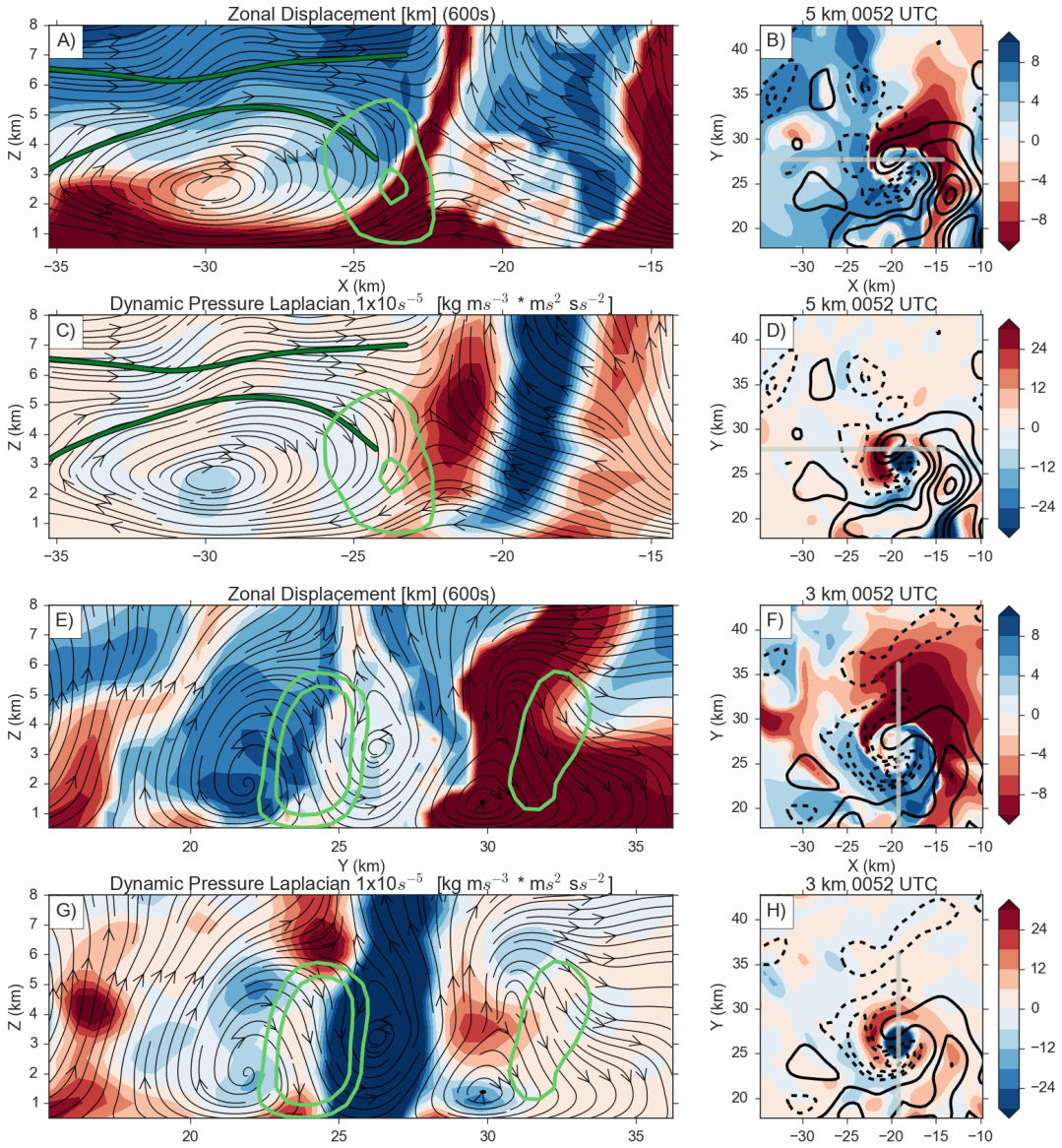

Fig. 5.18 Same as Figure 5.11, except for during the second RFD surge.

The north-south vertical cross-section taken through the occlusion downdraft at 3 km (Figure 5.18c) illustrates the dichotomy in zonal displace for the southern and northern portions of the downdraft. The southern portion was displaced several km eastward while the northern portion barely changed zonal position. Moreover, the southern portion was directly beneath a maximum in the dynamic pressure Laplacian

found above 5 km altitude while the northern portion appeared to be more embedded in a low pressure perturbation associated with the mesocyclone (Figure 5.18d).

Despite the upper-level portion of the occlusion downdraft being dynamically driven, the dominant source region for the low-level occlusion downdraft at 0052 UTC was storm-modified air parcels that had passed through the western updraft (Figure 5.17b). At low-levels, a region of western sourced air (Figure 5.15f, x = -20, y = 21; Figure 5.15i, x=-20, y = 22) can be seen effectively cutting off eastern sourced air from wrapping completely around the low-level mesocyclone. Subsequent trajectory maps of zonal displacement (Figure 5.16c, f, i) and individual trajectories (not shown) demonstrate that the western updraft remained the dominant source for the occlusion downdraft outflow throughout the occlusion stage and was the main source of air that pushed the primary RFD gust front southeastward. It is thus hypothesized that the mesocyclone occlusion process was initiated by the low-level merging of primary RFD and occlusion downdraft air between 0045 and 0048 UTC but advanced by the arrival of western updraft air at low-levels on the south side of the mesocyclone.

5.6. Downdraft Forcing Inferences

In the absence of thermodynamic observations and robust pressure retrievals, potential forcing mechanisms of downward acceleration have to be inferred using trajectory behavior. Bulk trajectory quantities, such as source altitude and future altitude, should exhibit distinctive behavior in downdrafts with different dominant forcing mechanisms, especially in downdrafts driven by dynamic pressure gradients. Additionally, the contribution by precipitation drag can be qualitatively estimated. Although different forcing mechanisms can be present simultaneously, dividing the

different downdrafts by region and flow region greatly aids in identifying downdrafts that have distinctly different forcing mechanisms. For example, trajectories in the occlusion downdraft should behave substantially different than trajectories originating in the rainy downdraft.

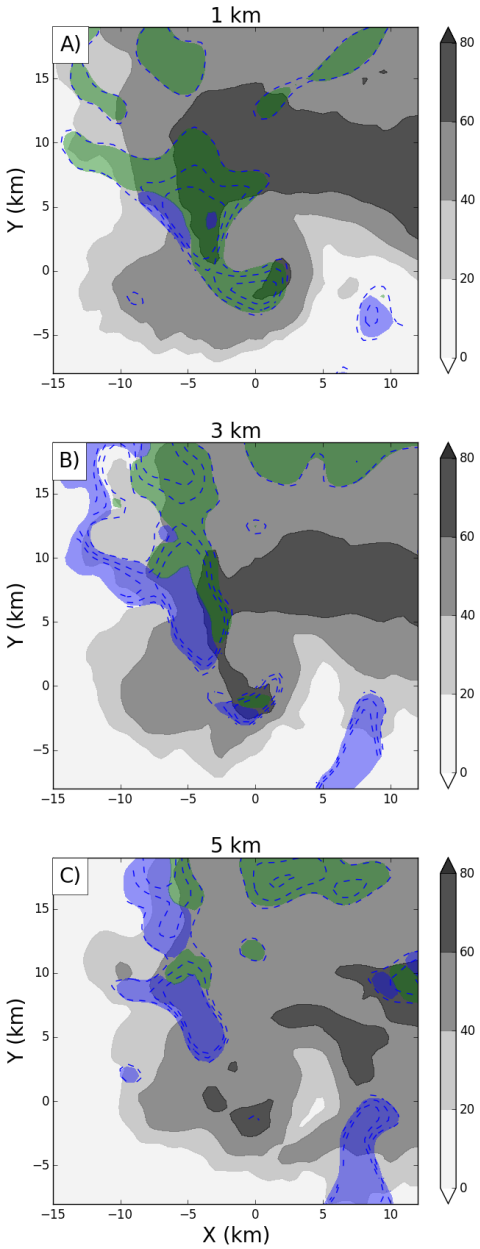

Fig. 5.19 Reflectivity color-filled in grey at 0028 UTC with eastern sourced downdraft regions shaded in green and western sourced regions shaded in blue at (a) 1km, (b) 3 km, (c) 5 km. Negative values of vertical velocity are contoured in dashed blue every 2 m s^{-1}.

As has been demonstrated through individual trajectories (Figures 5.9, 5.17) and trajectory maps of zonal displacement (Figures 5.10, 5.15), the RFD can be divide into two separate flow regimes, air that arrived from the east after passing through large-scale cyclonic flow around the north side of the circulation, and air parcels arriving from the west after passing through the western updraft. To further investigate how the behavior and history of the two flow regimes differed, trajectories were traced back to their highest prior altitude and if the location was in the primary updraft or on the eastern side of the circulation, the trajectory was classified as an eastern sourced trajectory. Similarly, if the trajectory's max altitude was found to be on the western side of the storm, the trajectory was classified as a western sourced trajectory. An example of the downdraft trajectory classification is given in Figure 5.19, where eastern sourced downdraft trajectories are colored in green and western sourced trajectories in blue. Furthermore, the classification scheme allows the RFD composition to be interrogated with time and height (Figure 5.20), revealing behavioral trends that would otherwise be difficult to infer.

As the individual trajectories (Figure 5.9 and Figure 5.17) generally suggested, the primary RFD was made up of an increasing amount of western sourced air with height (Figure 5.19; 21a, b). Indeed, below 1.5 km altitude, most of the RFD was comprised of air that had originated east of the mesocyclone. Downdraft flow rates (Figure 5.20c,d) in the distinct flow regimes correlated strongly with changes in the source region area. Interestingly, the downdraft mass flow rates of the two source regions were not maximized simultaneously, implying that different forcing mechanisms may have been responsible for the downward motion in the two source

regions. Additionally, the differential timing between the downdraft source region mass flow rate maxima changed between the two RFD surges.

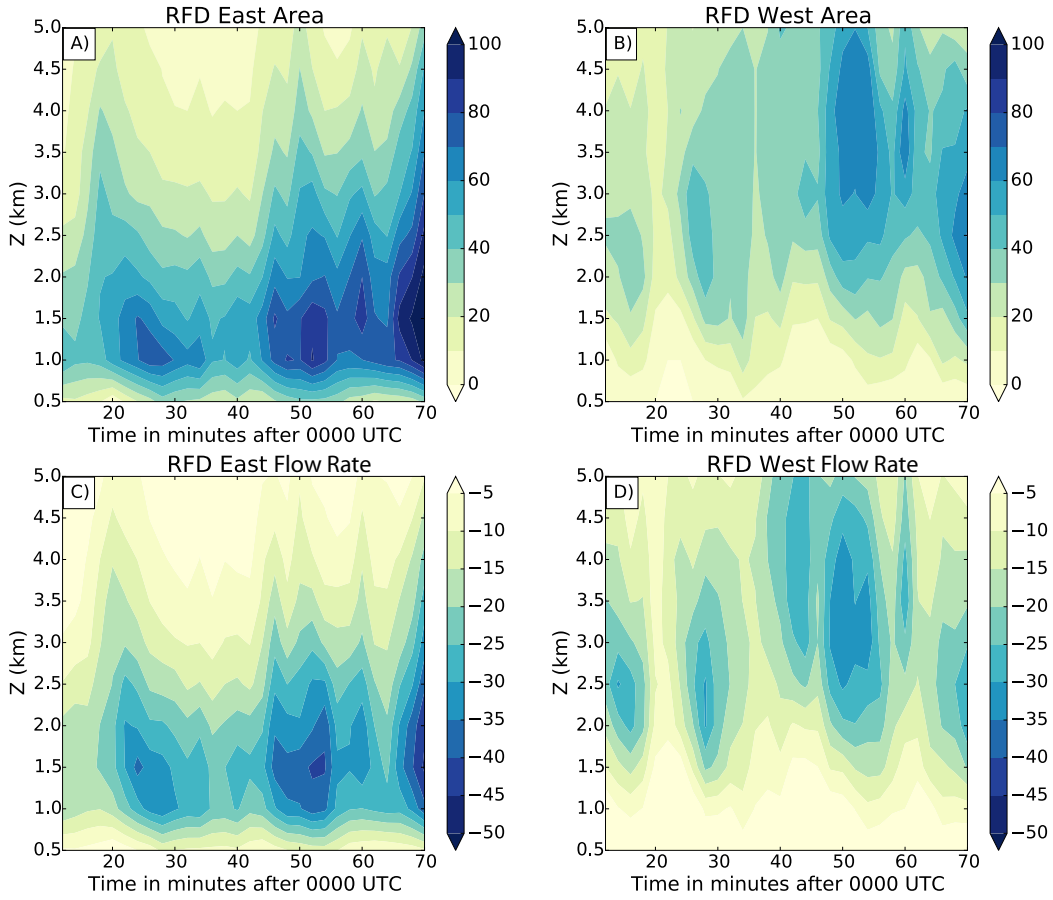

Fig. 5.20 Downdraft area (km^2) in time and height (upper panels) classified by eastern (a) and western (b) source regions. Total downdraft mass flow rate ($1x10^7$ $kg\ s^{-1}$, lower panels) classified by eastern (c) and western (d) source regions.

During the first RFD surge (0022-0032), the eastern sourced total mass flow rate (Figure 5.20c) can be seen strengthening before the western sourced RFD mass flow rate maxima observed at higher altitudes (Figure 5.20d). Conversely, the western and eastern sourced downdraft mass flow rates grew almost simultaneously during the second RFD surge (0045-0058 UTC). Therefore, it appears that the mechanism driving the downward acceleration of the eastern sourced trajectories was primarily responsible for the first near surface RFD surge. Meanwhile, the forcing mechanism(s) responsible

for the second near surface RFD surge appeared to generate a much deeper tropospheric response.

5.5.1 Trajectory Behavior Inferences

1) Source region altitude

To understand the potential impacts of the thermodynamic environmental profile on the composition of the individual downdrafts, time-height plots of *median* source altitude for each downdraft were generated by initializing backward trajectories every two minutes in time and 500 m in height (Figure 5.21). The backward trajectories were integrated for up to 3000 seconds.

Within the overall RFD, the median source altitude for downdraft trajectories in the lowest 5 km was below the stable layer in the environmental soundings (Z <1.5 km) until after 0100 UTC. During the first RFD surge (0022-0032 UTC), the air parcels were estimated to have originated within the moist boundary layer (< 1500m) (Figure 5.21a). During the second RFD surge (0045-0058 UTC) most of the downdraft below 5 km consisted of air that came from a shallow layer just above the region of stability.

If the RFD is separated into the previously found eastern and western flow regimes (Figure 5.21e, f), then it can be seen that air parcels originating from the west also originated at higher altitudes in the environment than those from the east. This is especially evident during the first RFD surge, when air parcels from the east originated around 1000 m or below, while those from the west originated above 1500 m. However, in the time between the two RFD surges, 0032 to 0042 UTC, air parcels from both sides originated from around 1500 m. The source altitude of the overall RFD

decreased with time during the second RFD surge, mostly the consequence of western air parcels decreasing in source altitude with time.

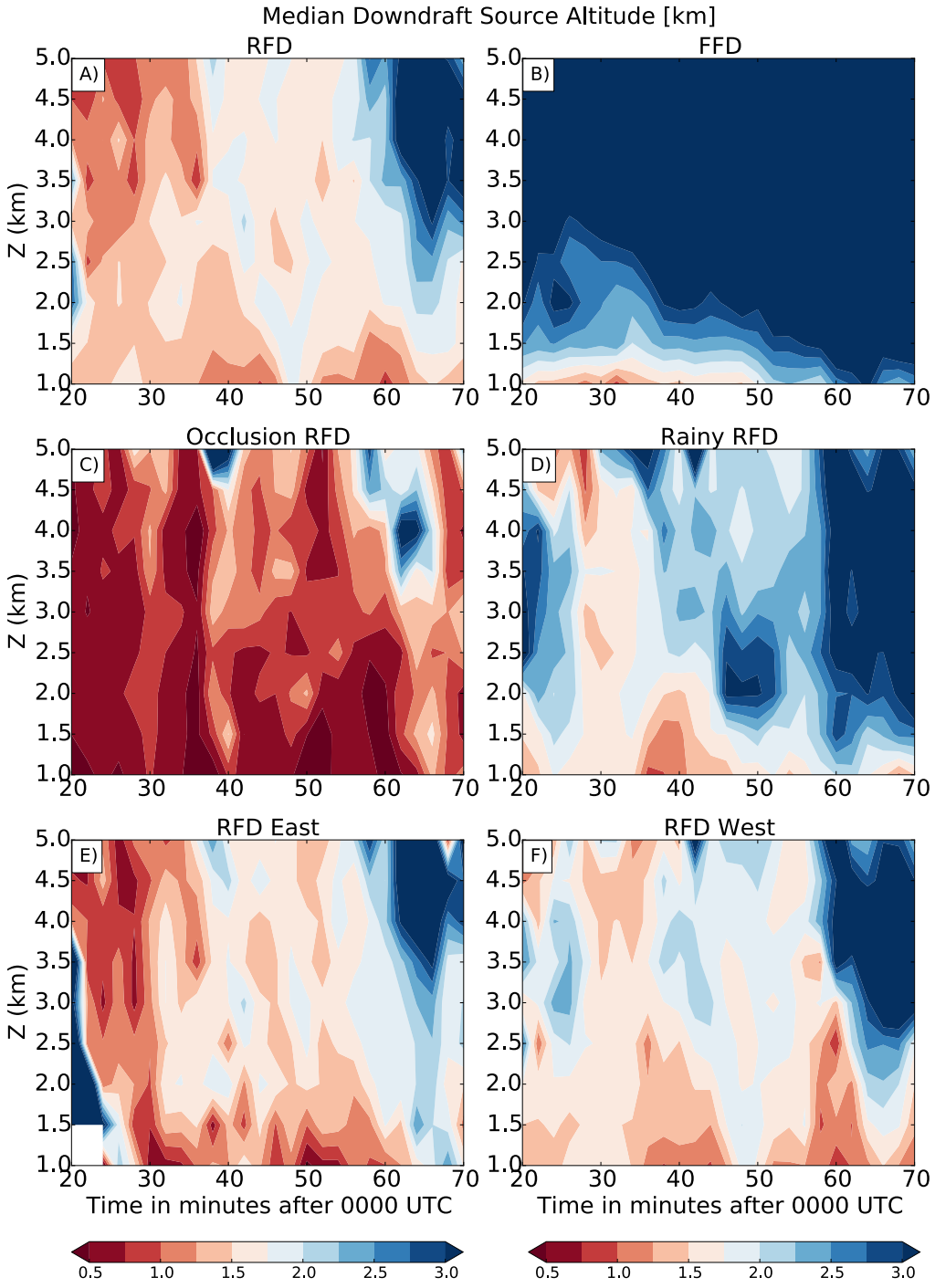

Fig. 5.21 Source altitude (km) in the overall RFD (a), FFD (b), occlusion downdraft part of the RFD (c), rainy downdraft part of the RFD (d), eastern sourced RFD (e), and western sourced RFD (f). Times are minutes after 0000 UTC.

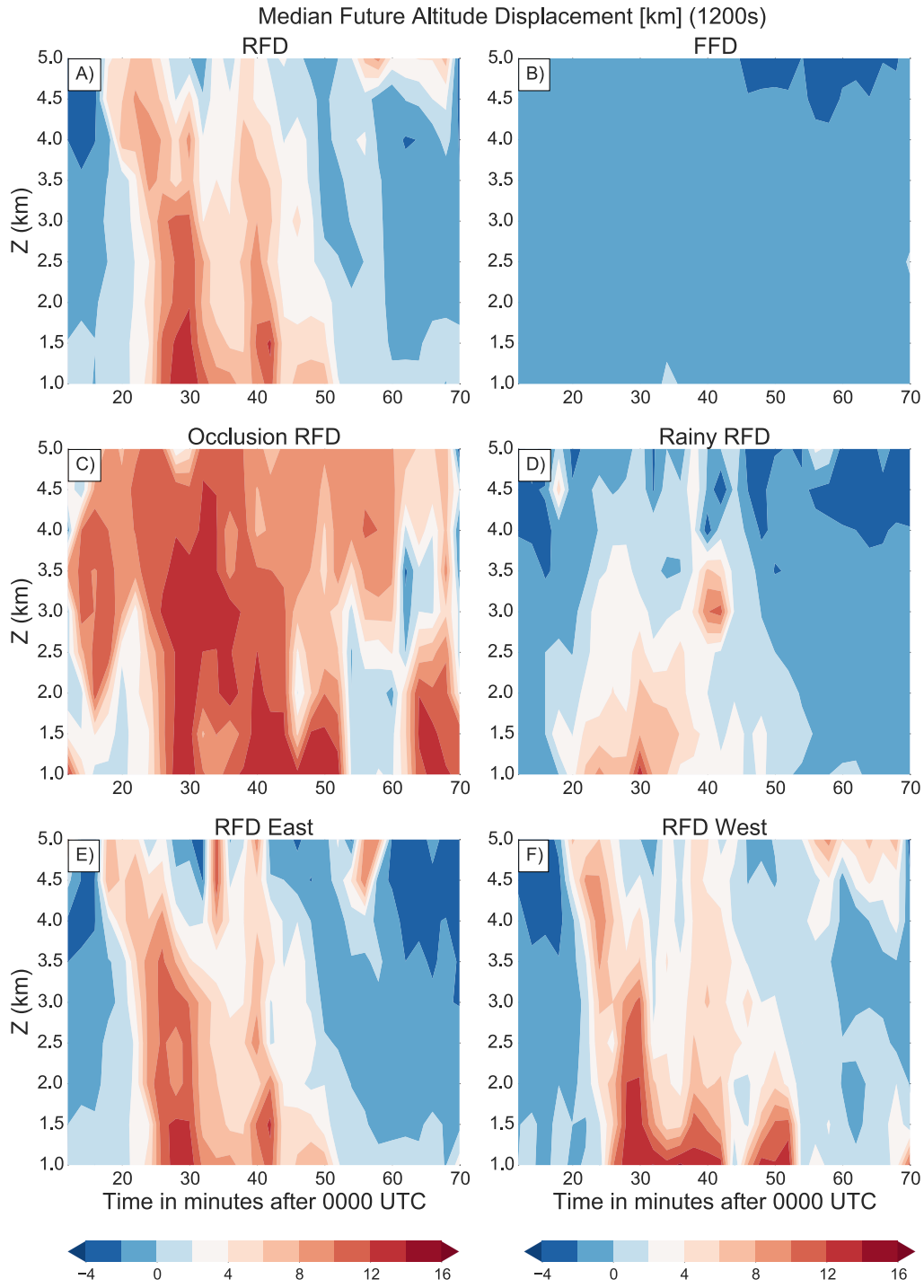

Fig. 5.22 Future altitude displacement (km) after 1200 s in the overall RFD (a), FFD (b), occlusion downdraft portion of the RFD (c), rainy downdraft portion of the RFD (d), eastern sourced RFD (e), and western sourced RFD (f). Times are minutes after 0000 UTC.

In contrast to the variability of source region air in the RFD, air parcels initialized in the occlusion downdraft consistently originated below 1 km (Figure 5.21c), even those initialized at midlevels. While source altitude in the overall RFD region downdrafts generally increased with height, within the occlusion downdraft the increase was minimal, suggesting that air near the ground was consistently being transported upward in the primary updraft before forced downward throughout the depth of the occlusion downdraft.

Meanwhile, the opposite structure was observed within the FFD (Figure 5.21b), where source altitude decreased with height, implying that air parcels experienced minimal time in an updraft and generally descended as they entered the forward flank of the storm from the environment. As the forward flank downdraft grew stronger during the occlusion stage, the source altitude at 1 km rose above 2.5 km, implying that air above the stable layer was descending to low-levels.

Finally, the rainy RFD (Figure 5.21d) was generally composed of air parcels originating from above the stable layer, except at altitudes below 1.5 km, implying that while the midlevel downdraft originated in a drier environment and experienced significant evaporational cooling, those air parcels had difficulty descending below the stable layer.

2) Future altitude displacement

One method to infer initial buoyancy is by assessing the future altitude of the parcel, as noted by Marquis et al. (2008). Trajectories with large, positive net altitude displacements over long periods (20 minutes) can be associated with initial positive buoyancy or strong future dynamic pressure driven updrafts. Surprisingly, the median

future altitude displacement of trajectories initiated within the overall RFD region (Figure 5.22a) was maximized during the first RFD surge (0028 UTC), reaching as high as 10 km. This behavior is consistent with the RFD air being ingested into the western updraft region during the mature stage of the mesocyclone, as noted in Chapter 3. In contrast, the future altitude displacement of RFD air during the second RFD surge decreased with time to near zero, consistent with the demise of the western updraft and the onset of the occlusion stage of the mesocyclone described in Chapter 3. Unlike source altitude, separating the downdraft into eastern (Figure 5.22b) and western (Figure 5.22c) flow regimes did not yield substantially different future trajectory behavior, meaning that air from both flow regimes had similar vertical displacements in the future.

Air parcels in the rainy downdraft (Figure 5.22d) were also recycled in the western updraft but only gained about half as much altitude in the future as the non-rainy portion of the RFD. Hence, it is likely that these air parcels were less buoyant on average than the non-rainy RFD air.

Amazingly, air parcels in the occlusion downdraft (Figure 5.22e) consistently attained future altitudes of 8-12 km, consistent with the near-ground source altitude (Figure 5.21e). Some of the occlusion downdraft air may have been ingested into the western updraft. But it is likely that the greatest percentage of the air from this downdraft was reingested into the primary updraft. Meanwhile air parcels initialized in the FFD (Figure 5.21f) experienced weak negative displacement, decreasing towards the surface, consistent with a weak FFD around and below the stable layer.

The general consensus between temporal trends in the prior and future trajectory behavior supports the idea that the RFD became less buoyant with time and was consistent drawn into the western or primary updrafts. Moreover, the consensus also suggests that the FFD was substantially colder than the RFD and yet not cold enough to descend below the stable layer, even as it passed through the heaviest precipitation core. Finally, trajectory behavior within the occlusion downdraft is consistent with a dynamically forced downdraft acting on buoyant air proceeding out of the main updraft.

5.5.2 Precipitation Loading Estimates

Unlike buoyancy due to temperature and water vapor, the condensate portion of the buoyancy term can be generally estimated through the reflectivity field. The downward acceleration of air due to precipitation loading (5.2) was estimated using the approximation of Hane and Ray (1985) (5.3) and used by Shabbott and Markowski (2006). In (5.2) and (5.3), r_h is the hydrometeor mixing ratio, ρ is the density of air, $\theta_{\rho 0}$ is the ambient density potential temperature, w_{pl} is the vertical motion associated with precipitation loading, and Ref is radar reflectivity.

$$\frac{dw_{pl}}{dt} = g\left[-\frac{\theta}{\overline{\theta_{\rho 0}}}\, r_h\right] \approx -g\, r_h \quad (5.2)$$

$$r_h = \frac{1}{\rho}\left(\frac{10^{0.1*Ref}}{1.73x10^4}\right)^{4/7} \quad (5.3)$$

This method omits frozen particles above the melting layer (~4.5 km) and the presence of mixed phases below the melting layer, leading to anomalously high values in regions with wet hail. Nevertheless, distinctive patterns are seen after integrating (5.2) over a five-minute period along trajectories that ended in downdraft regions (Figure 5.23) and

can be used qualitatively to infer which downdrafts were likely to have the highest accelerations due to precipitation loading.

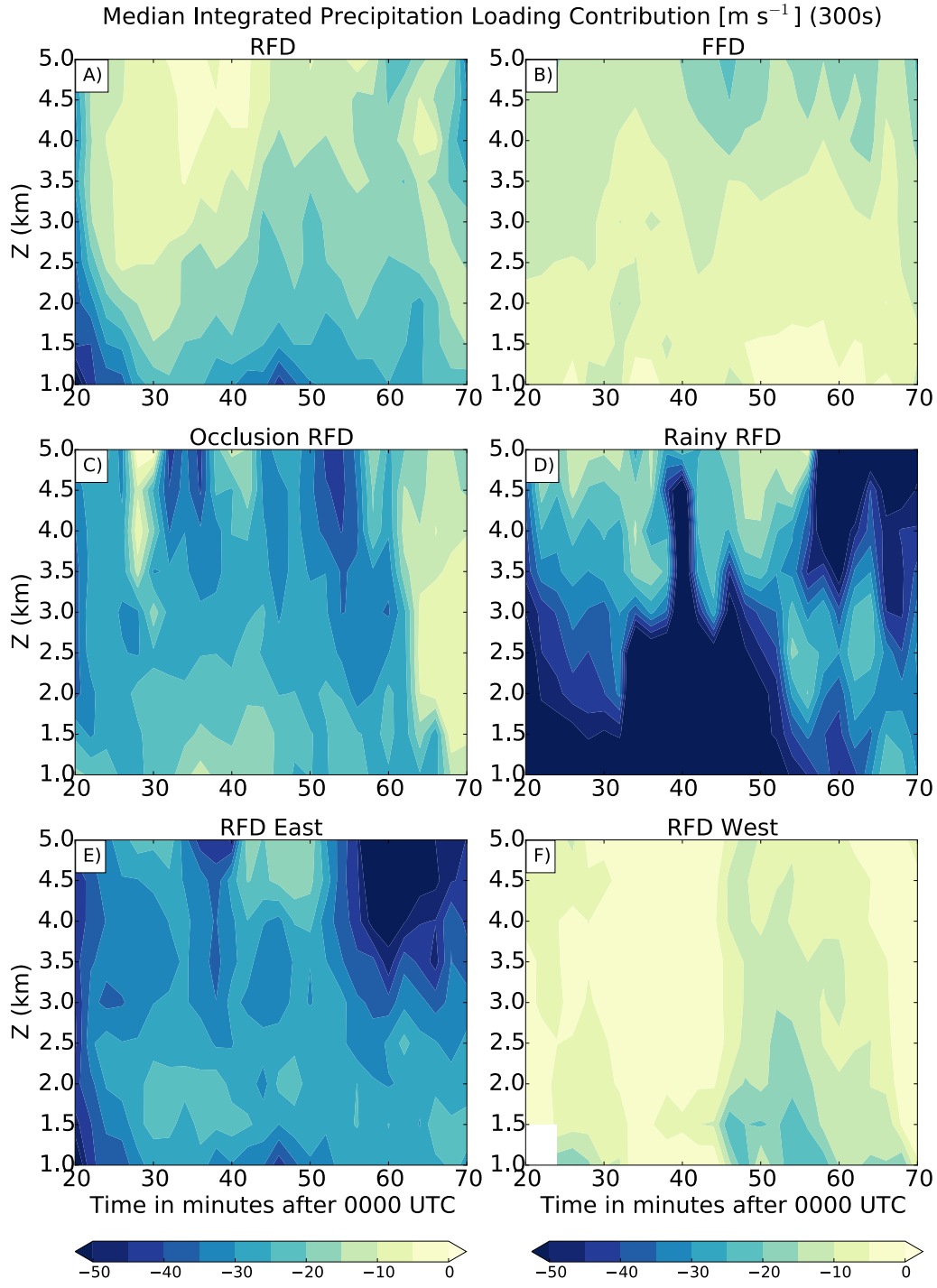

Fig. 5.23 Integrated precipitation loading contribution to vertical velocity (m s^{-1}) over 300 s in the in the RFD (a), FFD (b), occlusion downdraft (c), rainy downdraft (d), eastern sourced RFD (e), and western sourced RFD (f).

In the overall RFD (Figure 5.23a), the contribution of precipitation loading decreased substantially with height during the first RFD surge but increased and become more consistent with height during the second RFD surge. The partitioning of the RFD based on the flow regimes reveals that air parcels originating from the west (Figure 5.23f) experienced negligible precipitation loading until the occlusion stage. This behavior is consistent with previous studies (Kumjian 2011; French et al. 2015) which have suggested that rain drops fall faster than their fall speeds would otherwise dictate as the result of dynamically driven downdrafts in the western portion of RFDs.

Trajectories originating from the east (Figure 5.23e) experienced moderate amounts of precipitation loading, similar to the behavior of converging trajectories in the warm RFD surge of the SC16 simulation. Consistent with its name, the rainy downdraft (Figure 5.23d) experienced the most downward acceleration due to precipitation loading of any region. Melting of graupel and hail can be expected to be significantly larger in the eastern flow regime and particularly in the rainy downdraft, as the region was correlated with the highest reflectivity values and flowed through the northwest side of the hook echo, where the largest hail was typically found in the storm (Kumjian and Ryzhkov 2008, see their Figure 4a). Finally, the opposite pattern found in the FFD (Figure 5.23e) where trajectories acquired minimal downward forcing due to precipitation loading.

5.5.3 Maximum Downdraft Acceleration

An additional method to examine downdraft forcing mechanisms is to examine the regions of the storm where the downdraft trajectories experienced their maximum downward acceleration. Advection of momentum can make it difficult to discern where

downward motion is being generated. Although the downdraft trajectories are constantly exposed to vertical accelerations, regions where maximum acceleration is most prevalent can highlight the altitude and storm-relative location where the most important forcing is occurring. Using the same grid as was used for the previous trajectory behavior plots, this method was implemented by finding the (x, y, z) location and time that each individual downdraft trajectory reached their peak downward acceleration over the prior 20 minutes. The horizontal locations were adjusted to account for the storm-motion and aggregated together in a mesocyclone-relative framework. The vertical distribution (Figure 5.24) and the horizontal density (Figure 5.25) of maximum downward acceleration were found using a kernel density Gaussian function (Brooks et al. 1998) with a sigma of 250 m. It should be noted that the horizontal density does not represent every individual trajectory but rather highlights the regions where maximum downward acceleration predominantly occurred.

The vertical distribution of maximum downward acceleration was divided into the eastern and western RFD sources and the occlusion downdraft region. Although there is a large range of values at any one time, the temporal consistency of forcing altitudes for each downdraft region is remarkable. The eastern sourced trajectories demonstrated maximum forcing around 2 km (Figure 5.24a), whereas the western sourced trajectories (Figure 5.24b) were forced at significantly higher altitudes between 4 and 5 km. This result is consistent with a midlevel stagnation region primarily forcing western air downward at midlevels and eastern air at low-levels.

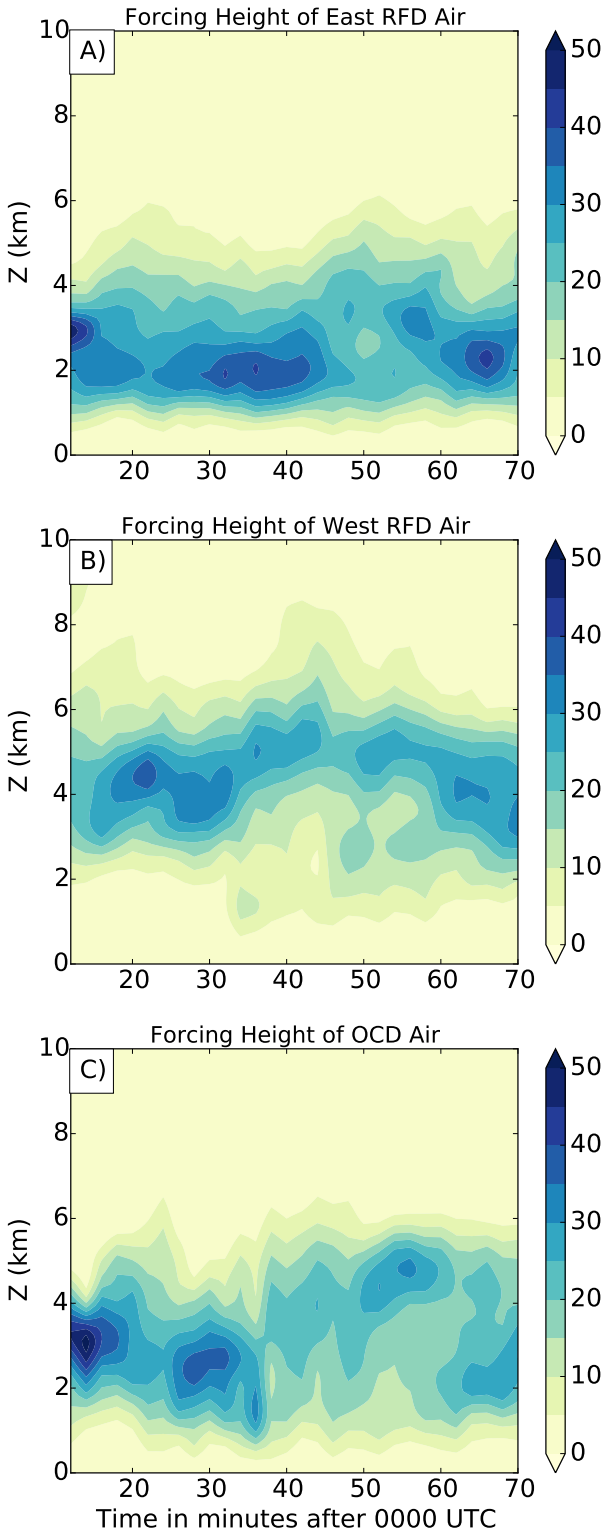

Fig. 5.24 Kernel density distribution with time of maximum downward acceleration altitude (km) for trajectories in the lowest 5 km of the overall RFD, originating from the east (a), west (b), and the occlusion downdraft portion of the RFD (c).

Meanwhile, the vertical distribution of maximum acceleration in occlusion downdraft trajectories (Figure 5.24c) was initially centered at 2.5 km. However, after 0038 UTC, the center of the forcing distribution abruptly rose to 4km, coinciding with the intensification and deepening of the mesocyclone and an upward shift in the altitude of the vertical vorticity gradient (Figure 5.13). The jump in altitude also corresponds to the period when the low-level mesocyclone transitioned from a two-cell, downdraft dominant structure to a single-cell, updraft dominant structure.

Horizontal distributions of maximum downdraft forcing during the first RFD surge (Figure 5.25c, e) reveals that the western trajectories were consistently accelerated in the low-reflectivity notch on the western flank of the storm (x=-7, y= 4). Indeed, the evolution of 3-km altitude reflectivity associated with the maximum downdraft acceleration of western sourced air suggests that the reflectivity notch itself was produced by this downdraft zone over time. Meanwhile, the eastern downdraft trajectories were accelerated in two different regions, the first was located in an elongated zone in the rear-flank reflectivity core associated with the rainy downdraft (x=0, y= 7). The second region was associated with the occlusion downdraft and was collocated with the vertical gradient in vertical vorticity (x=0, y=-2).

By the second RFD surge (Figure 5.25f), forcing near the occlusion downdraft was contained to a smaller area and the elongated zone in the rainy RFD had shifted westward, away from the reflectivity core and towards the midlevel convergence zone noted in Figure 5.15e.

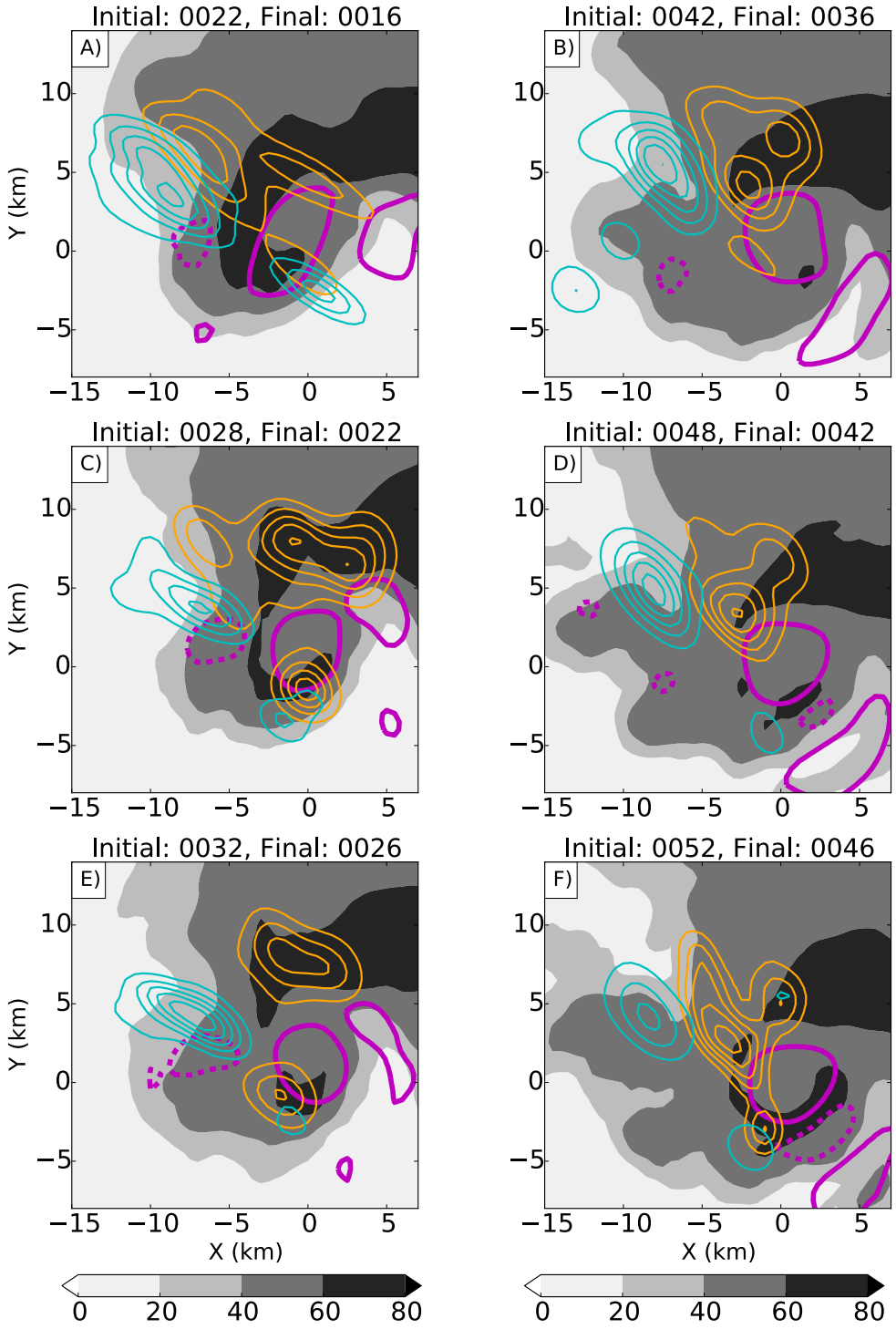

Fig. 5.25 Horizontal distribution of maximum downward acceleration from 0016 to 0046 UTC. Orange contours indicate eastern sourced trajectories, cyan contours indicate western sourced trajectories. Vertical vorticity 1x10-2 s^{-1} is contoured in magenta. Reflectivity at an altitude of 3 km is colored in grey in the background.

5.7. Low-level RFD Momentum Surges

Previous case studies have noted horizontal momentum surges behind the secondary RFGF to the south and west of mesocyclones (Skinner et al. 2014, 2015; Schenkman et al. 2014; Riganti and Houston 2017). Traditional tracking of individual, low-level momentum surges in the Geary storm, as was done in other studies, would be limited by the inherent spatiotemporal resolution of the data.. Instead, trajectory maps of changes in momentum are compared to regions where high momentum was observed Figure 5.26).

Analysis at the lowest grid level reveals an enhanced region of total momentum in the vicinity of the primary RFD on the west side of the low-level mesocyclone (Figure 5.26a, x=-45, y= 26). As the RFD intensified, the magnitude of the momentum also intensified, reaching a peak of 42 kg m s^{-1} at 0028 UTC (Figure 5.26d).

The low-level momentum maxima in previous studies were the result of a combination of local acceleration by pressure gradients (Skinner et al. 2015) and the vertical transport of momentum by downdrafts (Schenkman et al. 2016). The local acceleration is illustrated here by examining the mean change in three-dimensional momentum over the last 200 s within the 750-250 m layer and mapping the result at the horizontal beginning point of the backward trajectory (Figure 5.26b, e, h). Recently generated total mean momentum was maximized in the region underneath and downstream of the primary RFD, with some trajectories indicating that almost half of the total momentum was generated in the last 200 s (cf., Figure 5.26a, b). Horizontal and vertical transport accounted for much of the total momentum in the RFD region. But the maxima were the result of local accelerations mainly underneath the primary

RFD. Between 0042-0048 UTC (Figure 5.26h), the momentum acceleration underneath the primary RFD significantly decreased, suggesting that the local acceleration mechanism in the RFD region had dissipated.

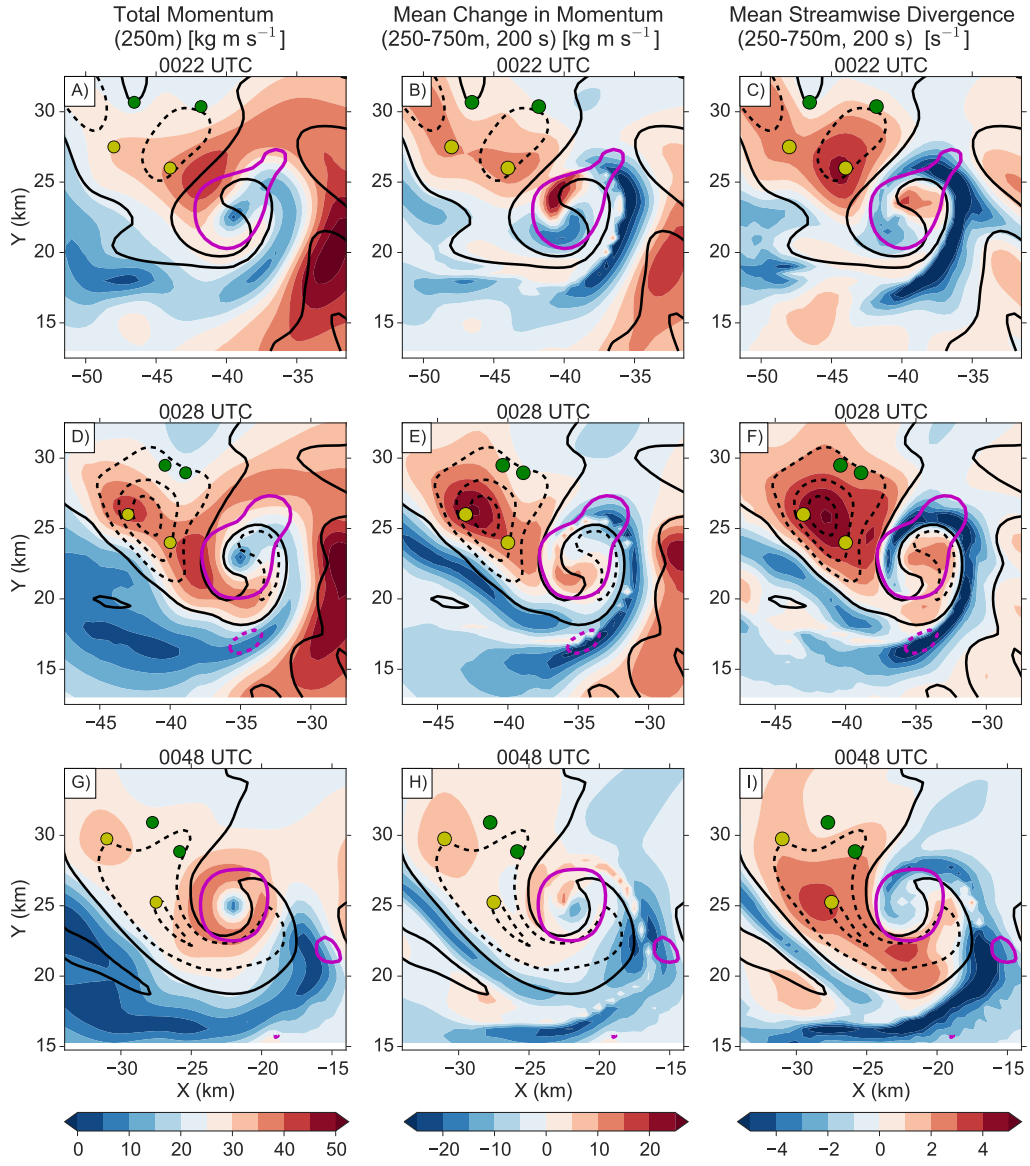

Fig. 5.26 Total momentum is illustrated at the indicated analysis time (a, d, g), mean change in momentum (250-750 m) over prior 200 s (b, e, h), and mean streamwise divergence (250-750m) (200 s) (c, f, i). Analyzed vertical velocity is contoured in (a, d, g) every 2 m s^{-1} in black at an altitude of 1 km, negative (positive) values are dashed (solid). The change in the vertical depth between trajectories initialized at 750 m and 250 m over (200s) is contoured in (b, c, e, f, h, i) every 500 m in black, negative (positive) value are dashed (solid). Yellow (green) dots show initial (final) horizontal position of select backward trajectories after 100 s of integration.

As noted previously, an implied stagnation high pressure aloft in the primary RFD region forced eastern sourced air to sink beneath a flow regime that originated from the west, forming a wedge of forward-flank/inflow air at the lower levels (Figure 5.11a). This configuration resulted in a downdraft region where the sinking midlevel air failed to reach the ground and spread out.

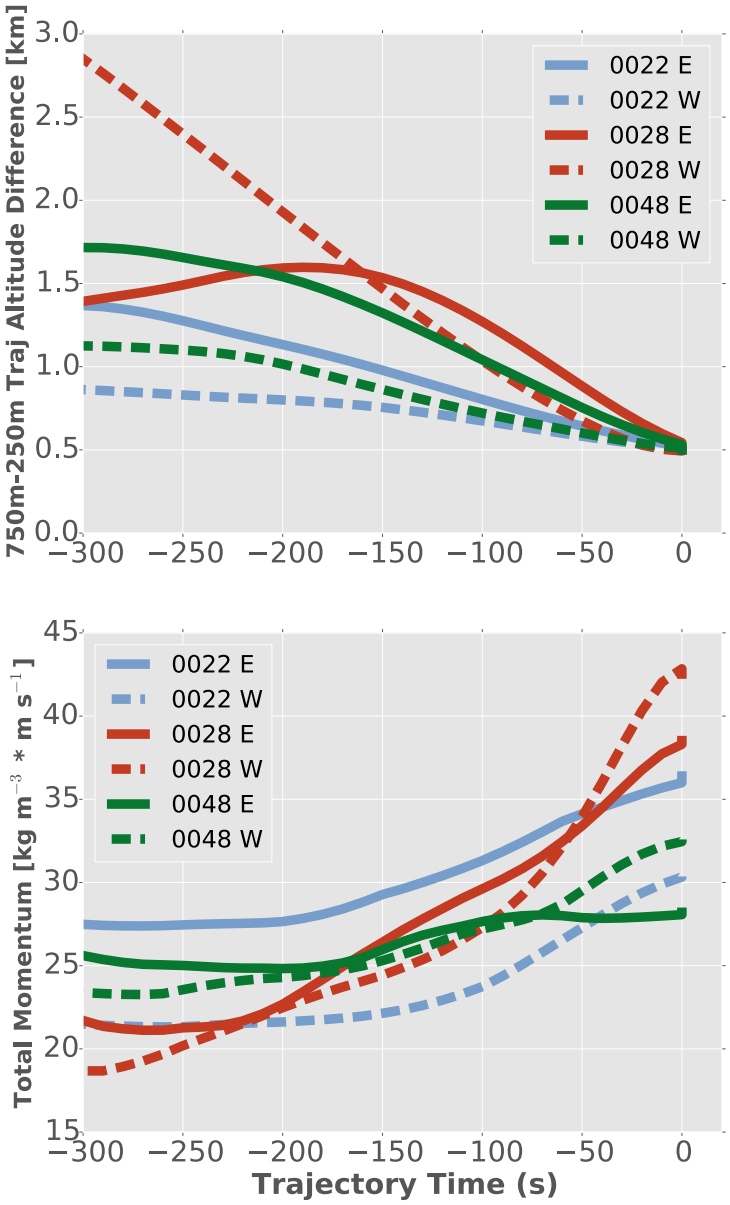

Fig. 5.27 For trajectories initialized at (x, y) locations denoted by yellow circles in Figure 5.26. (a) The difference between the altitude of trajectories initialized at 750 m and 250 m and (b) the total momentum with time for trajectories.

For a large region of flow to shrink in depth as it approaches a stagnation zone, mass conservation dictates that the flow must accelerate and diverge. In the case of the RFD region, the change in depth between trajectories initialized at 750 and 250 m (black contours in Figure 5.26b, c, e, f, h, i) was strongly correlated to the mean, streamwise, horizontal divergence (Figure 5.26 c, f, i), which is the horizontal divergence along the trajectory path rather than across. The strong correlation between streamwise horizontal divergence and depth of the initial 750-250 m layer implies that a significant portion of the mass flow rate was conserved by horizontally accelerating the flow underneath the primary RFD, which led to high values of total momentum.

The correlation between changes in depth between trajectories of air that wound up at 750 m and 250 m levels and total momentum is reinforced by the times series of individual trajectories in the momentum maxima with the initial positions denoted by yellow dots and the horizontal position after 100 s along backward trajectories denoted by green dots (Figure 5.26). Initially, the depth between the two trajectories (one initiated at 750 m and the other initiated at the same horizontal location at 250 m) is 500 m by definition. Examining the altitude difference between the two trajectories with time provides insight as to whether or not the layer was compressed in time (altitude difference increasing along the backward trajectory) or expanded vertically with time (altitude difference decreasing along the backward trajectory). A comparison between time series of the highlighted trajectories during the first (Figure 5.27, red lines) and second (Figure 5.27, green lines) RFD surges in the primary RFD region indicates that the low-level flow experienced a greater change in depth during the first surge than the second surge (Figure 5.27a). In turn, the flow also experienced greater momentum

accelerations during the first RFD surge (Figure 5.27b). Therefore, it appears that as the column was forced to shrink underneath the primary RFD aloft (illustrated in Figure 5.28), the flow accelerated in the direction of the mean flow and divergence normal to the flow was weak. The low-level dynamic pressure Laplacian (not shown) field was consistent with a strong horizontal pressure gradient centered below the nadir of the western flow regime. This phenomenon was significantly weaker or negligible before and after the first RFD surge. Indeed, during the second RFD surge the main downdraft shifted southeast and the western sourced air reached the surface (Figure 5.15).

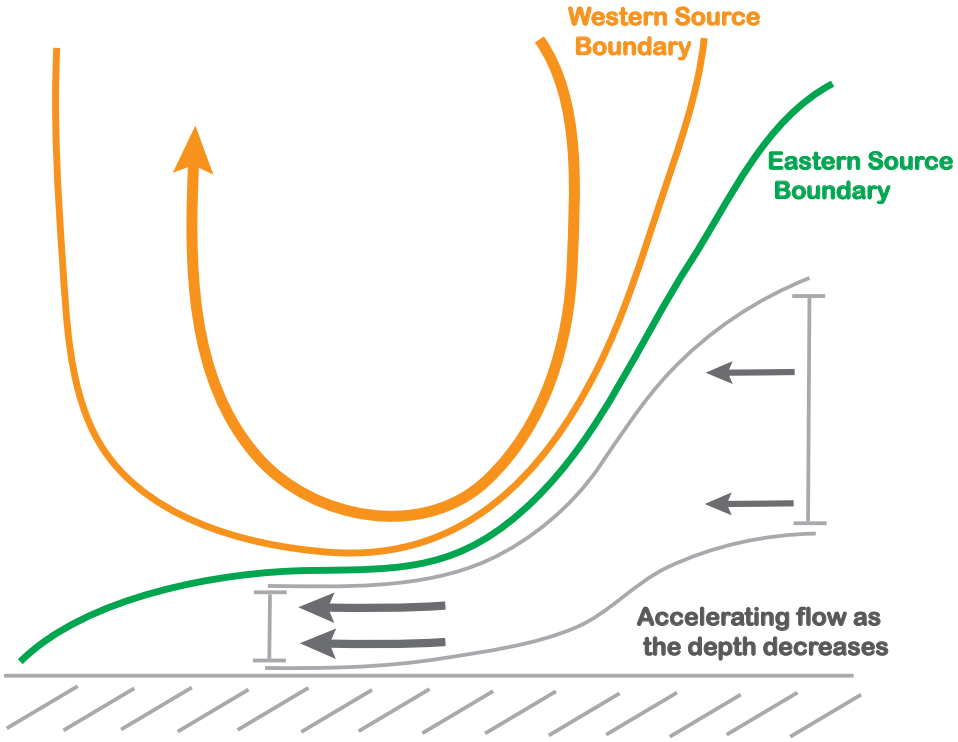

Fig. 5.28 Conceptual model of air sources and flow regimes within the primary RFD during the mature stage of the mesocyclone. Western sourced airflow regime is outlined in orange and eastern sourced boundary is outlined in green. Eastern sourced air was forced underneath western sourced air and accelerated horizontally to conserve mass. The vertically compressed eastern sourced flow is illustrated in grey.

5.8. Summary and Discussion

The majority of previous observational and numerical modeling based studies focused on the evolution of RFDs in classic supercells. The 29 May 2004 Geary, OK tornadic supercell was an abnormally large high-precipitation supercell thunderstorm in an environment with high instability, a low level stable layer, strong deep-layer shear, high SRH, but weak storm-relative midlevel flow between 3 and 5 km. The low-level stable layer appears to have significantly limited the ability of deep downdraft flow regimes to reach the surface, especially the FFD.

Two intensification periods of the continuously present RFD were investigated here, the first 0022-0032 which was associated with the transition from developing to the mature stage of the mesocyclone and the second 0045-0058 UTC, which corresponded to the transition between the mature and occlusion stage of the mesocyclone. In contrast to many previous studies that inferred a downdraft on the western side of the storm through strong reflectivity gradients, the storm herein had a persistent updraft on the western side of the storm during the mature stage of the mesocyclone that resulted in the primary RFD being shielded from mixing with dry midlevel environmental after beginning its descent, thus potentially limiting evaporation. Many of the conclusions of the study are based on large-scale trajectory behavior from a trajectory mapping analysis (Chapter 4) rather than individual trajectories in an effort to mitigate the accumulation of errors in the individual wind analyses, advection, and temporal errors.

Until the onset of the occlusion stage after 0045 UTC, the primary RFD was continually found in an elongated zone, maximized between 2 and 4 km, extending

northwest from the mesocyclone. At midlevels, air from the western updraft, carrying westerly momentum, converged with air carrying easterly momentum generated from the midlevel mesocyclone, resulting in a stagnation high pressure zone, inferred from vertical cross-sections of the dynamic pressure Laplacian. The RFD appears to have been forced in a very similar way as the warm downdraft surges in a high-resolution simulation by Schenkman et al (2016), except *environmental* midlevel flow was not reaching the stagnation high prior to the occlusion stage. Furthermore, the RFD is consistent with the placement and general structure described by Lemon and Doswell (1979), only deviating in the forcing mechanism, as their conceptual model relied heavily on inferences related to the storm-relative location and surface observations.

The strength of the stagnation high-pressure zone should be related to the westerly momentum carried into the storm via the western updraft and the strength of the cyclonic flow associated with the midlevel mesocyclone. Those two quantities can be roughly compared by subtracting the u-component storm-relative environmental flow from the mean tangential velocity of the mesocyclone at radii between 5 and 8 km. A time-height plot (Figure 5.29) shows that large-scale circulation was substantially stronger than the environmental flow at midlevels between 0020 and 0045 UTC, corresponding to the period when the downdraft convergent zone was strongest and located further west. However, as the midlevel circulation weakened at large radii, the large-scale flow became more balanced and the convergent region shifted eastwards. Therefore, it appears that the strength and position of the downdraft convergent region was consistent with the balance between the two primary momentum sources even though the downdraft region was generally shielded from true environment inflow by

the western updraft. The peak downdraft period, during the mature stage of the mesocyclone, is illustrated in Figure 5.30a and the balanced state before and after the peak downdraft period associated with the occlusion stage of the mesocyclone is illustrated in Figure 5.30b.

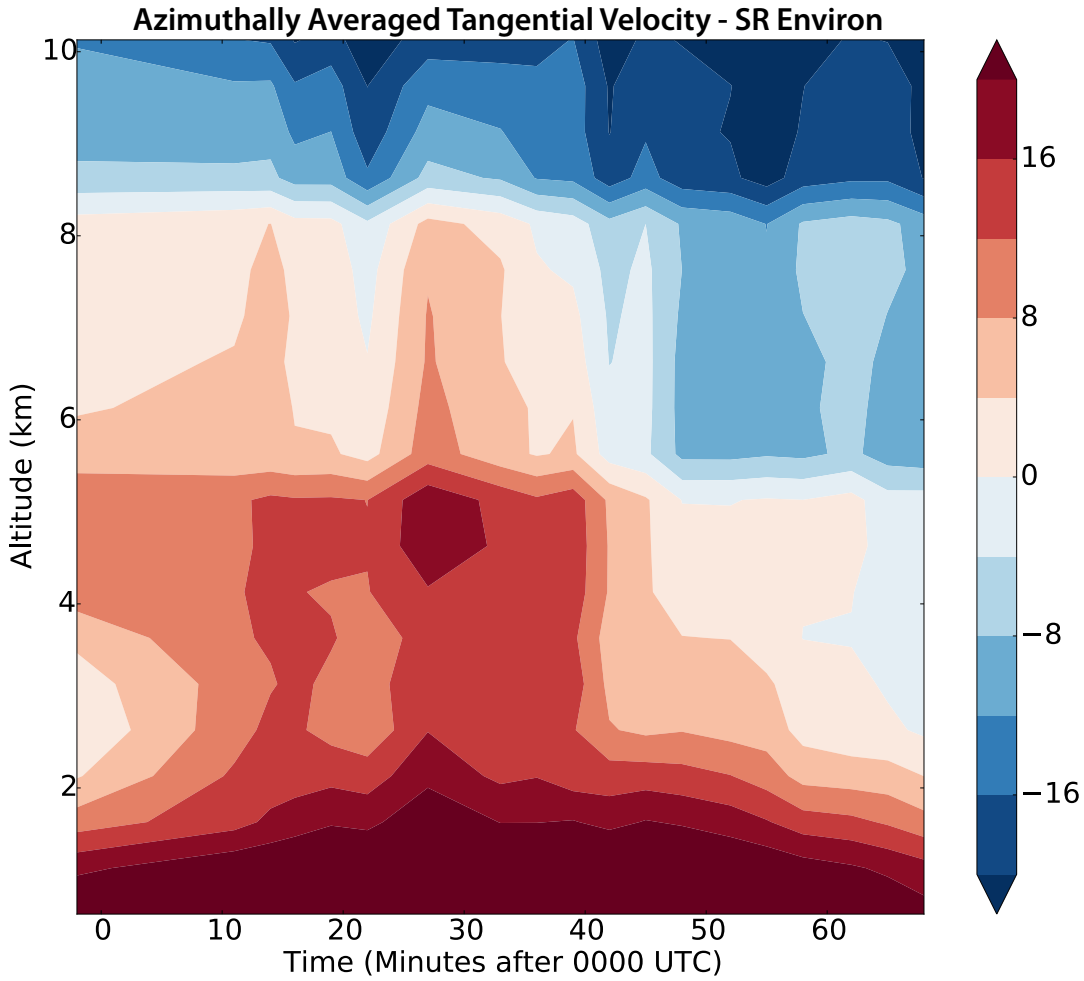

Fig. 5.29 Time-height plot of the difference between the mean tangential velocity between radii of 5-8 km and the storm-relative u-component of the environmental wind.

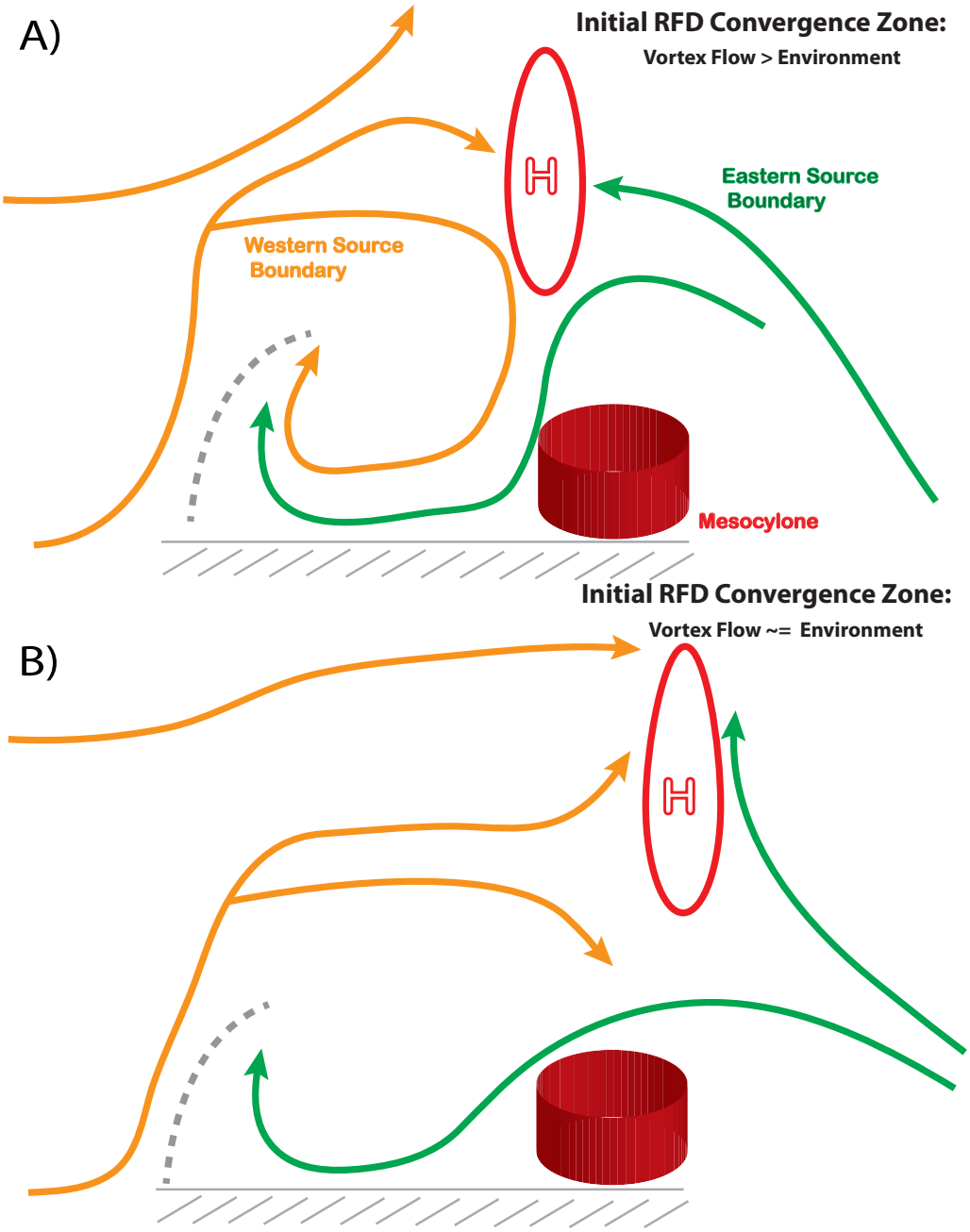

Fig. 5.30 Conceptual model of the RFD convergent zone during the mature stage of the mesocyclone (a) and during the occlusion stage of the mesocyclone when the midlevel circulation was weaker or balanced with the environmental flow (b). The western sourced air is represented by orange streamlines and eastern sourced streamlines in green. Additionally, the western portion of the SRFGF is illustrated as a dashed line, the high pressure stagnation zone is outlines in a red with a "H" at its center, and the low-level mesocyclone position is represented by the red cylinder.

The core of the rear-flank downdraft was comprised of air that had travelled through the western updraft. However, air parcels originating from the east composed an increasing fraction of the downdraft towards the surface with time. As the first RFD surge intensified, low-level convergence underneath the western updraft was enhanced and air originating from the east was drawn into the western updraft. Indeed, future altitude displacement suggests that downdraft trajectories from both the east and west were generally entrained into the deep updrafts after the first RFD surge. The recycled air in the western updraft eventually descended during the second RFD surge. After the second RFD surge, the future altitude displacement decreased with time, with negligible net displacements after 0050 UTC as the downdraft air began spreading out horizontally rather than getting entrained into the updrafts. Analysis in Chapter 3 showed that the western updraft diminished quickly after the mesocyclone transitioned into the occlusion stage.

The source altitude of trajectories originating from the east and west suggest that at low-levels the eastern air initially originated within the moist layer below the stable layer while the western trajectories originated from slightly above the moist layer at low-levels and above the stable layer at higher altitudes. However, after 0032 UTC, eastern and western trajectories initialized above 1500 m generally originated at similar altitudes around the top of the moist layer. Therefore, based on the source height of the trajectories, evaporation does not appear to be a strong forcing mechanism for the primary RFD during the first surge, as most of the air originated within a very moist portion of the environmental profile.

Precipitation loading was integrated along trajectories and demonstrated that while eastern trajectories passed through a significant amount of heavy precipitation, western trajectories passed through mostly light precipitation. The contrasting trajectory history is consistent with the trajectory history found by SC16, where negative buoyancy and precipitation loading were found to contribute more in trajectories originating from the east. The trajectory history is also consistent with polarimetric observations in the western hook echo, and in dynamically forced downdrafts where small drops are forced to sink faster than their fall speeds, limiting evaporation (Kumjian 2011; French et al. 2015).

As the midlevel circulation weakened after 0042 UTC, the flow balance in the convergence zone was reorganized, such that instead of an elongated zone extending towards the northwest, the zone was reoriented by 0048 UTC and extended east-northeast from the northwest corner of the circulation. The dramatic reorientation of the midlevel convergence zone resulted a deepening of the rainy downdraft, up to 7 km. Concurrently, the western updraft weakened and environmental air impinged on the western side of the circulation above 5 km, enhancing the stagnation high pressure aloft and resulting in a southward shift of the primary downdraft. The reorganization also resulted in the low-level merging of the primary and occlusion downdrafts, such that western sourced air began flowing into the occlusion downdraft region. After 0100 UTC, the convergent region continued shifting east, relative to the occluding mesocyclone, and was located above the weak primary RFD associated with a new developing mesocyclone (see Chapter 3).

Negative buoyancy appears to have played a larger role in forcing the downward acceleration of western sourced trajectories during the second RFD surge compared to the first surge. Median source altitude of western sourced trajectories rose ~500 m, originating just below the stable layer and potentially allowing more evaporational cooling to occur. Simultaneously, eastern sourced RFD air was increasingly being recycled back into the western updraft and descended in the western sourced downdraft. Lastly, the contribution from precipitation loading increased during the second surge. This hypothesis is consistent with the intrusion of western sourced trajectories down to the surface during the occlusion stage, particularly behind the surging primary RFD gust front.

In summary, during the mature phase of the mesocyclone, the primary RFD was manifested underneath an elongated convergence zone where air parcels with weak westerly momentum carried by the western updraft met air parcels with strong easterly momentum generated by the midlevel mesocyclone. In contrast to many early studies (Browning 1964; Barnes 1978a; Klemp and Wilhelmson 1978; Lemon and Doswell 1979) that hypothesized that midlevel environmental air comprised the bulk of the RFD, both flow regimes originated below a low level stable layer throughout the depth of the downdrafts. Prior to the occlusion stage, the midlevel mesocyclone flow at large radii was stronger than the storm-relative midlevel winds, resulting in a strong stagnation high pressure zone upstream of the mesocyclone. The persistent downdraft convergence zone forced air parcels originating from the east to sink beneath air parcels originating in the western updraft, resulting in impressive horizontal accelerations of the flow near the ground underneath the wedge of air. Meanwhile, strong vertical gradients

in vertical vorticity due to the tilt and strength of the vortex with height generated an occlusion downdraft whose air parcels remained distinct from the primary RFD. Despite the presence of a strong downdraft, the secondary RFD gust front did not significantly surge southward, either due to a lack of negative buoyancy in the descending air and/or the dominant presence of the mesocyclone flow.

The onset of the occlusion stage appears to have been the result of the weakening of the midlevel mesocyclone, resulting in an eastward shift in the convergence zone and stagnation high pressure was implied on the north and west sides of the mesocyclone at mid to upper levels, altogether causing a fundamental reorganization of the downdrafts. Furthermore, the vertical mesocyclone structure transitioned to favor occlusion downdraft air to sink on the outside of the circulation at low-levels, thus allowing the primary RFD and occlusion downdraft air parcels to merge together for the first time. The occlusion of the low-level mesocyclone by the primary RFD gust front occurred as western sourced downdraft air was directed towards the southern and southeastern portion of the hook echo as the two downdrafts merged, effectively secluding the eastern sourced air to the western portion of the hook echo. As the occlusion stage progressed, the stagnation zone aloft continued to weaken and shift eastward, while the leading edge of the surging downdraft outflow was involved in the mesocyclone redevelopment.

The evolution presented here suggests that inflow air was allowed to progress into the rear-flank of the storm at low-levels due to the strong, midlevel mesocyclone that pushed the main RFD upstream, relative to the main updraft, and the significant low level stable layer that discouraged midlevel air from reaching the surface and thus

cutting off the inflow flow regime. The inflow/eastern sourced flow regime was continually found at low-levels immediately behind the SRFGF, which surged southward and around the circulation as the main RFD intensified (see Figure 5.26) before passing into the occlusion downdraft during the occlusion stage. Many observational studies have demonstrated that moist low-level environments and warmer RFDs are more favorable for tornadogenesis. Thus, in certain situations, a previously underestimated role of the midlevel mesocyclone may be to allow the low-level air surrounding the circulation to be warmer than the environmental profile would suggest and thereby creating a low-level environment more favorable for tornadogenesis.

The correlation of warm RFDs and strong tornadoes in previous studies has focused on the direct impact on the low-level mesocyclone vertical velocity tendency by the buoyancy of the downdraft air. However, the buoyancy of the downdraft air is also significantly impacted by the forcing mechanism and thus related to the vertical mesocyclone structure. Therefore, the presence of warmer RFDs around tornadoes, in many cases, suggests that a vertical mesocyclone structure conducive to producing dynamically driven RFDs is more favorable to tornadogenesis than a vertical mesocyclone structure that does not significantly impact the primary forcing mechanism of the downdrafts. Early research suggested that only the occlusion downdraft on the south or east side of the mesocyclone was dynamically driven but radar analyses by Kosiba et al. (2013), data assimilation by SK15, simulations by SC16, and the results presented here suggest that the primary RFD or portions of the primary RFD on the west side of the mesocyclone may also be dynamically driven. Because these downdrafts are further upstream of the low-level circulation than the traditional

occlusion downdraft, they may have a larger impact on the buoyancy of air surrounding the developing tornado than the traditional occlusion downdraft. Future studies will focus on how the mesocyclone structure and evolution are impacted by the RFD position, structure, and evolution.

Chapter 6: Evolution and Source Regions for a Mesocyclone in a High-Precipitation Supercell Thunderstorm

6.1 Introduction

Radar-based studies have consistently shown backward air parcel trajectories passing through the RFD before entering the low-level mesocyclone during the mature stage of the mesocyclone (Johnson et al. 1987; Ziegler et al. 2001; Dowell and Bluestein 2002b; Markowski et al. 2012b; Kosiba et al. 2013). The benefits of trajectories passing through or near the RFD can be divided into three separate types. The first is the baroclinic generation and subsequent tilting of horizontal streamwise vorticity within in the downdraft region (Davies-Jones and Brooks 1993, Wicker and Wilhelmson 1995, Adlerman et al. 1999, Markowski et al. 2012a, and Dahl et al. 2014). The second is the augmented stretching associated with enhanced, low-level convergence produced from the outflow of the RFD (Mashiko et al. 2009; Schenkman et al. 2012, hereafter referred to as S12). Finally, the RFD also aids in the frictional generation of horizontal vorticity due to RFD momentum surges (Schenkman et al. 2014).

While the behavior of low-level trajectories in and around low-level mesocyclones has been studied extensively in previous studies, little research has focused on the storm-scale influence of the RFD on the organization and behavior of the deep mesocyclone. Brandes (1978) explored mesocyclone evolution in an axisymmetric framework in order to compare the observed behavior with that from previous laboratory tornado-vortex models. It was found that the vertical gradient in tangential velocity was positive during the pre-tornadic stage but transitioned to being

negative during the tornadic stage. The author speculated that tornadogenesis was thus the result of vortex breakdown on the mesocyclone scale, as an axial downdraft was potentially forced by the vertical pressure gradient associated with the vertical tangential velocity gradient. Once the downdraft reached the surface, it could cause local instabilities in the flow to grow to tornado strength outside of the center of the vortex but within the general mesocyclone flow. Wakimoto et al. (1998) observed similar behavior in the radar analyses of a tornadic storm near Garden City, KS, where the development of a tornado was preceded by the appearance of an occlusion downdraft near the axis of rotation. However, this hypothesis was challenged by Trapp (2000), who suggested that while two-celled vortex structure is possible, vortex breakdown on the mesocyclone-scale is unlikely. The difficulty arises in maintaining a boundary layer jet on the scale of a mesocyclone, as the vertical pressure gradient associated with the mesocyclone would overwhelm the near-ground convergence of the jet. Unfortunately, subsequent observational studies with sufficient spatial and temporal resolution have not expanded on this process.

In this chapter we will examine how the evolution of the RFD and occlusion downdrafts affected the structure of the mesocyclone during different phases of mesocyclone behavior. Forward trajectory maps are also used to detail the evolving sources regions, inflow depth, and potentially favored tilting regions for air parcels in the mesocyclone throughout the mature and occlusion stages. Finally, a comprehensive conceptual model of the evolving downdrafts and mesocyclone structure is presented in the conclusions section.

6.2 Methodology

As in Chapter 5, the wind analyses and trajectories in this chapter are based on the dual-Doppler analyses described and presented in Chapter 3 (Betten et al. 2018). The wind analyses were treated in identically to that in Chapter 5 with regards to the resolution, integration, and time-morphing scheme. Furthermore, horizontal winds were extrapolated from the lowest analysis level (250 m) down to the surface, thus assuming no vertical shear in the lowest 250 m. Although the grid spacing is coarser than recent radar analyses from VORTEX2 (Wurman et al. 2012), an average mesocyclone diameter of 7 km (Chapter 3) allows the circulation to be sufficiently resolved throughout the period.

The trajectory mapping framework (Chapter 4, Betten et al. 2017) has been demonstrated to be a robust way of viewing storm-scale trajectory behavior, even when data frequency is limited. They also presented a visualization of integrated trajectory vorticity budgets on a two-dimensional plane, using what they called "Lagrangian vorticity", the initial value of vertical vorticity in the past added to the integrated vertical vorticity tendency along trajectories. The vertical resolution of this dataset near the ground limits the accuracy of horizontal vorticity and thus the tilting of horizontal vorticity but regions of stretching are well resolved for the scales that are being examined. Fortunately, as Klemp and Rotunno (1983, hereafter KR83) demonstrated, the stretching term is the dominant contributor in vorticity budgets. Therefore, Lagrangian vorticity should not be substantially sensitive to ambiguous low-level tilting fields.

Lagrangian vorticity was estimated using the vertical vorticity tendency

equation in height coordinates (6.1) as in Betten et al. (2017), where, ζ is relative vertical vorticity, t is time, f is the Coriolis parameter, (u, v, w) are the zonal (u), meridional (v), and vertical (w) components of velocity, respectively. The turbulent diffusion and solenoidal terms were neglected as previous studies (Brandes 1984) demonstrated that for a coarse wind field, both terms were an order magnitude lower than the tilting and stretching terms.

$$\zeta_{Lagrangian} = \zeta_0 + \int \left[(f + \zeta) \left(\frac{\partial \mathrm{u}}{\partial \mathrm{x}} + \frac{\partial \mathrm{v}}{\partial \mathrm{y}} \right) + \frac{\partial \mathrm{u}}{\partial \mathrm{z}} \frac{\partial \mathrm{w}}{\partial \mathrm{y}} - \frac{\partial \mathrm{v}}{\partial \mathrm{z}} \frac{\partial \mathrm{w}}{\partial \mathrm{x}} \right] dt \quad (6.1)$$

An integration of Lagrangian vorticity after 300s is compared at two different times to the radial velocity from the SR2 radar and the Eulerian vertical vorticity field in Figure 6.1. In the first example at 0022 UTC, a broad circulation is present in the radial velocity (x=-40, y=23 km) with a noticeable distance between the maximum inbound and outbound velocities (Figure 6.1a). The corresponding analyzed vorticity field is symmetric about the vertical velocity gradient (Fig. 6.1c). Conversely, the Lagragian vorticity is actually negative at the center and maximized at the radius of maximum winds (Fig. 6.1e), suggesting unresolved structure in the original coarse analysis. The second example further illustrates the difference in structure between analyzed vorticity and derived vorticity from the trajectory mapping analysis during the onset of the occlusion stage at 0042 UTC when a tornado vortex signature (Brown et al. 1978) was present in radial velocity (Fig. 6.1b, x=-26, y=24). Once again the analyzed vorticity is smoothed with a distinct circular pattern, only now embedded in the occlusion updraft discussed in Chapter 3. However, there is no evidence of the smaller tornado vortex structure in the analyzed vorticity field whereas the Lagrangian derived vorticity is maximized at the center. In both cases, the Eulerian analyzed vorticity is

symmetric and maximized at the center and does not appear to have discriminating structure. Thus, the Lagrangian derived vorticity appears to be a better reflection of the smaller-scale rotation evident in the raw radial velocity data than the Eulerian vertical vorticity fields and can be used to better elucidate the vortex behavior.

6.3 Vorticity and Circulation Evolution

In Chapter 5, it was discovered that during the beginning of the mature stage of the supercell, descending trajectories were being directed into the center of the low-level circulation (Figure 5.8). This behavior was presumed to be analogous to axial downdrafts in laboratory vortex experiments and is evident in the first Lagrangian vorticity example (Fig. 6.1e). Additionally, the trajectory behavior is consistent with the average vertical *velocity* within the mesocyclone at radii less than 3 km (Fig. 6.2a). The time-height plot reveals weakly negative velocities present below 2 km in altitude between 0020 and 0030 UTC. Subsequently, as noted in Chapter 3, vertical velocity reversed and became positive during the mesocyclone intensification period that occurred just after the end of the first RFD surge (Chapter 5). The average vertical motion remained positive until the onset of the second RFD surge at 0045 UTC (Chapter 5) and the beginning of the occlusion stage (Chapter 3). Meanwhile, vertical velocity at larger radii (Fig. 6.2b) was nearly constant until 0030 UTC, after which it began decreasing with time, especially after 0045 UTC, when the primary updraft began shifting towards the southeast as the RFGF surged out.

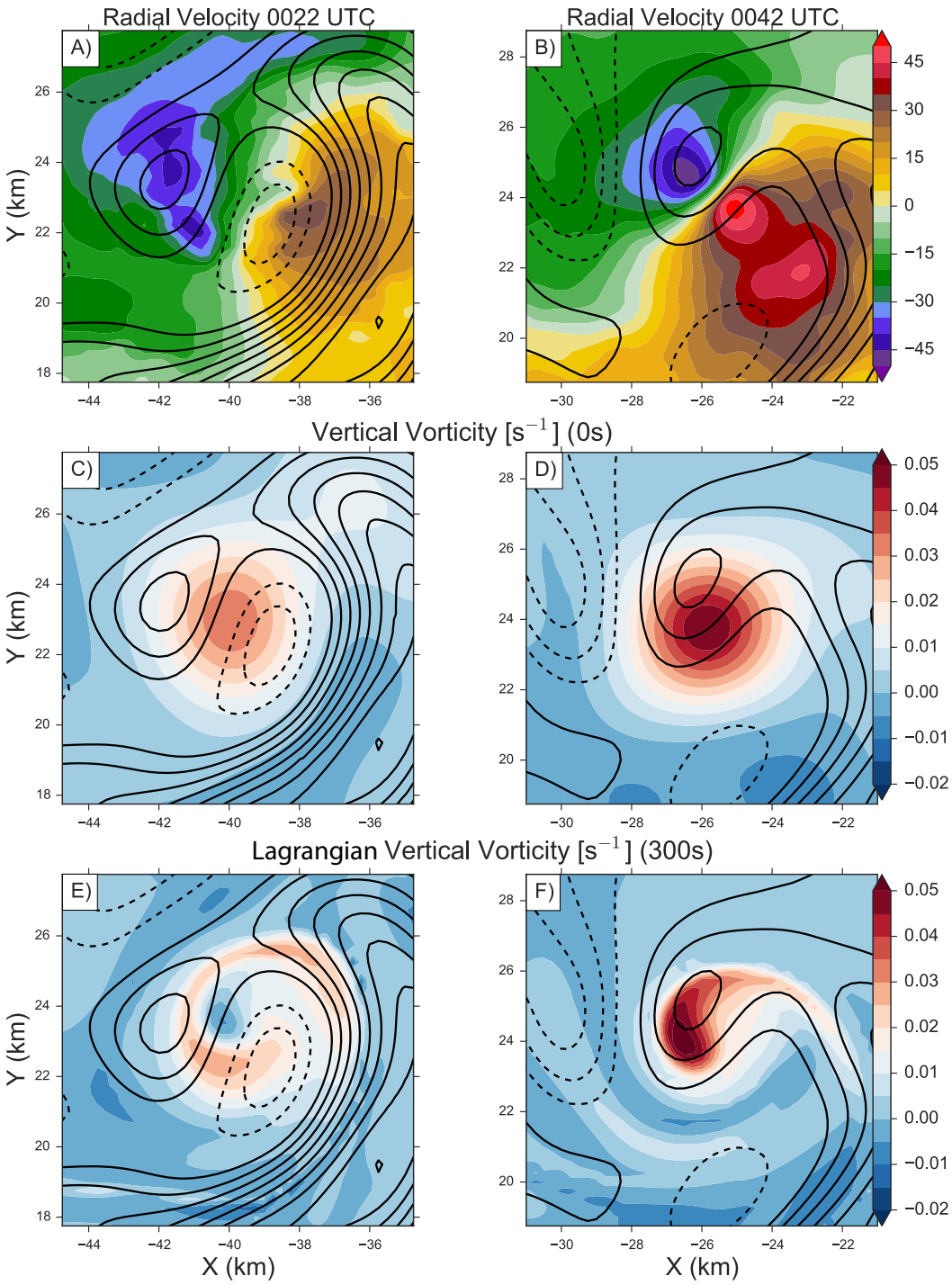

Fig. 6.1 Plan Position Indictor scans at 0.5^{o} elevation of radial velocity from SR2 is plotted at 0022 UTC (a) and 0042 UTC (b). Vertical velocity at an altitude of 1 km is contoured in black every 4 (2) m s^{-1} for positive (negative) values in every plot panel. Analyzed vertical vorticity is color-shaded in (c) and (d) at an altitude of 1 km. Lagrangian vorticity from backward trajectories initialized at 1 km altitude and integrated over the prior 300 seconds, is color-shaded in (e) and (f).

The opposing trends in vertical velocity after 0030 UTC in the inner and outer mesocyclone flows implies a transition took place in the circulation structure. To investigate this further, circulation at 2.5 km (Fig. 6.3a) and 10 km (Fig. 6.3b) radii was estimated at every grid point and the horizontal maximum was calculated at every analysis time to produce time-height plots for the mesocyclone and storm scale circulations. A comparison of the time-height plots of circulation demonstrates that rotation on the mesocyclone-scale (R~2.5 km) and storm-scale (R~10 km) evolved differently in time and height from each other and often had reverse vertical gradients. Initially, the mesocyclone-scale rotation was maximized below 5 km and reached a peak value at 0045 UTC, whereas the storm-scale rotation was maximized above 6 km and reached a peak value at 0028 UTC. Therefore it is necessary to examine the variation of circulation in height and radius for specific periods to draw conclusions about how it relates to the mesocyclone and tornado-cyclone scales.

6.3.1 Two-celled Vortex Period

Circulation is inherently an axisymmetric quantity and thus it makes sense to investigate the surrounding kinematic structure in an axisymmetric framework. Axisymmetric quantities, like vertical velocity (black contours, Fig. 6.4a,b), were estimated by finding the center of the mesocyclone at every level and then azimuthally averaging the quantity. Maximum vertical displacement, a new variable, was developed to elucidate trajectories that experienced substantial vertical descent over the previous 300s (Fig. 6.4a). The variable is found through subtracting the initial altitude from the maximum prior altitude over a specified period, therefore values near zero indicate a trajectory that has not experienced descent over the period of interest.

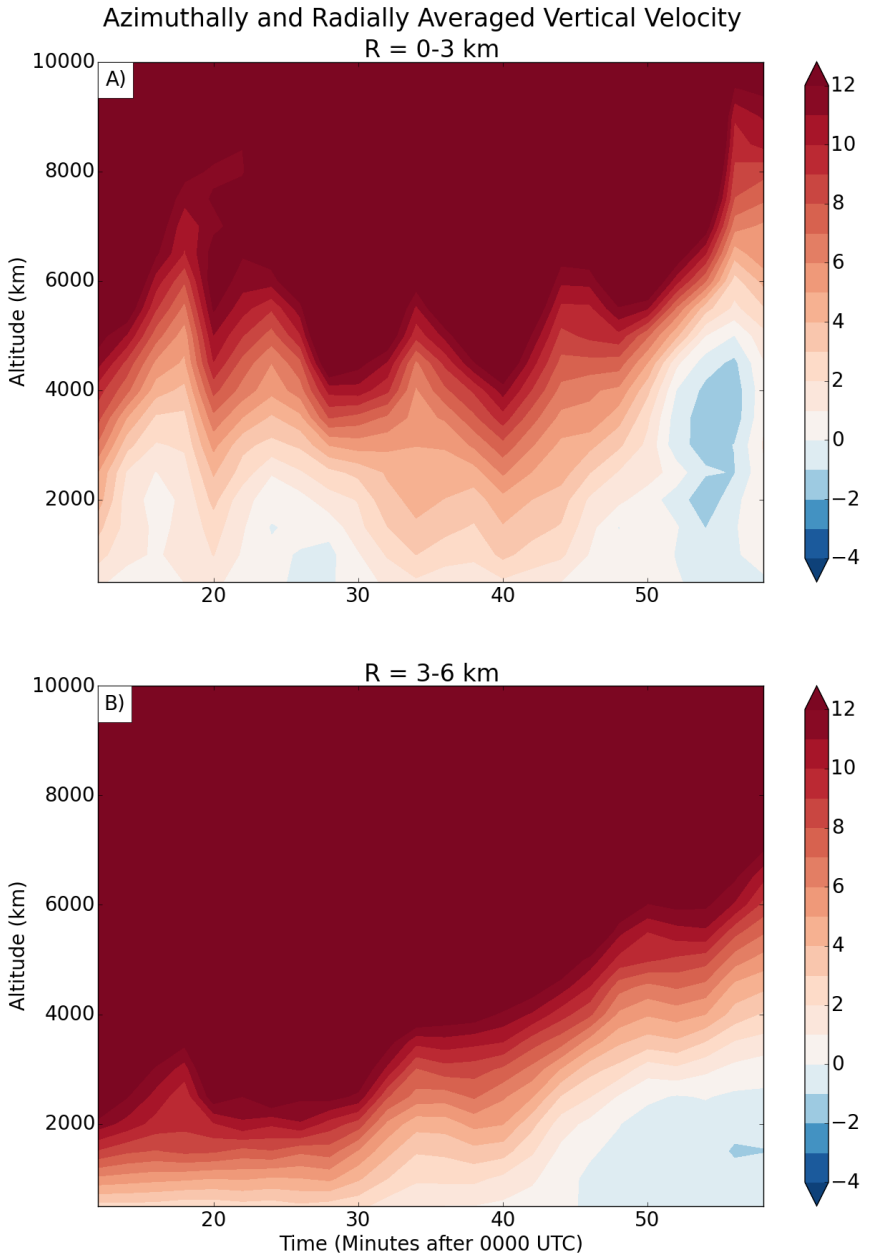

Fig. 6.2 Time-height plots of azimuthally and radially averaged vertical velocity in a reference frame centered on the mesocyclone at every height. Average vertical velocity between radii of 0 and 3 km is plotted in (a) and between 3 and 6 km in (b).

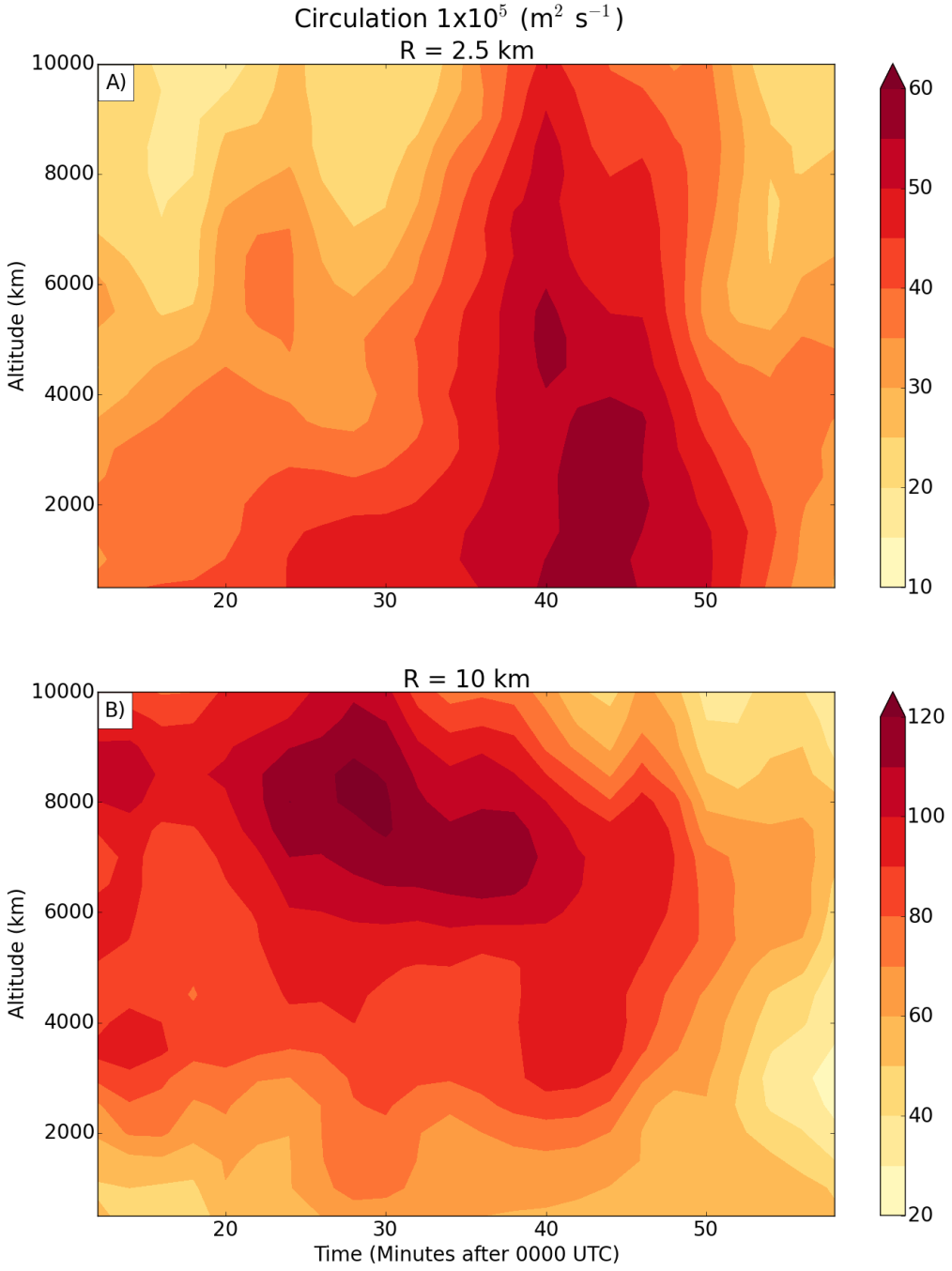

Fig. 6. 3 Time-height plot of maximum circulation (1x10^5 m^2 s^{-1}) at radii of 2.5 km (a) and 10 km (b), centered on the mesocyclone at every altitude.

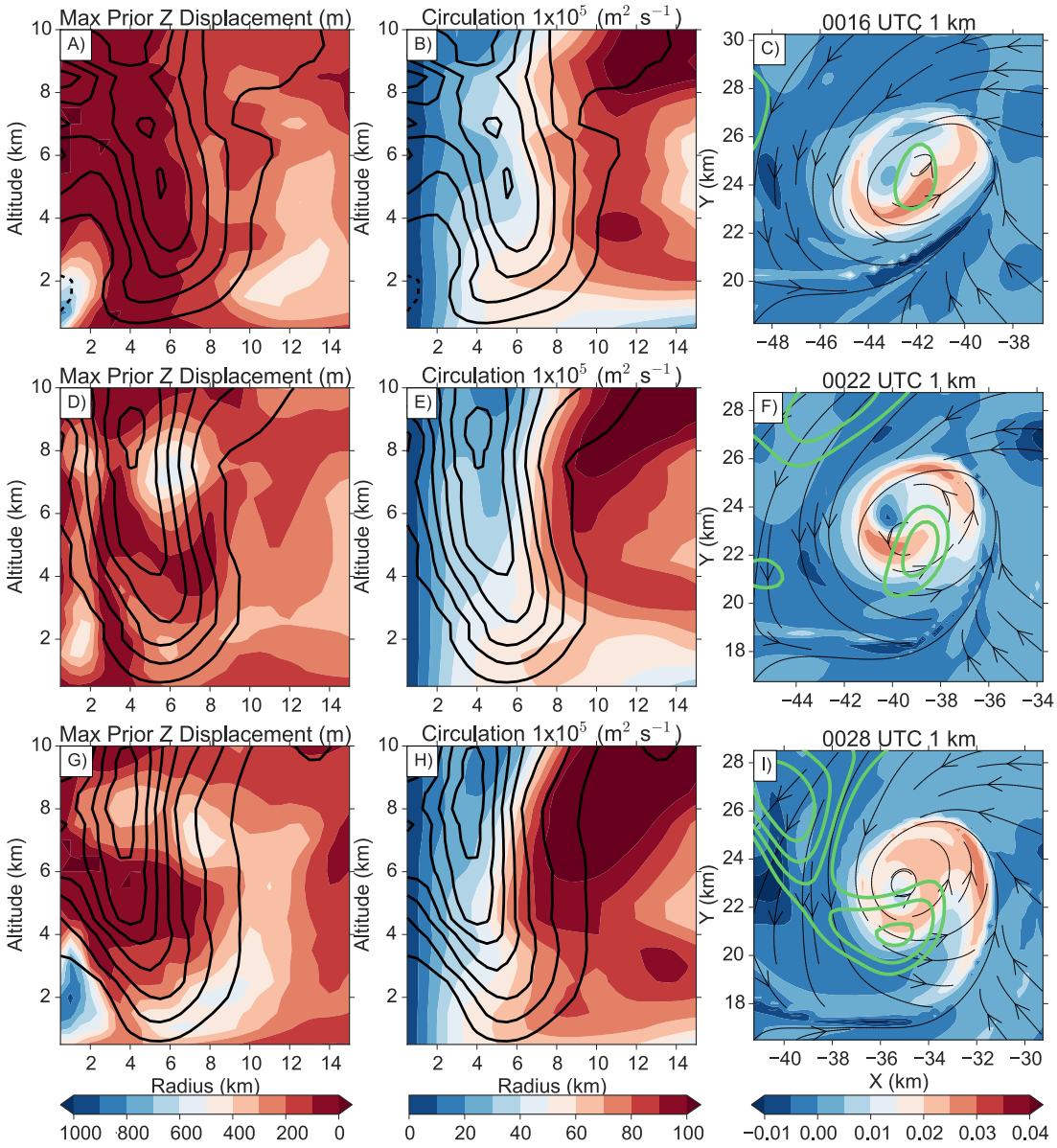

Fig. 6.4 Radius-height plots with azimuthally averaged vertical velocity contoured in black (every 4 m s^{-1} with positive [negative] values solid [dashed]) on top of maximum prior altitude displacement (color-shaded) in (a, d, g) and circulation centered on the mesocyclone (color-shaded) in (b, e, h), at the times listed in (c, f, i). Lagrangian vorticity indicated based on trajectories initialized at an altitude of 1 km and integrated backward 300s (color-shaded) with downward vertical velocity contoured in green (every 2 m s^{-1}).

The early mature stage (0016-0022 UTC) of the mesocyclone was characterized by two-celled vortex behavior. The initial low-level vortex had descending trajectories at the center of the circulation (Fig. 6.4a, R = 1 km, Z = 1 km) and rising motion at

larger radii (R=5 km). The strongest descending tendencies were consistently found below 4km as the vertical gradient in circulation was maximized at 3.5 km altitude (Fig. 6.3a) and a radius of 4-6 km during the two-celled vortex period (R=4 km, Fig. 6.4b). As previously noted, circulation generally increased with radius until about 12 km, demonstrating that even though the mesocyclone had yet to reach the mature stage, the storm-scale circulation played a significant role in the flow evolution.

The axially descending air resulted in a Lagrangian vertical vorticity field (Fig. 6.4c) that was maximized on the outer edge of the mesocyclone and minimized at the center (x=-42, y=24 km), as only the air parcels on the outer edge of the circulation were being stretched, particularly the southeastern side of the circulation. Although annular vorticity patterns are not usually present in reported high-resolution mobile-radar analyses (Wurman et al. 2007; Wurman et al. 2010; Marquis et al. 2012; Kosiba et al. 2013), the tornado-cyclone presented in Marquis et al. (2008) briefly broadened and developed an annular structure due to divergence near the center of the circulation (see their Fig. 6i-j). There are also examples from nested numerical simulations during periods of strong occlusion downdrafts (Klemp and Rotunno 1983, Wicker and Wilhelmson 1995, and Schenkman et al. 2014).

The most interesting evolution occurred between 0022 and 0028 UTC, where the Lagrangian vorticity increased substantially near the center of the circulation even as the occlusion downdraft was intensifying, resulting in the maximum vertical displacement increasing along the vertical axis (Fig. 6.4d, g). This behavior is best explained through the asymmetric advection of stretched air parcels, which as Gaudet and Cotton (2006) demonstrated, can lead to increasing vertical vorticity in spite of a

divergent tendency. An additional consequence of the downdraft development was the vertical advection of circulation at large radii towards the ground, which can be seen when comparing the circulation at R = 6 km at 0016 UTC (Fig. 6.4b) to 0028 UTC (Fig. 6.4h). At low-levels, this vertical transport of circulation is reflected in the gust front pushing southward from the southern end of the circulation (Fig. 6.4a, i) and the horizontal winds increasing in magnitude on the western side of the circulation.

6.3.2 Transition Period

Between 0028 and 0042 UTC, the mesocyclone transitioned from being centered on the vertical velocity gradient at low-levels and the updraft at mid levels (Fig. 6.4g), to being centered on the updraft throughout its entire depth (Fig. 6.5a, d, g). By 0032 UTC, max vertical displacement across the vortex below 2 km had shifted from being strongly negative (Fig. 6.4g) to almost zero (Fig. 6.5a), indicating that air parcels had gone through negligible downdrafts over the previous 300 s. Despite minimal increase in the circulation strength at a radius of 2 km (Fig. 6.4h and Fig. 6.5b), the Lagrangian vorticity on the southwest side of the circulation (Fig. 6.4i, Fig. 6.5c) almost doubled in magnitude as air parcels were being stretched for longer periods as the vortex became more correlated with the updraft. It is interesting to note that the effects of the stretching were most evident in parcels on the western side of the circulation at 0032 UTC (Fig. 6.5c, x=-33, y= 23) rather than near the center where it was maximized just a few minutes later at 0042 UTC (Fig. 6.5f). Concurrently, circulation was increasing aloft at radii smaller than 4 km (Fig. 6.4h; Fig. 6.5b; Fig. 6.5e) as the mesocyclone vortex aloft was beginning to intensify due to more favorable

low-level stretching. The radial gradient of circulation increased significantly within 3 km from the vortex axis.

Circulation on the mesocyclone scale above 3 km in altitude rapidly increased between 0032 and 0042 UTC (Fig. 6.3a), after which it slowly weakened due to the occlusion of the vortex. By 0042 UTC, the transition to a single-celled vortex was accomplished as the maximum vertical displacement at radii less than 2 km (Fig. 6.5g) was negligible all the way up to 10 km. However, while the smaller scale vortex was strengthening, the storm-scale circulation aloft between 6-10 km altitude began weakening, a trend which persisted in time throughout the occlusion stage. Chapter 5 associated the strength of the rotation at radii of 5-8 km to the RFD strength on the northwest side of the circulation. Thus, as rotation on that scale weakened, so did the RFD. In Chapter 3 the formation of an apparent horizontal rotor on the north side of the low-level circulation evident between 0032 and 0038 UTC was described. This rotor can be seen in the confluence of the streamlines (Fig. 6.5c, x=-33, y=27; Fig. 6.5f, x=-30, y=27). The position and timing of the rotor formation correlates with the enhanced stretching seen in the derived vertical vorticity at 0032 and 0036 UTC. Comparable behavior was noted by S12 who attributed tornadogenesis to enhanced stretching from a horizontal rotor.

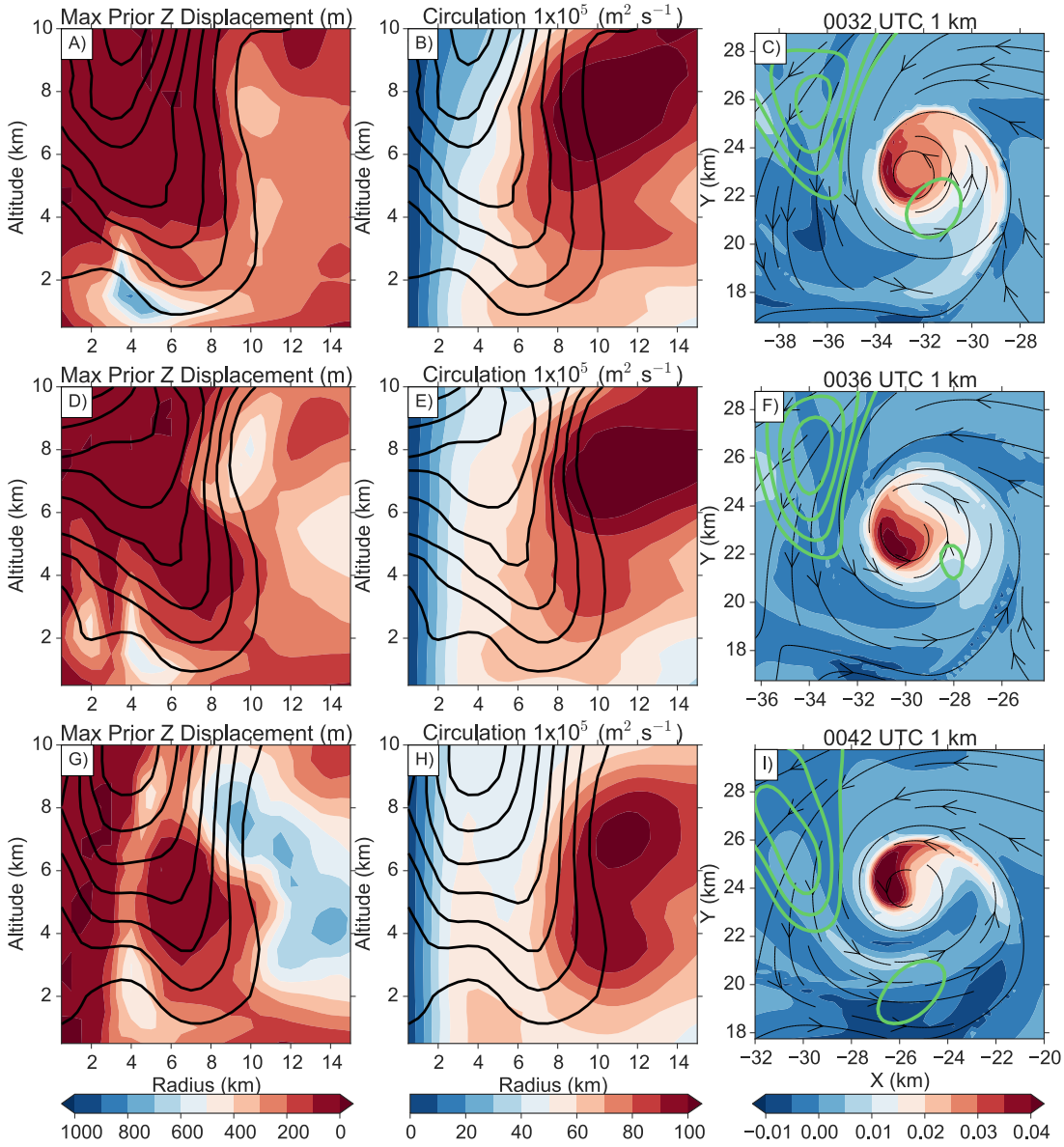

Fig. 6.5 Same as Figure 6.4, except for 0032 – 0042 UTC, which corresponds to the time between the first and second RFD surge.

6.3.3 Occlusion Stage

As the mesocyclone transitioned into the occlusion stage, the mid to upper-level storm-scale circulation (R > 5 km) continued to weaken dramatically with time, resulting in circulation noticeably and consistently decreasing with radius between 4 and 8 km from the center of the mesocyclone (Fig. 6.6b). The weakening suggests a separation between the mesocyclone scale circulation at radii below 4 km from the

storm-scale circulation at radii greater than 8 km. In Chapter 5, it was demonstrated that the re-intensified occlusion downdraft at 0048 UTC was associated with the strong vertical gradient in circulation associated with the mid to upper-level decrease in circulation strength. Moreover, it was also found that the air parcels pushing the RFGF away from the circulation passed through the enhanced occlusion downdraft. Therefore, it appears that the occlusion process began at mid levels, with the weakening of the circulation, before it was evident at low-levels.

By 0048 UTC, descending air was being ingested by the outer portion of the circulation (Fig. 6.5a, R=4) as the RFD merged with the occlusion downdraft and expanded southward. The region of descending air parcels continued to expand radially inward and outward with time, eventually only leaving a sliver of parcels near the vortex axis that hadn't recently passed through the downdraft (Fig. 6.6d, g). The expansion of the downdraft was reflected in the shrinking positive Lagrangian vorticity region (Fig. 6.6c, f, i). Unlike the previous occlusion downdraft during the first RFD surge, the occlusion downdraft now aided in decreasing the scale of the mesocyclone. This finding is consistent with theoretical (Burgers 1948; Rott 1958), laboratory (Ward 1972), and numerical simulation (Rotunno 1984) studies that have shown that vortex stability is sensitive to the axial vertical velocity tendency of the vortex. One-celled vortices are inherently more stable and resistant to deformation by outside instabilities, such as a downdraft surge, compared with two-celled vortices. In the present study, once the mesocyclone transitioned to a one-celled structure, the Lagrangian vorticity evolution was much more consistent in time compared to during the two-celled period.

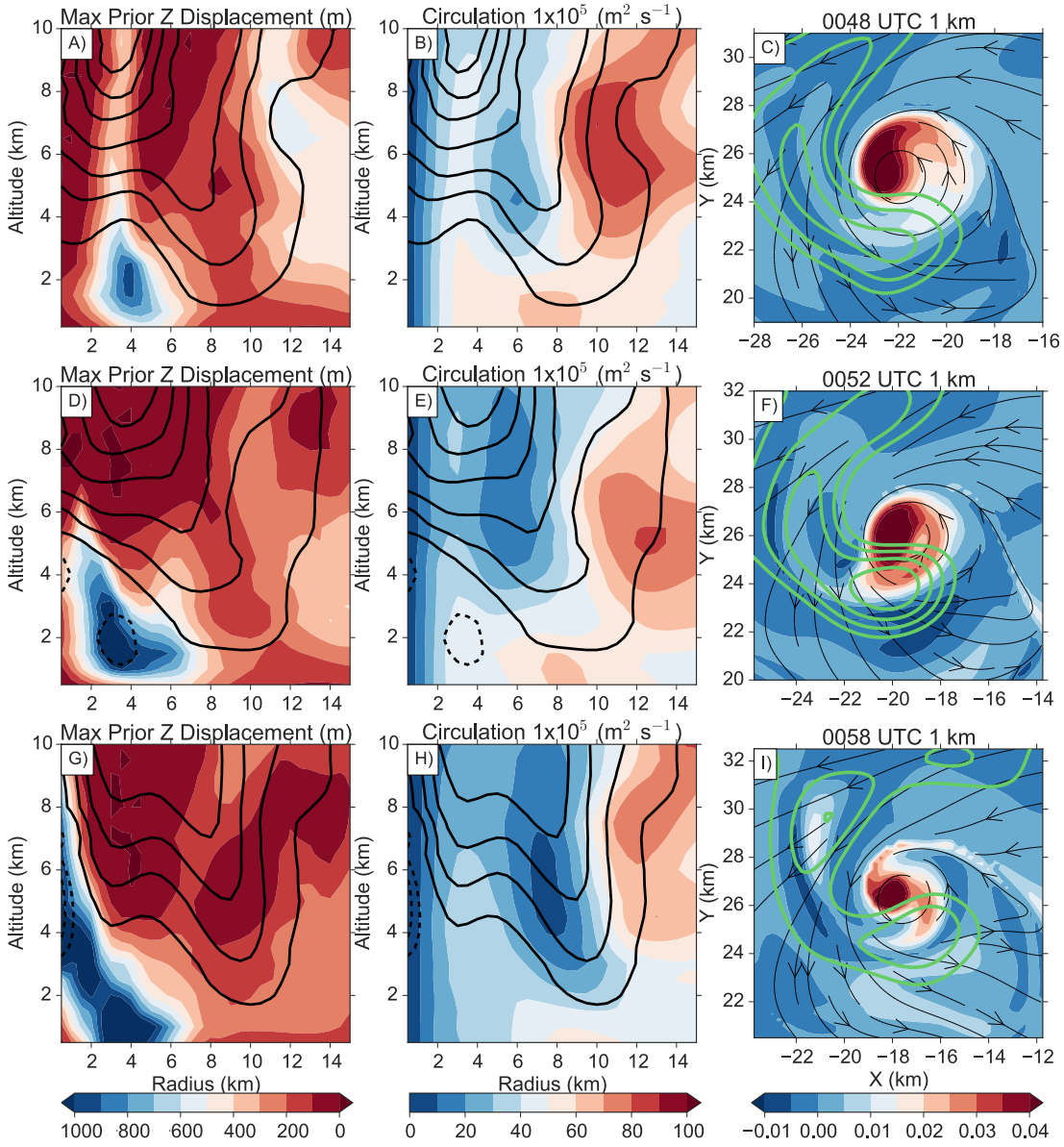

Fig. 6.6 Same as Figure 6.4, except for during the second RFD surge.

6.3.4 Axisymmetric Trajectory Behavior

Using an analytical model, Davies-Jones (1973) established that in idealized, axisymmetric vortex models, the axial vertical velocity tendency of the vortex varied directly with the inflow volume rate. The model predicts that as the volume rate increases, the axial vertical velocity becomes more positive. As has been already shown, vertical velocity structure surrounding the mesocyclone is often asymmetrical in

nature. Consequently, vortex inflow estimates using azimuthally averaged radial inflow will lead to an oversimplification of the complex, asymmetric flow surrounding the mesocyclone and perhaps overestimate the depth of air flowing into the circulation itself.

Therefore, a method was developed to estimate the volume of air flowing into the mesocyclone from outside the core flow using forward trajectories. The core flow here is defined as the mesocyclone flow inside the radius of maximum winds, at radii of approximately 2-3 km. Forward trajectories were initialized every two minutes in a three-dimensional volume following the mesocyclone with a depth of 5 km and a radius of 10 km. The mesocyclone region is defined as vertical vorticity of at least 0.015 s^{-1} and within 4 km of the circulation center, which is defined at every altitude where the mesocyclone vortex was evident. Only trajectories with initial values of vertical vorticity below 0.015 s^{-1} were considered and they had to enter the mesocyclone below an altitude of 5 km and within 200 seconds. The inflow volume can be approximated by calculating the horizontal area of the future mesocyclone trajectories at each altitude. When the trajectory area is zero, the volume flow rate is negative or negligible. Alternatively, when the trajectory area is large, the inflow volume flow rate is also large. In this way, the volume of air being drawn into the mesocyclone is vertically apportioned according to its future rather than instantaneous behavior.

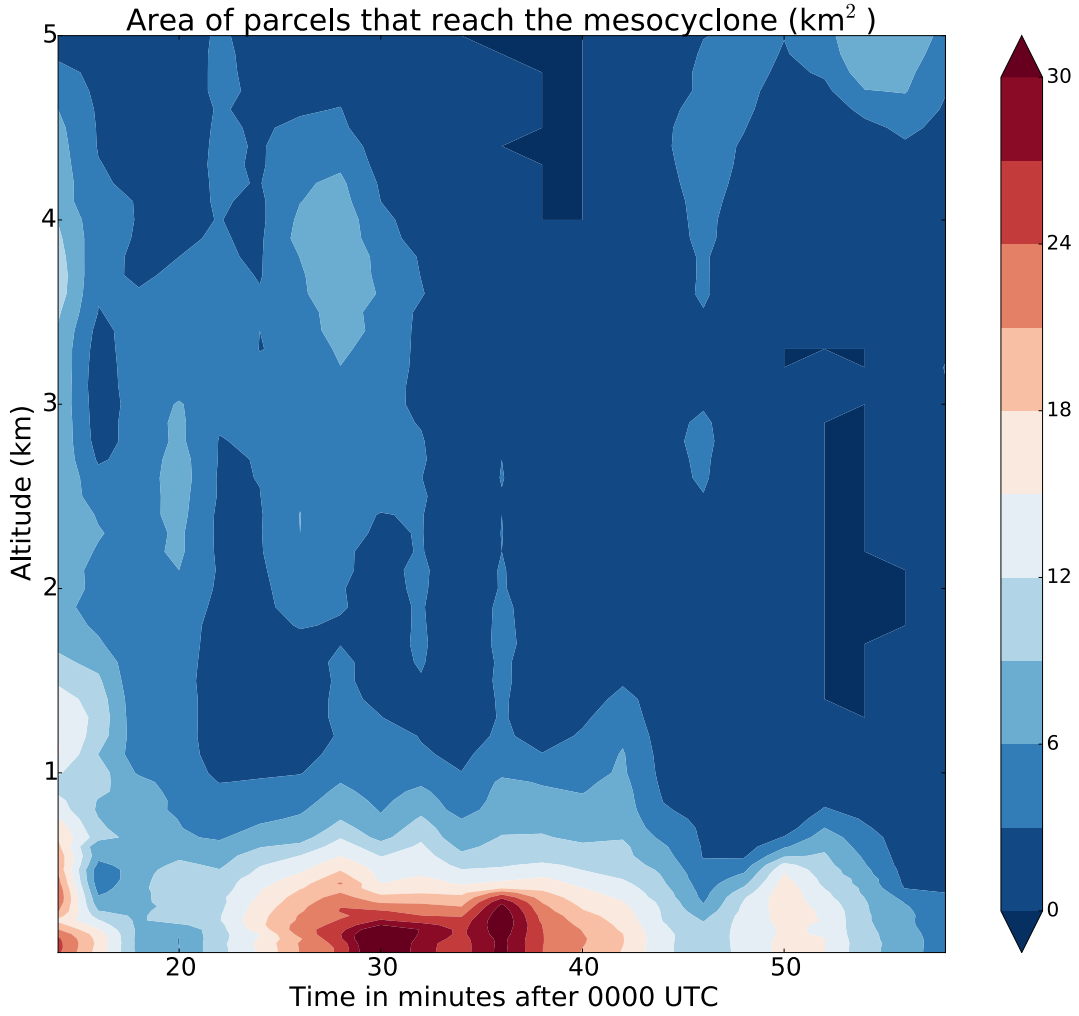

Fig. 6.7 Time-height plot of horizontal area encompassing future mesocyclone trajectories that will gain at least 0.015 s^{-1} vertical vorticity within the next 200 seconds. The area is a proxy for mesocyclone horizontal inflow rate.

Throughout the mature (0020 – 0045 UTC) and occlusion (0045 – 0120 UTCT) stages of the mesocyclone, the inflow volume was consistently maximized in the lowest 500 m and demonstrated a sharp decrease above 1 km (Fig. 6.7). This structure is not particularly surprising given that many simulations suggest that the tilting of horizontal vorticity into the vertical is maximized in the lowest 500 m (Wicker and Wilhelmson 1995; Adlerman et al. 1999). Thus, it follows that the inflow must be strong in the layer where the tilting is occurring. However, the inflow depth remained relatively constant

from the early mature stage through the intensification and transition period, suggesting that the transition of the mesocyclone from a two-celled to one-celled vortex was not instigated by a substantial change in inflow depth. Rather, the inflow depth remained relatively constant while the inflow volume increased dramatically.

The greatest increase in volume rate was seen between 0022 and 0030 UTC, during the first RFD surge and coinciding with Lagrangian vorticity becoming increasingly positive at the center of the vortex (Fig. 6.4f, i). This period also coincides with the development of a tornado vortex at the center of the broader mesocyclone flow, as seen in the raw radial velocity data from SR2 (Fig. 3.10). Therefore, while the mesocyclone maintained general two-celled structure, the low-level inflow volume rate was sufficient to concentrate vorticity over a shallow depth on the tornado-cyclone scale.

Meanwhile, as the inflow volume increased, the RFD was shifting westward, in association with the strengthening midlevel circulation (Chapter 5). Streamlines during this period, 3-5 km north of the mesocyclone, were highly confluent upstream of the RFD (Fig. 6.4i, Fig. 6.5c, f), suggesting that as the RFD shifted westward and intensified, the outflow was diverted southward into the outer portions of the low-level mesocyclone. As the mesocyclone entered the occlusion stage (around 0045 UTC), the RFD expanded and began shifting back eastward, corresponding to a rapid decrease in inflow depth and volume (Fig. 6.7). Thus, the RFD position and the inflow volume appear to be strongly correlated.

Lewellen and Lewellen (2007) hypothesized that a previously unattributed role of the RFD in the tornadogenesis process is for the downdraft to transport high-angular

momentum air towards the ground, cutting off the influx of low-angular momentum air into the circulation and thus instigating corner-flow collapse on the mesocyclone-scale. While such a mechanism does not appear to have been a factor during the intensification and transition phase, the rapid inflow depth decrease did precede a decrease in the size of the mesocyclone-scale circulation at low-levels. Regrettably, a more detailed investigation of this mechanism requires substantially more observations in the lowest 500m of the atmosphere.

The decreased inflow rate was short-lived, as the second RFD surge corresponded to an increase in the inflow rate and depth between 0045 – 0055 UTC. A new, more significant tornado formed around 0052 UTC and appeared to last for about 25 minutes before dissipating (Chapter 3).

Additional insight to mesocyclone trajectory behavior can be gleaned from examining backward trajectories initialized in the same framework as that used for the inflow volume rate estimate. Backward trajectories were initialized every 2 minutes in the same three-dimensional, vortex-following volume. Instead of estimating the inflow volume, the backward trajectories were used to estimate the fractional amount of air parcels trapped in the mesocyclone flow by determining the fraction of trajectories that maintained vertical vorticity greater than 0.15 s^{-1} throughout the 300 s backward integration. The fraction of trajectories trapped in the circulation during this period helps distinguish whether the mesocyclone was a one or two-celled vortex. The time-height plot of the fraction of trapped air parcels (Fig. 6.8) is amazingly consistent with the axial tendencies presented in section 3. The circulation was diagnosed as a two-celled vortex prior to 0034 UTC. During the two-celled stage, rising motion was

suppressed along the circulation axis below 4 km (Fig. 6.4a), resulting in at least 50% of the mesocyclone trajectories being trapped in the circulation below 1 km. The trapped air reached a maximum fraction at 0028 UTC of 80 percent near the ground, coincident with the strongest axial downdraft (Fig. 6.4g). Above 1 km, the fraction of trapped air remained at 40 percent or below until 0028 UTC when it uniformly rapidly increased between 1 and 3.5 km altitude. The circulation briefly consisted of at least 60 percent trapped air parcels from the ground up to 3 km just prior to transitioning from a two-celled vortex to a one-celled vortex (Fig. 6.8).

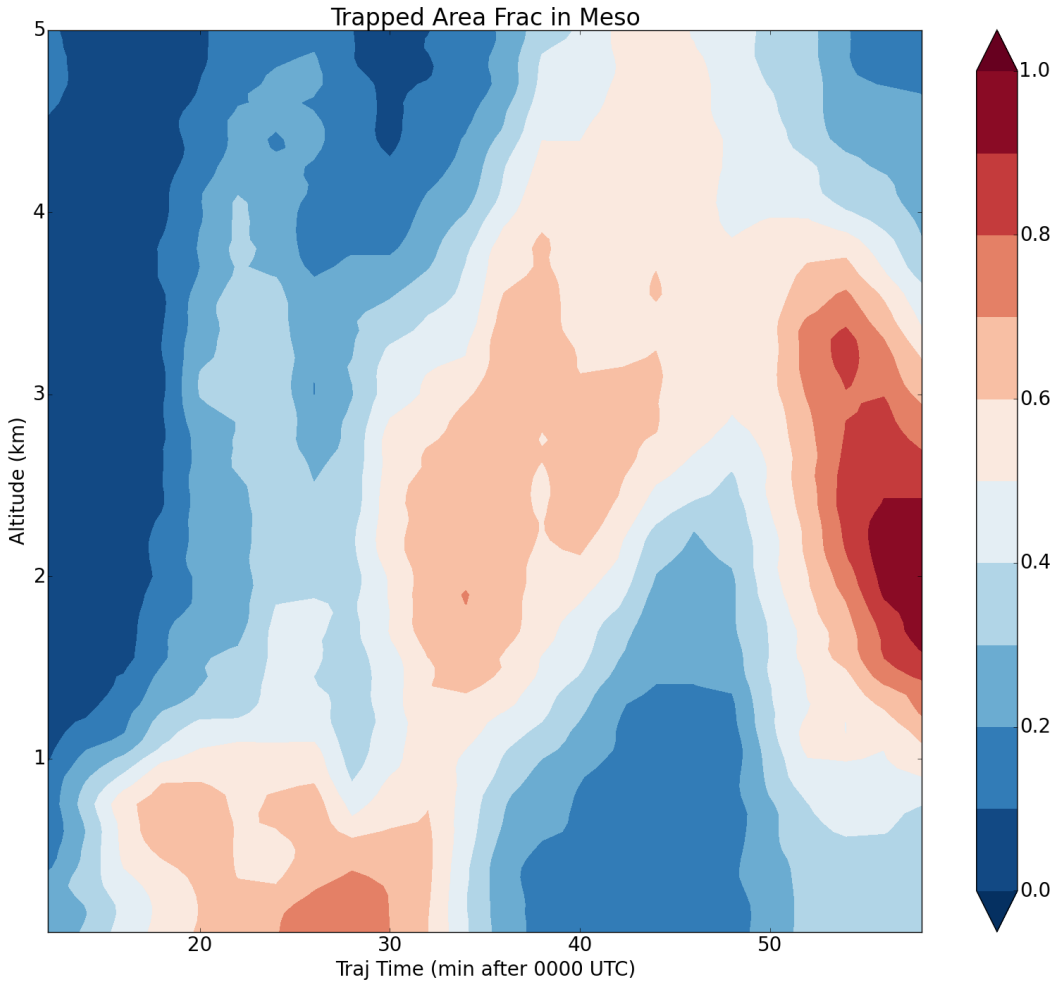

Fig. 6.8 Time-height plot of the fraction of backward trajectories that remained in the mesocyclone (> .015 s^{-1}) for at least 300s.

After 0034 UTC, the mesocyclone exhibited behavior consistent with a one-celled vortex. As the axial vertical velocity tendency became positive (Fig. 6.5a, d, g), new air was rapidly drawn into the low-level mesocyclone and the fraction of trapped air below 1 km altitude dropped to 20-30 percent by 0036 UTC. However, the fraction of trapped air between 1-3 km altitude quickly increased again after 0050 UTC during the occlusion stage and around the onset of the significant tornado. This increase in trapped air aloft was also coincident with descending trajectories becoming more prevalent near the circulation axis (Fig. 6.6d, g), suggesting that the vortex was developing a two-cell structure again.

6.4 Evolution of circulation along material circuits

Many previous studies (Rotunno and Klemp 1985; Davies-Jones and Brookes 1993; Markowski al. 2014) have utilized the circulation conserving property of material circuits to reveal sources of rotation in the mesocyclone. According to Bjerknes theorem (Eliassen and Kleinschmidt 1957), only baroclinic zones and turbulent mixing can modify circulation around a material circuit, therefore preserving the initial environmental value. Material circuits are particularly useful for observationally-based studies (Dowell and Bluestein 1997 and Markowski et al. 2012a,b) as averaging the behavior of thousands of trajectories, rather than an individual trajectory, helps to mitigates analysis errors. In the present study, material circuits were generated by initializing a ring of trajectories with an average initial spacing of 20 m and integrated backwards 1200 seconds in time. Following Markowski (2016), new trajectories were added where the spacing between adjacent trajectories exceeded 25 m, therefore

ensuring an accurate estimate of circulation and a smooth material circuit in the presence of strong deformation.

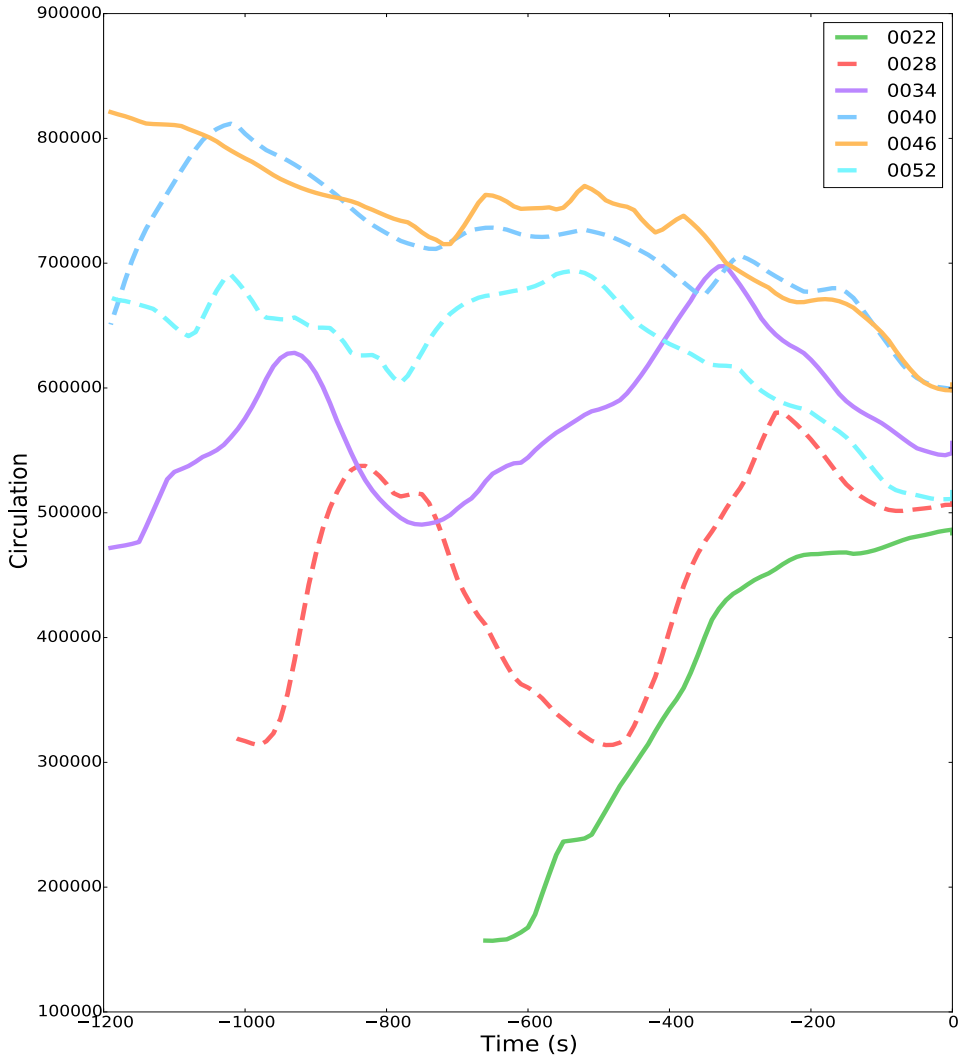

Fig. 6.9 Circulation following material circuits integrated backwards in time and initialized at an altitude of 1 km and a radius of 3 km. Each time series is presented relative to the initial trajectory time and is terminated after 1200 seconds or when the trajectory reaches 0012 UTC.

Despite limited vertical resolution near the ground and trapped airflow in the vortex, fundamental changes in circulation behavior can still be used to elucidate circulation generating processes. Material circuits were initialized at a radius of 3 km from the center of the mesocyclone at an altitude of 1 km for six different analysis times

summarized in Figure 6.9. The earliest available material circuit, 0022 UTC (Fig. 6.10a), reveals that circulation increased dramatically as the circuit passed through the forward flank of the storm. This finding is consistent with observations from Markowski et al. (2012b) and simulations by Rotunno and Klemp (1985), both of whom found that the behavior was indicative of baroclinic generation of horizontal vorticity in the forward flank of their respective supercell storms. It should be noted that the inability to trace the full circuit back to the environment introduces some ambiguity into the magnitude of the baroclinic generation of circulation along this circuit.

As the mesocyclone shifted into the mature stage, material circuits at 0028 and 0034 UTC experienced significant oscillations in magnitude (Fig. 6.9), but experienced net circulation increases of 40 percent and 10 percent, respectively, over the previous 1000 seconds. Reduced circulation growth in the material circuits may imply a decreasing role in the baroclinic generation of circulation. After 400s (Fig. 6.10b, c), both circuits encompassed significantly more area in the inflow region than the earlier circuit, potentially suggesting a transition in the source region. However, a significant portion of the circuit remained in the hook region, leaving open the possibility that circulation had been baroclinically generated in the past.

The transition to a one-celled mesocyclone structure was accompanied a dramatic shift in the circuit behavior as material circuits initialized at 0040, 0046, and 0052 UTC experienced decreasing circulation in time (Fig. 6.9). Amazingly, the circuits initialized at 0040 and 0046 UTC had nearly identical circulation histories, which is impressive considering the variability observed in the other circuits.

Horizontal traces of the material circuits reveals that as rising motion was favored in the low-level mesocyclone, the circulation was drawing air from a larger, more symmetric region (Fig. 6.10d, e).

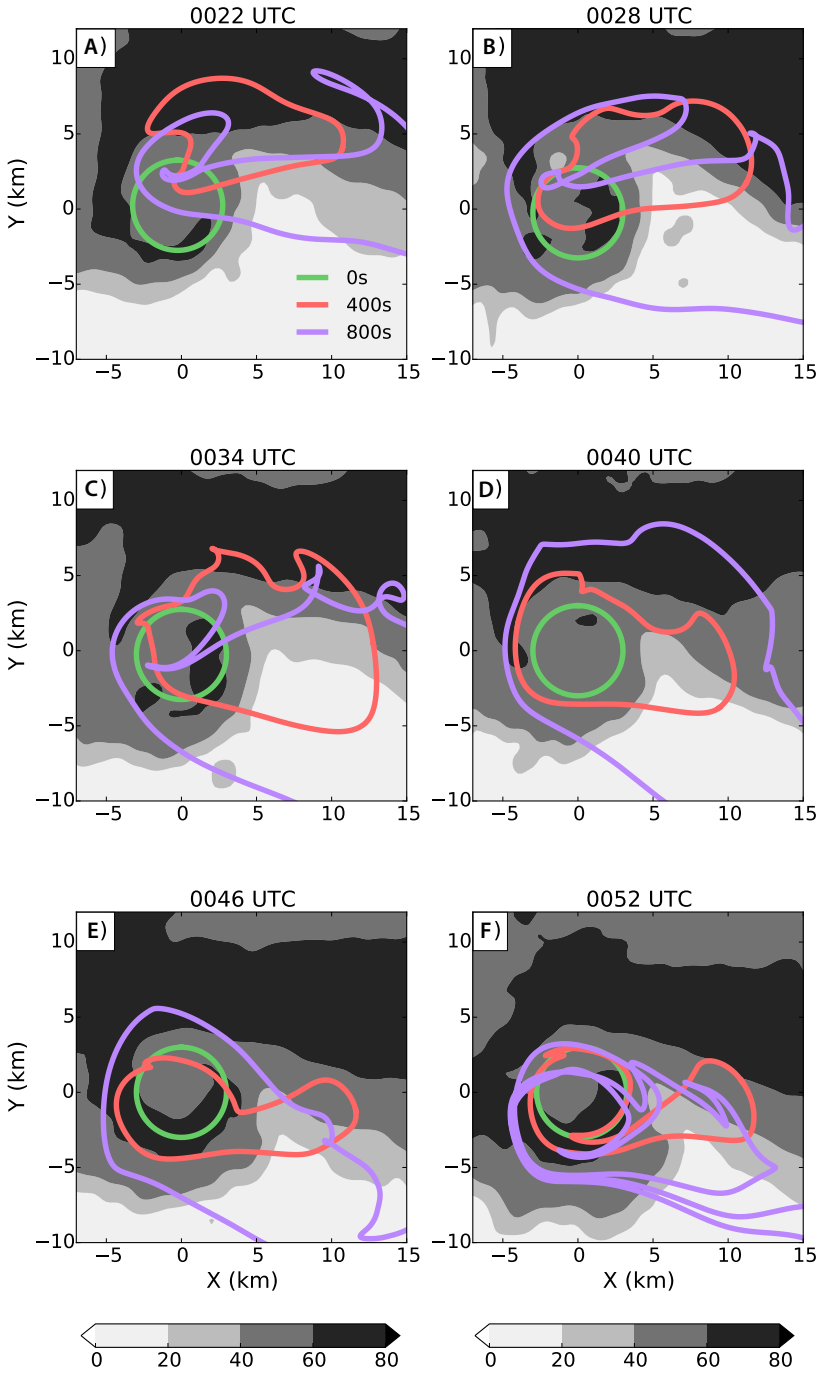

Fig. 6.10 Snapshots of the material circuits presented in Figure 6.9. The circuits are colored based on the integration time, green (0s), red (200s), and purple (400s). Radar reflectivity at an altitude of 1 km is contoured in shades of grey.

6.5 Evolution of Source Regions

6.5.1 Source Regions

Traditional trajectory analysis of mesocyclone air parcels is used to illustrate representative trajectories that enter the mesocyclone and contribute to the analyzed vorticity. However, individual backward trajectories are prone to error growth in strong confluent zones (Dahl et al. 2014). This is problematic because much of the air in the mesocyclone passes through strong confluence on the north side of the circulation that deforms the broad flow regime into a narrow stream entraining into the mesocyclone. Fortunately, error growth can be limited by mapping out future mesocyclone trajectories following Betten et al. (2017) whereby forward trajectories are initialized on a regular grid and future trajectory behavior is illustrated at their initial locations. The resulting future maximum vertical vorticity can then be used to elucidate which forward trajectories acquire mesocyclone level vertical vorticity. Trajectories entering the mesocyclone vortex can be isolated from those entering the midlevel mesocyclone embedded in the updraft through limiting the distance from the vortex and the altitude at which the trajectory gains vorticity. The isolation of future vorticity to the mesocyclone vortex is especially important for forward trajectories initialized in the inflow sector.

A volume of trajectories covering the entire analysis domain was initialized on a regular grid with a horizontal spacing of 250 m and a vertical spacing of 50 m extending up to 1500 m AGL. Trajectories had to gain at least 0.015 s^{-1} of vertical vorticity over the next ten minutes below an altitude of 2 km to be defined as a future, the low-level mesocyclone trajectory. At every horizontal grid point, attributes of the forward trajectories initialized in the columns were averaged together for those trajectories that

reached the mesocyclone. In the subsequent figures (12,14,17-19), only grid points with future mesocyclone trajectories in the vertical column have been color shaded. A logarithmic wind profile was explored assuming a neutrally stratified boundary layer, as in Markowski et al. (2012), but did not show any structural difference in forward trajectory maps than those using the zero-shear assumption.

In the first example, the mean initial altitude of future mesocyclone air parcels has been overlaid on top of reflectivity and contours of vertical vorticity at an altitude of 1 km (Fig. 6.11). Future mesocyclone trajectories were primarily found in three regions during the early mature stage (0016 UTC), the first region was located on the north and northwestern side of the circulation (c.f., Fig. 6.11a, x=-1, y=4) and fed into the occlusion updraft prior to entering the low-level mesocyclone. Trajectories in this region had a mean initialization altitude of 500 m, extending up to 1000 m. The second source region was located in the inflow region near or in the forward flank reflectivity gradient (Fig. 6.11a, x=10, y=0). In contrast to the first region, these trajectories originated primarily in the lowest 150 m above which trajectories rose too quickly to gain substantial vertical vorticity below 2 km in altitude. A third region is also apparent, just behind the main RFGF on the southeast side of the circulation (Fig. 6.11a, x=2, y=-2), where air parcels had previously descended in the occlusion downdraft after previously residing in the mesocyclone at higher altitudes. Although the inflow source region expanded north and south during the mature stage (Fig. 6.11b, c, d), the general structure remained persistent. The primary difference was found in the forward flank where source altitude averaged 250 m (Fig. 6.11b, x=10, y= 6).

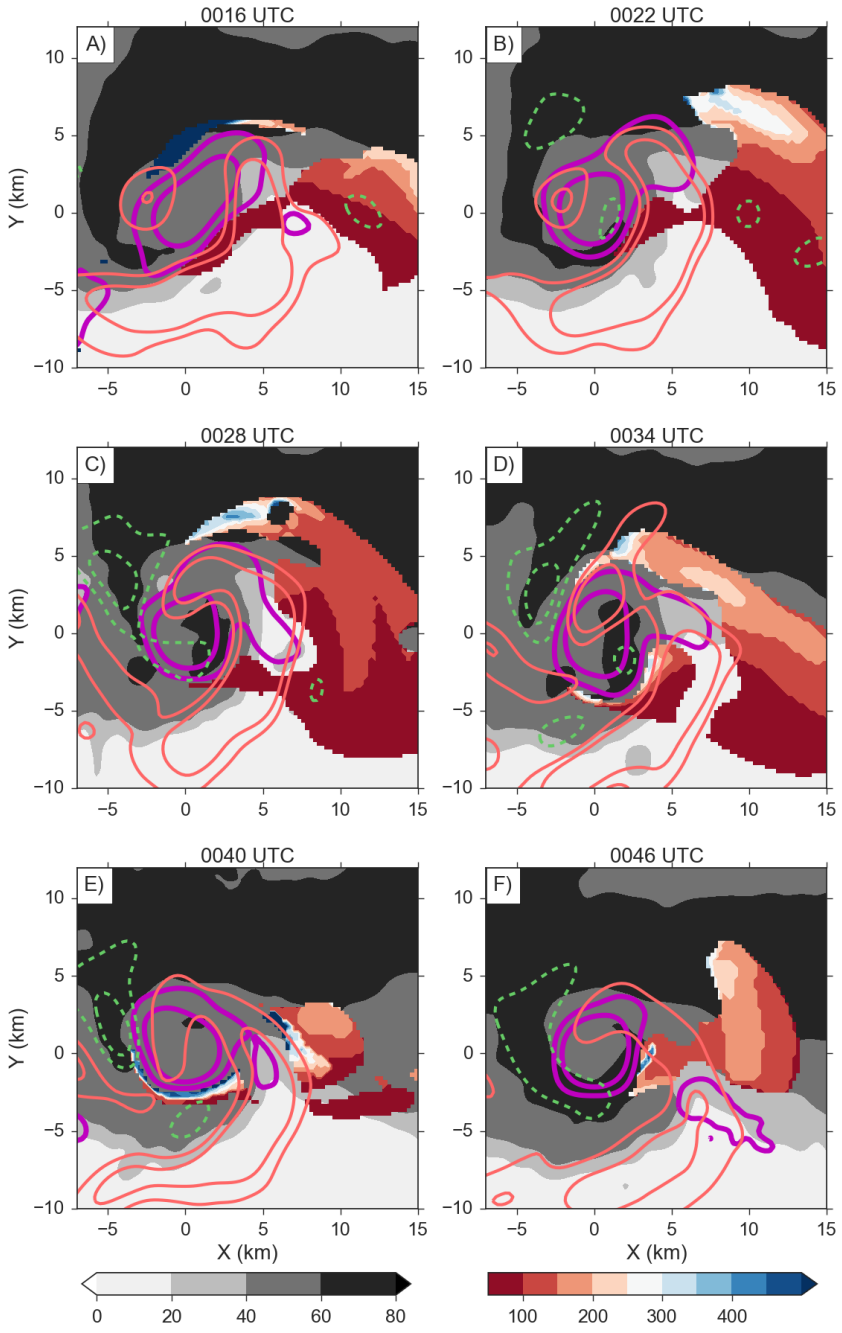

Fig. 6.11 Column average of the initial altitude (in meters) of future mesocyclone trajectories has been color-shaded. Only grid points with future mesocyclone trajectories have been color-shaded Unlike previous figures, the grid origin is centered on the mesocyclone. Vertical vorticity at an altitude of 1 km is contoured in purple (at 0.01, 0.02 s^{-1}), positive vertical velocity in red (at 5, 10 m s^{-1}), negative vertical velocity in dashed green (at -5, -10 m s^{-1}), and radar reflectivity is contoured in shades of grey.

The time just prior to the onset of the occlusion stage (~0040-0045 UTC) was marked by a rapid reduction in the horizontal expanse in future mesocyclone trajectories (Fig. 6.11e) as air parcels were rapidly cutoff from entering the mesocyclone north of the mesocyclone and in the unmodified inflow region. As previously noted, after 0040 UTC, the weakening of the RFD was reflected in the veering of the winds on the north side of the circulation (Fig. 6.5f, i), reducing the inflow. Additionally, as the primary updraft shifted southward, the forward flank reflectivity core also shifted southward, such that by 0040 UTC, the entire source region was contained within the 20 dBZ contour (Fig. 6.11e). While the occlusion of the circulation is often connected to the wrapping of cold air around the southern and eastern edge of the circulation, the primary manifestation of the onset of the occlusion stage in this case was the rapid concentration in the source area of mesocyclone air to the region just along the strong reflectivity gradient in the forward flank of the storm just east of the updraft inflow notch in radar reflectivity Fig. 6.11 e, x=5, y=0). The shrinking inflow area is also reflected in the material circuit initialized at 0046 UTC (Fig. 6.10f), reinforcing the idea that the mesocyclone was drawing in air from an increasingly smaller area during the onset of the occlusion process leading up to tornadogenesis at 0052 UTC.

6.5.2 Influence of Downdraft Divergence on Source

The influence of the RFD on the low-level mesocyclone behavior can be elucidated through trajectory maps of future maximum divergence, here initialized at 500 m (Fig. 6.12). Individual forward trajectories were initialized in the forward flank at constant, mesocyclone-relative locations to reveal how they respond to changes in the downdraft. In each analysis, three trajectories were initiated at varying ranges from the

circulation center to the northeast, north-northeast, and north of the mesocyclone. As documented in Chapter 5 and shown in Figure 6.13, the rainy downdraft portion of the RFD didn't appear until after 0019 UTC and thus trajectories during the early mature stage (Fig. 6.12a) didn't experience significant divergence. In general the trajectories maintained their distance away from the circulation center as they flowed around the storm-scale mesocyclone. However, as the downdraft developed (Fig. 6.13b, x=-2, y=6), the influence of the divergence was felt over a large region, represented as a cyclonically curving streak in the future divergence field (Fig. 6.12b, x=1, y=8). Trajectories initialized just south of the divergence region, represented by the easternmost initiated 8 km (purple) trajectory, were abruptly directed southward after the development of the downdraft and merged with air parcels originating further south (Fig. 6.12b, x=-2, y= 4). In other words, the air in this region was forced southward by the divergence associated with the rainy downdraft.

As the RFD strengthened and impinged on the outer portions of the mesocyclone during the first surge (Fig. 6.13 c, d), the future maximum divergence intensified and was closer to the northwestern edge of the mesocyclone (Fig. 6.12 c, d). Again, air trajectories that were initiated or traveled along the southern and eastern edge of the divergence zone were forced in towards the circulation center with time (Fig. 6.12 c). Indeed, throughout the period, the mesocyclone inflow region did not overlap with the future maximum divergence streak, even as it shifted closer to the circulation with time (Fig. 6.13c, d). Moreover, as the influence of the RFD divergence expanded eastward and southward with time (Fig. 6.12e, f), fewer forward trajectories were being diverted into the mesocyclone flow (Fig. 6.13e, f).

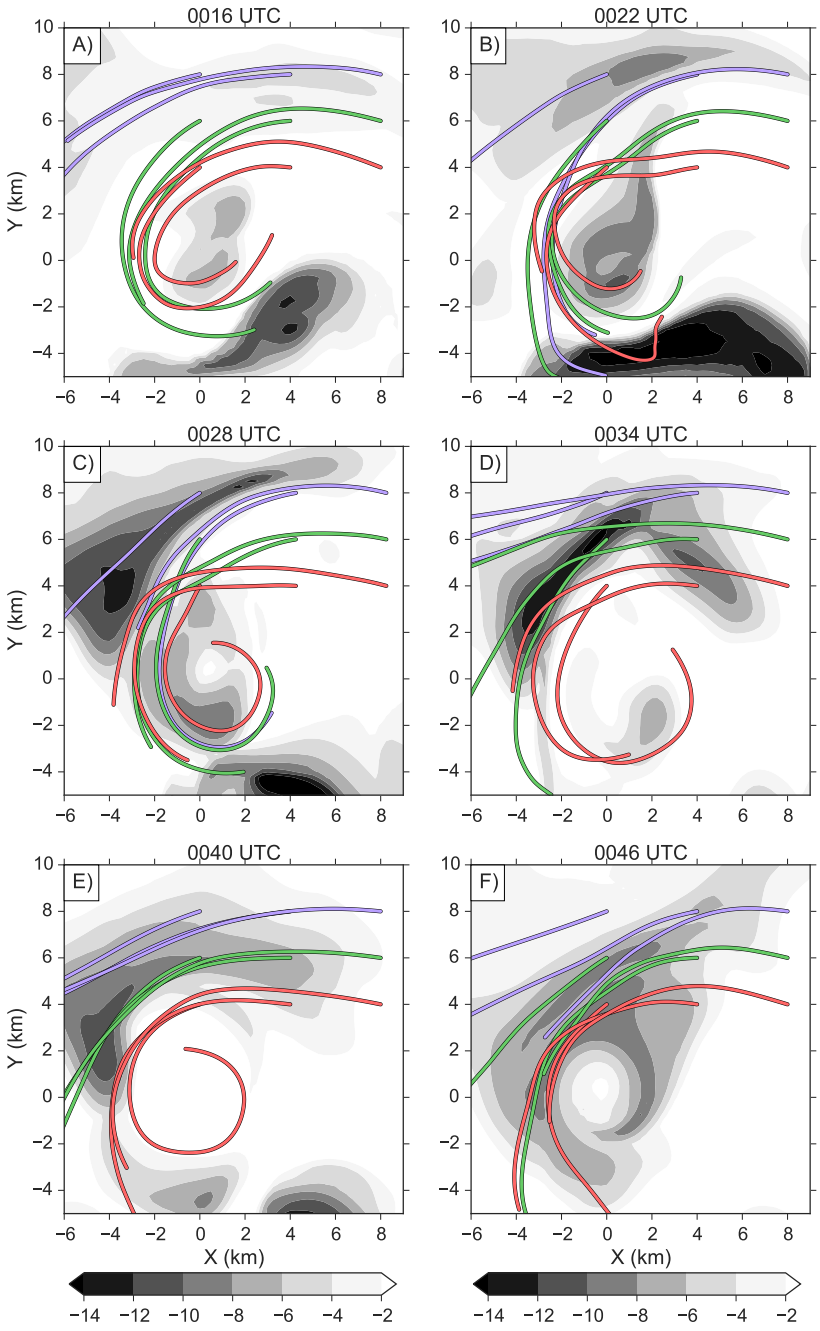

Fig. 6.12 Trajectory map of future maximum divergence ($1x10^{-3}$ s^{-1}, contoured in shades of grey according to the scale) over the next 300 seconds for forward trajectories initialized at 500 m altitude at their initial positions. Horizontal traces of individual forward trajectories, also initialized at 500 m, are overlaid with colors indicating trajectories initiated along constant values of y. Purple, green, and red lines indicate initiation meridional positions of 8, 6, and 4 km respectively.

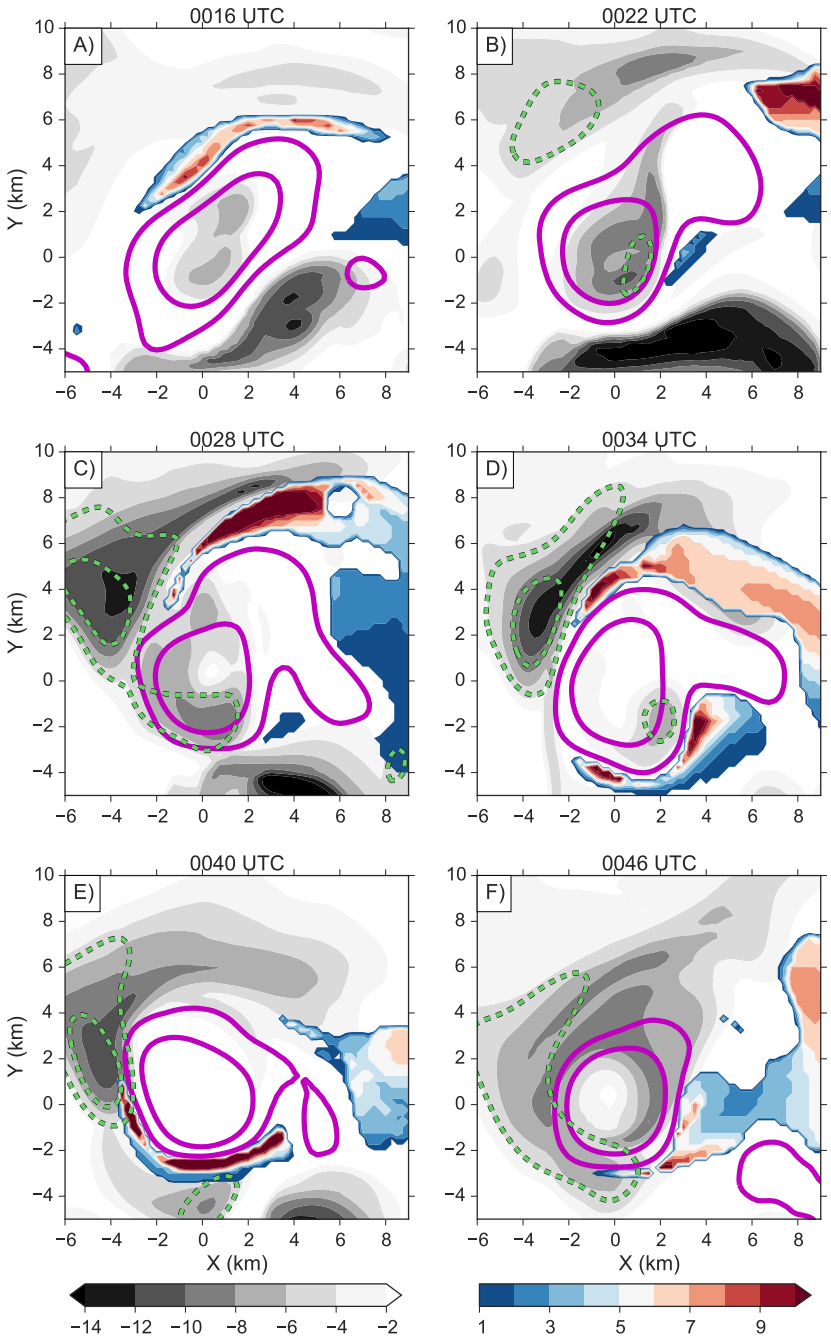

Fig. 6.13 Grey contours indicated maximum future divergence as in Fig. 6.12. Total number of future mesocyclone trajectories in the vertical column is color-shaded. Negative vertical velocity at an altitude of 1 km is contoured in dashed green (-5, -10 m s^{-1}) and vertical vorticity in solid magenta (.001, .002 s^{-1}).

In association with weakening of the midlevel storm-scale circulation, the RFD and occlusion updraft both weakened after 0040 UTC resulting in forward trajectories maintaining their distance from the vortex as they flowed around it (Fig. 6.12e), as they

had done during the early mature stage (Fig. 6.12a). Even forward trajectories initialized just northeast of the circulation (Fig. 6.12e, f, x=4, y=4) wrapped around the outside of the circulation in contrast to those trajectories that entered the circulation during the previous 20 minutes. Therefore, the development of the rainy downdraft and the intensification of the RFD can be directly correlated to the expansion of the mesocyclone source region and inflow volume rate, as the RFD divergence field forced air to converge into the mesocyclone that was previously remaining at larger radii from the mesocyclone. The individual trajectories demonstrate a sharp distinction in flow behavior across the future maximum divergence gradient, implying a sharp separation between air parcels that flow beneath the RFD and those that were ingested into the low-level mesocyclone.

Between the first and second RFD surge (0032 – 0045 UTC), there was a well-defined mesocyclone source region diagnosed from the trajectory analysis along the southern and southeastern outer edge of the mesocyclone (Fig. 6.13 d, e, f). This source region was closely related to the future maximum divergence boundary associated with occlusion downdrafts. Hence, the divergence field from the occlusion downdraft also helped force neighboring air trajectories inward towards the center for the mesocyclone.

Noticeably absent during the mature to early occlusion stage of the mesocyclone were mesocyclone source regions originating from the rear-flank downdraft region itself. The lack of resolution in the lowest 500 m may have limited the diagnosis of RFD air being entrained into the circulation at low levels. However, sensitivity tests using a logarithmic wind profile below 500 m to allow for shear below the lowest analysis level did not significantly change the patterns seen in Figures 6.11-6.13.

Strong northerly flow north of the circulation would have been required to direct downdraft air into the low-level mesocyclone. In contrast, northeasterly streamlines emanating from the RFD (see Chapter 5 and Fig. 6.4c) indicate that the outflow from the RFD had already acquired storm-scale cyclonic rotation. Hence, the storm-scale circulation heavily influenced the low-level flow extending out at least 10 km from the mesocyclone center (Fig. 6.4c).

Also absent from the mesocyclone source regions were air from the forward flank downdraft. As demonstrated in Chapters 3 and 5, an organized low-level downdraft never developed in the forward flank region. The strength of the storm-scale circulation and the lack of organized forward flank downdrafts combined to allow the mesocyclone to primarily ingest inflow or modified inflow air. In a storm without a significant storm-scale circulation, the wind field north of the low-level circulation would likely be less cyclonic and more aligned with the divergence field from the downdrafts.

6.6 Preferred Tilting Zones

6.6.1 Tilting Zones

Previous studies have indicated that air reaching the low-level mesocyclone originated behind the forward flank gust front (Rotunno and Klemp 1985; Wicker and Wilhelmson 1995; Adlerman et al. 1999; Dahl et al. 2014) or from downdrafts in the rear-flank (Schenkman et al. 2014; Dahl et al. 2014). Moreover, all the studies agree that the tilting of horizontal vorticity occurred at low-levels and on the north or western sides of the circulation. In contrast, future mesocyclone trajectories in the Geary supercell suggest that air originated in the inflow and southern forward flank regions.

The size of the circulation and the presence of positive vertical vorticity along the primary RFGF, suggest that tilting was occurring over a broad area. Coarse resolution at low-levels makes it difficult to correctly estimate where tilting is occurring and which tilting zones are most important for trajectories going into the circulation. Nevertheless, tilting will be examined using both a Eulerian and Lagrangian perspective to investigate this process for the Geary storm.

Throughout the entire mature stage of the mesocyclone, positive tilting was generally maximized where the RFGF bowed out producing a southeastward protrusion in the primary updraft at low-levels (c. f., Fig. 6.14a, x=7, y=-4). Additionally, positive tilting was also observed on the north side of the circulation downstream from the forward flank source region (Fig. 6.11a). However, the tilting pattern near the mesocyclone varied with time in contrast to the steady positive tilting along the RFGF (Fig. 6.14). At 0034 UTC, the mesocyclone region tilting extended farther northeastward to include the inflow notch on the updraft side of the horizontal rotor (Fig. 6.14d, x=2, y=5) identified in Chapter 3 where ample streamwise vorticity was available to tilt. A third region of positive tilting of horizontal vorticity appeared at 0028 UTC, located in the area between the RFD and the western updraft documented in Chapter 3. Additional short-lived pockets of positive tilting were diagnosed in gradients of vertical motion between the occlusion downdraft and primary updraft at 0028 UTC (Fig. 6.14c, x= 1, y = -4) and occlusion downdraft and western updraft at 0040 UTC (Fig. 6.14e, x= -2, y = -4). It is possible that limited vertical resolution of data near the surface contributed to the temporal variability in tilting regions, which could lead to misinterpretation of the most important regions of tilting. Fortunately,

forward trajectory behavior can be used to further elucidate the regions in which tilting was essential to the development of vertical vorticity.

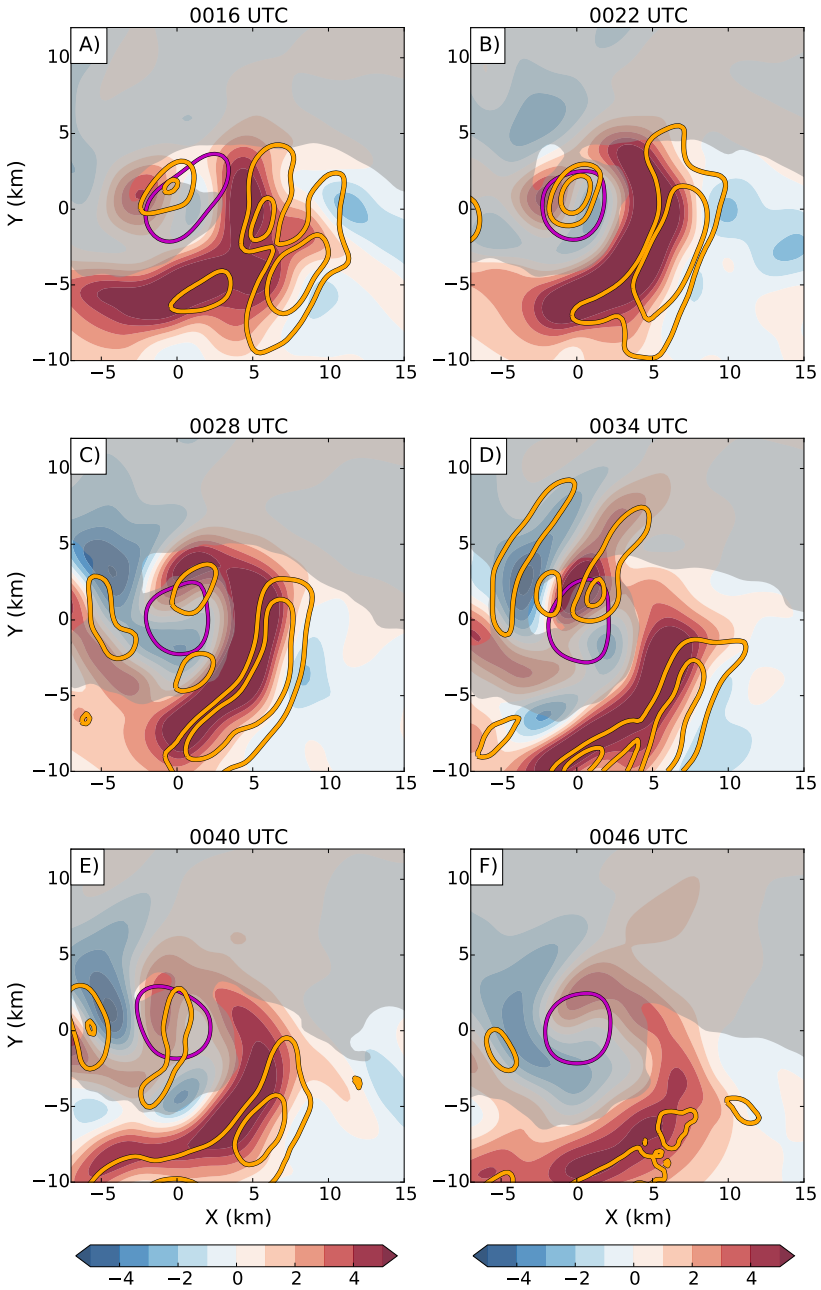

Fig. 6.14 Contours of positive Eulerian tilting of horizontal vorticity into the vertical (yellow, every 1X10^{-5} s^{-2}) at an altitude of 500 m for different times are overlaid on color-shaded contours of vertical velocity (in m s^{-1} according to the color scale) at the corresponding time. The concurrent 0.02 s^{-1} vertical vorticity contour is colored in magenta.

6.6.2 Lagrangian Tilting Zones

Estimates of vertical vorticity are likely more robust than horizontal vorticity due to horizontal vorticity naturally have strong gradients near the ground. Indeed, previous studies showed significant tilting often occurs below an altitude of 500 m (Wicker and Wilhelmson 1995; Adlerman et al. 1999). Therefore, a trajectory mapping technique is introduced whereby the mesocyclone-relative location of forward trajectories is recorded at the moment that they gain substantial vertical vorticity, thus creating a proxy for the low-level tilting location. Since the scale of the horizontal gradients in vertical vorticity is better resolved than vertical gradients in horizontal vorticity near the ground, the tilting proxy can elucidate important tilting regions from a qualitative perspective that might otherwise have been misdiagnosed due to the vertical resolution of data near the surface. In this manner, the proxy tilting zone can elucidate which Eulerian tilting regions are most important. Due to the smoothness of the wind analysis, a value of $5X10^{-3}$ s^{-1} was chosen as the criteria for the contoured tilting region and 0.015 s^{-1} was again defined as the mesocyclone level vorticity.

Throughout the end of the developing and entire mature stage of the mesocyclone lifecycle (0016 – 0045 UTC), air parcels were gaining substantial vertical vorticity northeast of the mesocyclone along the RFGF (Fig. 6.15a-e, x=5, y=1 to 5 km). This region was diagnosed in the Eulerian reference frame analysis during the early portion of this period (Fig. 6.14a, b), but not during the later periods. While this region has not been highlighted by previous numerical modeling studies, vertical vorticity was consistently found extending along the RFGF, especially at 0028 UTC (Fig. 6.13c, x=4, y= 2). Interestingly, Dowell and Bluestein (2002a) found similar low-

level vorticity structure during tornado #4 of the Mclean storm (see their Fig. 6.7d), with positive low-level tilting also evident along the northeastern portion of the RFGF and a few backward trajectories originating in the inflow. These storms may represent only a small portion of the supercell spectrum, as they were both cyclic tornadic supercells with large storm-scale rotation.

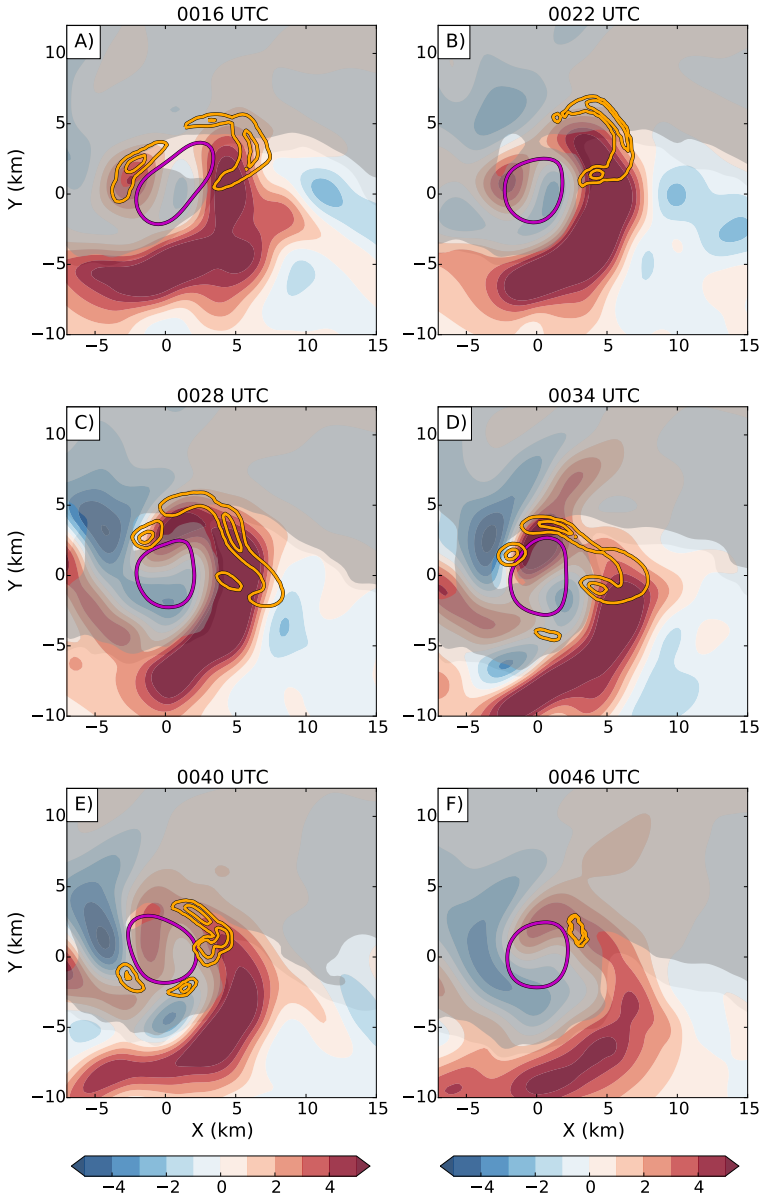

Fig. 6.15 Same as Fig. 6.14 except for the proxy tilting inferred by aggregating the locations that forward trajectories first gain substantial vertical vorticity. Contours of proxy tilting indicate regions of enhanced trajectory kernel density.

Prior to the occlusion stage before 0045 UTC, inferred tilting was also consistently found in the more the traditional tilting zone on the northwestern side of the circulation (Fig. 6.15a, x=-3, y=2) in agreement with the numerical simulations. This region was briefly collocated with positive Eulerian tilting at 0016 and 0034 UTC, supporting the legitimacy of the proxy analysis. Between 0028 and 0034 UTC, trajectories gained initial substantial vorticity along or near the horizontal rotor axis (Fig. 6.15c, d x=-1, y=3). Just prior to the onset of the occlusion stage, this region shifted cyclonically to the edge of the secondary RFGF (Fig. 6.15e, x=-4, y=-1), which was located near an elongated region of analyzed positive tilting (Fig. 6.14e, x=0, y=-2). Radar analyses presented by Kosiba et al. (2013) revealed a similar tilting region along the secondary RFGF just south of the developing tornado in their case.

The inferred tilting zones can be connected to the previously identified mesocyclone source regions through averaging the mesocyclone-relative, inferred tilting east-west position over the column of future mesocyclone trajectories (Fig. 6.16), similar to the average source altitude (Fig. 6.11). Throughout the mature stage of the mesocyclone, a strong gradient in future tilting location was present (Fig. 6.16b, c, d). Trajectories originating in the inflow south of the forward flank ~50 dBZ reflectivity region were tilted on the eastern side of the circulation (positive values; c.f., Fig. 6.16a, x=10, y=0), whereas those initialized in the higher reflectivity portions of the forward flank were tilted on the western side of the circulation (negative values, Fig. 6.16b, x=10, y=7). The two source regions were clearly and consistently divided along the forward reflectivity gradient even as it shifted north and south, relative to the low-level mesocyclone. It is interesting to note that reflectivity values around 50 dBZ typically

separate heavy rain from rain mixed with hail in this portion of supercell storms (Kumjian and Ryzhkov 2008).

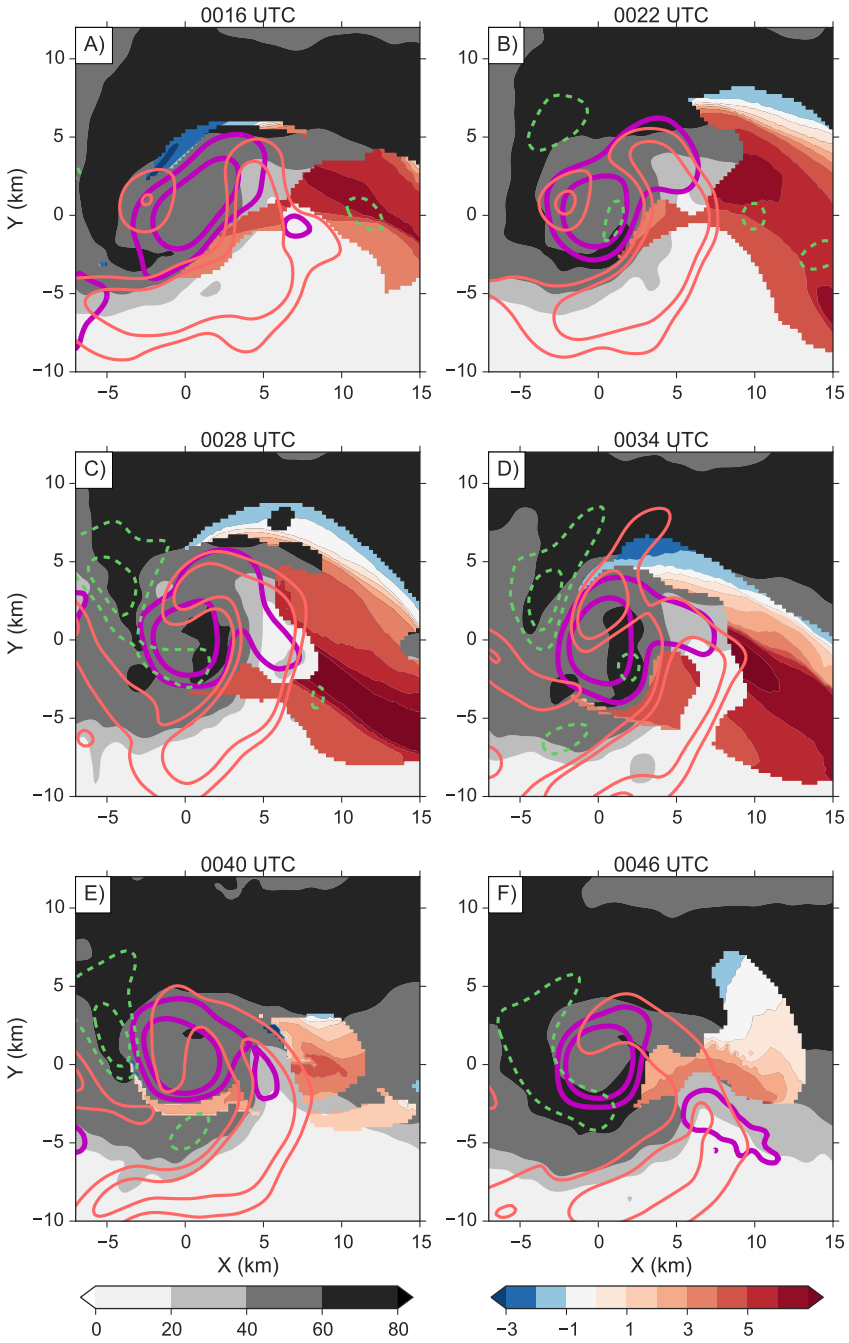

Fig. 6.16 Similar to Fig. 6.11 except for the column mean east-west location, relative to the center of the mesocyclone, where the inferred tilting of horizontal vorticity took place. Warm colors indicate trajectories tilted on the east or northeast of the circulation center, while cool colors indicate that tilting took place on the west or northwest side of the circulation.

Only trajectories that had been in heavy precipitation with strong reflectivity gradients for prolonged periods had inferred tilting on the northwestern side of the circulation. These trajectories likely gained some baroclinically generated horizontal vorticity, in part due to the gradient in precipitation loading as well as possible thermodynamic gradients. While vorticity budgets along the trajectory path are limited by the vertical resolution of the data near the surface, the history of the air parcels and the tilting location in the forward flank are consistent with the so-called "feet-first" tilting method described by Davies-Jones and Brooks (1993). Moreover, the inferred tilting occurred after the trajectories turned cyclonically in what Davies-Jones et al. (2001) referred to as the "river-bend" effect, whereby cross-wise vorticity is exchanged into streamwise vorticity. Therefore, it appears likely that air parcels originating in the southern forward flank were gaining vertical vorticity in a manner consistent with previous studies.

In contrast, air parcels originating near the ground in the low radar reflectivity inflow consistently gained initial substantial vertical vorticity in the eastern inferred tilting zone along the RFGF. Additionally, these trajectories gained their vorticity prior to entering the "river-bend" region and would not have spent enough time in the storm to acquire much baroclinic horizontal vorticity. Therefore, it is likely these trajectories represent low-level environmental horizontal vorticity that was tilted as the air parcels were forced to rise over the gust front.

6.6.3 Individual Trajectory Examples

While the primary goal of this study has been to rely on bulk trajectory behavior to elucidate the storm evolution, carefully selected individual trajectories can still

provide valuable information that is difficult to illustrate as a trajectory map quantity. The following section will focus on two different individual forward trajectories to illustrate the behavior of air parcels that originated in the lower radar reflectivity inflow and those in the higher reflectivity forward flank or horizontal rotor. In both cases, forward trajectories were initialized at 0034 UTC, at the beginning of the intensification period and thus represent trajectories that reached the mesocyclone core during the intensification phase. Estimates of horizontal vorticity below 500 m are not considered robust due to the limited data availability below that level (only 1 grid point). However, vertical velocity gradients can be projected into the streamwise/crosswise planes to judge whether tilting of streamwise/crosswise vorticity was likely favored.

A forward trajectory representative of the lower reflectivity inflow source region was initialized at an altitude of 200 m and in a local maximum in future mesocyclone trajectory density (Fig. 6.17a, x=9, y=2). The trajectory originated in the near environment of the forward flank and passed through moderately heavy precipitation before entering the mesocyclone on the northeast side of the circulation (x=3, y=2). The trajectory first gained substantial vertical vorticity of at least 0.005 s^{-1} between 0036 and 0038 UTC (Fig. 6.17b, highlighted in grey) before reaching a peak of 0.035 s^{-1} a few minutes later due to intense stretching as the air parcel rose into the core of the mesocyclone. The initial acquisition of substantial vertical vorticity was coincident with a vertical velocity gradient primarily oriented in a streamwise manner (Fig. 6.17c, purple line), resulting in weak positive tilting of streamwise vorticity (Fig. 6.17d). Positive total tilting was observed at a slightly higher altitude (500 m, Fig. 6.17a, yellow contours) and reveals that the trajectory acquired vertical vorticity as it crossed the

positive tilting zone and got stretched in the occlusion updraft, enhanced by the rising motion of the rotor (Fig. 6.14d, x=0, y = 2.). Furthermore, material circuits traced back from 0040 UTC, revealed decreasing circulation with time, consistent with material circuits in the S12 simulation. S12 showed that the horizontal rotor's primary impact was to enhance the stretching taking place on the north side of the mesocyclone. Our analysis suggests a similar storm-scale structure and stretching process.

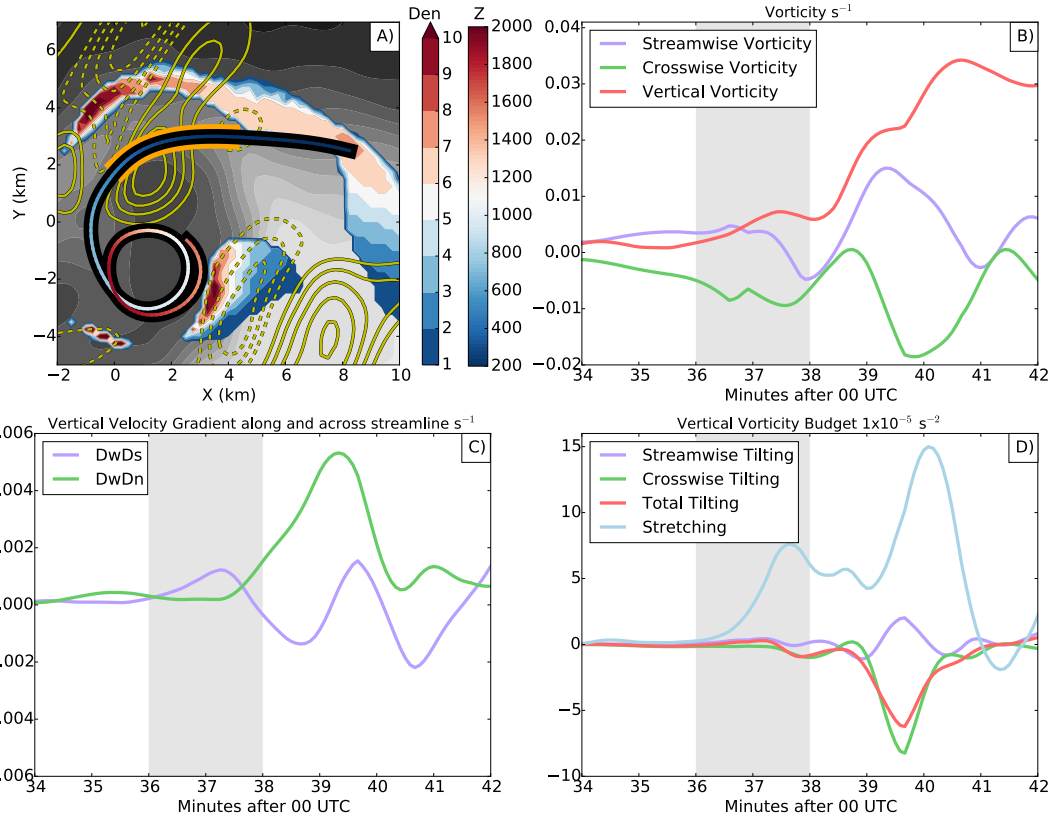

Fig. 6.17 Example forward trajectory, initialized at 0034 UTC at a height of 200 m in the modified low radar reflectivity inflow source region. The horizontal path is plotted in (a), colored by the trajectory altitude, with the period of interest highlight in orange corresponding to the period shaded in grey in (b-d). Radar reflectivity at an altitude of 1km has been grey-shaded (every 5 dBZ, starting at 0) and analyzed tilting of horizontal vorticity into the vertical is contoured in yellow (every 1X10^{-5} s^{-2}). Additionally, similar to Fig. 6.13, the total number of future mesocyclone trajectories in the column has been color-shaded. Time series along the example trajectory of vorticity (b), vertical velocity gradients in natural coordinates (c), and terms in the vertical vorticity budget (d) are presented.

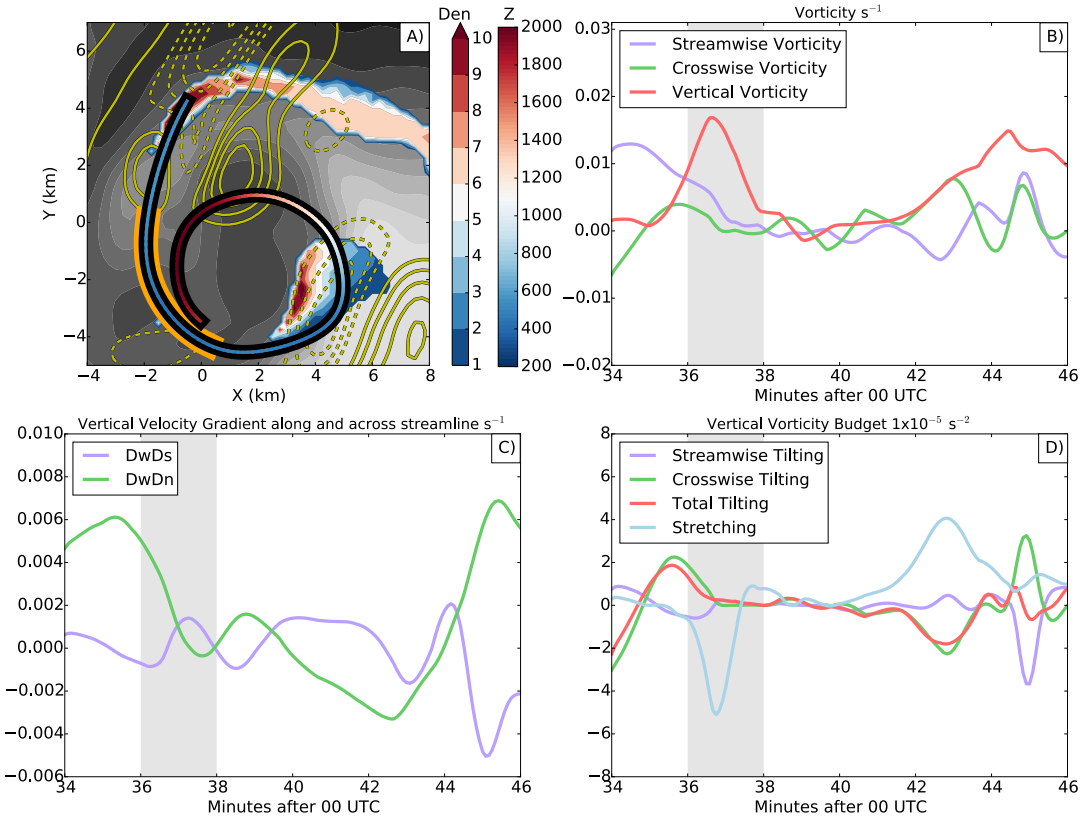

Fig. 6.18 Same as Figure 6.17 except the forward trajectory was initialized at a height of 500 m in the forward flank source region at 0034 UTC.

Forward trajectories initiated in the horizontal rotor along a path taken by a large number of future mesocyclone trajectories demonstrated more complex behavior (Fig. 6.18). Here, a forward trajectory was initialized at the peak column density (Fig. 6.18a, x=-1, y=4) at an altitude of 500 m in a higher radar reflectivity area. The air parcel passed through the outside of the circulation, briefly attaining a maximum vertical vorticity of $0.017s^{-1}$ (Fig. 6.18b) around 0037 UTC, before getting entrained into the occlusion downdraft and experiencing significant compression, reducing relative vertical vorticity to negative values. However, the trajectory remained in the storm-scale circulation and rose back into the circulation five minutes after the previous peak. This trajectory demonstrates the behavior of trajectories originating both in the rotor (Fig. 6.18a, x=-1, y=4) and in the region behind the gust front on the southeast side of

the circulation (Fig. 6.18a, x=4, y=-2). Trajectories initialized at larger radii from the center of the circulation (not shown) remained even further outside the circulation and did not reenter the circulation later. Therefore, while trajectories do enter the outside of the circulation after passing through the center of the rotor, the rotor source region appears to be a less important source for the inner core of the low-level mesocyclone than the lower radar reflectivity inflow region during the intensification stage.

Preceding the acquisition of significant vertical vorticity between 0035 and 0037 UTC (Fig. 6.18b), the trajectory experienced significantly stronger vertical velocity gradients across the streamline compared to along the streamline (Fig. 6.18c), resulting in the majority of the positive tilting occurring in the crosswise, rather than streamwise, direction (Fig. 6.18d). Even assuming that the low-level horizontal vorticity magnitudes are susceptible to errors, the orientation of the horizontal vertical velocity gradient suggests that the tilting of crosswise vorticity was favored among trajectories entering the mesocyclone from the rotor during this period. The lack of subsequent stretching after the occurrence of positive tilting, is consistent with the expected displacement of stretching and tilting which occurs when crosswise horizontal vorticity is tilted (Davies-Jones 1984). These results must be taken cautiously as the horizontal vorticity estimates at low-levels and in strong gradients of flow are not considered particularly robust and are inconsistent with previous simulations which all show that the northwestern sector of the mesocyclone is a region of positive, streamwise tilting. Additional observational cases with finer near surface resolution are needed to further evaluate this discrepancy between past simulations and this observation.

6.7 Summary and Discussion

The storm-scale vortex evolution, source regions of air entering the mesocyclone, and regions in which tilting led to the initial substantial gain in vertical vorticity have been examined for a long-lived mesocyclone in a cyclic tornadic, high-precipitation supercell that occurred on 29 May 2004 over central Oklahoma. The exceptionally long duration of dual-Doppler radar coverage allowed for the analysis of the mesocyclone over a prolonged period, which covered the mature and occlusion stages. Based on the axisymmetric and trajectory mapping framework analyses, a conceptual model that summarizes the evolution from the early mature stage through the occlusion stage of the tornadic mesocyclone in presented in Figure 6.19. Although the mesocyclone was dominated by rising motion during the organizing stage (Chapter 3, see Fig. 3.3b, d), the early mature stage of the mesocyclone took on a divided vertical velocity structure that favored the concentration of descending air parcels near the axis of low-level rotation (Fig. 6.19a). The position of descending air parcels is suggestive of a low-level mesocyclone with a two-celled structure, further supported by the fact that outside two km radius the vertical gradient in circulation was found to be negative throughout the two-celled period, consistent with the relationship between vertical circulation gradients and the vortex vertical velocity tendency found by Coffer and Parker (2017). Throughout the lifecycle of the storm, the occlusion downdraft was located on the edge of the mesocyclone, just inside of the radius of maximum winds. during the two-celled periods and just outside the core radius during one-celled behavior.

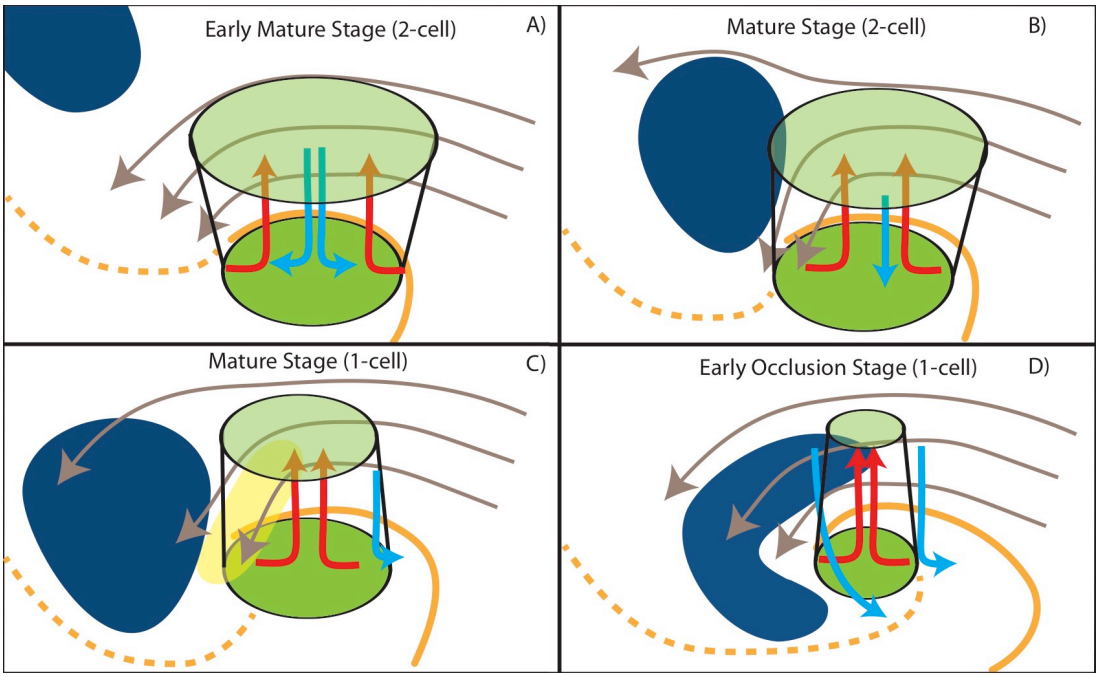

Fig. 6. 19 Conceptual model illustrating the position and evolution of the low-level mesocyclone flow (green circle with blue and red streamlines indicating descending and ascending air), RFD position (dark blue region), forward flank trajectory behavior (grey trajectories), and RFGF (SRFGF) are drawn in solid (dashed) orange lines. In (a), the early mature stage is drawn, illustrating the period when the mesocyclone exhibited two-cell vortex behavior and the main RFD was still positioned well to the northwest of the low-level circulation. In (b), the transition from the early mature to the mid-mature stage is instigated by the appearance of the first RFD surge, around 0028 UTC (Chapter 5), which causes the low-level forward flank trajectories to converge into the low-level circulation. In (c), the one-celled vortex period of the mature stage is drawn just after the transition has occurred, outwardly displacing the occlusion downdraft and coincident with the development of a horizontal rotor, drawn in transparent yellow. The occlusion stage (d) occurred as the RFD expanded and merged with the occlusion downdraft without disrupting the ascending axial flow in the mesocyclone, allowing it to maintain one-celled vortex structure. The increased outflow resulted in the surging out of the RFGF and the progression of the SRFGF around the southern and eastern sides of the circulation.

The next phase was initiated as the midlevel circulation strengthened and the midlevel convergence zone developed (see Chapter 5), resulting in the repositioning of the RFD to the northwestern periphery of the low-level circulation (Fig. 6.19b). Divergence from the repositioned downdraft channeled a swath of air from the forward

flank towards the south, enhancing low-level convergence and radial inflow around the circulation, causing the area of descending air in the low-level circulation to shrink. Further aloft, enhanced stretching aided in the intensification of the midlevel mesocyclone despite the low-level circulation maintaining a broad, two-celled structure (Fig. 6.5). The continued presence of the axial downdraft during the mature stage potentially prevented enhanced low-level convergence, from the RFD surge, from further concentrating the low-level circulation, as was seen later during the occlusion stage.

As the midlevel mesocyclone intensified faster than the low-level mesocyclone, the vertical gradient in circulation became negligible and thus no longer favored an axial downdraft. The modification of the axial tendency is reflected in the radially outward displacement of the occlusion downdraft and thus the transition of the mesocyclone from being two-cell in nature to being one-cell (Fig. 6.19c). Air parcels flowing out of the occlusion downdraft were now being directed outside the radius of maximum winds and primarily on the eastern side of the circulation. The tilt of the mesocyclone, rather than the vertical gradient in strength, was primarily driving the vertical pressure gradient at this stage. (see Chapter 5). This transition was also coincident with the counterclockwise shift of the RFD to being positioned on the west-northwest side of the circulation and the development of what appears to be a horizontal rotor, analogous in appearance to the rotor simulated by S12. Circulation budgets following forward integrated material circuits suggest that, similar to the S12 simulation, the rotor's primary contribution was to provide enhanced stretching on the

northwest side of the circulation, further encouraging the intensification of the low-level mesocyclone.

Eventually, the midlevel mesocyclone began to weaken during the occlusion stage, with the midlevel storm-scale circulation weakening before the mesocyclone core circulation. The resulting flow structure appeared akin to that of the Goshen County storm illustrated in Kosiba et al. (2013). The weakening of the midlevel storm-scale circulation caused the midlevel RFD convergence zone to expand eastward on the north side of the circulation and resulted in downdraft air wrapping around the low-level circulation as the RFD merged with the occlusion downdraft flow on the south side of the circulation (Fig. 6.19d). The merging of the RFD and occlusion downdrafts allowed the SRFGF to finally wrap around the circulation to the south. Furthermore, the outward displacement of the occlusion downdraft, from the circulation axis, instigated the southeastward surge of the RFGF as described in Chapter 5. Simultaneously, the divergence field associated with the eastward expanding RFD cut off the high reflectivity forward flank inflow feeding into the low level circulation. The combined effect of the downdraft evolution resulted in the concentration of the low-level circulation as air parcels rose at the center but descended on the outside of the mesovortex. The final cyclonic tornado of the mesocyclone cycle developed during this process even as the primary RFGF continued to surge out to the southeast.

Forward trajectories were used to estimate the mesocyclone inflow depth and volume by aggregating the total number of trajectories that entered the low-level mesocyclone in the following 200 seconds. This proxy estimate was maximized between 0028 and 0040 UTC, coinciding with the intensification and transition of the

mesocyclone. Additionally, the inflow volume magnitude appears to have been strongly modulated by the appearance, position and strength of the RFD. Inflow volume appear to be modulated by the location of the RFD, relative to the mesocyclone, as it was maximized when the RFD was at its most western point but minimized as the RFD shifted eastward. The evolution appears similar to the RFD corner-flow collapse hypothesis of Lewellen and Lewellen (2007), whereby the RFD cuts off the influx of low-angular momentum into the mesocyclone. While it is difficult to modify the corner-flow collapse conceptual model for an asymmetric, three-dimensional vortex, the diameter of the mesocyclone did substantially decrease in size as the inflow depth decreased between 0042 and 0052 UTC (Figs. 6.5, 6.6). Furthermore, descending air in the occlusion downdraft was collocated with high values of circulation, and would therefore be transporting high angular momentum towards the ground, within the vicinity of the inflow region. Unfortunately, the lack of observations below 500 m prevented the detection of either a near-ground inflow jet or substantial vertical gradients in angular momentum near the ground.

Fine-scale vorticity structures inside the mesocyclone were elucidated using trajectory maps of Lagrangian vorticity that demonstrated strong agreement with structures in the radial velocity fields (Figs. 6.1, 3.10). The temporal evolution of the Lagrangian vorticity revealed a rapid transition from an annular pattern during the two-celled stage (Fig. 6.4c), to one concentrated at the center of the mesocyclone during the late mature and occlusion stages (Fig. 6.6c). This behavior is consistent with observations by a Doppler-On-Wheels (DOW, Wurman et al. 1997) radar in close proximity to the mesocyclone (Wurman, personal communiqué 2004). During the two-

celled and transition phases, the radar observed four tornadoes embedded within broader mesocyclone flow prior the final, long-lived tornado (see Chapter 3, Fig. 3.1). Indeed, damage that was rated as F2 on the Fujita-scale (Fujita 1981) was estimated to have occurred as the result of mesocyclonic winds, rather than the tornadic winds, as the tornadic winds were weaker than those associated with the mesocyclone and RFD. The tornadic behavior is also consistent with previous observations (Brandes 1978; Wakimoto et al. 1998) of tornadoes occurring in two-celled mesocyclones, where tornadogenesis was hypothesized to grow out of vortex instabilities. While not directly observed by the SMART-radars, the similar structure and annular Lagrangian vorticity pattern suggests that at least some of the tornadoes grew out of vortex instabilities during the two-celled vortex period.

Finally, mesocyclone source regions were elucidated through highlighting forward trajectories that ended up in the mesocyclone vortex ($\zeta > 0.015$ s^{-1}). The first highlighted region was located in the southern forward flank reflectivity core, consistent with radar-based analyses (Johnson et al. 1987; Ziegler et al. 2001; Dowell and Bluestein 2002b; Markowski et al. 2012a,b; Kosiba et al. 2013) and numerical simulations (Klemp and Rotunno 1982; Wicker and Wilhelmson 1995; Alderman et al. 1999). A tilting proxy, developed to overcome the coarse vertical grid spacing, suggested that air parcels in this region experienced favorable tilting on the northwest side of the circulation, consistent with previous studies. Counter-intuitively, vertical velocity gradients along the streamlines had a crosswise orientation, thus favoring the tilting of crosswise horizontal vorticity. However, individual forward trajectories suggested that while the forward flank air did acquire mesocyclonic values of vertical

vorticity, they experienced little stretching and quickly descended in the occlusion downdraft, only to be recycled later on (Fig. 6.18). The decorrelation between tilting and future stretching is consistent with the analytical model developed by Davies-Jones (1984), which suggested that the tilting of crosswise vorticity leads to a displacement of the stretching region from the tilting region. It is possible that limited vertical resolution resulted in underestimates of the northerly component of the wind underneath the RFD and the slope of the RFD towards the mesocyclone, smoothing out the near-ground gradients that typically favor the tilting of streamwise vorticity.

Alternatively, the most temporally consistent source region was located in the near-ground inflow sector (Fig. 6.11). In contrast to forward flank air parcels, they entered the mesocyclone on the northeast side of the circulation along the RFGF, where vertical velocity gradients were primarily oriented parallel to the streamlines, favoring the tilting of streamwise vorticity. Moreover, inflow air parcels were much more likely to experience prolonged stretching than their forward flank counterparts, which would be consistent with their preferred tilting orientations. While it is tempting to discredit this source region due to the limited data below 1000 m, radar analyses by Dowell and Bluestein (2002b) and Brandes (1981) also consistently observed vertical vorticity along the RFGF and found a few trajectories entering the mesocyclone from the inflow. It should also be noted that the simulation in Chapter 4 (Betten et al. 2017) demonstrated a propensity for future mesocyclone trajectories to be concentrated in the inflow and southern forward flank regions (Figure 4.4).

Chapter 7: Mesocyclone Source Regions in a Numerically Simulated Supercell

7.1 Introduction

Individual air parcel histories in supercell thunderstorms have been traditionally elucidated through overlaying the horizontal trace of three-dimensional trajectories on top of reflectivity or other Eulerian fields. Based on wind analyses from numerical simulations (Rotunno and Klemp 1985; Brooks et al. 1993; Wicker and Wilhelmson 1995; Adlerman et al. 1999) or observational studies (Johnson et al. 1987; Wakimoto et al. 1998; Ziegler et al. 2001; Markowski et al. 2012a,b), they have proven to be a key tool in understanding the behavior of supercell dynamics. However, new ways of viewing Lagrangian trajectory behavior have been demonstrated using a numerical simulation (Betten et al. 2017, Chapter 4) and extensively using dual-Doppler radar analyses in Chapters 5 and 6 to explain the evolution of an observed, tornadic supercell. The radar-based analysis suggested that in addition to the traditional forward flank source region, air parcels originating in the inflow acquired positive vorticity on the northeast side of the circulation, before being modified through evaporational cooling. Previous radar-based analyses (Johnson et al. 1987; Ziegler et al. 2001; Dowell and Bluestein 2002b; Markowski et al. 2012a,b; Kosiba et al. 2013) and simulations (Klemp and Rotunno 1982; Wicker and Wilhelmson 1995; Alderman et al. 1999; Dahl et al. 2012) suggest that the primary source region for air entering the mesocyclone is along the southern periphery of the forward flank reflectivity core, often behind the forward flank gust front. However, in all of these previous studies, individual trajectories were used to identify the source regions for backward trajectories except in the case of Dahl

et al. (2012) who released a cloud of forward trajectories to illustrate how inflow air parcels were not reaching the circulation.

Due to the limited observations below 1 km, the plausibility of the inflow source below 250 m, as described in Chapter 6, needs to be evaluated in a numerical framework. Nevertheless, the shallowness of the tilting layer was consistent with the findings of several numerical simulation studies where most of the tilting of horizontal vorticity into vertical vorticity occurred below 250m (Wicker and Wilhelmson 1995; Adlerman et al. 1999).

Here, forward trajectory maps from a simulation of a supercell that produces a long-lived mesocyclone are used to highlight sources regions of air going into the low-level mesocyclone. The trajectory maps are consistent with previous studies in showing the primary source region being positioned behind the surface gust front. However, the trajectory maps also depict the temporary development of an inflow source region during the mature stage of the mesocyclone. Examples of mesocyclone trajectories originating in both source regions are presented.

7.2 Methodology

7.2.1 The model

A modified version of the numerical simulation experiment from Betten et al. (2017) was performed using the CM1 Cloud Model (Bryan and Fritsch 2002), version 17. Similar to Betten et al. (2017), the model used the Ziegler Volume-Density (ZVD, Mansell et al. 2010), two-moment microphysics scheme and the weighted essentially nonoscillatory (WENO) advection scheme (Shen and Zha 2010) was applied for both kinematic and scalar quantities. The simulation was initialized with a single warm

bubble in a homogenous environment based on a modified version of the composite sounding used in Betten et al. (2017), where a capping inversion was added and the hodograph was simplified (Fig. 7.1). The capping inversion was added to mimic the stable layer present in the environmental sounding taken near the Geary, OK supercell (Chapter 3, Betten et al. 2018). Additionally, a number of wind profile experiments were run before the simulation produced a supercell with prolonged mesocyclone cycles. After the wind profile was finalized, a storm motion was found that kept the storm near the domain center.

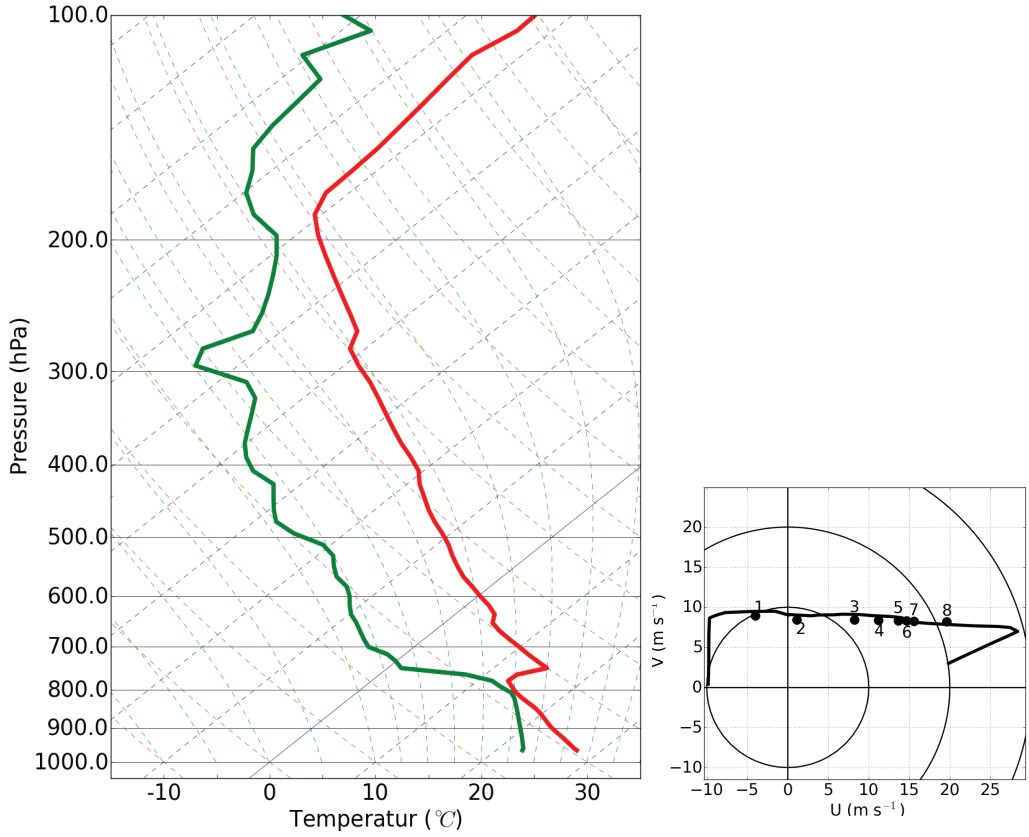

Fig. 7.1 Thermodynamic profile (left panel) and the storm-relative hodograph (right panel) with heights labeled in km. A capping inversion was added to the composite of the 1800 UTC and 0000 UTC soundings at Topeka, KS 8 May 2003. A simplified hodograph was used in place of the original hodograph.

The horizontal grid spacing was reduced to 200 m in the middle 70 km of the domain and was stretched to 5000 m on the outer boundaries. The vertical spacing was reduced near the ground due to trajectory behavior as illustrated in Chapter 6, suggesting that future mesocyclone air parcels originated in the lowest 250 m. A preliminary simulation using an initial vertical spacing of 100 m also suggested the majority of air parcels reaching the mesocyclone originated near the ground. Therefore, the vertical resolution was substantially reduced such that it stretched from 10 m at the bottom to 469 m at the top. The increased resolution resulted in ten more vertical levels and a model domain of 174x174x18.4 km^3.

Frictionally generated horizontal vorticity has been shown to be a potentially important contributor to the generation of intense, near-ground vortices in recent studies (Schenkman et al. 2012; Schenkman et al. 2014; Roberts et al. 2016). Nevertheless, the addition of friction was deemed an interesting but unnecessary step of complexity for the primary questions posed and beyond the scope of this study. Thus, a free-slip lower boundary condition was kept to be consistent with the bulk of previous numerical simulations of supercells and to simplify the analysis.

7.2.2 Trajectory Methodology

Air parcel trajectories were calculated following the same methodology as in Betten et al. (2017) where a fourth-order Runge-Kutta integration scheme was used to integrate over time steps of 0.5 seconds, with a data frequency of 4 seconds. Spatial interpolation was done using a three-dimensional spline while temporal interpolation was performed using a linear function where weights were changed for each of the small time steps in the Runge-Kutta integration scheme. Finally, local gradients were

again calculated on a cube by interpolating the model data on the Arakawa C grid, ensuring maximum accuracy.

7.3 Results

7.3.1 Storm overview

During the initial 10,000 seconds of the simulation, two intense mesocyclone lifecycles occurred (Fig. 7.2a), the most intense beginning around 5200 s and lasting roughly 2000 s. Updraft speeds throughout the depth of the storm peaked during the mature stages of the mesocyclone lifecycles (Fig. 7.2b). Updrafts below 2 km were especially enhanced, reaching a peak of 50 m s^{-1} below 1 km during the peak intensity of the first mesocyclone.

Similar to the Geary supercell, vertical vorticity decreased in height between 2 and 4 km in the first quarter of the lifecycle, 5200-5800 s, prior to the intensification and deepening of the circulation. The mesocyclone eventually extended above 8 km with an impressive peak vertical vorticity above 0.5 s^{-1} in the lowest 500 meters. Although a horizontal grid spacing of 200 m is insufficient to resolve a tornado, the vorticity magnitude and vorticity structure suggest that the mesocyclone spawned a tornado-like vortex (TLV). The second cycle was associated with a shallower vortex, as a minimum in vertical vorticity was present between 1 km and 2 km in altitude (Fig. 7.2a) between 8000 and 10000 seconds.

In Chapter 6, forward trajectory behavior was used to estimate the inflow depth of trajectories flowing into the mesocyclone based on future vertical vorticity values. The same process was applied to the numerical simulation with forward trajectories being initialized every 200 m horizontally and 50 m vertically in a 20x20x1 km^3 box

centered on the circulation. Future mesocyclone trajectories are classified as forward trajectories that start outside the circulation (< .01s^{-1}) and within the following 200 seconds gain mesocyclonic vorticity, O(0.05s^{-1}). The time span allowed for air parcels to enter the circulation was reduced from a value of 300 seconds used in the radar-based analysis because the scale of the storm is substantially smaller, less than half the size.

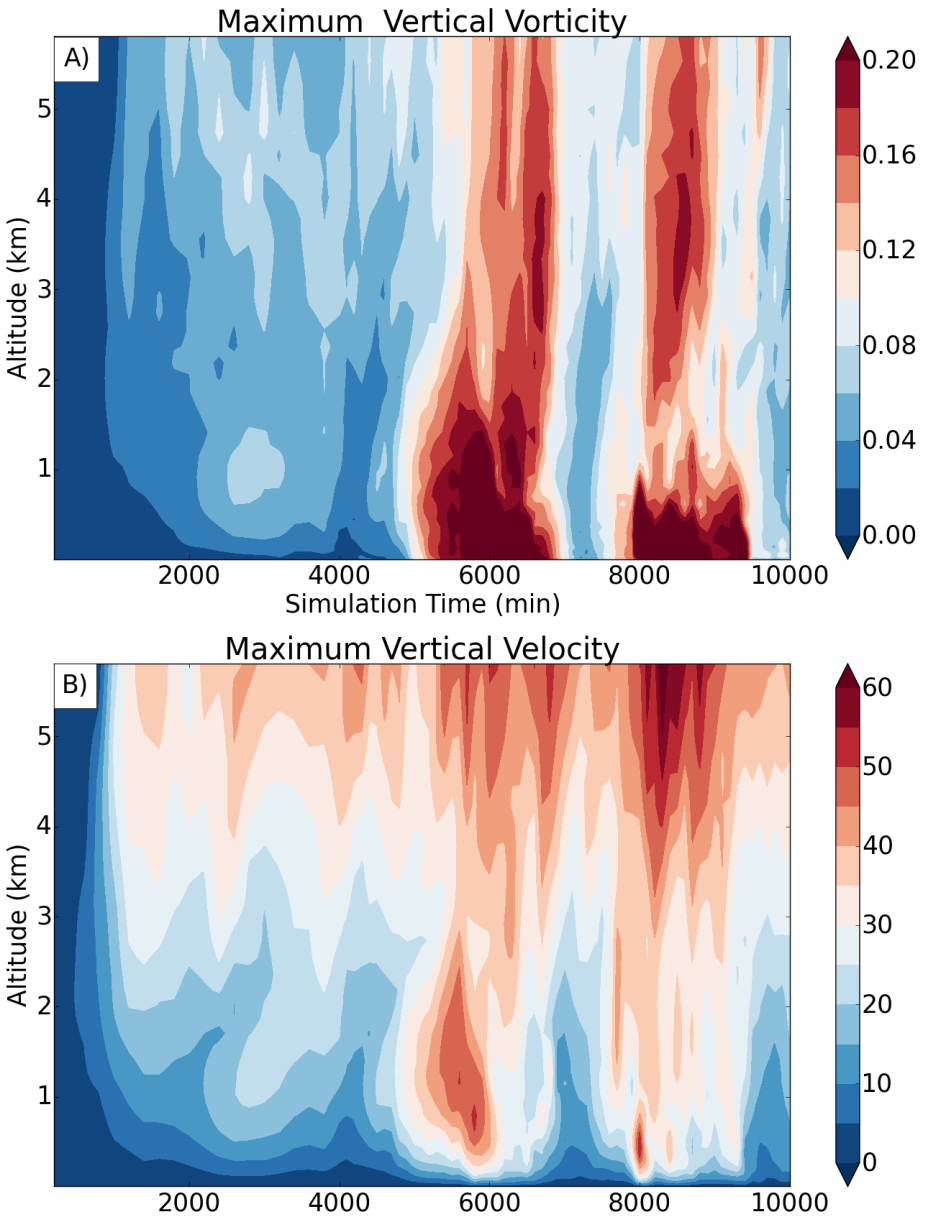

Fig. 7.2 Time-height plot of domain (a) and maximum vertical velocity (m s^{-1}) (b).

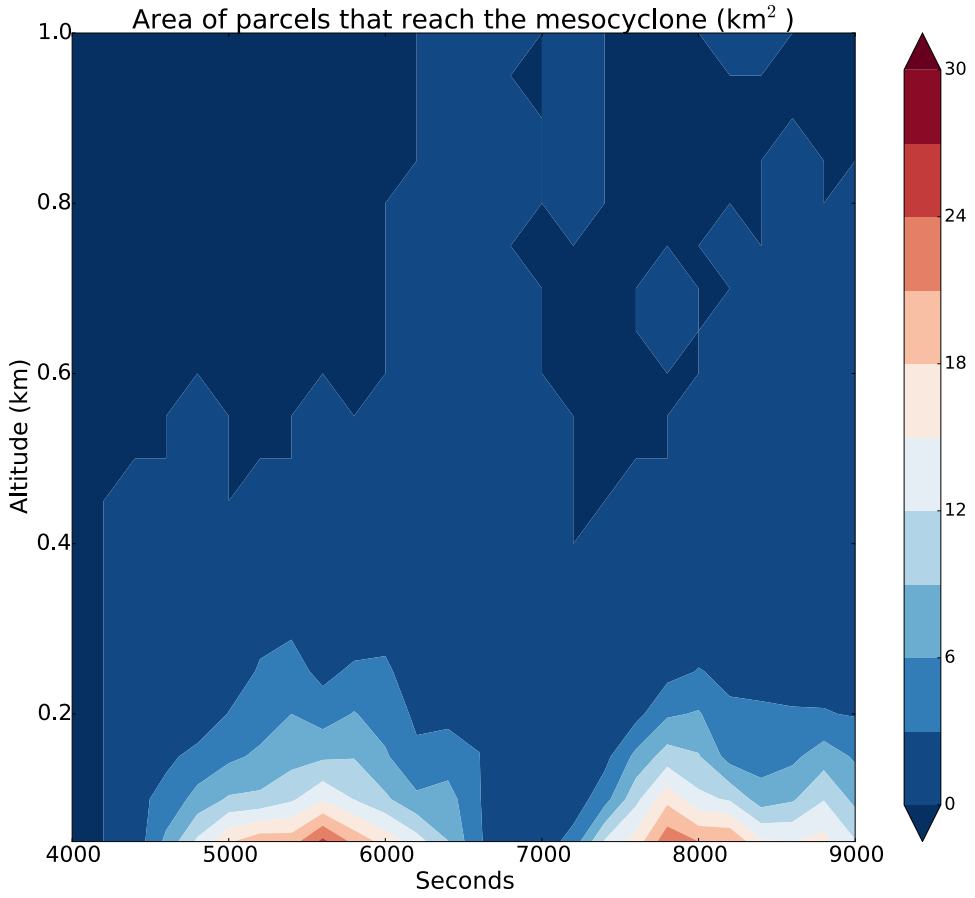

Fig. 7.3 Mesocyclonic inflow depth defined as the horizontal area (km^2) encompassing air parcels that reach the mesocyclone ($\zeta \sim .05$ s^{-1}) below an altitude of 1 km and within the proceeding 200 seconds.

As was observed in the trajectory analysis of the Geary storm, the primary inflow depth into the mesocyclone remained below 500 m throughout the first three hours of the simulation (Fig. 7.3). Moreover, the majority of inflow air was concentrated in the lowest 200 m. Two peaks in inflow depth can be seen corresponding to the two mesocyclone lifecycles with both peaks displaced earlier backward in time from peaks in vorticity as the inflow depth decreased sharply as the circulation began to occluded (not shown ~6300 s). The structure and behavior are similar to that seen in the Geary storm except that the concentrated inflow depth is shallower, 200 m compared to 500 m. This difference is likely due to the limited data

below 1 km in the observational case. Nevertheless, the overall structure of the inflow depth in the numerical model supports the retrieved inflow depth structure derived from the dual-Doppler analysis.

7.3.2 Temporal Evolution of Mesocyclone Source Regions

The cold pool structure surrounding the low-level circulation was fundamentally different between the two mesocyclones. During the first cycle, a weak north-south oriented baroclinic zone (Fig. 7.4a, x=1, y=5) extended into the forward flank reflectivity core from the developing circulation. As the circulation intensified, the buoyancy gradient weakened, reaching a minimum at 6000 s into the simulation when equivalent potential temperature, θ_e, deficits were between -1 and -2 K (Fig. 7.4d). The evolution of the buoyancy gradient is similar in appearance and behavior to the left-flank convergent boundary noted by Beck and Weiss (2012) who also found that it progressed cyclonically, with respect to the circulation, as the circulation strengthened.

In contrast, the second mesocyclone formed above a strong baroclinic gradient with θ_e deficits exceeding -10 K (Fig. 7.4e). Moreover, below the circulation at 300 m, θ_e deficits were 2-3 K during the first cycle but 8-10 K during the second cycle, indicating that the circulation developed in cold air and even as the left-flank convergent boundary (LFCB, Beck and Weiss 2012) shifted slightly westward. Thus, even as the second mesocyclone intensified, the cold air remained entrenched around and underneath it. The negative buoyancy within the second circulation may explain the discontinuity in the maximum vertical vorticity with height between 1 and 2 km (Fig. 7.2b). Air within the circulation near the ground would have opposed dynamically

driven positive vertical velocities associated with the mesocyclone, similar to arguments made by Markowski and Richardson (2014).

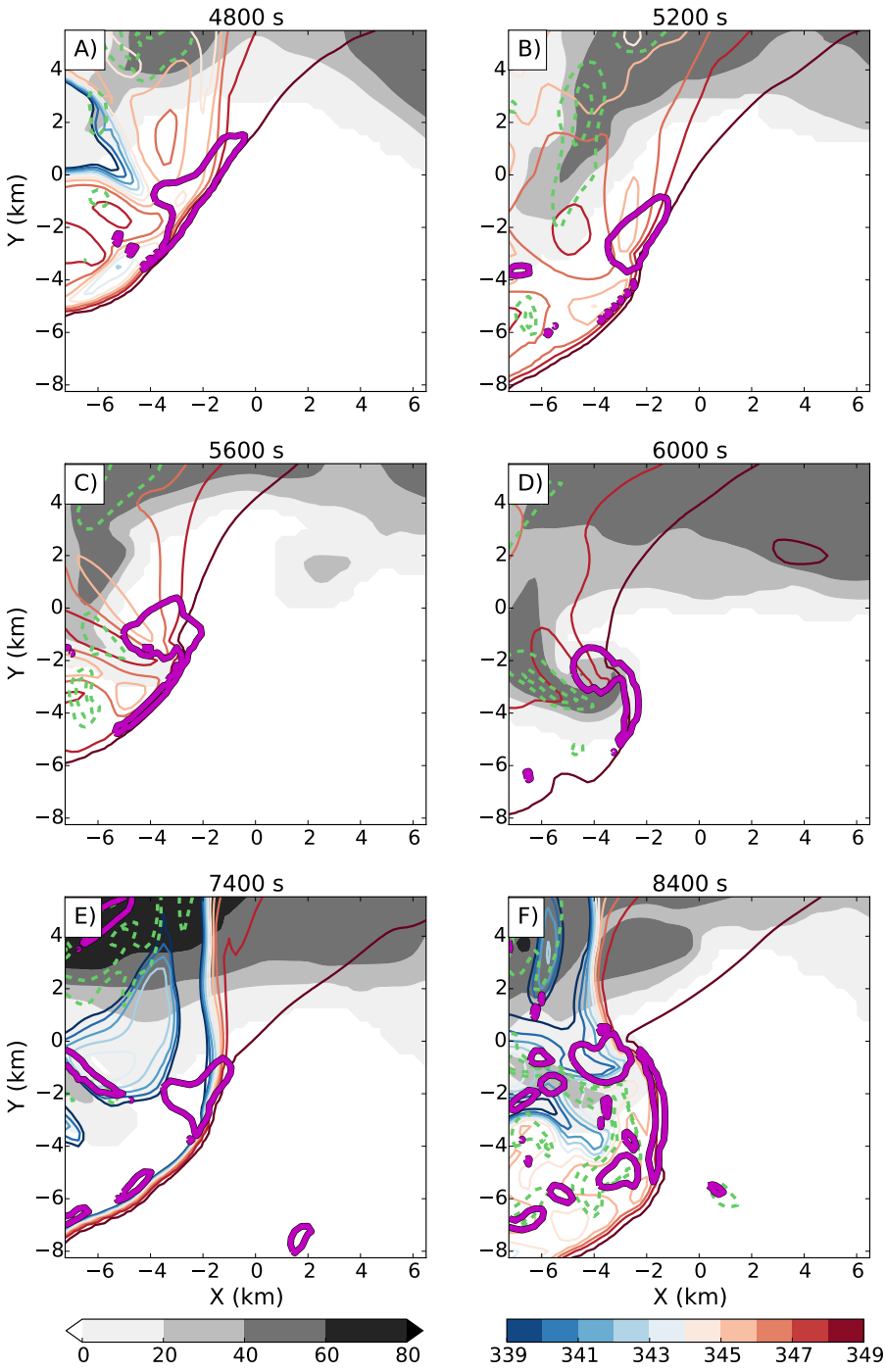

Fig. 7.4 Radar reflectivity at an altitude of 300 m is grey-filled with color contours of equivalent potential temperature (every 1 K) at according to the lower right color scale. Additionally, negative vertical velocity in dashed green (at -1, -2 m s^{-1}) and the 0.01 s^{-1} vertical vorticity contour is plotted in magenta.

Inferences made using the near-ground thermodynamics are generally consistent with the evolution of the mesocyclone source regions. As in Chapter 6, aggregating future mesocyclone trajectories with height elucidates these source regions (Fig. 7.5). Throughout the lifecycle of the first mesocyclone and the beginning of the second cycle, the mesocyclone was drawing in air from the north, in the vicinity of the southern forward flank reflectivity core (Fig. 7.5a, x=0.5 km, y=3 km) but east of the LFCB. Although rotated counter-clockwise, the relative location of this zone is similar to that seen in the Geary storm (Fig. 6.11). Demonstrating in both observed and simulated first cycle mesocyclones, air inside the circulation was not being drawn from the RFD outflow.

However, just as the near-ground buoyancy field suggests, the second mesocyclone departed significantly in behavior and drew in air from behind the LFCB during the organizing (Fig. 7.5e, x=0.5, y=0.5 km) and mature phases (Fig. 7.5f, x=-2, y= 2 km). The peak depth in future mesocyclone air parcels was found within θ_e deficits exceeding -10 K at 7400 (Fig. 7.4e) and -6 K at 8400 seconds (Fig. 7.4f) into the simulation. The ingestion of negatively buoyant air no doubt played a role in the behavior of the circulation and the lack of vertical continuity. Thus, the mesocyclone source regions can vary widely from cycle to cycle within the same environment and are partially responsible for shifts in structure and behavior from cycle to cycle. In this case, the RFD outflow became progressively colder and although the outflow did not undercut the circulation, it did dramatically affect the vertical extension of the low-level vortex.

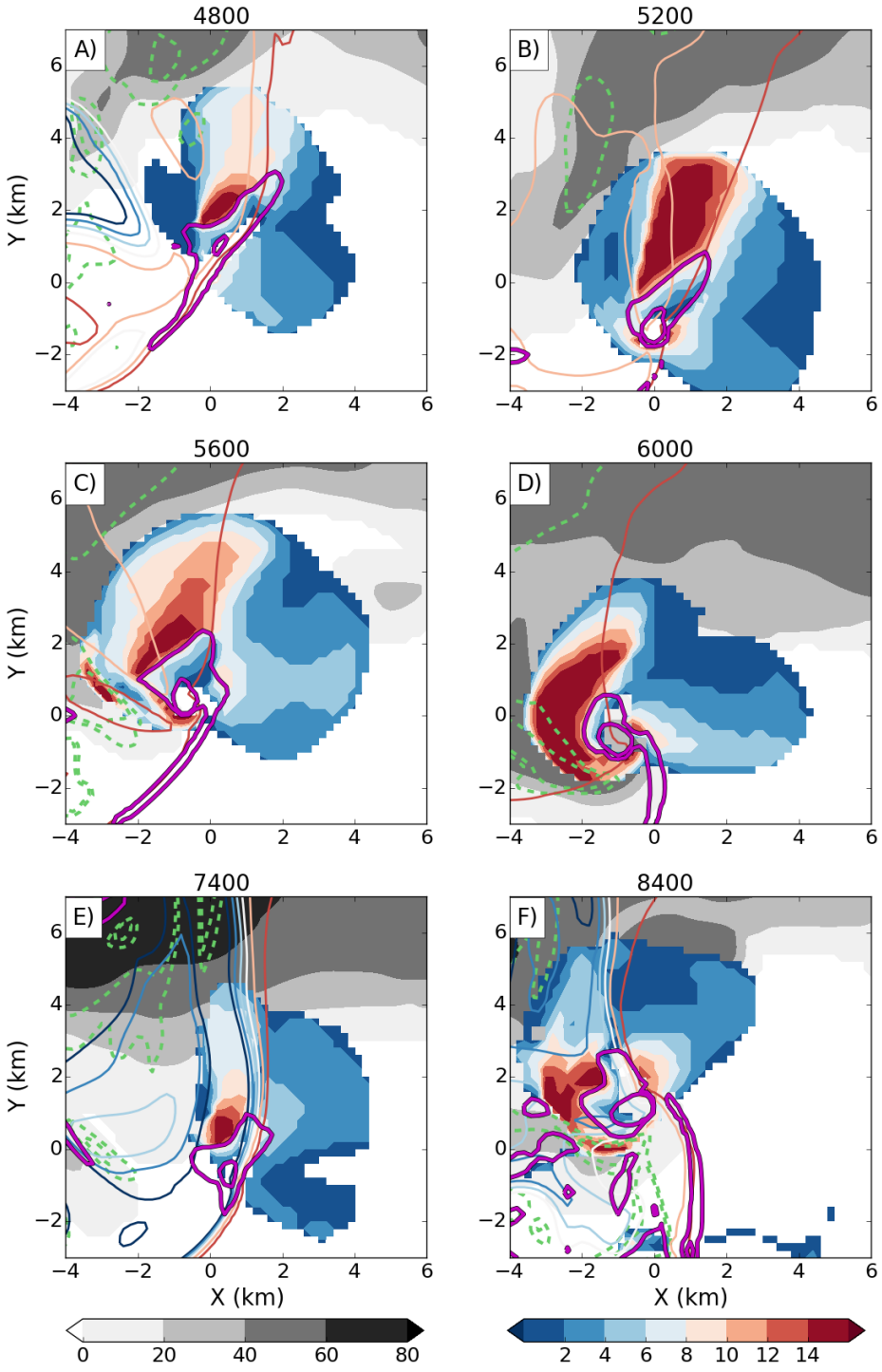

Fig. 7.5 Radar reflectivity at an altitude of 200 m is grey-filled while column density of future mesocyclone trajectories has been color-shaded. Masked points indicate columns absent future mesocyclone trajectories. The grid origin was centered on the mesocyclone. Vertical vorticity at an altitude of 1 km is contoured in purple (at 0.01, 0.02 s^{-1}) and negative vertical velocity in dashed green (at -1, -2 m s^{-1}).

As in the observational case, both mesocyclone cycles demonstrated the ability to drawn in unmodified inflow air into the vortex once the circulation gained sufficient strength. A shallow layer of air parcels originating in the inflow began flowing into the first circulation as the baroclinic zone north of the circulation rapidly warmed (Fig. 7.5b-d, Fig. 7.4b-d) or at least shifted westward (Fig. 7.5f). Additionally, the development of the inflow source region during both cycles appears to be correlated with the eastward bulging of the RFGF. As the RFGF bowed out towards the east (Fig. 7.5d, x =-3, y= -3), the gust front orientation shifted from northeast-southwest to being northwest-southeast oriented; parallel to the low-level inflow. As the LFCB dissipated or at least shifted westward, air parcels accelerating into the inflow of the updraft would no longer be forced upwards by a gust front and thus allowing them to flow around the northern side of the circulation and into the vortex. Unfortunately, the Geary storm was too far away from the radars to generate trajectory analysis during the organizing stage but the peak depth in inflow trajectories did occur after the RFGF bulged out to the east, supporting the occurrence of analogous behavior in the observed and simulated storms.

c. Individual Trajectory Examples

Individual trajectories were examined to further explore the behavior of air parcels entering the mesocyclone from the forward flank and inflow regions. Trajectories were selected based on the column density of trajectories within each region using a finer vertical spacing, 20 m, from 20 m up to 300 m. It was generally found that air parcels originating near the ground acquired substantially more vertical vorticity in the future than parcels originating at higher altitudes (not shown). Therefore, example trajectories were initiated at an altitude of 20 m to maximize future vertical

vorticity while remaining above the lowest model scalar level of 10 m, preventing quantities from being extrapolated down to the individual trajectories.

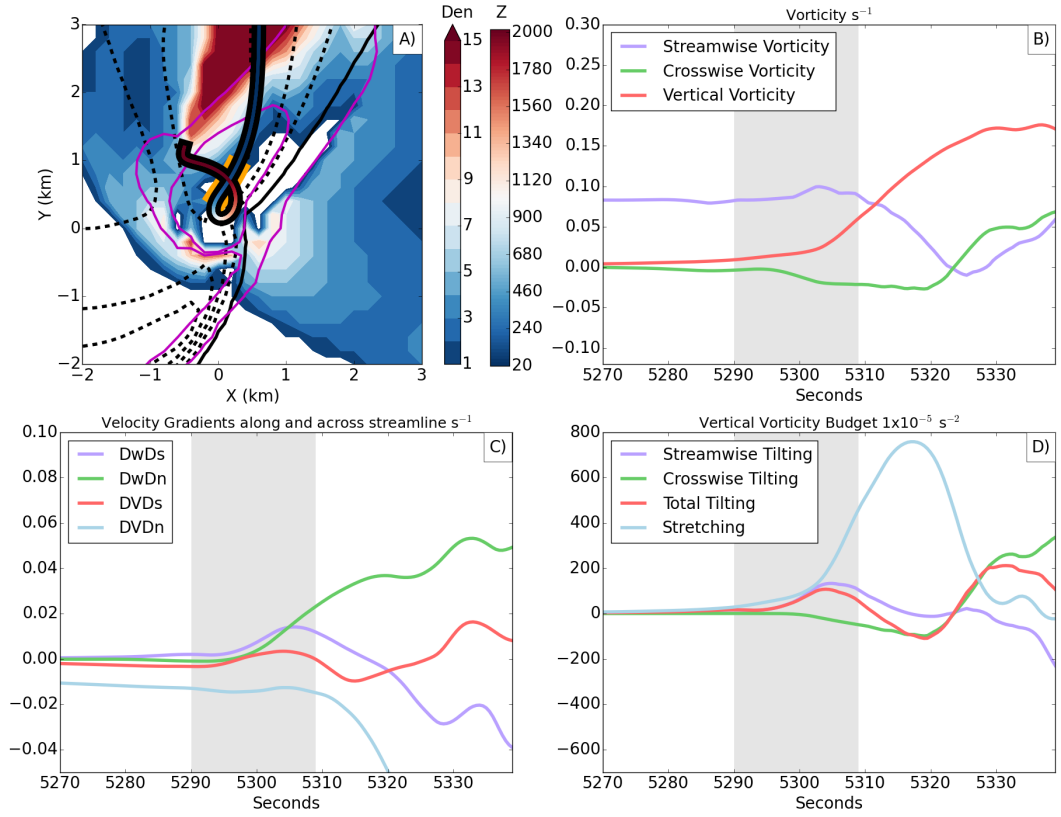

Fig. 7.6 Example individual trajectory initialized at 5200s in the forward flank region. Column density of future mesocyclone trajectories is color-filled in (a), where the number is the sum of the trajectories that reach the mesocyclone from a vertical grid stretching from 20 m to 200 m, and evenly spacing 20 m apart. The individual forward flank trajectory is overlaid and colored according to the altitude associated with the color scale. Perturbation equivalent potential temperature contours are in black (every 1 K) at an altitude of 20 m and vertical vorticity (magenta, 0.01 and 0.02 s^{-1}) at an altitude of 300 m. In (b) the time series of vertical vorticity, horizontal streamwise vorticity, and horizontal crosswise vorticity is plotted. In (c), the time series of streamwise and crosswise gradients of vertical velocity (w) and horizontal velocity (V) are plotted. Finally, in (d), the time series of stretching, tilting, streamwise component of tilting, and crosswise component of tilting, are plotted. Finally, the period of interest when the air parcel is gaining positive vertical vorticity is highlighted in yellow in (a) and grey in (b-d).

A representative forward flank trajectory was initialized at 5200 seconds into the simulation 3 km north of the mesocyclone within the cooler air of the forward flank

reflectivity core at an altitude of 20 m (Fig. 7.6a). Although the primary period of vertical vorticity generation occurred just after 5305 s, the air parcel was slowly gaining positivity vertical vorticity as early as 5280 s with weak stretching occurring within the broader region of positive vertical motion (Fig. 7.6b-d). As the trajectory approached the mesocyclone from the north it remained near the ground but within very weak rising motion rising while exceptional horizontal vorticity, 0.08 s^{-1}, aligned with the buoyancy gradient, was slowly tilted into the vertical (Fig. 7.6d). Around 5298 s, the tilting term substantially increased, briefly attaining the same magnitude as the stretching term by 5302 s (Fig. 7.6d) before the air parcel reached the north side of the vortex, at which time the trajectory turned upward and the primary updraft stretched the seed vorticity. Overall, the forward flank trajectory was generally consistent with the behavior found in numerical simulations (Klemp and Rotunno 1982; Wicker and Wilhelmson 1995; Alderman et al. 1999; Dahl et al. 2012) which demonstrated that horizontal vorticity associated with the forward flank buoyancy gradient was tilted into the vertical, with the exception that the air parcel did not pass through a downdraft on its way to the vortex.

Meanwhile, a representative trajectory from the inflow region (Fig. 7.7) also reach the core of the mesocyclone ($\zeta > 0.2$ s^{-1}) after being initialized 2 km east of the mesocyclone at 6000 seconds and an altitude of 20 m. Impressively, streamwise horizontal vorticity within the inflow was initially 0.08 s^{-1} (Fig. 7.7b), roughly the same as the forward flank trajectory but within a substantially more shallow layer. As the air parcel approached the vortex from the east, the streamwise gradient of the horizontal wind rapidly increased (Fig. 7.7c), the air parcel accelerated, nearly doubling its horizontal velocity (not shown), amplifying the available streamwise horizontal

vorticity (Fig. 7.7b). Unlike the forward flank trajectory, the inflow trajectory experienced minimal or negative stretching until 6068 s (Fig. 7.7d), at which point the air parcel rapidly gained positive vertical vorticity, with a maximum of almost 0.3 s^{-1}. Although not seen in previous numerical simulations, the inflow source region and vorticity behavior of the air parcel is consistent with the behavior of the inflow trajectories in the Geary storm (Chapter 6).

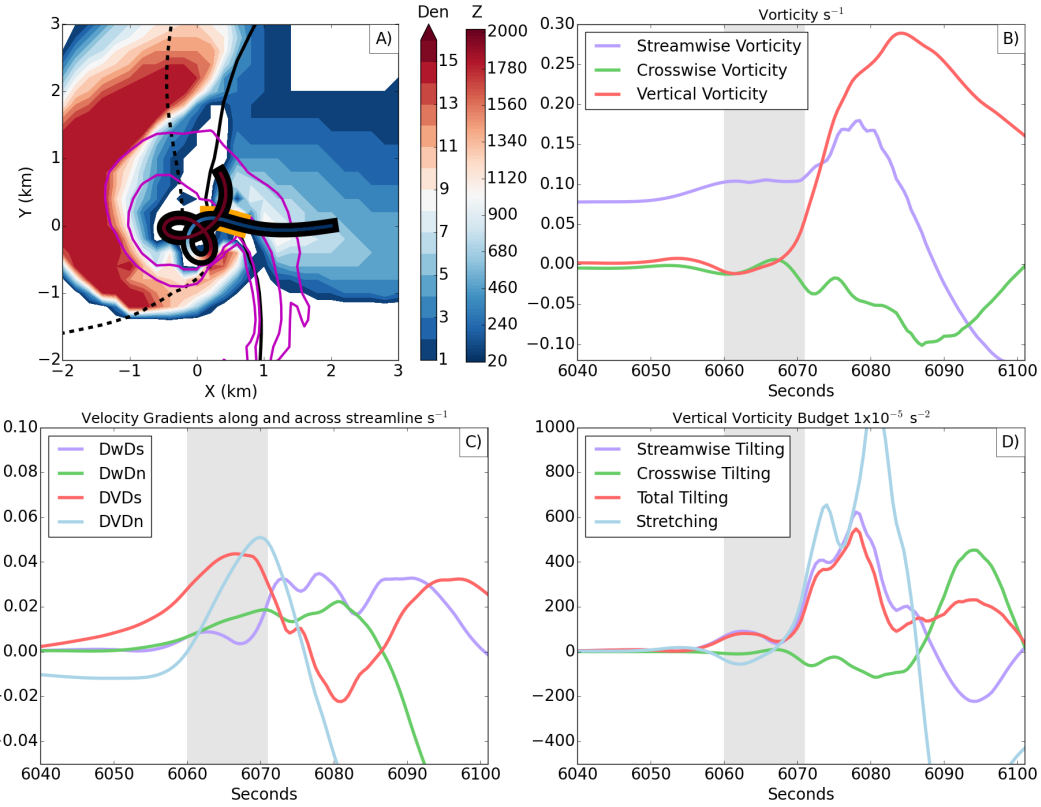

Fig. 7.7 Same as Fig. 7.6 except for the case of an individual trajectory initialized in the inflow region at 6000 s.

7.4.Conclusions

A high-resolution numerical simulation has been used to investigate whether future mesocyclone trajectory behavior within the observed Geary supercell discussed in Chapter 6 is similar to higher vertical resolution numerical simulation of an analogous supercell storm. Trajectory calculations in the Geary supercell relied on data

available only every three minutes with limited resolution near the ground. Alternatively, forward trajectories based on the numerical simulation were integrated using model data frequency of 4 seconds and a vertically stretched grid with an initial scalar level of 10 m. The fine vertical resolution eliminated the need to extrapolate downward to near-ground trajectories and thus maximized the accuracy of trajectory calculations. It is important to note that unlike previous studies, trajectory behavior was investigated during the mature phase of the mesocyclone and a mature vortex was in contact with the lowest grid level when the example trajectories were initiated.

The present study is believed to be the first time that temporally evolving source regions for air within the mesocyclone of a cyclic supercell have been spatially elucidated in a high-resolution numerical simulation. During both mesocyclone cycles, the trajectory behavior bore a striking resemblance to the behavior in the observed Geary supercell discussed in previous chapters. In both cases, the inflow depth, based on the depth of future mesocyclone air parcels, is maximized below 500 m and increases during the intensification phase of the mesocyclone. Furthermore, the depth of future mesocyclone air was substantially greater in the forward flank regions while only found in a shallow layer in the inflow region. These spatial patters, which were consistent in time and between mesocyclone cycles, is consistent with trajectory behavior exhibited in the radar-based Geary storm.

The greatest disadvantage of the dual-Doppler derived wind fields was the lack of data below 250m, creating the need for downward extrapolation and thus limited with regard to near-surface boundaries. Individual trajectory examples in the forward flank and inflow regions revealed future mesocyclone trajectories originating in *both*

regions flowed into the core of the vortex. It was also shown that the depth of inflow trajectories reaching the mesocyclone was directly correlated with the strength of the vortex and the westward displacement of the LFCB. This suggests that inflow trajectories only reach the inner mesocyclone when the broader-scale circulation is strong enough to deform the buoyancy field and reduce near-ground convergence in the inflow notch, which would otherwise force the inflow trajectories to rise into the updraft rather than be ingested by the mesocyclone, as has been found be previously by Dahl et al. (2012). Additionally, the strengthening mesocyclone is thought to enhance the low-level inflow and augment the ambient streamwise vorticity, allowing it to be comparable in magnitude to the baroclinically-generated horizontal vorticity found behind the LFCB.

Based on the results of this single, idealized numerical simulation, the trajectory behavior in the Geary storm appears to at least be well diagnosed and not purely the consequence of coarse temporal resolution or the lack of near-ground data. Vorticity budgets along individual trajectories in the radar-based analysis are still questionable but the overall structure of trajectory behavior appears robust. However, since trajectory behavior was examined during the mature phase of the observed and simulated mesocyclones, caution should be taken when comparing the results presented herein directly to previous conceptual models of the origins of rotation in the initial low-level mesocyclone during the development stage.

Chapter 8: Conclusions

This dissertation has sought to detail consistent and fundamental relationships between the three-dimensional structure of the mesocyclone and the storm's downdrafts and gust fronts in a high-precipitation supercell thunderstorm. These relationships have been explored using radar-based analyses with unparalleled longevity collected during the TELEX project on 29 May 2004 in central Oklahoma. In addition to traditional kinematic analyses, the derived dual-Doppler winds serve as the basis for a novel technique whereby three-dimensional trajectory behavior is mapped out in two-dimensional space. The trajectory mapping technique is vigorously explored and used to elucidate the evolution of flow associated with the downdrafts and mesocyclone circulations; providing key insights into the relationship between the two ubiquitous storm-scale structures. A numerical simulation was used to demonstrate the validity of the trajectory mapping technique and the limited sensitivity of patterns in trajectory behavior to data frequency and resolution degradation. An additional high-resolution simulation was run to explore the temporal evolution of source regions of air in low-level mesocyclones and to compare the patterns with those from the radar-based analysis.

As with many observed high-precipitation supercells (Rasmussen and Strake 1998), the storm-scale flow was continually organized by a deep, intense mesocyclone that grew to a depth exceeding 12 km and a width of 7 km. Throughout the lifecycle of the mesocyclone, broad cyclonic flow at low-levels in the forward and rear flanks of the storm were evidence of the unusually far reaching pressure influence of the circulation. A persistent forward flank gust front was notably absent at low-levels prior to the

dissipation stage of the storm, most likely the result of abnormally high relative humidity in the lowest 1 km of the environment and the lack of an organized forward flank downdraft. Trajectory behavior revealed that the absence of a strong forward flank downdraft allowed modified inflow air to collide with rear flank air along a convergence zone deeper than 8 km in the rear flank of the storm. The depth and horizontal orientation of the convergence zone was associated with the strength of the mesocyclone relative to the ambient, westerly storm-relative flow. As the mesocyclone intensified and deepened, the convergence zone deepened and shifted westward, relative to the circulation. Alternatively, when the midlevel circulation weakened, the midlevel convergence zone also weakened and shifted eastward.

Despite a nearly nonexistent forward-flank downdraft, the rear-flank downdraft was exceptionally strong during the mature phase of the mesocyclone, with speeds exceeding 10 m s^{-1} at an altitude of 1 km. The rear-flank downdraft was continuously spatially correlated with the midlevel convergence zone and the strength of the low-level downdraft was correlated with the strength of the convergence zone at midlevels. Therefore, it appears that the midlevel convergence zone was a primary forcing mechanism for the strength and position of the rear-flank downdraft. The thermodynamic properties of the rear-flank downdraft could not be directly investigated due to an absence of observations at the surface. However, considering the impressive magnitude of the downdraft, trajectory behavior of air parcels emanating out of the downdraft were consistent with a RFD in which buoyancy was a secondary forcing mechanism for vertical momentum. Furthermore, none of the three observed mesocyclones appeared to be uncut by cold downdrafts and in fact persisted long after

they were cut off from their warm inflow. Thus, it is plausible that the presence of strong, organizing mesocyclones may encourage downdrafts to be primarily dynamically driven around the circulation and thus mitigate tornadogenesis failure mechanisms related to the thermodynamic characteristics of the downdrafts.

Prior to the occlusion stage of the mesocyclone, the RFD and occlusion downdrafts remained spatially distinct, with discrete flow regimes implied by their trajectory behavior. The vertical structure of the mesocyclone played an instrumental role in keeping the downdraft flow regimes discrete as a negative vertical circulation gradient promoted an axial downdraft during the early mature phase due to the implied vertical pressure gradient. Trajectory behavior suggested that the majority of air parcels within the occlusion downdraft remained within the circulation with a minority descending outside the circulation. The secondary RFD gust front represented the boundary between the two flow regimes with air behind the SRFGF originating in the primary RFD and air between the primary and secondary RFGFs originating within the occlusion downdraft and emanating out of the mesocyclone circulation. Immediately following a period of rapid intensification and deepening, the vertical circulation gradient reversed and the majority of occlusion downdraft air parcels began descending outside of the circulation flow and merged with the primary RFD. The merging of the two downdraft flow regimes resulted in the secondary RFGF rotating around the low-level mesocyclone and the surging out of the primary RFGF away from the mesocyclone. Secondary RFGFs were observed with three different mesocyclone cycles, suggesting that they were ubiquitous during the tornadic phase of the Geary supercell.

The inflow volume of air parcels flowing into the mesocyclone was tracked and correlated to the strength and position of the RFD. Inflow increased as the downdraft shifted westward, associated with a westward shift in the convergence zone due to the strengthening of the midlevel mesocyclone. Alternatively, as the midlevel circulation weakened, especially during the occlusion stage, the mesocyclone inflow dropped off precipitously as the RFD shifted eastward, cutting off the inflow. In fact, the period of intensification and deepening responsible for reversing the vertical circulation gradient was preceded by a brief surge in mesocyclone inflow correlating to the westward shift of the RFD. Therefore, the dynamic enhancement of the RFD and its influence on the mesocyclone inflow provides an indirect mechanism by which the midlevel circulation can influence the structure of the low-level circulation.

Meanwhile, the occlusion downdraft appeared to have alternating influences. Enhanced convergence from RFD surges was opposed by divergence from the axial downdraft during the two-celled mesocyclone period, secluding convergence to the outer core of the circulation and thus preventing the low-level vortex from concentrating further. Conversely, as the axial downdraft tendency relaxed and the downdraft flow regimes merged, the augmented convergence quickly concentrated the low-level vortex. Tornadic behavior during the mesocyclone's lifecycle was consistent with a prolonged period of two-celled behavior prior to single-celled behavior during the late mature and occlusion phases.

Temporally evolving mesocyclone source regions were spatially mapped out for the first known time in both observed and numerically simulated storms using forward trajectory behavior. In both cases, future mesocyclone air parcels were found within a

moderately deep layer (~250-500m) in the southern forward flank reflectivity core and extended to a shallow layer (< 100m) in the unmodified inflow sector. Additionally, a trajectory tilting proxy was used to highlight the area where forward trajectories were consistently gaining their vertical vorticity through a combination of tilting and stretching. In the Geary supercell, forward flank trajectories entered the circulation on the northwestern side of the circulation while inflow trajectories appeared to gain their vertical vorticity on the northeast side of the circulation as they flowed parallel to the RFGF. Similar behavior was found in the numerical simulation despite a significantly smaller circulation than in the observed case. Interestingly, in the idealized numerical simulation, the mesocyclone initially ingested air from the forward flank region but eventually expanded to include the inflow sector once the larger-scale mesocyclone gained sufficient influence to deform the forward flank gust front. This pattern, found across multiple simulated mesocyclone cycles, suggests the possibility that the initial circulation was formed through the tilting of baroclinically generated horizontal vorticity but later on took advantage of strong ambient, barotropic horizontal vorticity near the ground.

Unfortunately, the 29 May 2004 dataset represents one of only a couple datasets with sufficient spatial and temporal coverage to allow for such an in-depth study of the relationship between the mesocyclone and the RFD. Many more high-precipitation supercells will need to be observed and simulated to generalize the findings of this study, in particular the balance between the midlevel mesocyclone flow and the environmental wind flow. It is our hope that the 29 May Geary storm will be used as a

barometer for the robustness of future numerical simulations with respect to high-precipitation supercell thunderstorms.

References

Agee, E.M., J.T. Snow, and P.R. Clare, 1976: Multiple vortex features in the tornado cyclone and the occurrence of tornado families. *Mon. Wea. Rev*., **104**, 552–563

Anderson-Frey, A.K., Y.P. Richardson, A.R. Dean, R.L. Thompson, and B.T. Smith, 2016: Investigation of near-storm environments for tornado events and warnings. *Wea. Forecasting*, **31**, 1771–1790

Adlerman, E. J., and K. K. Droegemeier, 2002: The sensitivity of numerically simulated cyclic mesocyclogenesis to variations in model physical and computational parameters. *Mon. Wea. Rev*., **130**, 2671–2691.

Adlerman, E. J., and K. K. Droegemeier, 2005: The dependence of numerically simulated cyclic mesocyclogenesis upon environmental vertical wind shear. *Mon. Wea. Rev.,* **133**, 3595–3623.

Adlerman, E. J., K. K. Droegemeier, and R. P. Davies-Jones, 1999: A numerical simulation of cyclic mesocyclogenesis. *J. Atmos. Sci.*, **56**,2045–2069.

Barnes, S.L., 1968: On the source of thunderstorm rotation. Natl. Severe Storms Lab., Tech. Memo. ERLTM-NSSL **38**, 38pp.

Barnes, S. L., 1970: Some aspects of a severe, right-moving thunderstorm deduced from mesonetwork rawinsonde observations. *J. Atmos. Sci*., **27**, 634–648,

Barnes, S. L., 1978a: Oklahoma thunderstorms on 29–30 April 1970. Part I: Morphology of a tornadic storm. *Mon. Wea. Rev.*, **106,** 673–684.

Barnes, S. L., 1978b: Oklahoma thunderstorms on 29–30 April 1970. Part II: Radar-observed merger of twin hook echoes. *Mon. Wea. Rev.*, **106,** 685–696.

Beck, J. and C. Weiss, 2013: An assessment of low-level baroclinity and vorticity within a simulated supercell. *Mon. Wea. Rev.,* **141**, 649–669.

Beck, J.R., J.L. Schroeder, and J.M. Wurman, 2006: High-resolution dual-Doppler analyses of the 29 May 2001 Kress, Texas, cyclic supercell. *Mon. Wea. Rev*., **134**, 3125–3148.

Beebe R.G., 1956: Tornado composite charts. *Mon. Wea. Rev*., **84**, 127–142.

Betten, D.P., M.I. Biggerstaff, and L.J. Wicker, 2017: A trajectory mapping technique for the visualization and analysis of three-dimensional flow in supercell storms. *J. Atmos. Oceanic Technol.,* **34**, 33–49

Betten, D. P., M.I. Biggerstaff, and C.L. Ziegler, 2018: Three-dimensional storm structure and low-level boundaries at different stages of cyclic mesocyclone evolution in a high-precipitation tornadic supercell. *Adv. Meteor.* 2018, 9432670.

Biggerstaff, M. I. and R. A. Houze, Jr., 1993: Kinematics and microphysics of the transition zone of the 10-11 June, 1985 squall-line system. *J. Atmos. Sci., **50***, 3091-3110.

Biggerstaff, M. I., and Coauthors, 2005: The Shared Mobile Atmospheric Research and Teaching Radar: A collaboration to enhance research and teaching. *Bull. Amer. Meteor. Soc*., **86**, 1263–1274.

Brandes, E.A., 1977: Flow in severe thunderstorms observed by dual-Doppler radar. *Mon. Wea. Rev.,* **105**, 113–120

Brandes, E. A., 1978: Mesocyclone evolution and tornadogenesis: Some observations. Mon. Wea. Rev., **106**, 995–1011.

Brandes, E. A.. 1981: Finestructure of the Del City–Edmond tornadic mesocirculation. *Mon. Wea. Rev.*, **109,** 635–647.

Brandes, E.A., 1984: Vertical vorticity generation and mesocyclone sustenance in tornadic thunderstorms: The observational evidence. *Mon. Wea. Rev.,* **112**, 2253–2269.

Brooks, H. E., C. A. Doswell III, and R. P. Davies-Jones, 1993: Environmental helicity and the maintenance and evolution of low-level mesocyclones. The Tornado: Its Structure, Dynamics, Prediction, and Hazards, Geophys. Monogr., No. 79, *Amer. Geophys. Union*, 97–104.

Brooks, H. E., C. A. Doswell III, and R. B. Wilhelmson, 1994: The role of midtropospheric winds in the evolution and maintenance of low-level mesocyclones. *Mon. Wea. Rev.,* **122**, 126–136.

Brooks, H. E., M. Kay, and J. A. Hart, 1998: Objective limits on forecasting skill for rare events. Preprints, 19th Conf. on Severe Local Storms, Minneapolis, MN, *Amer. Meteor. Soc*., 552–555.

Brown, R.A., L.R. Lemon, and D.W. Burgess, 1978: Tornado Detection by Pulsed Doppler Radar. *Mon. Wea. Rev.,* **106**, 29–38

Browning, K. A., 1962: The cellular structure of convective storms, *Met. Magazine*, **91**, 341-350

Browning, K. A. (1964). Airflow and precipitation trajectories within severe local storms which travel to the right of the winds. *J. Atmos. Sci*. **021**,1520-0469.

Browning, K. A., and F. H. Ludlam, 1962: Airflow in convective storms. *Quart. J. Roy. Meteor. Soc.*, **88,** 117–135.

Browning, K. A., and R. J. Donaldson, 1963: Airflow and structure of a tornadic storm. *J. Atmos. Sci*., **20,** 533–545.

Bruning, E. C., W. D. Rust, D. R. MacGorman, M. I. Biggerstaff, and T. J. Schuur, 2010: Formation of charge structures in a supercell. *Mon. Wea. Rev.*, **138**, 3740–3761.

Bryan, G. H., and J. M. Fritsch, 2002: A benchmark simulation for moist nonhydrostatic numerical models. *Mon. Wea. Rev.*, **130**, 2917–2928.

Burgers, J. M., 1948: A mathematical model illustrating the theory of turbulence. *Adv. Appl. Mech.*, **1**, 171–199

Burgess, D. W., V. T. Wood, and R. A. Brown, 1982: Mesocyclone evolution statistics. Preprints, *10th Conf. on Severe Local Storms,* Omaha, NE, *Amer. Meteor. Soc.,* 422–424.

Burgess, D. W., R. A. Brown, L. R. Lemon, and C. R. Safford, 1977: Evolution of a tornadic thunderstorm. Proc. 10th Conf. on Severe Local Storms, Omaha, NE, *Amer. Meteor. Soc.,* 84–89.

Byers, H. R., R. R. Braham, 1949: The Thunderstorm, U.S. Govt. Printing Office, Washington, DC, 287 pp.

Calhoun, K. M., D. R. MacGorman, C. L. Ziegler, and M. I. Biggerstaff, 2013: Evolution of lightning activity and storm charge relative to dual-Doppler analysis of a high-precipitation supercell storm. *Mon. Wea. Rev.,* **141**, 2299–2223.

Charba, J, and Y. Sasaki, 1968: structure and movement of the severe thunderstorms of 3 April 1964 as revealed from radar and surface mesonetwork data analysis. Natl. Severe Storms Lab., Tech. Memo. ERLTM-NSSL 41, 47 pp.

Coffer, B.E. and M.D. Parker, 2017: Simulated supercells in nontornadic and tornadic VORTEX2 environments. *Mon. Wea. Rev.*, **145**, 149–180,

Cohen, R.A. and D.M. Schultz, 2005: Contraction rate and its relationship to frontogenesis, the Lyapunov exponent, fluid trapping, and airstream boundaries. *Mon. Wea. Rev.,* **133**, 1353–1369

Cressman, G. P., 1959: An operational objective analysis system. *Mon. Wea. Rev.*, **87**, 367–374.

Dahl, Johannes M. L., Matthew D. Parker, Louis J. Wicker, 2012: Uncertainties in trajectory calculations within near-surface mesocyclones of simulated supercells. *Mon. Wea. Rev.*, **140**, 2959–2966.

Dahl, J. M., M. D. Parker, and L. J. Wicker, 2014: Imported and storm-generated near-ground vertical vorticity in a simulated supercell. *J. Atmos. Sci.*, **71**, 3027–3051.

Darkow, G. L., 1969: An analysis of over sixty tornado proximity soundings. Preprints, Sixth Conf. on Severe Local Storms, Chicago, IL, *Amer. Meteor. Soc.*, 218–221.

Darkow, D. L. and C.J. Roos, 1970: Multiple tornado producing thunderstorms and their apparent cyclic variations in intensity. *Preprints Fourteenth Conf. on Radar Meteorology*, Tuscon, *Amer. Meteor. Soc.*, 305-308.

Darkow, G. L., and D. W. McCann, 1977: Relative environmental winds for 121 tornado bearing storms. Preprints, 10th Conf. on Severe Local Storms, Omaha, NE, *Amer. Meteor. Soc.*, 413–417.

Davies-Jones, R.P., 1973: The Dependence of Core Radius on Swirl Ratio in a Tornado Simulator. *J. Atmos. Sci.,* **30**, 1427–1430,

Davies-Jones, R. P., 1982: Observational and theoretical aspects of tornadogenesis. *Topics in Atmospheric and Oceanographic Sciences: Intense Atmospheric Vortices,* L. Bengtsson and J. Lighthill, Eds., Springer-Verlag, 175–189.

Davies-Jones, R. P., 1984: Streamwise vorticity: The origin of updraft rotation. *J. Atmos. Sci.,* **41**, 2991–3006.

Davies-Jones, R. P., 1986: Tornado dynamics. Vol. 2, Thunderstorms: A Social and Technological Documentary. 2d ed. E. Kessler, Ed., University of Oklahoma Press, 197–236.

Davies-Jones, R. P., and H. E. Brooks, 1993: Mesocyclogenesis from a theoretical perspective. *The Tornado: Its Structure, Dynamics, Prediction, and Hazards, Geophys. Monogr.,* No. **79**, Amer. Geophys. Union, 105–114.

Davies-Jones, R. P., R. J. Trapp, and H. B. Bluestein, 2001: Tornadoes and tornadic storms. Severe Convective Storms, Meteor Monogr., No. **28**, *Amer. Meteor. Soc.,* 167–222.

DiGangi, E., D. R. MacGorman, C. L. Ziegler, D. Betten, M. Biggerstaff, M. Bowlan, C. Potvin, 2016: An overview of the 29th May 2012 Kingfisher supercell during DC3, *J. Geophys. Res.,* **121***, 14316-14343*.

Doswell, C. A., and P. M. Markowski, 2004: Is buoyancy a relative quantity? *Mon. Wea. Rev.*, **132,** 853–863.

Dowell, D. C., and H. B. Bluestein, 1997: The Arcadia, Oklahoma, storm of 17 May 1981: Analysis of a supercell during tornadogenesis. *Mon. Wea. Rev.,* **125**, 2562–2582.

Dowell, D. C., and H. B. Bluestein, 2002a: The 8 June 1995 McLean, Texas, storm. Part I: Observations of cyclic tornadogenesis. *Mon. Wea. Rev.,* **130**, 2626–2648.

Dowell, D. C., and H. B. Bluestein, 2002b: The 8 June 1995 Mclean, Texas, storm. Part II: cyclic tornado formation, maintenance, and dissipation. *Mon. Wea. Rev.,* **130**, 2649–2670.

Eliasson, A., and E. Kleinschmidt, 1957: Dynamic Meteorology. Handbuch der Physik, Vol 48, Springer Verlag, 1-154.

Fawbush, E. J., and R. C. Miller, 1952: A mean sounding representative of the tornadic air mass environment. *Bull. Amer. Meteor. Soc.,* **33**, 303-307.

Fawbush, E. J., and R. C. Miller,, 1954: The types of air masses in which North American tornadoes from. *Bull. Amer. Meteor. Soc*., **35**, 154-165

Finley, C. A., and B. D. Lee, 2004: High resolution mobile mesonet observations of RFD surges in the June 9 Basset, Nebraska supercell during project ANSWERS 2003. Extended Abstracts, 22nd Conf. on Severe Local Storms, Hyannis, MA, Amer. Meteor. Soc., 11.3. [Available online at http://ams.confex.com/ams/11aram22sls/techprogram/paper_82005.htm].

Finley, C. A., and B. D. Lee, 2008: Mobile mesonet observations of an intense RFD and multiple RFD gust fronts in the May 23 Quinter, Kansas tornadic supercell during TWISTEX 2008. Preprints, 24th Conf. on Severe Local Storms, Savannah, GA, Amer. Meteor. Soc., P3.18. [Available online at http://ams.confex.com/ams/pdfpapers/142233.pdf].

Fisher, M., A. O'Neill, and R. Sutton, 1993: Rapid descent of mesospheric air in the stratospheric polar vortex. *Geophys. Res. Lett.*, **20**, 1267–1270. Froidevaux, L., J. W. Waters, W. G. Read, L. S.

French, M. M., Burgess, D. W., Mansell, E. R., & Wicker, L. J. (2015). Bulk hook echo raindrop sizes retrieved using mobile, polarimetric Doppler radar observations. *J. Appl. Meteor. Climatol.,* **54**, 423–450.

French, M. M., H. B. Bluestein, I. PopStefanija, C. Baldi, and R.T. Bluth, 2014: Mobile, phased-array, Doppler radar observations of tornadoes at X band. *Mon. Wea. Rev.*, **142**, 1010–1036.

French, M. M., Bluestein, H. B., Dowell, D. C., Wicker, L. J., Kramar, M. R., & Pazmany, A. L. (2008). High-resolution, mobile Doppler radar observations of cyclic mesocyclogenesis in a supercell. *Mon. Wea. Rev*, *136*, 4997–5016.

Fujita, T. 1973: Proposed mechanism of tornado formation from rotating thunderstorm. Preprints, *8th Conf. on Severe Local Storms,* Denver, CO, Amer. Meteor. Soc., 191-196.

Fujita, T. T., . 1975: New evidence from the April 3–4, 1974 tornadoes. Preprints, *Ninth Conf. on Severe Local Storms,* Norman, OK, *Amer. Meteor. Soc*., 248–255.

Fujita, T. T., 1981: Tornadoes and downbursts in the context of generalized planetary scales. *J. Atmos. Sci.*, **38,** 1511–1534.

Gaudet, B. J., and W. R. Cotton, 2006: Low-level mesocyclonic concentration by nonaxisymmetric processes. Part I: Supercell and mesocyclone evolution. *J. Atmos. Sci.*, **63**, 1113–1133.

Griffin, C.B., D. J. Bodine, and R.D. Palmer, 0: Kinematic and polarimetric radar observations of the 10 May 2010, Moore-Choctaw Oklahoma, tornadic debris signature. *Mon. Wea. Rev.,* **145**, 2723–2741.

Grzych, M. L., B. D. Lee, C. A. Finley, 2007: Thermodynamic analysis of supercell rear-flank downdrafts from project ANSWERS. *Mon. Wea. Rev.*, **135**, 240–246.

Hane, C.E. and P.S. Ray, 1985: Pressure and buoyancy fields derived from Doppler radar data in a tornadic thunderstorm. *J. Atmos. Sci.,* **42**, 18–35

Heinselman, P. L., D. L. Priegnitz, K. L. Manross, T. M. Smith, and R. W. Adams, 2008: Rapid sampling of severe storms by the National Weather Radar Testbed phased array radar. *Wea. Forecasting*, **23**, 808–824.

Hirth, B. D., J. L. Schroeder, C. C. Weiss, 2008: Surface Analysis of the Rear-Flank Downdraft Outflow in Two Tornadic Supercells. *Mon. Wea. Rev.,* **136**, 2344–2363.

Houston, A. L., 2016: The sensitivity of deep ascent of cold-pool air to vertical shear and cold-pool buoyancy. *Electron. J. Severe Storms Meteor*., **11** (3), 1–29.

Howells, P. A. C., R. Rotunno, and R. K. Smith, 1988: A comparative study of atmospheric and laboratory-analogue numerical tornado-vortex models. *Quart. J. Roy. Meteor. Soc*., **114**, 801–822.

Isom, B., and Coauthors, 2013: The atmospheric imaging radar: Simultaneous volumetric observations using a phased array weather radar. *J. Atmos. Oceanic Technol.*, **30**, 655–675.

Jensen, B., T. P. Marshall, M. A. Mabey, and E. N. Rasmussen, 1983: Storm scale structure of the Pampa storm. Preprints, *13th Conf. on Severe Local Storms,* Tulsa, OK, Amer. Meteor. Soc., 85–88.

Johnson, K. W., P. S. Ray, B. C. Johnson, and R. P. Davies-Jones, 1987: Observations related to the rotational dynamics of the 20 May 1977 tornadic storms. *Mon. Wea. Rev.*, **115,** 2463–2478.

Klemp, J. B., and R. B. Wilhelmson, 1978: The simulation of three-dimensional convective storm dynamics. *J. Atmos. Sci.,***35,** 1070–1096.

Klemp, J. B., and R. B. Wilhelmson, P. S. Ray, 1981: Observed and Numerically Simulated Structure of a Mature Supercell Thunderstorm. *J. Atmos. Sci.*, **38**, 1558–1580.

Klemp, J. B., R. Rotunno, 1983: A study of the tornadic region within a supercell thunderstorm. *J. Atmos. Sci*., **40**, 359–377.

Knupp, K.R., T.A. Murphy, T.A. Coleman, R.A. Wade, S.A. Mullins, C.J. Schultz, E.V. Schultz, L. Carey, A. Sherrer, E.W. McCaul, B. Carcione, S. Latimer, A. Kula, K. Laws, P.T. Marsh, and K. Klockow, 2014: Meteorological overview of the devastating 27 April 2011 tornado outbreak. *Bull. Amer. Meteor. Soc*., **95**, 1041–1062.

Kosiba, K., Wurman, J., Richardson, Y., Markowski, P., Robinson, P., & Marquis, J. (2013). Genesis of the Goshen County, Wyoming tornado on 05 June 2009 during VORTEX2. *Mon. Wea. Rev*, ***151***, 1157–1181.

Kumjian, M. R., 2011: Precipitation properties of supercell hook echoes. *Electron. J. Severe Storms Meteor.*, **6** (5).

Kumjian, M. R., and A. V. Ryzhkov, 2008: Polarimetric signatures in supercell thunderstorms. *J. Appl. Meteor. Climatol.,* **47**, 1940–1961.

Lee, B. D., C. A. Finley, and P. Skinner, 2004: Thermodynamic and kinematic analysis of multiple RFD surges for the 24 June 2003 Manchester, South Dakota cyclic tornadic supercell during Project ANSWERS 2003. Extended Abstracts, 22nd Conf. on Severe Local Storms, Hyannis, MA, Amer. Meteor. Soc., P11.2. [Available online at http://ams.confex.com/ams/11aram22sls/techprogram/paper_82000.htm].

Lee, B. D., C. A. Finley, and T. M. Samaras, 2011: Surface analysis near and within the Tipton, Kansas, tornado on 29 may 2008. *Mon. Wea. Rev*., **139**, 370–386.

Leise, J. A., 1981: A multidimensional scale-telescoped filter and data extension package. NOAA Tech. Memo. ERL WPL-82, 18 pp. [NTIS PB82-164104.].

Lemon, L. R., 1976: The flanking line, a severe thunderstorm intensification source. *J. Atmos. Sci.*, **33,**686–694.

Lemon, L. R., and C. A. Doswell III, 1979: Severe thunderstorm evolution and mesocyclone structure as related to tornadogenesis. *Mon. Wea. Rev.*, **107,** 1184–1197.

Lemon, L.R., D.W. Burgess, and R.A. Brown, 1978: Tornadic storm airflow and morphology derived from single-Doppler radar measurements. *Mon. Wea. Rev.,* **106**, 48–61.

Lewellen, D. C., and W. S. Lewellen, 2007b: Near-surface vortex intensification through corner flow collapse. *J. Atmos. Sci.*, **64**, 2195–2209.

Lilly, D. K., 1982: The development and maintenance of rotation in convective storms. Intense Atmospheric Vortices, L. Bengtsson and J. Lighthill, Eds., Springer-Verlag, 149-160.

Ludlam, F. H., 1963: Severe Local Storms: A review. Severe Local Storms, Meteor. Monogr., No. 27, 1–30.

Lugt, H. J., 1989: Vortex breakdown in atmospheric columnar vortices. *Bull. Amer. Meteor. Soc*., **70**, 1526–1537.

Lund, N. R., D. R. MacGorman, T. J. Schuur, M. I. Biggerstaff, and W. D. Rust, 2009: Relationship between lightning location and polarimetric radar signatures in a small mesoscale convective system. *Mon. Wea. Rev.*, **137**, 4151–4170.

MacGorman, D. R., and Coauthors, 2008: TELEX: The Thunderstorm Electrification and Lightning Experiment. *Bull. Amer. Meteor. Soc.*, **89**, 997–1013.

Maddox, R.A., 1976: An evaluation of tornado proximity wind and stability data. *Mon. Wea. Rev*., **104**, 133–142.

Mansell, E. R., C. L. Ziegler, and E. C. Bruning, 2010: Simulated electrification of a small thunderstorm with two-moment bulk microphysics. *J. Atmos. Sci.*, **67**, 171–194.

Markowski, P. M., 2002: Mobile mesonet observations on 3 May 1999. *Wea. Forecasting*, **17**, 430–444.

Markowski, P. M., 2002: Hook echoes and rear-flank downdrafts: A review. *Mon. Wea. Rev.,* **130**, 852–876.

Markowski, P. M., 2016: An idealized numerical simulation investigation of the effects of surface drag on the development of near-surface vorticity in supercell thunderstorms. *J. Atmos. Sci.*, **73**, 4349–4385.

Markowski, P.M. and Y.P. Richardson, 2014: The influence of environmental low-level shear and cold pools on tornadogenesis: Insights from idealized simulations. *J. Atmos. Sci*., **71**, 243–275.

Markowski, P.M. and Y.P. Richardson, 2017: Large sensitivity of near-surface vertical vorticity development to heat sink location in idealized simulations of supercell-like storms. *J. Atmos. Sci*., **74**, 1095–1104.

Markowski, P.M., J. M. Straka, and E. N. Rasmussen, 2002: Direct surface thermodynamic observations within the rear-flank downdrafts of nontornadic and tornadic supercells. *Mon. Wea. Rev*., **130**, 1692–1722.

Markowski, P.M., J. M. Straka, and E. N. Rasmussen, 2003: Tornadogenesis resulting from the transport of circulation by a downdraft: Idealized numerical simulations. *J. Atmos. Sci*., **60**, 795–823.

Markowski, P.M, M. Majcen, Y. P. Richardson, J. Marquis, and J. Wurman, 2011: Characteristics of the wind field in three nontornadic low-level mesocyclones observed by the Doppler On Wheels radars. *Electron. J. Severe Storms Meteor*. **6** (3), 1–48.

Markowski, P.M., Y. Richardson, E. Rasmussen, J. Straka, R. Davies-Jones, R. J. Trapp, 2008: Vortex lines within low-level mesocyclones obtained from pseudo-dual-Doppler radar observations. *Mon. Wea. Rev.*, **136**, 3513–3535.

Markowski, P. M., Richardson, Y., Marquis, J., Davies-Jones, R. P., Wurman, J., Kosiba, K., Dowell, D.C. 2012: The Pretornadic Phase of the Goshen County, Wyoming, Supercell of 5 June 2009 Intercepted by VORTEX2. Part I: Evolution of Kinematic and Surface Thermodynamic Fields. *Mon. Wea. Rev*, ***140***, 2916–2938.

Markowski, P. M., and Coauthors, 2012: The pretornadic phase of the Goshen County, Wyoming, supercell of 5 June 2009 intercepted by VORTEX2. Part II: Intensification of low-level rotation. *Mon. Wea. Rev.*, **140**, 2916–2938.

Marquis, J., Y. Richardson, J. Wurman, and P. Markowski, 2008: Single- and dual-Doppler analysis of a tornadic vortex and surrounding storm-scale flow in the Crowell, Texas, supercell of 30 April 2000. *Mon. Wea. Rev.,* **136**, 5017–5043.

Marquis, J., Y. P. Richardson, P. M. Markowski, D. C. Dowell, and J. Wurman, 2012: Tornado maintenance investigated with high-resolution dual-Doppler and EnKF analysis. *Mon. Wea. Rev*., **140**, 3–27.

Marquis, J., Y. Richardson, P. Markowski, J. Wurman, K. Kosiba, and P. Robinson, 2016: An investigation of the Goshen County, Wyoming, tornadic supercell of 5 June 2009 using EnKF assimilation of mobile mesonet and radar observations collected during VORTEX2. Part II: Mesocyclone-scale processes affecting tornado formation, maintenance, and decay. *Mon. Wea. Rev.,* **144**, 3441–3463

Marwitz, J. D., 1972: The structure and motion of severe hailstorms. Part I: Supercell storms. *J. Appl. Meteor*., **11**, 166-179

Mashiko, W., H. Niino, T. Kato, 2009: Numerical simulation of tornadogenesis in an outer-rainband minisupercell of typhoon Shanshan on 17 September 2006. *Mon. Wea. Rev*., **137**, 4238–4260.

Miller, L. J., and S. M. Fredrick, 1998: Custom Editing and Display of Reduced Information in Cartesian space (CEDRIC) manual. National Center for Atmospheric Research, Mesoscale and Microscale Meteorology Division, Boulder, CO, 130 pp.

Mohr, C. G., L. J. Miller, R. L. Vaughan, and H. W. Frank, 1986: The merger of mesoscale datasets into a common Cartesian format for efficient and systematic analyses. *J. Atmos. Oceanic Technol*., **3**, 143–161.

Moller, A. R., C. A. Doswell, M. P. Foster, G. R. Woodall, 1994: The operational recognition of supercell thunderstorm environments and storm structures. *Wea. Forecasting*, **9**, 327–347.

Moncrieff, and M. J. Miller, 1976: The dynamics and simulation of tropical cumulonimbus and squall lines. *Quart. J. Roy. Meteor. Soc*.,**102**, 373–394.

Naylor, J., M. A., Askelson, and M. S.Gilmore, 2012. Influence of low-level thermodynamic structure on the downdraft properties of simulated supercells. *Mon. Wea. Rev*, **140**, 2575–2589.

Nelson, S. P., 1977: Rear flank downdraft: A hailstorm intensification mechanism. *Preprints 10th Conf. on Severe Local Storms, Omaha, Amer. Meteor. Soc., 521-525*.

Newton, C.W., 1963: Dynamics of severe convective storms. *Severe Local Storms, Meteor. Monogr.*, No. **5**, *Amer. Meteor. Soc.,* 33–58.

Newton, C.W. and H. Rodebush Newton, 1959: Dynamical interactions between large convective clouds and environment with vertical shear. *J. Meteor.*, **16**, 483–496.

Newton, C.W. and J.C. Fankhauser, 1964: On the movements of convective storms, with emphasis on size discrimination in relation to water-budget requirements. *J. Appl. Meteor.,* **3**, 651–668

O'Brien, J. J., 1970: Alternative solutions to the classical vertical velocity problem. *J. Appl. Meteor.*, **9**, 197–203

Pauley, R. L., and J. T. Snow, 1988: On the kinematics and dynamics of the 18 July 1986 Minneapolis tornado. *Mon. Wea. Rev.*, **116**, 2731–2736

Ramond, D., 1978: Pressure perturbations in deep convection: An experimental study. *J. Atmos. Sci.* **35**, 1704-1711

Rasmussen, E.N. and J.M. Straka, 1998: Variations in supercell morphology. Part I: Observations of the role of upper-level storm-relative flow. *Mon. Wea. Rev.,* **126**, 2406–2421

Rasmussen, E. N., R. E. Peterson, J. E. Minor, and B. D. Campbell, 1982: Evolutionary characteristics and photogrammetric determination of wind speeds within the Tulia outbreak tornadoes 28 May 1980. Preprints, *12th Conf. on Severe Local Storms,* San Antonio, TX, *Amer. Meteor. Soc.*, 301–304.

Ray, P.S., C.L. Ziegler, W. Bumgarner, and R.J. Serafin, 1980: Single- and multiple-Doppler radar observations of tornadic storms. *Mon. Wea. Rev.,* **108**, 1607–1625.

Ray, P. S., B. C. Johnson, K. W. Johnson, J. S. Bradberry, J. J. Stephens, K. K. Wagner, R. B. Wilhelmson, and J. B. Klemp, 1981: The morphology of severe tornadic storms on 20 May 1977. *J. Atmos. Sci.,* **38**, 1643-1663.

Richardson, Y., P. M. Markowski, J. Marquis, J. Wurman, K. Kosiba, P. Robinson, D. Burgess, and C. Weiss, 2012: Tornado maintenance and demise in the Goshen County, Wyoming supercell of 5 June 2009 intercepted by VORTEX2. 26th Conf. on Severe Local Storms, Nashville, TN, Amer. Meteor. Soc., 13.3. [Available online at https://ams.confex.com/ams/26SLS/webprogram/Paper212526.html.]

Riganti, C.J. and A.L. Houston, 2017: Rear-Flank Outflow Dynamics and Thermodynamics in the 10 June 2010 Last Chance, Colorado, Supercell. *Mon. Wea. Rev.,* **145**,2487–2504.

Palucki, J. L., M. I. Biggerstaff, D. R. MacGorman, and T. Schuur, 2011: Comparison between low-flash and non-lightning-producing convective areas within a mature mesoscale convective system. *Wea. Forecasting*, **26**, 468–486,

Payne, C. D., T. J. Schuur, D. R. MacGorman, M. I. Biggerstaff, K. Kuhlman, and W. D. Rust, 2010: Polarimetric and electrical characteristics of a lightning ring in a supercell storm. *Mon. Wea. Rev.*, **138**, 2405–2425.

Rott, N., 1958: On the viscous core of a line vortex. *Z. Angew. Math. Phys.*, **9**, 543–553.

Rotunno, R., 1981: On the evolution of thunderstorm rotation. *Mon. Wea. Rev*., **109**, 577–586.

Rotunno, R., 1984: Investigation of a three-dimensional asymmetric vortex. *J. Atmos. Sci.,***41,** 283–298.

Rotunno, R., and J. B. Klemp, 1982: The influence of the shear-induced pressure gradient on thunderstorm motion. *Mon. Wea. Rev.*, **110,** 136–151.

Rotunno, R., and J. B. Klemp, 1985: On the rotation and propagation of simulated supercell thunderstorms. *J. Atmos. Sci.*, **42**, 271–292

Schenkman, A. D., M. Xue, and A. Shapiro, 2012: Tornadogenesis in a simulated mesovortex within a mesoscale convective system. *J. Atmos. Sci.*, **69**, 3372–3390.

Schenkman, A. D., M. Xue, and M. Hu, 2014: Tornadogenesis in a high-resolution simulation of the 8 May 2003 Oklahoma City supercell. *J. Atmos. Sci.*, **71**, 130–154.

Schenkman, A.D., M. Xue, and D.T. Dawson II, 2016: The cause of internal outflow surges in a high-resolution simulation of the 8 May 2003 Oklahoma City tornadic supercell. *J. Atmos. Sci*., **73**, 353–370.

Schlesinger, R.E., 1975: A three-dimensional numerical model of an isolated deep convective cloud: Preliminary results. *J. Atmos. Sci*., **32**, 934–957,

Schlesinger, R.E., 1978: A three-dimensional numerical model of an isolated thunderstorm: Part I. Comparative experiments for variable ambient wind shear. *J. Atmos. Sci*., **35**, 690–713.

Sibson, R., 1981: A brief description of natural neighbor interpolation. *Interpreting Multivariate Data*, V. Barnett, Ed., Wiley, 22–36.

Simpson, J.,1982: Cumulus rotation: Model and observations of a waterspout-bearing cloud system. *Intense Atmospheric Vortices.* L. Bengtsson and J. Lighthill, Editors. Springer-Verlag, 161–173.

Shabbott, C. J., and P. M. Markowski, 2006: Surface in situ observations within the outflow of forward-flank downdrafts of supercell thunderstorms. *Mon. Wea. Rev.*, **134,** 1422–1441.

Shen, Y., and G. Zha, 2010: Improvement of the WENO scheme smoothness estimator. *Int. J. Numer. Methods Fluids*, **64**, 653–675.

Skinner, P. S., C. C. Weiss, J. L. Schroeder, L. J. Wicker, and M. I. Biggerstaff, 2011: Observations of the surface boundary structure within the 23 May 2007 Perryton, Texas, supercell. *Mon. Wea. Rev*., **139**, 3730–3749.

Skinner, P. S., Weiss, C. C., French, M. M., Bluestein, H. B., Markowski, P. M., & Richardson, Y. P. (2014). VORTEX2 observations of a low-level mesocyclone with multiple internal rear-flank downdraft momentum surges in the 18 May 2010 Dumas, Texas, supercell. *Mon. Wea. Rev*, ***142***, 2935–2960.

Skinner, P.S., C.C. Weiss, L.J. Wicker, C.K. Potvin, and D.C. Dowell, 2015: Forcing mechanisms for an internal rear-flank downdraft momentum surge in the 18 May 2010 Dumas, Texas, Supercell. *Mon. Wea. Rev.,* **143**, 4305–4330

Smagorinsky, J., 1963: General circulation experiments with the primitive equations. I. The basic experiment. *Mon. Wea. Rev.*, **91**, 99–164.

Storm Data is a list of severe weather observations across the United States. It is published on a monthly basis by the National Climatic Data Center (Available from NCDC, Federal Building, Asheville, NC 28801-2696). NCDC, 2004: *Storm Data*. Vol. 48, No. 6, 486 pp.

Straka, J. M., E. N. Rasmussen, and S. E. Fredrickson, 1996: A mobile mesonet for finescale meteorological observations. *J. Atmos. Oceanic Technol.*, **13**, 921–936

Straka, J. M., E. N. Rasmussen, R. P. Davies-Jones, and P. M. Markowski, 2007: An observational and idealized numerical examination of low-level counter-rotating vortices in the rear flank of supercells. *Electron. J. Severe Storms Meteor.*

Supinie, T.A., Y. Jung, M. Xue, D.J. Stensrud, M.M. French, and H.B. Bluestein, 2016: Impact of VORTEX2 observations on analyses and forecasts of the 5 June 2009 Goshen County, Wyoming, supercell. *Mon. Wea. Rev.,* **144**, 429–449.

Thompson, R. L., R. Edwards, J. A. Hart, K. L. Elmore, and P. M. Markowski, 2003: Close proximity soundings within supercell environments obtained from the Rapid Update Cycle. *Wea. Forecasting*, **18**, 1243–1261.

Trapp, R.J., 1999: Observations of nontornadic low-level mesocyclones and attendant tornadogenesis failure during VORTEX. *Mon. Wea. Rev.*, **127**, 1693–1705.

Trapp, R J., and B.H. Fiedler, 1995: Tornado-like vortexgenesis in a simplified numerical model. *J. Atmos. Sci.,* **52**, 3757–3778,

Trapp, R.J., G.J. Stumpf, and K.L. Manross, 2005: A Reassessment of the percentage of tornadic mesocyclones. *Wea. Forecasting*, **20**, 680–687

van den Heever, S. C., and W. R. Cotton, 2004: The impact of hail size on simulated supercell storms. *J. Atmos. Sci.*, **61**, 1596–1609

Waugh, S., and S. E. Fredrickson, 2010: An improved aspirated temperature system for mobile meteorological observations, especially in severe weather. 25th Conf. on Severe Local Storms, Denver, CO, *Amer. Meteor. Soc.*, P5.2. [Available online at https://ams.confex.com/ams/25SLS/webprogram/ Paper176205.html.]

Wakimoto, R. M., and C. Liu, 1998: The Garden City, Kansas, storm during VORTEX 95. Part II: The wall cloud and tornado. *Mon. Wea. Rev.*, **126**, 393–408.

Wakimoto, R. M., and H. Cai, 2000: Analysis of a nontornadic storm during VORTEX 95. *Mon. Wea. Rev.*, **128,** 565–592.

Walko, R. L., 1993: Tornado spin-up beneath a convective cell: Required basic structure of the near-field boundary layer winds. *The Tornado: Its Structure, Dynamics, Prediction, and Hazards, Geophys. Monogr.,* No. 79, Amer. Geophys. Union, 89–95.

Ward, N. B., 1972: The exploration of certain features of tornado dynamics using a laboratory model. *J. Atmos. Sci.*, **29**, 1194–1204.

Weisman, M.L. and J.B. Klemp, 1984: The structure and classification of numerically simulated convective storms in directionally varying wind shears. *Mon. Wea. Rev.,* **112**, 2479–2498.

Weiss, C. C., and J. L. Schroeder, 2008: StickNet—Anew portable, rapidly-deployable, surface observing system. Preprints, 25th Int. Conf. on Interactive Information Processing Systems for Meteorology, Oceanography, and Hydrology, New Orleans, LA, Amer. Meteor. Soc., P4A.1. [Available online at http:// ams.confex.com/ams/pdfpapers/134047.pdf.]

Weiss, S.A., D.R. MacGorman, and K.M. Calhoun, 2012: Lightning in the anvils of supercell thunderstorms. *Mon. Wea. Rev.*, **140**, 2064–2079.

Weiss, C. C., D. C. Dowell, J. L. Schroeder, P. S. Skinner, A. E. Reinhart, P. M. Markowski, and Y. P. Richardson, 2015: A comparison of near-surface buoyancy and baroclinity across three VORTEX2 supercell intercepts. *Mon. Wea. Rev.*, **143**, 2736–2753.

Wicker, L. J., and R. B. Wilhelmson, 1995: Simulation and analysis of tornado development and decay within a three-dimensional supercell thunderstorm. *J. Atmos. Sci.*, **52**, 2675–2703.

Wood, V.T., R.A. Brown, and D.W. Burgess, 1996: Duration and movement of mesocyclones associated with southern great plains thunderstorms. *Mon. Wea. Rev.,* **124**, 97–101.

Wurman, J. and K. Kosiba, 2013: Finescale radar observations of tornado and mesocyclone structures. *Wea. Forecasting*, **28**, 1157–1174

Wurman, J., J. Straka, E. Rasmussen, M. Randall, and A. Zahrai, 1997: Design and deployment of a portable, pencil-beam, pulsed, 3-cm Doppler radar. *J. Atmos. Oceanic Technol.*, **14,** 1502–1512.

Wurman, J., Y. Richardson, C. Alexander, S. Weygandt, and P. Zhang, 2007: Dual-Doppler and single-Doppler analysis of a tornadic storm undergoing mergers and repeated tornadogenesis. *Mon. Wea. Rev.,* **135**, 736–758.

Wurman, J., Kosiba, K., Markowski, P., Richardson, Y., Dowell, D., & Robinson, P. (2010). Finescale single-and dual-Doppler analysis of tornado intensification, maintenance, and dissipation in the Orleans, Nebraska, Supercell. *Mon. Wea. Rev., **138***, 4439–4455

Wurman, J., D. Dowell, Y. Richardson, P. Markowski, E. Rasmussen, D. Burgess, L. Wicker, and H. B. Bluestein, 2012: The second Verification of the Origins of Rotation in Tornadoes Experiment: VORTEX2. *Bull. Amer. Meteor. Soc.*, **93**, 1147–1170,

Ziegler, C. L., 1985: Retrieval of thermal and microphysical variables in observed convective storms. Part I: Model development and preliminary testing. *J. Atmos. Sci.*, **42**, 1487–1509.

Ziegler, C. L., 2013: A diabatic Lagrangian technique for the analysis of convective storms. Part I: Description and validation via an observing system simulation experiment. *J. Atmos. Oceanic Technol.*, **30**, 2248–2265

Ziegler, C.L., 2013: A diabatic Lagrangian technique for the analysis of convective storms. Part II: Application to a radar-observed storm. *J. Atmos. Oceanic Technol*., **30**, 2266–2280

Ziegler, C. L., E. R. Mansell, J. M. Straka, D. R. MacGorman, D. W. Burgess, 2010: The impact of spatial variations of low-level stability on the life cycle of a simulated supercell storm. *Mon. Wea. Rev.*, **138**, 1738–1766.

Ziegler, C. L, E. N. Rasmussen, T. R. Shepherd, A. I. Watson, and J. M. Straka, 2001: The evolution of low-level rotation in the 29 May 1994 Newcastle–Graham, Texas, storm complex during VORTEX. *Mon. Wea. Rev.*, **129,** 1339–1368.